2013-05-10

Determinants of Synaptic Integration in Cerebellar Neurons

Engbers, Jordan David Thomas

UNIVERSITY OF CALGARY

Determinants of Synaptic Integration in Cerebellar Neurons

by

Jordan David Thomas Engbers

A THESIS

SUBMITTED TO THE FACULTY OF GRADUATE STUDIES

IN PARTIAL FULFILMENT OF THE REQUIREMENTS FOR THE

DEGREE OF DOCTOR OF PHILOSOPHY

DEPARTMENT OF NEUROSCIENCE

CALGARY, ALBERTA

MAY, 2013

Abstract

The integration of synaptic inputs by neurons relies on protein channels that conduct specific ions. Cav3 calcium (Ca^{2+}) channels can amplify excitatory postsynaptic potentials (EPSPs) while Ca^{2+}-activated potassium (K_{Ca}) channels decrease EPSP amplitude. By comparison, inhibitory postsynaptic potentials (IPSPs) can activate hyperpolarization-activated (HCN) channels that generate a rebound excitatory current at the end of an inhibitory stimulus. This thesis examines how Cav3, K_{Ca}, and HCN channels control synaptic integration in cerebellar Purkinje cells and deep cerebellar nuclei (DCN) neurons. These two populations of neurons are central to cerebellar function and represent a dichotomy of synaptic processing, as Purkinje cells receive primarily excitatory inputs, while DCN neurons receive mainly inhibitory inputs.

I tested the hypothesis that Cav3-mediated Ca^{2+} current activates K_{Ca} channels to control the summation of parallel fibre EPSPs in Purkinje cells. Patch clamp recordings from *in vitro* slices of rat cerebellum showed that Cav3 current activates intermediate conductance K_{Ca} ($K_{Ca}3.1$) channels, which have previously never been found in central neurons. $K_{Ca}3.1$ channels are activated at hyperpolarized membrane voltages, due to an extended Cav3 channel window current, and suppress summation of low-frequency EPSPs. Dynamic clamp experiments and computer simulations revealed that the Cav3-$K_{Ca}3.1$ complex increases the signal-to-noise ratio for sensory-like parallel fibre inputs undergoing short-term facilitation by selectively suppressing background inputs.

In DCN neurons, I tested the hypothesis that Cav3 and HCN channels control the frequency and timing of rebound bursts following inhibition by IPSPs. The results demonstrate that Cav3 and HCN currents are activated during physiological levels of hyperpolarization and modulate rebound bursts. A novel model of a DCN neuron showed that Cav3 current is solely responsible for generation of the rebound burst, while HCN channels increase burst frequency and temporal precision.

Together, this research demonstrates how a novel Cav3-$K_{Ca}3.1$ channel complex participates in the processing of excitatory inputs, and identifies a new synergistic interaction between ion channels that enables processing of inhibitory inputs. These findings illustrate the importance of ion channel interactions for signal processing in the cerebellum, with far reaching implications for neural circuits throughout the brain.

Acknowledgements

First and foremost, I would like to thank my supervisor, Dr. Ray W. Turner, for the years of guidance, instruction and support he has given me. He is a shining example of what it means to be a mentor. I would also like to thank the members of my supervisory committee, Drs. Patrick Whelan and Anders Nygren, for their ever-constructive input on my thesis and for many useful insights that improved the quality of my research. I also thank Dr. Dustin Anderson, who has been a steadfast friend and collaborator throughout my graduate studies. During my years in the Turner lab, I have had the opportunity to work with many great people who have trained me and inspired me to continuously improve. I would like to thank Drs. Bruce McKay, Hamish Mehaffey, Fernando Fernandez, and Michael Molineux for training me when I started in the lab and for always pushing me to be a better scientist. Dr. Gerald Zamponi and the members of his lab, including Shahid Hameed and Renata Rehak, were great collaborators on several projects and provided valuable data and insights. Finally, I thank all the members of the lab, past and present, including Mirna Kruskic and Drs. Colin Heath, Theodore Bartoletti, Reza Tadayonnejad, and Hadhimulya Asmara for their continuous support. The work in this thesis was funded by operating grants from the Canadian Institute for Health Research (CIHR) and by several studentships, including the Alberta Innovates – Health Solutions (AI-HS) Doctoral Studentship, CIHR CGS Banting and Best Doctoral Award, Dr. T. Chen Fong Doctoral Scholarship in Neuroscience, and Izaak Walton Killam Doctoral Scholarship.

Dedication

To my father and mother, who taught me the value of a critical mind.

To my loving wife, whose support has never wavered.

Table of Contents

List of Tables

List of Figures and Illustrations

List of Symbols, Abbreviations and Nomenclature

Symbol	Definition
4-AP	4-aminopyridine
aCSF	Artificial cerebrospinal fluid
ADP	Afterdepolarization
AgTx	ω-Agatoxin-IVA
AHP	Afterhyperpolarization
AMPA	(2-amino-3-(3-hydroxy-5-methyl-isoxazol-4-yl)propanoic acid)
Ba^{2+}	Barium
BAPTA	1,2-Bis(2-Aminophenoxy)ethane-*N,N,N′,N′*-tetraacetic acid
Ca^{2+}	Calcium
$[Ca^{2+}]_i$	Intracellular calcium concentration
$[Ca^{2+}]_o$	Extracellular calcium concentration
CaM	Calmodulin
Cav3	Low voltage-gated calcium channel, T-type
CB1	Endocannabinoid receptor
CbTx	Charybdotoxin
Cs^{+}	Cesium
Cd^{2+}	Cadmium
CF	Climbing fibre
Cl^{-}	Chloride
CNS	Central nervous system
DCN	Deep cerebellar nuclei
DIC-IR	Differential interference contrast microscopy with infrared light
DL-AP5	DL-2-Amino-5-phosphonopentanoic acid
DNQX	6,7-dinitroquinoxaline-2,3-dione
dynEPSC	Dynamic clamp excitatory postsynaptic current
dynEPSP	Dynamic clamp excitatory postsynaptic potential
E_x	Reversal potential for ionic species *x*
EGTA	Ethylene glycol tetraacetic acid
EPSC	Excitatory postsynaptic current
EPSP	Excitatory postsynaptic potential
FSL	First spike latency
GABA	γ-amino butyric acid
HCN	Hyperpolarization-activated nucleotide-gated channel
HEPES	4-(2-hydroxyethyl)-1-piperazineethanesulfonic acid
HVA	High voltage-activated
IbTx	Iberiotoxin
IC_{50}	Half-maximal concentration
I_H	Hyperpolarization-activated inward current
I_{sAHP}	Current underlying a slow afterhyperpolarization
IP_3	Inositol triphosphate
IPSC	Inhibitory postsynaptic current
IPSP	Inhibitory postsynaptic potential
ISI	Interspike interval

I_T	T-type calcium current
K^+	Potassium
K_{Ca}	Calcium-dependent potassium channel
K_D	Dissociation constant
LVA	Low voltage-activated
MF	Mossy fibre
Mg^{2+}	Magnesium
mGluR	Metabotropic glutamate receptor
Na^+	Sodium
Ni^{2+}	Nickel
NMDA	N-methyl D-aspartate
PF	Parallel fibre
PKA	Protein kinase A
PSC	Postsynaptic current
R_m	Membrane resistance
simEPSC	Simulated excitatory postsynaptic current
simEPSP	Simulated excitatory postsynaptic potential
SNR	Signal-to-noise ratio
TEA	Tetraethylammonium
TRAM-34	1-[(2-Chlorophenyl)diphenylmethyl]-1H-pyrazole
V_a	Half-activation voltage
VGCC	Voltage-gated calcium channel
V_h	Half-inactivation voltage
V_m	Membrane voltage

Epigraph

Go, wondrous creature! Mount where science guides,
Go, measure earth, weigh air, and state the tides;
Instruct the planets in what orbs to run,
Correct old time, and regulate the sun;
Go, soar with Plato to th' empyreal sphere,
To the first good, first perfect, and first fair;
Or tread the mazy round his followers trod,
And quitting sense call imitating God;
As Eastern priests in giddy circles run,
And turn their heads to imitate the sun.
Go, teach Eternal Wisdom how to rule—
Then drop into thyself, and be a fool! …

Could he, whose rules the rapid comet bind,
Describe or fix one movement of his mind?

- Alexander Pope, *An Essay on Man*

Chapter One: Introduction

1.1 General introduction

The neuron is the principle unit of computation within the brain (Mcculloch and Pitts, 1990; Zador, 2000). Complex neural functions, such as learning and memory, rely on the ability of individual neurons to continuously perform computations in parallel, communicate effectively and adapt to information over time. Therefore, each neuron must be able to process, communicate and store information. In order to perform computations, neurons express *ion channels* with complex gating mechanics and temporal dynamics that, when combined, are capable of generating highly nonlinear voltage responses, such as *action potentials* (**Fig. 1.1**). The action potential, or *spike*, is an "all-or-nothing", large-amplitude voltage deviation capable of being transmitted over large distances and can be thought of as the fundamental unit of information in the brain (**Fig. 1.1*B***). As such, all neuronal processing depends on the appropriate generation and transmission of action potentials. The ion channel conductances underlying action potentials have been studied extensively, beginning with Hodgkin and Huxley's characterization of sodium (Na^+) and potassium (K^+) currents in the squid giant axon (Hodgkin and Huxley, 1952). Likewise, the transmission of the action potential is well understood. Na^+-dependent spikes are typically generated near the soma and propagate down the axon resulting in the release of neurotransmitter from synaptic terminals, which, in turn, activates receptors on the postsynaptic cell. Nevertheless, the mechanisms by which a neuron can integrate hundreds of thousands of synaptic inputs to generate the correct series of action potentials are still under active investigation.

While the action potential is the fundamental unit of neuronal information, the synapse is the principle substrate for communication between neurons, transmitting information regarding spike timing and frequency to other neurons. Depolarization of the presynaptic terminal during a spike causes a calcium (Ca^{2+}) -dependent release of neurotransmitters into the synaptic cleft. Neurotransmitters bind to receptors in the postsynaptic membrane, causing ion channels to open and generate postsynaptic currents (PSCs) that cause deflections in membrane potential. For example, glutamate can activate N-methyl-D-aspartate (NMDA) or 2-amino-3-(3-hydroxy-5-methyl-isoxazol-4-yl)propanoic

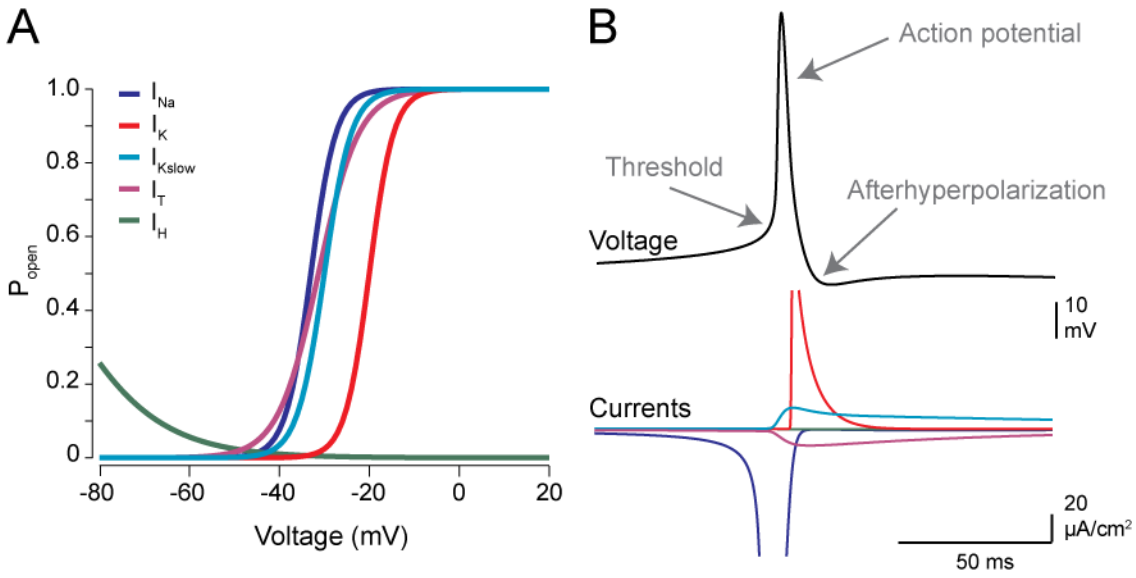
A
1.0
0.8
0.6
0.4
0.2
0
P open
I Na
I K
I Kslow
I T
I H
-80
-60
-40
-20
0
20
Voltage (mV)
B
Action potential
Threshold
Afterhyperpolarization
Voltage
10
mV
Currents
20
μA/cm2
50 ms

Figure 1.1: Voltage-dependent ion channels interact to generate nonlinear phenomena

(A) Steady-state activation plots show voltage-dependencies for several different ion channel models. Voltage-dependent activation curves are described by a Boltzmann function. I_H shows a reversed voltage-dependence compared to the K^+, Na^+, and Ca^{2+} conductances. Variability in voltage-dependencies allows currents to be activated at different times during action potentials. **(B)** The voltage trace (*top*) and underlying current traces (*bottom*) for an action potential from a model of a DCN neuron. Interactions of inward (negative-going) and outward (positive-going) currents with different voltage-dependencies and kinetics allow for generation of action potentials.

acid (AMPA) ionotropic receptors, resulting in excitatory postsynaptic currents (EPSCs). On the other hand, binding of the neurotransmitter γ-aminobutyric acid (GABA) to $GABA_A$ receptors results in inhibitory postsynaptic currents (IPSCs). Synaptic integration – the summation of changes in membrane voltage caused by synaptic inputs – ultimately drives the generation of action potentials in synaptic targets, propagating information throughout the network.

Some neural network models simplify the process of synaptic integration to the linear sum of weighted synaptic inputs (Mcculloch and Pitts, 1990). However, synaptic integration is a complex, nonlinear process which involves presynaptic components of synaptic plasticity, such as short-term facilitation and depression of transmitter release, as well as postsynaptic determinants, such as receptor subtype, dendritic morphology, and ion channel expression. Understanding how these factors govern synaptic integration is essential to understanding how the nervous system functions.

The cerebellum is an ideal area to study synaptic processing in individual neurons and the contributions of neuron behaviour to circuit function. It has a well-characterized connectivity and a comparatively small number of neuronal classes with clearly defined subsets of excitatory and inhibitory synaptic inputs, allowing for comparisons of synaptic processing behaviour. Furthermore, the two principal neurons of the cerebellum, Purkinje cells and neurons of the Deep Cerebellar Nuclei (DCN) represent a dichotomy of synaptic processing, with Purkinje cells receiving primarily excitatory inputs and DCN neurons receiving primarily inhibitory inputs.

This thesis examines the role of postsynaptic ion channels on synaptic integration in the principal neurons of the cerebellum, as well as their interplay with presynaptic short-term plasticity.

1.2 Postsynaptic ion channels

The electrical potential or *voltage* that exists across a neuron's membrane results from ionic gradients generated by both passive distribution and active transport of ions. These electrochemical gradients are the driving force for neural activity, reflected in the movement of ions into and out of the cell. Ion channels allow the movement of otherwise membrane-impermeant ions across the membrane, thus generating voltage changes which

are the basis for neuronal function. Currents that result in membrane depolarization, or movement towards positive potentials, are conventionally termed *inward* currents; currents resulting in hyperpolarization, or movements to more negative potentials, are termed *outward* currents. The direction of current flow is determined by the distance of the *membrane voltage* (V_m) to the *reversal potential* (E) for the particular ion species, the voltage at which the electrical and chemical gradients for an ion are at equilibrium. Each ion channel has specific permeabilities for various ionic species, most commonly K^+, Na^+, Ca^{2+}, and chloride (Cl^-). At physiological potentials, influx of Na^+ and Ca^{2+} causes depolarization while K^+ efflux and Cl^- influx are hyperpolarizing.

Most ion channels do not allow the passive movement of ions across the membrane, but tightly regulate currents by a complex gating process of activation, deactivation, and inactivation. Furthermore, gating of the channel can be controlled by a variety of signals, such as changes in voltage, binding of neurotransmitters as receptor ligands, or changes in intracellular Ca^{2+} concentration ($[Ca^{2+}]_i$). In the following sections, I will examine the properties of several voltage-gated ion channels and Ca^{2+}-dependent K^+ (K_{Ca}) channels relevant to this thesis.

1.2.1 Voltage-gated ion channels

Voltage-gated ion channels have a nonlinear relationship with voltage that is different for each channel subtype (**Fig. 1.1*A***). Furthermore, ion channel subtypes exhibit specific dynamics, allowing various currents to be active at different times and voltages (**Fig. 1.1*B***), providing sources of both voltage- and time-dependent nonlinearities. When different currents are combined, a wide variety of voltage responses can be observed, such as action potentials (**Fig. 1.1*B***).

While there are many voltage-gated ion channels, we will limit our discussion to two different families: voltage-gated Ca^{2+} channels (VGCCs), particularly low voltage-activated Cav3 Ca^{2+} channels, and hyperpolarization-activated cyclic nucleotide-gated (HCN) channels.

1.2.1.1 Cav3 Ca^{2+} channels

Ca^{2+} is an important intracellular signalling molecule with a multitude of effects on cellular processes. Firstly, Ca^{2+} entry causes membrane depolarization and can result in the generation of Ca^{2+} spikes, burst activity and excitatory postsynaptic potential (EPSP) amplification. Secondly, Ca^{2+} acts as a second-messenger, interacting with intracellular proteins to control signalling cascades. In neurons, Ca^{2+} entry is necessary for the release of vesicles from synapses and for induction of long-term synaptic plasticity. Furthermore, rises in $[Ca^{2+}]_i$ activate certain K^+ and Cl^- channels. Due to the varying effects of Ca^{2+} on intracellular processes, $[Ca^{2+}]_i$ must be tightly regulated. Ca^{2+} is quickly bound upon entry by intracellular buffers, sequestered in internal organelles, or extruded through channel pumps. However, the initial entry of Ca^{2+} itself is tightly controlled by VGCCs.

VGCCs conduct Ca^{2+} into the neuron at physiological potentials. Ca^{2+} channels are heterotetrameric proteins made up of a single polypeptide of four homologous domains (I-IV), each one containing six transmembrane segments (Talavera and Nilius, 2006) (**Fig. 1.2*A***). The N- and C-termini are cytosolic, as are the three linkers between the domains, and provide sites for interaction with other intracellular proteins, such as protein kinases, ion channels, and calmodulin (Iftinca et al., 2007; Iftinca and Zamponi, 2009; Turner et al., 2011). Like other voltage-gated channels, voltage-dependence is conferred via positively charged residues on the fourth transmembrane segment (S4) in each domain. A low resting level of $[Ca^{2+}]_i$ in neurons (~100 nM) but high (1.5 mM) extracellular Ca^{2+} concentration ($[Ca^{2+}]_o$) establishes a positive reversal potential for Ca^{2+} (E_{Ca}), providing a strong inward driving force during physiological processes. While VGCCs have greatest permeability for Ca^{2+}, permeability to K^+ and other ions causes E_{Ca} to deviate from the predicted Nernst potential, approaching approximately +40 mV under physiological conditions, as determined by the more appropriate Goldmann-Hodgkin-Katz equation.

Multiple VGCC subtypes have been identified in neurons. These can be broadly classified as high voltage-activated (HVA) and low voltage-activated (LVA). HVA Ca^{2+} channels include Cav1.1-1.4 (L-type), Cav2.1 (P/Q-type), Cav2.2 (N-type) and Cav2.3 (R-type), although Cav2.3 has an activation voltage that tends to be more hyperpolarized.

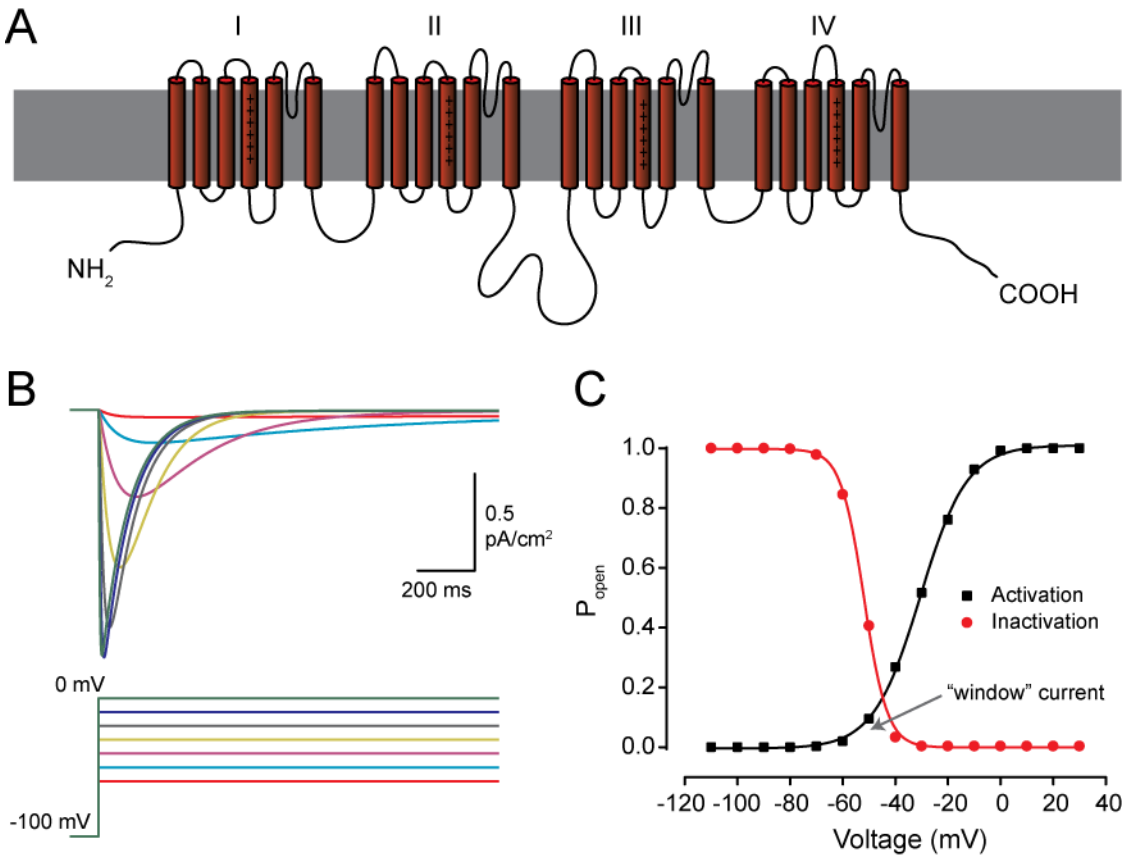
A
I
II
III
IV
NH2
COOH
B
0.5
pA/cm2
200 ms
0 mV
-100 mV
C
1.0
0.8
0.6
0.4
0.2
0.0
Popen
Activation
Inactivation
"window" current
-120 -100 -80 -60 -40 -20 0 20 40
Voltage (mV)

Figure 1.2: Structure and properties of Cav3 channels

(A) A diagram of the heterotetrameric structure of the Cav3 channel α-subunit illustrates the four homologous domains (I - IV) joined by intracellular linkers. Each domain is comprised of six transmembrane segments with the fourth segment (S4) containing positive residues involved with voltage gating. Intracellular linkers and N- and C-termini provide sites for intracellular protein-protein interactions and phosphorylation. **(B)** Simulated I_T based on a published model (Chen and Hess, 1990). The model was held at -100 mV and voltage was increased in 10 mV steps (*bottom*). Currents are detected by -60 mV (*red*), with larger depolarization causing increased activation and faster inactivation, resulting in a transient current that exhibits a "cross-over" at higher levels of depolarization due to the voltage-dependence of inactivation. **(C)** Activation (*black*) and inactivation (*red*) plots of Cav3 channels overlap to create a "window" current that straddles resting potential and spike threshold where Cav3 channels are constitutively active.

LVA Ca^{2+} channels are also known as T-type channels and are comprised solely of the Cav3 family of Ca^{2+} channels. To date, three family members (Cav3.1-Cav3.3) have been discovered and all are prominently expressed throughout the CNS (Craig et al., 1999; Talley et al., 1999; McKay et al., 2006; Talavera and Nilius, 2006).

Cav3 channels have distinct biophysical and pharmacological properties. They have a small single-channel conductance, approaching 1-2 pS at physiological $[Ca^{2+}]_o$ and 7 pS in 10 mM $[Ca^{2+}]_o$ (Mouginot et al., 1997; Lee et al., 1999; Talavera and Nilius, 2006; Weber et al., 2010), much lower than other VGCCs. Cav3 channels have an activation threshold between -75 and -60 mV, 20 to 30 mV below HVA channels (Talavera and Nilius, 2006) (**Fig. 1.2*B, C***). They also display fast, macroscopic, voltage-dependent inactivation at low voltages (Talavera and Nilius, 2006), in contrast to the Ca^{2+}-dependent inactivation seen with Cav1 channels (**Fig. 1.2*B***). The combination of low conductance and rapid inactivation results in "tiny" and "transient" currents (I_T). Importantly, overlap of Cav3 activation and inactivation curves provides a "window" current between -70 and -40 mV where a small percentage of channels remains in the active state (Talavera and Nilius, 2006; Dreyfus et al., 2010) (**Fig. 1.2*C***). This window current provides continual Ca^{2+} influx at resting potentials which may constitute only 2% of total available current, yet is sufficient to increase $[Ca^{2+}]_i$ at subthreshold potentials and affect neuronal firing (Huguenard, 1996; Perez-Reyes, 2006). The size of the window current depends critically on the exact extent of overlap of Cav3 voltage for activation and inactivation, resulting in cell-to-cell variability depending on the biophysical properties of Cav3 channels (Dreyfus et al., 2010). Indeed, in some cases a window current is undetectable (Mouginot et al., 1997). The role for Cav3 window current in controlling membrane excitability must then be carefully assessed in individual cell classes.

Cav3 channels have a unique pharmacology that allows them to be distinguished from other VGCCs. They are insensitive to dihydropyridines, prototypical antagonists for Cav1 Ca^{2+} channels, as well as the Cav2.2 channel blocker ω-conotoxin-GVIA, the Cav2.1 channel blocker ω-Agatoxin-IVA (AgTx), and the general HVA blocker cadmium (Cd^{2+}) (at low concentrations). Common Cav3 channel blockers include nickel (Ni^{2+})

(low concentrations), mibefradil, amiloride, and kurtoxin (Randall and Tsien, 1997; McDonough and Bean, 1998; Lee et al., 1999; Sidach and Mintz, 2002).

Due to their unique low voltage of activation, Cav3 channels have been implicated in burst generation in thalamocortical relay neurons (McCormick and Pape, 1990), control of cerebellar stellate cell gain (Anderson et al., 2010b), stabilization of pacemaker activity in dopaminergic midbrain neurons (Wolfart and Roeper, 2002), and regulation of a variety of other cellular functions (for reviews see: Huguenard (1996); Perez-Reyes (2003); Yunker and McEnery (2003); Talavera and Nilius (2006)). Their subthreshold voltage profile places them in an ideal position to regulate spike generation in neurons and provide a site for modulation of cell excitability as they are targets of a number of neurotransmitters, hormones, and neuroactive drugs (Talavera and Nilius, 2006).

Despite a growing understanding of Cav3 channels following their molecular characterization (Huguenard, 1996), their role in synaptic integration is only now beginning to be investigated. I_T in CA1 and CA3 pyramidal neurons is activated during subthreshold excitatory postsynaptic potentials (EPSPs), resulting in EPSP amplification (Magee and Johnston, 1995; Gillessen and Alzheimer, 1997; Urban et al., 1998). Similar effects were reported in layer V neocortical pyramidal cells, as well as a potential for activation of K_{Ca} currents (Markram and Sakmann, 1994). A series of studies in cerebellum have highlighted the role for Cav3 channels in signal processing. In particular, work in DCN neurons show that different Cav3 channel isoforms are associated with specific phenotypes of rebound burst generation (Molineux et al., 2006; Molineux et al., 2008). Finally, a novel first spike latency (FSL) relationship in cerebellar stellate cells was shown to be due to an interaction between A-type K^+ and Cav3 channels that allows coincident inhibitory postsynaptic potentials (IPSPs) to promote spike firing by an EPSP (Molineux et al., 2005). Therefore, postsynaptic Cav3 channels can be activated during synaptic inputs and affect individual EPSPs and IPSPs; however, the role of Cav3 channels on the integration of sustained patterns of input still needs to be fully elucidated.

1.2.1.2 HCN channels

Early studies of currents in cardiac cells and neurons showed a paradoxical inward current that activated with increasing hyperpolarization, opposite to other voltage-

activated currents. This current was termed "funny", "queer", or "hyperpolarization-activated" (I_H). The channels mediating this current are encoded by the genes HCN1-4 and are activated by hyperpolarization and gated by cytosolic cyclic nucleotides. HCN channels are part of the superfamily of voltage-gated K^+ channels, but conduct both Na^+ and K^+ ions (Wahl-Schott and Biel, 2009). E_{HCN} is, therefore, between -25 and -40 mV (Robinson and Siegelbaum, 2003). HCN channels are sensitive to ZD-7288 and millimolar concentrations of extracellular cesium (Cs^+), blockers that generally do not affect K^+ channels.

Like other K^+ channels, HCN channels are tetrameric proteins formed by the assembly of four separate α-subunits. Voltage-dependence is conferred via positively charged amino acids on the S4 segment. All four HCN isoforms are expressed in neurons, though with different expression levels and distribution (Robinson and Siegelbaum, 2003). Each isoform has distinct voltage and kinetic properties, and isoforms can coassemble to form heterotetramers with still different kinetics than homomeric channels (Robinson and Siegelbaum, 2003). Therefore, the properties of I_H vary wildly between neuronal subtypes and brain regions.

HCN channels show an increased probability of opening at voltages negative to -60 mV (Robinson and Siegelbaum, 2003)(**Fig. 1.3*A***). Half-activation voltages (V_a) are typically between -60 and -90 mV with measurements as low as -120 mV in cardiac cells (Robinson and Siegelbaum, 2003). HCN channels have a cyclic nucleotide binding domain on the cytosolic C-terminus that provides a tonic inhibitory effect on gating. Binding of cAMP relieves the inhibition, causing a positive shift in V_a that allows the channel to function in the physiological range of membrane potentials (Robinson and Siegelbaum, 2003). Temporally, channel opening is relatively slow, and can follow single or double exponential time constants ranging from milliseconds to seconds. This wide range of biophysical properties allows the HCN channel to fulfill a variety of roles through the nervous system. The presence of I_H in neurons can be observed by a characteristic "sag" in membrane voltage that is seen when hyperpolarizing current is injected into the neuron. This "sag" is due to the slow activation of I_H during the hyperpolarization, resulting in a slow depolarization (**Fig. 1.3*B***).

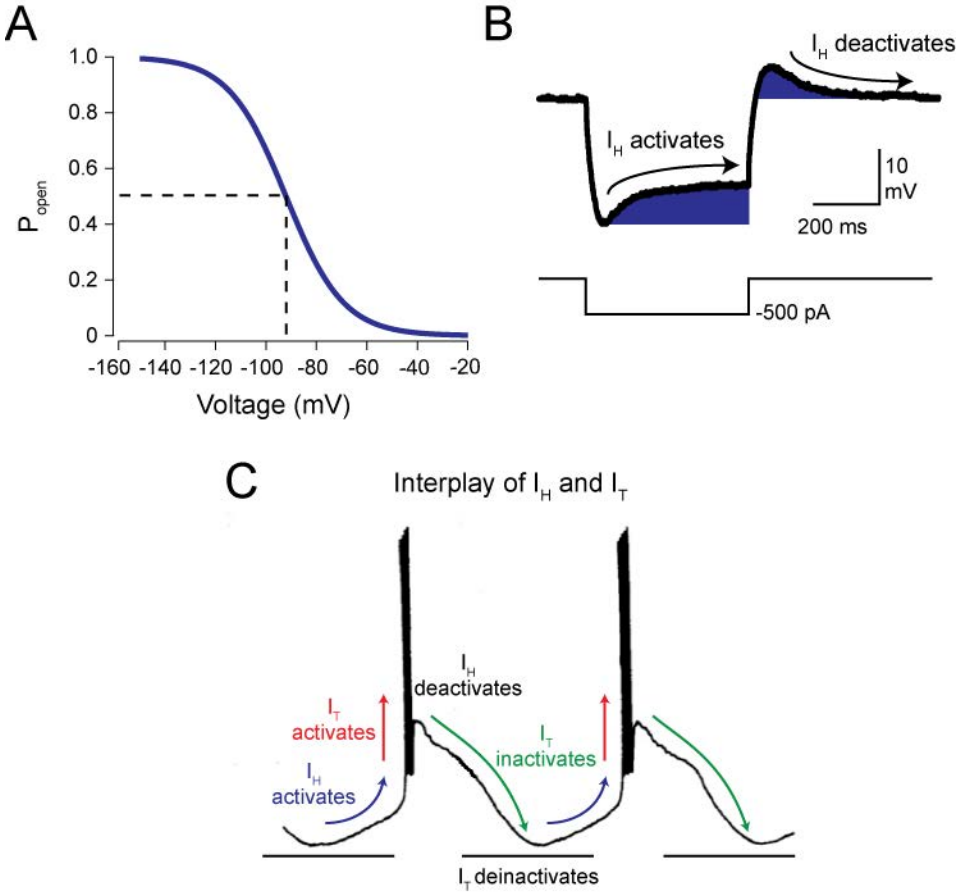
A
1.0
0.8
0.6
0.4
0.2
0
P open
-160 -140 -120 -100 -80 -60 -40 -20
Voltage (mV)
B
I H deactivates
I H activates
10
mV
200 ms
-500 pA
C
Interplay of I H and I T
I T
activates
I H
activates
I H
deactivates
I T
inactivates
I T deinactivates

Figure 1.3: Properties of HCN channel activation and functional consequences
(A) A plot of HCN channel voltage dependence reveals an "inverse" relationship where open probability (P_{open}) increases with hyperpolarization. In this case, V_a is -93 mV (*dashed line*). **(B)** A voltage trace from a cerebellar Purkinje cell in response to hyperpolarizing current injection shows the voltage "sag" characteristic of I_H. I_H activates during hyperpolarization, resulting a slow depolarization during the current injection (*blue*). After the hyperpolarizing influence is removed, I_H deactivates slowly, resulting in a tail current and rebound depolarization (*blue*). **(C)** In thalamic neurons, I_H and I_T interact to generate rhythmic bursting. At hyperpolarized potentials, I_H activates and depolarizes the neuron, activating I_T. I_T activation results in a low threshold spike and plateau potential that supports generation of Na^+-K^+ action potentials. I_H deactivation and I_T causes the neuron to repolarize, ending the burst. At hyperpolarized potentials, I_T deinactivates and I_H reactivates, continuing the cycle. **(C)** Adapted from (McCormick and Pape, 1990).

The first defined function for I_H was pacemaking in cardiac cells and neurons (Robinson and Siegelbaum, 2003; Santoro and Baram, 2003). Extensive early work in thalamic relay neurons revealed how I_H interacts with I_T to generate rhythmic bursting (McCormick and Pape, 1990; Huguenard and McCormick, 1992)(**Fig. 1.3*C***). It has now become recognized that I_H also contributes to rebound bursts (Aizenman and Linden, 1999), sustains tonic firing (Luthi and McCormick, 1998), produces oscillations in entorhinal cortex neurons (Brauer et al., 2001), and decreases the bistable range in Purkinje cells (Williams et al., 2002; Fernandez et al., 2007).

The profound and wide-ranging effects of I_H show that it has a pivotal role in the dynamics of neurons. Not surprisingly, I_H has profound effects on synaptic integration. Since I_H is active at resting membrane potentials, it has a large effect on membrane resistance (R_m) and dendritic integration. In cortical neurons, I_H shapes EPSPs, promoting the equalization of distal and proximal EPSPs via a gradient of dendritic expression (Magee, 1999; Tsay et al., 2007). Thus, I_H normalizes EPSPs to compensate for the broadening effect of the membrane depolarization due to dendritic filtering. By decreasing R_m and shunting synaptic currents, I_H reduces the summation of EPSPs by shortening EPSP width in cerebellar Purkinje cells (Angelo et al., 2007). Its effects are not limited to excitatory inputs, however. Due to its unique voltage-dependent properties, I_H is ideally suited to affect the processing of inhibitory inputs. Indeed, I_H limits hyperpolarization during trains of IPSPs and produces an afterdepolarization (ADP) that contributes to postinhibitory rebound bursts (McCormick and Pape, 1990; Molineux et al., 2006; Atherton et al., 2010). However, its interactions with other subthreshold currents in this region during inhibitory trains still require examination.

1.2.2 Ca^{2+}-dependent K^+ channels

Ligand-gated ion channels are gated by the binding of a molecule to a domain on the ion channel. K_{Ca} channels are activated by the binding of Ca^{2+} to intracellular Ca^{2+}-binding domains on the channel or an associated subunit positioned in the cytosol. By conducting outward current and hyperpolarizing the neuron at physiological potentials, K_{Ca} channels provide a negative feedback mechanism for increases in $[Ca^{2+}]_i$ associated with membrane depolarization and action potential discharge. Like HCN channels, K_{Ca}

channels are comprised of four separate α-subunits and are highly permeable to K^+. To date, three different families of K_{Ca} channels have been found and termed $K_{Ca}1$, $K_{Ca}2$ and $K_{Ca}3$. Each of these channels have different Ca^{2+}- and voltage-dependencies, single-channel conductances, and pharmacological profiles.

1.2.2.1 $K_{Ca}1.1$ channels

"Big conductance" K_{Ca} channels (also known as $K_{Ca}1.1$ or BK) are both voltage- and Ca^{2+}-dependent. These channels have a large single-channel conductance, reaching up to 260 pS in symmetrical K^+ and 100 pS under physiological conditions. Unlike other K^+ channels, $K_{Ca}1.1$ α-subunits have an extra transmembrane segment near the N-terminus and an additional four transmembrane domains on the intracellular C-terminus, which form a "Ca^{2+} bowl" (**Fig. 1.4*A***). Binding of Ca^{2+} to the Ca^{2+} bowl results in a left-ward shift in the voltage-dependence of the channel, increasing open probability (**Fig. 1.4*B***). Functionally, they require relatively large increases in $[Ca^{2+}]_i$ (1-10 μM range) for activation, and thus are typically activated by Ca^{2+} influx during an action potential to contribute to spike repolarization and generation of a subsequent fast afterhyperpolarization (AHP) (Storm, 1987; Berkefeld et al., 2010; van Welie and du Lac, 2011).

The pharmacology of $K_{Ca}1.1$ channels has been well characterized and there are several blockers of $K_{Ca}1.1$ channels that can be used to experimentally determine $K_{Ca}1.1$ channel function. KCa1.1 channels are highly sensitive to tetraethylammonium (TEA), charybdotoxin (CbTx), iberiotoxin (IbTx), and paxilline. However, they are insensitive to apamin and 1-[(2-Chlorophenyl)diphenylmethyl]-1H-pyrazole (TRAM-34), important blockers of other K_{Ca} channels. Therefore, the presence and effects of $K_{Ca}1.1$ current can be readily distinguished from those of other K_{Ca} channels.

1.2.2.2 $K_{Ca}2$ channels

In contrast to KCa1.1 channels, "small-conductance" K_{Ca} channels (also known as $K_{Ca}2.1$-2.3 or SK1-3) have a tiny single-channel conductance (~6 pS in physiological K^+) and are purely Ca^{2+}-dependent, showing no voltage-dependent gating. Correspondingly,

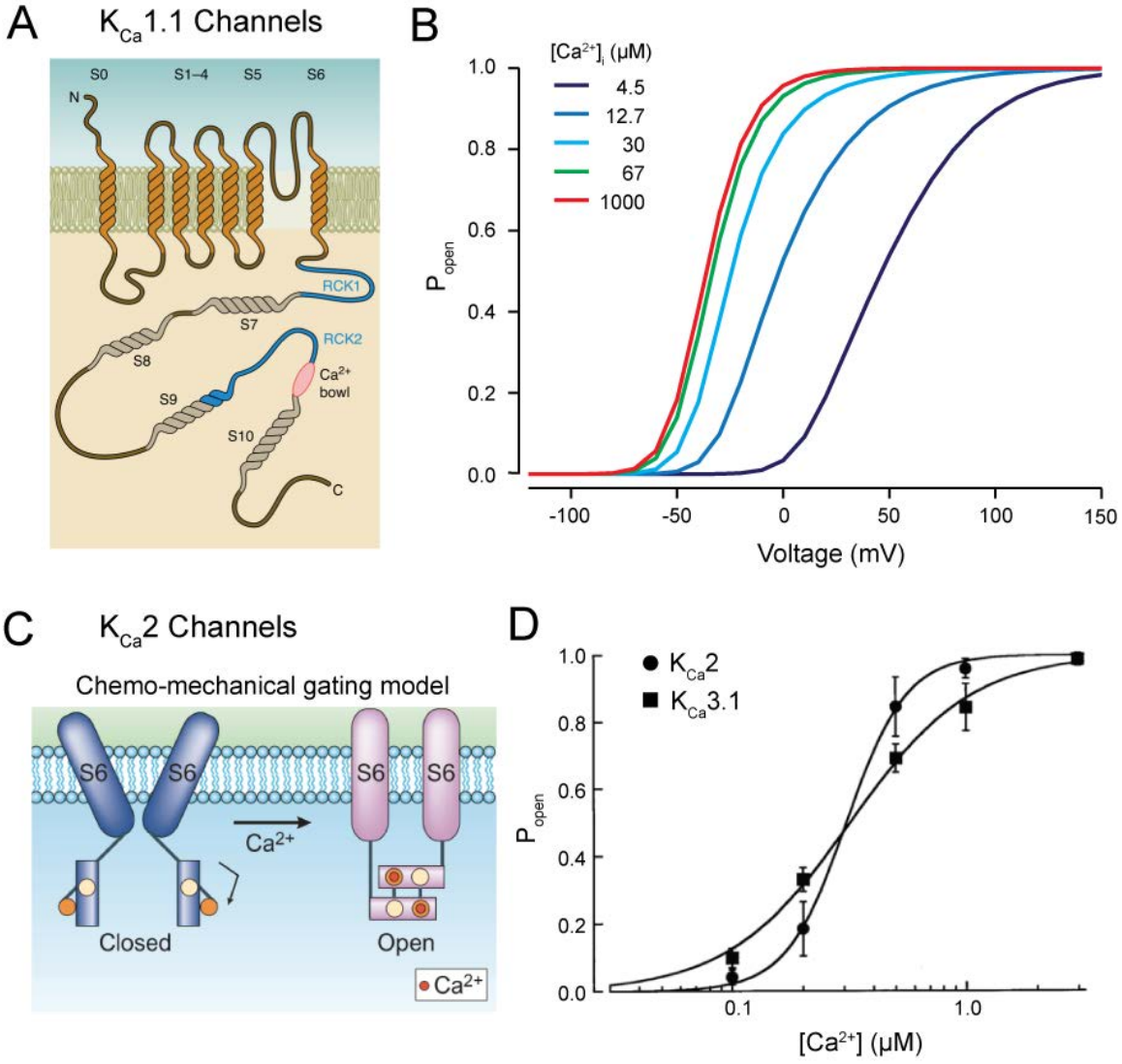
A
K_{Ca}1.1 Channels
S0
S1–4
S5
S6
N
RCK1
S7
RCK2
S8
Ca^{2+} bowl
S9
S10
C
B
$[Ca^{2+}]_i$ (μM)
4.5
12.7
30
67
1000
P_{open}
1.0
0.8
0.6
0.4
0.2
0.0
-100
-50
0
50
100
150
Voltage (mV)
C
K_{Ca}2 Channels
Chemo-mechanical gating model
S6
S6
S6
S6
Ca^{2+}
Closed
Open
Ca^{2+}
D
K_{Ca}2
K_{Ca}3.1
P_{open}
1.0
0.8
0.6
0.4
0.2
0.0
0.1
1.0
$[Ca^{2+}]$ (μM)

Figure 1.4: Structure and physiology of K_{Ca} channels

(A) A diagram of $K_{Ca}1.1$ channel structure illustrates the 11 transmembrane domains of the $K_{Ca}1.1$ α-subunit (S0 – S10). The Ca^{2+} bowl is located between the intracellular S9 and S10 segments on the C-terminus. **(B)** Binding of Ca^{2+} to the Ca^{2+} bowl causes a left-ward shift in $K_{Ca}1.1$ voltage dependence in a concentration-dependent manner. Graphs of voltage and calcium relationships are based on a model of $K_{Ca}1.1$ gating. **(C)** $K_{Ca}2$ chan-nels have CaM proteins (*rectangles*) constitutively bound to their intercellular C-terminus. In the dimer-dimer model of gating, binding of Ca^{2+} to CaM results in a dimer-ization of CaM on opposite subunits, causing a conformational change in the channel and an opening of the channel gate. **(D)** Ca^{2+}-dependent dose-responses of $K_{Ca}2$ and $K_{Ca}3.1$ channel gating show that $K_{Ca}2$ and $K_{Ca}3.1$ are more sensitive to Ca^{2+} than $K_{Ca}1.1$, with IC_{50} values around 300 nM. **(A)** Adapted from (Berkefeld et al., 2010). **(C)** Adapted by permission from Macmillan Publishers Ltd: Nature Reviews Neuroscience (Stocker, 2004). **(D)** Adapted from (Ishii et al., 1997b).

they only have two of the seven charged amino acids on the S4 transmembrane segment that present on voltage-gated channels. Instead, channel opening is controlled by calmodulin (CaM) proteins that are constitutively bound to the C-termini of the channel in a Ca^{2+}-independent manner (Hirschberg et al., 1998) (**Fig. 1.4*C***). Current models of $K_{Ca}2$ channel gating show that Ca^{2+} binds to CaM, resulting in a dimerization of CaM proteins attached to different α-subunits of the $K_{Ca}2$ channel construct. This "dimer-of-dimers" model results in a conformational change in the S6 segment and opening of the $K_{Ca}2$ gate (Stocker, 2004) (**Fig. 1.4*C***). While they do not show voltage-dependent activation, $K_{Ca}2$ channels do show inward rectification due to internal magnesium (Mg^{2+}) block during outward current flow (Zhang et al., 2006); however, in physiological voltage ranges, their I-V relationship is essentially linear.

There are several distinct features of the pharmacology of $K_{Ca}2$ channels that facilitate their study or blockade under experimental conditions. The prototypical $K_{Ca}2$ antagonist is the bee venom toxin apamin, which is highly selective and binds at specific sites on the external face of the channel pore. Not all $K_{Ca}2$ channels are equally apamin sensitive, with $K_{Ca}2.2$ channels showing high sensitivity (half-maximal concentration (IC_{50}) of 27 - 140 pM) while $K_{Ca}2.1$ and $K_{Ca}2.3$ channels show variable apamin sensitivity according to species and expression system (IC_{50} of 0.7-12 nM and 0.6-19.0 nM respectively) (Ishii et al., 1997a; Shah and Haylett, 2000; Strobaek et al., 2000; Benton et al., 2003). However, efficient block of all $K_{Ca}2$ isoforms is achieved experimentally by applying 100 nM apamin. In contrast, $K_{Ca}2$ channels are insensitive to TEA, IbTx, CbTx, and TRAM-34, thus having a distinct pharmacology from other K_{Ca} channels.

Since Ca^{2+}-sensitivity is conferred via CaM, $K_{Ca}2$ channels have a much higher Ca^{2+} sensitivity than $K_{Ca}1.1$ channels (EC_{50} = 300 - 700 nM) (**Fig. 1.4*D***). They also have a longer time course of activation. $K_{Ca}2$ channels activate a few milliseconds following action potentials and can remain activated for hundreds of milliseconds, generating a long-lasting AHP that can act to maintain tonic firing frequency (Pedarzani and Stocker, 2008). $K_{Ca}2$ channels regulate tonic firing in neocortical pyramidal cells, hippocampal pyramidal neurons, Purkinje cells, Golgi cells, dopaminergic and GABAergic cells of the

substantia nigra, and DCN neurons, suggesting a near global role for $K_{Ca}2$ channels (Pedarzani and Stocker, 2008). Various Ca^{2+} sources have been shown to activate $K_{Ca}2$ channels, including influx through VGCCs, intracellular Ca^{2+} stores (inositol triphosphate (IP_3) mediated Ca^{2+} release), and NMDA receptor mediated current (Faber et al., 2005). $K_{Ca}2$ channels are also highly regulated by intracellular kinases which can decrease Ca^{2+} sensitivity as well as regulate internalization of $K_{Ca}2$ channels (Pedarzani and Stocker, 2008).

With their central role in controlling neuronal output, it is not surprising that $K_{Ca}2$ channels have roles in controlling synaptic integration. $K_{Ca}2$ channels control the rebound burst in DCN cells following inhibition (Aizenman and Linden, 1999). Cav2.3-mediated Ca^{2+} influx in hippocampal pyramidal cell dendritic spines activate $K_{Ca}2$ channels to dampen synaptically-driven Ca^{2+} influx (Bloodgood and Sabatini, 2007). $K_{Ca}2$ channels also act in concert with synaptic inputs in ventral tegmental area neurons to control release of retrograde messengers (Riegel and Lupica, 2004). Most dramatically, they are activated directly by Ca^{2+} influx through NMDA receptors to control the EPSP waveform in hippocampus, lateral amygdala, and medial prefrontal cortex (Faber et al., 2005; Ngo-Anh et al., 2005; Bloodgood and Sabatini, 2007; Faber, 2010). Therefore, $K_{Ca}2$ channels can have direct effects on synaptic integration and provide another method for postsynaptic cells to perform complex operations on synaptic inputs.

1.2.2.3 $K_{Ca}3.1$ channels

"Intermediate-conductance" K_{Ca} channels ($K_{Ca}3.1$, IK) are related to $K_{Ca}2$ channels but only exhibit 42-44% sequence homology (Ishii et al., 1997b). Like $K_{Ca}2$ channels, they are directly gated by CaM and are highly sensitive to $[Ca^{2+}]_i$ with an EC_{50} of 100-300 nM (Ishii et al., 1997b; Joiner et al., 1997) (**Fig. 1.4*D***). They exhibit little or no voltage dependence, with both inward and outward rectification having been reported depending on cell type, expression system or K^+ concentrations. Their single-channel conductance is larger than $K_{Ca}2$ and is between 20 and 80 pS. Unlike $K_{Ca}2$ channels, which are abundantly present in central neurons, mRNA for KCa3.1 has been widely assumed to be found only in the periphery, specifically in smooth muscle tissues (Pedarzani and Stocker, 2008), enteric or myenteric neurons (Vogalis et al., 2002b), microglia (Kaushal

et al., 2007) and T lymphocytes (Khanna et al., 1999). In **Chapter 3** of this thesis I present new evidence for the expression of $K_{Ca}3.1$ channels in cerebellar Purkinje cells (Engbers et al., 2012b).

While related to $K_{Ca}2$ channels, $K_{Ca}3.1$ channels exhibit a completely different pharmacological profile. They lack the amino acids in the outer vestibule of the channel pore required to bind apamin or IbTx and are not sensitive to either blocker. However, they are sensitive to CbTx and clotrimazole derivatives. In particular, TRAM-34 has been designed to block $K_{Ca}3.1$ channels with high potency and specificity (Wulff et al., 2000; Wulff et al., 2001). TRAM-34 is a lipophilic molecule that blocks from the cytosolic side of the channel and shows no activity with $K_{Ca}1.1$, $K_{Ca}2$, or a wide range of voltage-gated K^+ or Ca^{2+} channels (Wulff et al., 2000; Wulff et al., 2001). This makes TRAM-34 a highly effective pharmacological tool to test for the expression of $K_{Ca}3.1$ channels in neurons.

Several roles for $K_{Ca}3.1$ channels have been elucidated in non-neuronal cell types and include cell volume regulation, smooth muscle relaxation, and microglial migration (Wulff et al., 2007). However, since $K_{Ca}3.1$ channels were not previously thought to be expressed in central neurons, little is known of their function in the brain. Nevertheless, their expression, regulation and function has been studied in enteric and myenteric neurons and these findings could translate to central nervous system (CNS) function. $K_{Ca}3.1$ channels mediate a slow AHP current (I_{sAHP}) in enteric neurons that can last several seconds following depolarization, with much longer kinetics than the AHP mediated by $K_{Ca}2$ channels. Furthermore, deactivation of $K_{Ca}3.1$ requires phosphorylation of protein kinase A (PKA) (Vogalis et al., 2003). Given the magnitude and timecourse of the slow AHP generated by $K_{Ca}3.1$ channels, the underlying I_{sAHP} is likely responsible for spike frequency adaptation. In myenteric neurons, activation of I_{sAHP} requires Ca^{2+} influx through Cav2.2 Ca^{2+} channels that causes release of intracellular Ca^{2+} stores through Ca^{2+}-induced Ca^{2+}-release (Vogalis et al., 2001). All of these facts suggest that $K_{Ca}3.1$ could be an important regulator of neuronal excitability and be highly modulated by association with different proteins including VGCCs. However, the potential expression of

KCa3.1 channels in central neurons has been regularly discounted, even though expression is recognized in both microglia and endothelial cells throughout the CNS.

1.2.2.4 K_{Ca} association with VGCCs

The Ca^{2+} signal supplied though VGCCs has a precise spatiotemporal localization, elevating $[Ca^{2+}]_i$ transiently in a small domain before being reduced by intracellular buffers (Fakler and Adelman, 2008). Therefore, in order to sense Ca^{2+} entry through VGCCs, K_{Ca} channels are often located within the VGCCs Ca^{2+} domain (**Fig. 1.5*A***). Ca^{2+} domains have been divided into two categories based on the distance from the channel and the ability for the exogenous buffers 1,2-Bis(2-Aminophenoxy)ethane-*N,N,N′,N′*-tetraacetic acid (BAPTA) and ethylene glycol tetraacetic acid (EGTA) to disrupt interactions between the Ca^{2+} source and effector. Since BAPTA is approximately 150 times faster than EGTA in buffering Ca^{2+}, interactions that are disrupted by BAPTA but not EGTA must reside in close proximity (20 - 50 nm), reflecting a "nanodomain" interaction. However, if EGTA and BAPTA are equally effective at blocking the interaction, the source and effector must be at least 50 nm apart, constituting a "microdomain" interaction (Fakler and Adelman, 2008). This experimental criterion is commonly used to characterize K_{Ca} and VGCC channel interactions.

$K_{Ca}1.1$ channels are usually located within the Ca^{2+} channel nanodomain, which provides access to the 1-10 μM concentration of Ca^{2+} needed to provide sufficient activation of the $K_{Ca}1.1$ channel (Berkefeld et al., 2010; van Welie and du Lac, 2011) (**Fig. 1.5*A, C***). $K_{Ca}1.1$ channels are associated with a variety of VGCCs, including Cav1, Cav2.1 and Cav2.2 channels (Lancaster and Nicoll, 1987; Storm, 1987; Marrion and Tavalin, 1998; Edgerton and Reinhart, 2003; Grunnet and Kaufmann, 2004; Berkefeld et al., 2006). Such a tight association allows the Ca^{2+} channel to imparts its own particular kinetic and voltage-dependent properties onto the K_{Ca} channel, reflecting the time course of the Ca^{2+} domain. For example, $K_{Ca}1.1$ channels that are associated with Cav2.1 channels show a much faster and more negative activation than those complexed with Cav1.2 channels (Fakler and Adelman, 2008) (**Fig. 1.5*B***). A direct interaction between $K_{Ca}1.1$ channels and the low voltage-activated family of Cav3 calcium channels has not been

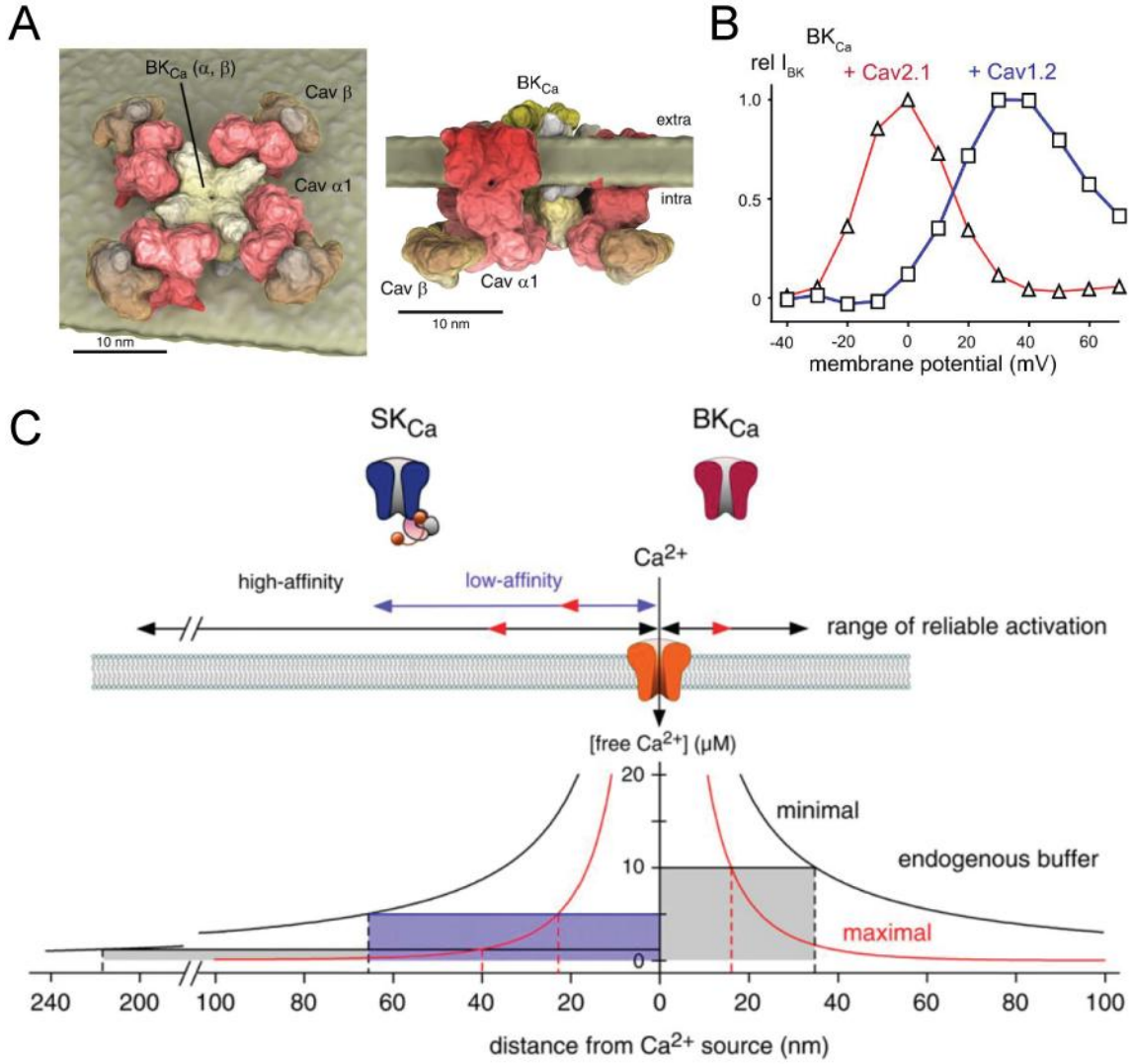
A
BKCa (α, β)
Cav β
Cav α1
10 nm
BKCa
extra
intra
Cav β
Cav α1
10 nm
B
BKCa
rel IBK
+ Cav2.1
+ Cav1.2
1.0
0.5
0
-40
-20
0
20
40
60
membrane potential (mV)
C
SKCa
BKCa
Ca2+
high-affinity
low-affinity
range of reliable activation
[free Ca2+] (μM)
20
10
0
minimal
endogenous buffer
maximal
240
200
100
80
60
40
20
0
20
40
60
80
100
distance from Ca2+ source (nm)

Figure 1.5: Nano- and microdomain coupling of K_{Ca} and VGCCs control the gating of K_{Ca} channels

(A) Structural model of $K_{Ca}1.1$ and Ca^{2+} channel supercomplex shows a single $K_{Ca}1.1$ channel surrounded by four Ca^{2+} channels and associated β-subunits. Physical coupling of K_{Ca} and VGCCs places the K_{Ca} channel within the Ca^{2+} channel nanodomain. **(B)** The properties of the associated Ca^{2+} channel can be conferred onto K_{Ca} channel. Here, $K_{Ca}1.1$ shows a greater probability of opening at hyperpolarized potentials when associated with Cav2.1 channels than with Cav1.2 channels. **(C)** The ability for a K_{Ca} channel to be activated by a Ca^{2+} channel depends on the distance between the channels and the spatial extent of rises in $[Ca^{2+}]_i$ as determined by endogenous buffers. *Black* line indicates the $[Ca^{2+}]_i$ profile with minimal buffering. *Red* line shows the $[Ca^{2+}]_i$ profile with maximal buffering. $K_{Ca}1.1$ channels must reside within the Ca^{2+} channel nanodomain (less than 50 nm distance). Conversely, $K_{Ca}2$ channels have can be activated at greater distances, allowing for microdomain interactions at distances of at least 70 nm when in a low-affinity state. **(A)** and **(B)** adapted from (Berkefeld et al., 2010). **(C)** adapted from (Fakler and Adelman, 2008) with permission from Elsevier.

established at the molecular level, although at least a functional interaction has been reported in a select number of cell types (Williams et al., 1997; Smith et al., 2002; Wolfart and Roeper, 2002). By conferring different properties onto the $K_{Ca}1.1$ channel, VGCCs fine-tune the K^+ current to match the particular requirements of the neuron, which may include negative-feedback to curtail Ca^{2+} influx and ensure precise timing of synaptic transmission or just to prevent overexcitation of the neuron (Fakler and Adelman, 2008).

$K_{Ca}2$ channels have also been shown to interact at least functionally with specific Ca^{2+} sources. In fact, the higher sensitivity of $K_{Ca}2$ channels to $[Ca]_i$ greatly extends the range of potential Ca^{2+} sources, including: Cav1, Cav2.3, and Cav3 calcium channels, NMDA receptors, and Ca^{2+}-permeable nicotinic acetylcholine receptors (Marrion and Tavalin, 1998; Oliver et al., 2000; Ngo-Anh et al., 2005; Bloodgood and Sabatini, 2007; Cueni et al., 2008; Fakler and Adelman, 2008; Faber, 2010). While $K_{Ca}1.1$-VGCC complexes underlie nanodomain interactions, $K_{Ca}2$ can reside both in the Ca^{2+} nanodomain, as with NMDA receptors in CA1 pyramidal cells (Ngo-Anh et al., 2005), and in the microdomain, as is the case with Cav3 channels in thalamic relay neurons (Cueni et al., 2008) (**Fig. 1.5*C***). $K_{Ca}2$ channels can, therefore, be situated to sense small, localized increases in $[Ca^{2+}]_i$ though a single channel or global increases through a population of channels (Fakler and Adelman, 2008). While $K_{Ca}3.1$ channels are more sensitive than either $K_{Ca}1.1$ or $K_{Ca}2$ channels and could, therefore, be activated by any number of Ca^{2+} sources, specific Ca^{2+} sources that increase the probability of $K_{Ca}3.1$ activation have not been fully determined (Vogalis et al., 2002a; Vogalis et al., 2002b).

1.3 Modelling neuronal excitability

Having examined the physiology and function of various ion channels, it is now important to describe how current flow through ion channels and the resulting neuronal excitability can be modelled mathematically. As previously mentioned, the basis for neuronal excitability is the existence of electrochemical gradients across the membrane due to the asymmetrical distribution of membrane-impermeable ions (**Fig. 1.6*A***). Movement of ions according to these gradients is caused by two different processes: the diffusion of molecules according to an chemical gradient, as described by Fick's Law of Diffusion;

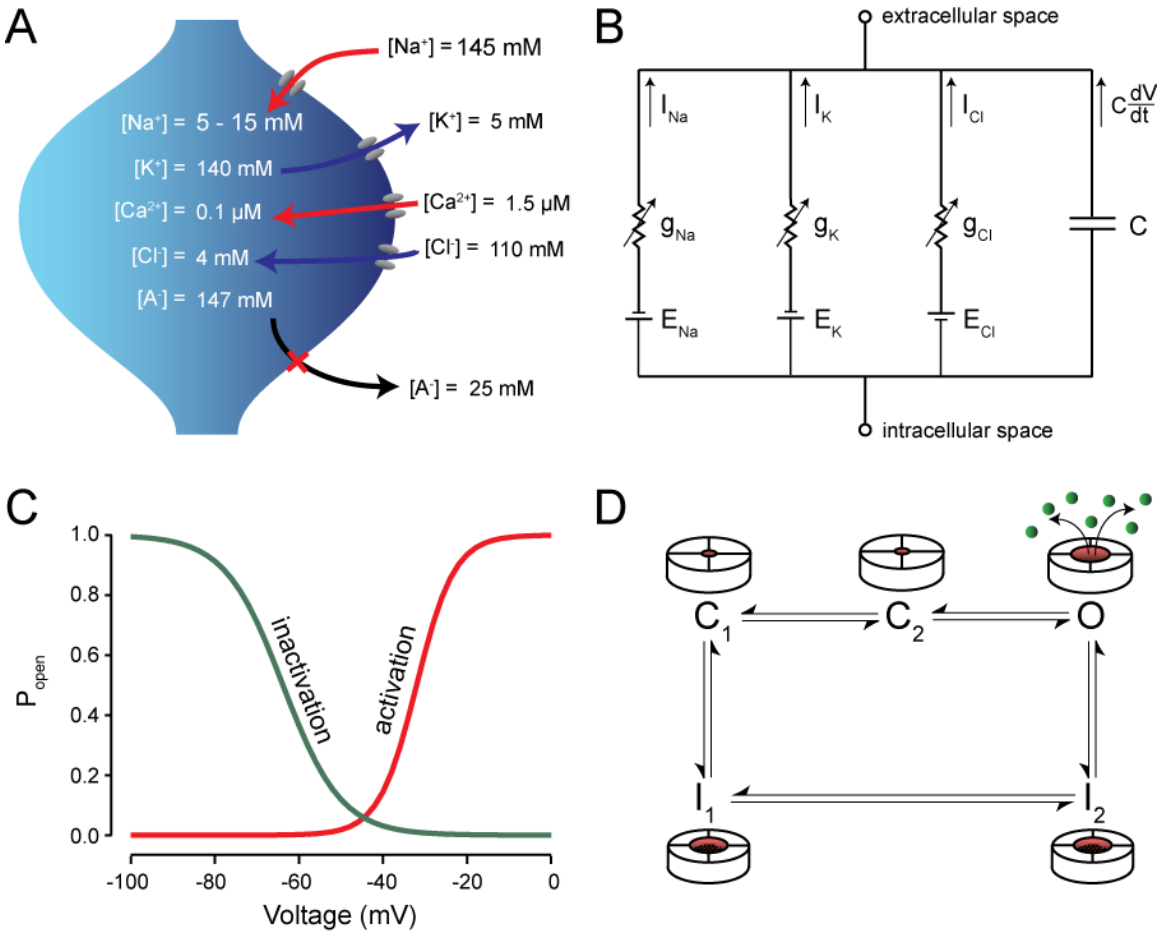
A
[Na+] = 145 mM
[Na+] = 5 - 15 mM
[K+] = 5 mM
[K+] = 140 mM
[Ca2+] = 1.5 µM
[Ca2+] = 0.1 µM
[Cl-] = 110 mM
[Cl-] = 4 mM
[A-] = 147 mM
[A-] = 25 mM
B
extracellular space
intracellular space
INa
IK
ICl
C dV/dt
gNa
gK
gCl
C
ENa
EK
ECl
C
P open
1.0
0.8
0.6
0.4
0.2
0.0
-100
-80
-60
-40
-20
0
Voltage (mV)
inactivation
activation
D
C1
C2
O
I1
I2

Figure 1.6: Principles behind modelling neuronal excitability

(A) Electrochemical gradients exist across the neuronal membrane and are maintained by active processes. Arrows indicate the direction of the driving force for permeable ions. *Red* arrows indicate a depolarizing influence and *blue* arrows indicate a hyperpolarizing influence. Large anions (A^-) cannot cross the membrane (indicated by X). **(B)** Diagram of equivalent circuit for the neuronal membrane. The driving force for each ionic species is represented by a voltage source while channels are represented as variable resistors. **(C)** Examples of steady-state activation (*blue*) and inactivation (*green*) curves for the Cav3 channel. **(D)** Example of a Markov state model of Cav3 channel gating adapted from (Chen and Hess, 1990). Movement between closed, open, and inactivated states is explicitly modelled.

and the movement of charged particles in an electrical field, as described by Ohm's Law for Drift. The Nernst-Plank equation combines these processes into a single equation providing an explicit expression of ionic current under relevant chemical and electrical gradients. Of particular interest is the voltage at which the these forces are at steady-state, resulting in zero net current across the membrane. This *reversal potential* is described by the Nernst equation:

$$E_C = \frac{RT}{zF} ln \frac{[C]_{out}}{[C]_{in}}$$

where E_C is the reversal potential for an ionic species; R is the universal gas constant (8,315 mJ/(K°·Mol)); z is the valence of the ion; F is Faraday's constant (96,480 coulombs/Mol); T is temperature (K° = 273.16 + °C); and $[C]$ is the concentration of the ion.

Having determined the reversal potential, we are able to describe an ionic current at a given voltage. According to Ohm's Law,

$$I = \frac{V}{R}$$

where I is current, V is voltage, and R is resistance. The *driving force* for an ion is the difference between membrane voltage and its reversal potential, or $V = (V_m - E)$. Furthermore, a channel's maximal conductance, g, is the inverse of R, giving us the equation

$$I = g(V - E)$$

Therefore, the current associated with a given ionic species is the product of its driving force and the conductance of the mediating ion channel.

Central to neuronal modelling is the understanding that the neuronal membrane can be described by an equivalent electrical circuit (**Fig. 1.6*B***). In accordance with Kirchoff's Law, the total current in the circuit is the sum of the ionic and capacitive currents:

$$I = I_{Na} + I_K + I_{Cl} + C\frac{dV}{dt}$$

where I_x is the current due to ionic species x, C is the neuron's capacitance, and $\frac{dV}{dt}$ is the change in voltage over time. This equation can be rearranged and currents substituted to give us the differential equation:

$$C\frac{dV}{dt} = I - g_{Na}(V - E_{Na}) - g_K(V - E_K) - g_{Cl}(V - E_{Cl})$$

This equation describes the change in membrane voltage over time when a given set of conductances are present; however, it does not include voltage-dependencies which are necessary to generate the complex excitability characteristic of neurons.

1.3.1 Empirical description of channel gating

One method of modelling the voltage-dependence of channels is to fit a set of equations to key measurements, avoiding a mechanical description of movement between channel states. It is common practice to experimentally determine the voltage-dependence of a current by measuring the steady-state properties of the current in *voltage-clamp*. By applying voltages across the membrane and measuring the current in steady-state conditions, the open probability of a channel can be determined for a given set of potentials. The open probability of a channel has a sigmoidal relationship with voltage that is readily described by a Boltzmann function (**Fig. 1.6*C***)

$$m_\infty(V) = \frac{1}{1 + \mathrm{e}^{\left(-\frac{\mathrm{V}-\mathrm{V_a}}{\mathrm{k}}\right)}}$$

where $m_\infty(V)$ is the asymptotic value for activation, V_a is the voltage at which open probability is 0.5, and k is the slope factor. For activation, k is positive (with the exception of I_H), while k is negative for inactivation (**Fig. 1.6*C***). A gating variable will approach its asymptotic value as $t \to \infty$ according to the differential equation

$$\frac{dm}{dt} = \frac{m_\infty(V) - m}{\tau_m(V)}$$

where $\tau_m(V)$ is the voltage-dependent time constant for channel gating. An ionic current is then fully described by

$$I = gm^a h^b (V - E)$$

where *a* and *b* are the number of activation and inactivation gates respectively. As an example, the excitability of a neuron containing Na^+, K^+, and leak currents, such as the giant squid axon described by Hodgkin and Huxley (1952), can be described by the following system of differential equations:

$$C\frac{dV}{dt} = I - g_{Na}m^3h(V - E_{Na}) - g_K n^4(V - E_K) - g_L(V - E_L)$$

$$\frac{dm}{dt} = \frac{m_\infty(V) - m}{\tau_m(V)}$$

$$\frac{dh}{dt} = \frac{h_\infty(V) - h}{\tau_h(V)}$$

$$\frac{dn}{dt} = \frac{n_\infty(V) - n}{\tau_n(V)}$$

The steady-state functions describing the voltage-dependence of the gating variables and time constants have been excluded for brevity. This set of differential equations can be used to simulate a spiking neuron, using any numerical method for integrating a system of differential equations.

1.3.2 Markov models of channel kinetics

Another method of modelling channel kinetics is using Markov state models that explicitly describe the movement between multiple gating states. In order to develop this type of model, in-depth single-channel studies must be conducted and the number of states and transitions between those states determined by measuring a large number of parameters. While this requires more work than empirical descriptions of channels, it al-

lows for more accurate descriptions of drug binding, kinetics of deactivation, and activation by intracellular signalling molecules, such as Ca^{2+} (e.g. (Liu and Rasmusson, 1997)).

Cav3 channel gating has been fully characterized in expression systems and is best described by a model with two closed states, an open state, and two inactive states (Chen and Hess, 1990) (**Fig. 1.6*D***). The Ca^{2+}-dependent gating of $K_{Ca}2$ channels has also been characterized in a kinetic model (Hirschberg et al., 1998). By explicitly modelling the movement between unbound and bound states, Markov models more accurately describe the complex gating of these currents.

The majority of the currents modelled in this thesis will be based on the empirical Hodgkin-Huxley formulism, as these equations are less computationally expensive and physiological parameters were more readily available. However, when examining the nature of the interaction between Cav3-mediated Ca^{2+} influx and $K_{Ca}3.1$ activation, I used a kinetic model for $K_{Ca}3.1$ activation to more accurately portray channel activation.

1.4 Overview of the cerebellum

The cerebellum is an ideal structure to study the effects of postsynaptic ion channels on synaptic integration due to its relatively small number of neuronal subtypes which express a wide variety of ion channels and its well-defined circuit structure. The cerebellum is a large structure located caudal to the cerebrum. Research into the function of the cerebellum has established its involvement in motor learning and classical conditioning, the coordination of fine motor movements, vestibular function, reflex control, regulation of posture, and even cognitive processes (Arbib and Amari, 1985; Robinson and Fuchs, 2001; Barlow, 2002; Gebhart et al., 2002; Ito, 2002; Ohyama et al., 2003; Thach and Bastian, 2004; Bastian, 2006; Dean and Porrill, 2008; D'Angelo and De Zeeuw, 2009; Stoodley, 2011). The near-crystalline organization of the cerebellum's anatomical framework has been the basis of many theories of cerebellar function. Beginning with Marr and Albus' perceptron based models (Marr, 1969; Albus, 1971) and Braitenberg's Timing Organ hypothesis (Braitenberg, 1967) and continuing with modern adaptive control (Barlow, 2002) and adaptive filter (Dean et al., 2010) theories, models of cerebellar function are largely based on anatomical observations and the classic principles of synaptic plasticity (e.g. long-term depression in the cerebellar cortex). However, each neuron in

the cerebellar circuit is capable of complex computations and the physiological properties of each neuronal type must be taken into account when considering network operations.

As described in detail below, the cerebellum contains two principal output neurons: the Purkinje cell of the cerebellar cortex and the neurons of the DCN, the efferent targets of Purkinje cell inhibition. Both of these principal neurons are targets of a large number of convergent inputs. Yet, how these neurons integrate their inputs is still largely unknown. As these cell types lay at the center of the cerebellar function, it is important to identify and characterize the postsynaptic determinants that control synaptic integration and thus spike output in these neurons.

1.4.1 Cerebellar anatomy

Cerebellar Cortex: The structure of the cerebellum can be described in several ways based on its circuitry, gross anatomy, and function. Cerebellar circuitry can be divided into three distinct regions: the cerebellar cortex, internal white matter, and the deep cerebellar nuclei. The cortex contains many transverse invaginations, giving the cerebellum a foliated appearance. Two large transverse folds, the primary fissure and posterolateral fissure, divide the cerebellum anatomically into three lobes: the anterior lobe, the posterior lobe, and the flocculonodular lobe. However, with the exception of the flocculonodular lobe, it is difficult to correlate specific functions with any of the other 10 lobules that make up the anterior and posterior poles of cerebellar cortex. The cerebellum can thus be further divided functionally along the medio-lateral plane into the spinocerebellum and cerebrocerebellum, with an additional caudal vestibulocerebellum (**Fig. 1.7**). Each functional division receives distinct afferent inputs and projects to distinct areas of the nervous system. The vestibulocerebellum is comprised of the flocculonodular lobe and is primarily responsible for controlling balance and eye movement in higher vertebrates. The spinocerebellum contains the vermis (area of the medial cerebellum between the two longitudinal furrows) and intermediate hemispheres adjacent to the vermis. It receives visual, auditory, and vestibular input and projects to cortical, brainstem, and spinal targets. Functionally, the spinocerebellum is involved in posture, locomotion, movement of limbs and digits, and gaze. Finally, the cerebrocerebellum includes the lateral hemispheres, which receive input from the cerebral cortex via pontine

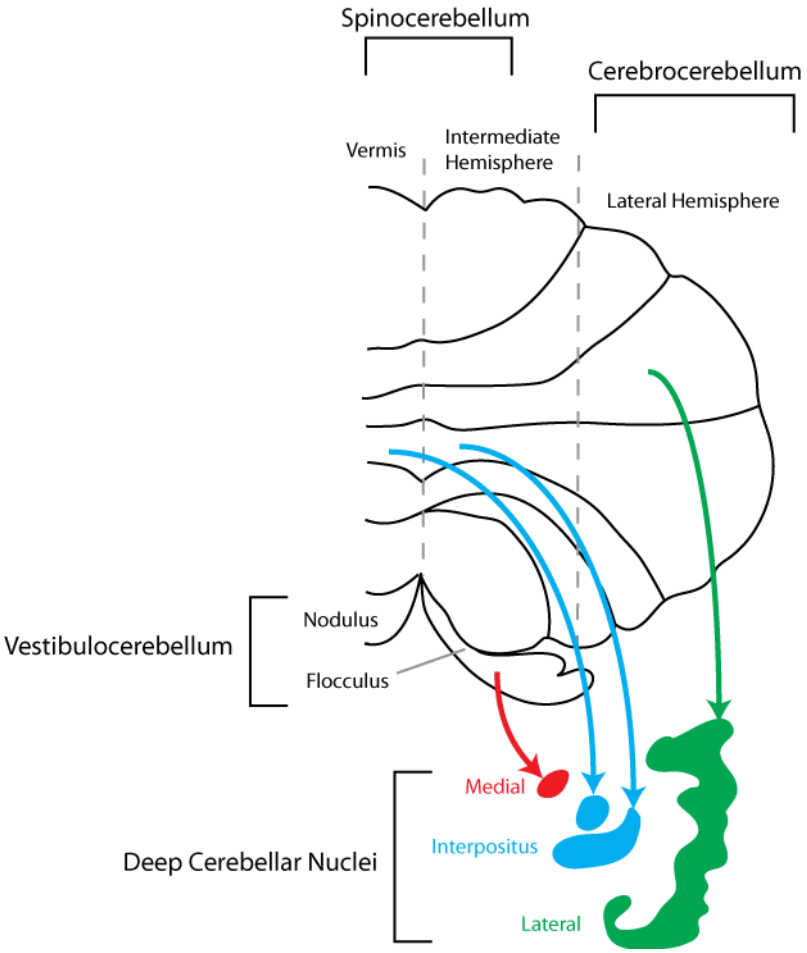
Spinocerebellum
Cerebrocerebellum
Vermis
Intermediate Hemisphere
Lateral Hemisphere
Vestibulocerebellum
Nodulus
Flocculus
Deep Cerebellar Nuclei
Medial
Interpositus
Lateral

Figure 1.7: Principal anatomical and functional divisions of the human cerebellum. The cerebellum can be divided functionally along the mediolateral plane into the vestibulocerebellum, spinocerebellum, and cerebrocerebellum. Different cortical areas project to the bilateral medial (*red*), interpositus (*blue*), or lateral (*green*) nuclei.

nuclei, and projects to the ventrolateral thalamic nucleus as well as motor, premotor, and prefrontal cortices. It is involved in the planning and assessment of complex motor tasks. The majority of work in this thesis centered on cells in the vermal region.

Cerebellar Nuclei: Purkinje cells provide the sole output of the cerebellar cortex and innervate the cerebellar nuclei located within the white matter at the base of the cerebellum. There are three bilateral nuclei (medial, interpositus, and lateral) which receive input from all areas of the cerebellar cortex (**Fig. 1.7**) with the exception of the vestibulocerebellum, which projects to the vestibular nuclei in the brainstem. Projections from the cerebellar cortex are topographic and the input and output projections form laminar modules. Thus climbing fibres (CFs) synapse onto DCN cells and Purkinje cells, the latter of which project back to the same cerebellar nucleus (Garwicz et al., 1998; Ito, 2006; Apps and Hawkes, 2009) (**Fig. 1.8**). GABAergic DCN neurons project to inferior olive neurons, the source of the CFs, to create an inhibitory olivo-cortico-nuclear feedback loop (Jacobson et al., 2008). The central placement of the DCN in cerebellar anatomy and circuitry shows its importance in cerebellar processing as the final output from cerebellum after signal processing in the cortical region.

1.4.2 Cerebellar circuitry

The circuitry of the cerebellum can be most easily explained by examining the movement of information in the cerebellum from input to output. There are two types of afferent inputs to the cerebellum: *mossy fibres* (MFs) arising from spinocerebellar, vestibular, reticular and pontine nuclei and CFs originating from the inferior olive. MFs give excitatory input to granule cells in the granular layer of the cerebellar cortex as well as excitatory collaterals to the DCN. The axons of the granule cells, called *parallel fibres* (PF), extend into the outer molecular layer, where they bifurcate and extend parallel to the surface of the cortex, but perpendicular to the Purkinje cell dendrites (**Fig. 1.8**). This arrangement allows the PFs to provide excitatory input to a large number of Purkinje cells. PFs also give excitatory input to three types of inhibitory interneurons in the cerebellar cortex. Golgi cells inhibit granule cells, forming an inhibitory feedback loop which allows the Golgi cells to suppress excitation of the granule cells and shorten PF bursts.

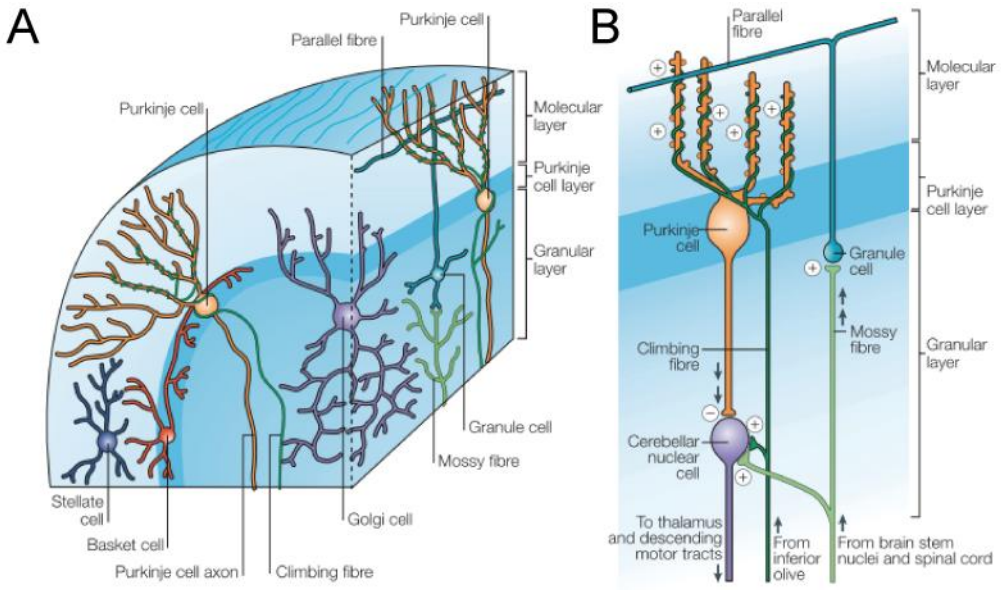
A
Parallel fibre
Purkinje cell
Purkinje cell
Molecular layer
Purkinje cell layer
Granular layer
Granule cell
Mossy fibre
Golgi cell
Stellate cell
Basket cell
Purkinje cell axon
Climbing fibre
B
Parallel fibre
Molecular layer
Purkinje cell layer
Purkinje cell
Granule cell
Mossy fibre
Granular layer
Climbing fibre
Cerebellar nuclear cell
To thalamus and descending motor tracts
From inferior olive
From brain stem nuclei and spinal cord

Figure 1.8: Basic circuitry of the cerebellum

(A) An illustration of the cerebellar cortex shows the basic cortical cell types as well as their connectivity. The two main efferent inputs are shown. CFs synapse solely on Purkinje cells, while MFs provide excitatory input to granule cells, which in turn give rise to parallel PFs. PFs provide input to Purkinje cells. **(B)** A simplified view of cerebellar circuitry shows the structure of the cerebellar module. Afferent MFs provide excitatory input to both DCN neurons and cortical granule cells. Granule cells relay these inputs to Purkinje cells. CFs provide collaterals to the same DCN neurons and Purkinje cell. The Purkinje cell provides inhibitory input to the DCN neuron, completing the circuit. DCN neurons then project to thalamic and motor targets, as well as the inferior olive. Adapted by permission from Macmillan Publishers Ltd: Nature Reviews Neuroscience (Apps and Garwicz, 2005).

Stellate and basket interneurons in the molecular layer provide feedforward inhibition to Purkinje cells, synapsing onto the distal dendrites and proximal dendrites and soma, respectively (**Fig. 1.8**). The integration of PF inputs in cerebellar Purkinje cells will be the focus of **Chapters 3 and 4**.

While MF inputs are relayed to every cell type in the cortex, CFs ascending through the white matter provide collaterals to DCN cells within a given laminar module, and are distinct in synapsing solely on Purkinje cells at the cortical level. Each Purkinje cell thus receives only one CF but upwards of 150,000 PF inputs (Barlow, 2002). However, each CF synapses several hundred times on the Purkinje cell soma and dendrites, providing a massive depolarization resulting in a *complex spike*. In contrast to a *simple spike*, which is a single, Na^+ dependent action potential, a complex spike is a single, large-amplitude spike of ~50 ms duration that supports the discharge of several high-frequency simple spikes.

Purkinje cells form a monolayer between the granular and molecular layers and provide the sole output from the cerebellar cortex in the form of inhibitory input to neurons in the DCN. There are three types of DCN neurons: large diameter glutamatergic projection neurons, small diameter GABAergic neurons, and local interneurons (Chan-Paly, 1978; Uusisaari and Knopfel, 2010; Uusisaari and De Schutter, 2011). The GABAergic neurons provide inhibitory input to the inferior olive. Glutamatergic DCN neurons provide cerebellar output to the thalamus, red nucleus, vestibular nucleus and other areas of the brain (Teune et al., 2000). Glutamatergic DCN neurons also project back to the cerebellar cortex as MFs, forming a feedback loop between the cortical and nuclear areas (Stanton, 1980). As indicated above, the DCN also receive excitatory input from collaterals of MFs and CFs.

Cortical and nuclear processing in the cerebellum therefore represents a dichotomy of synaptic processing. Purkinje neurons receive mainly excitatory input, whereas DCN neurons receive principally inhibitory input. Both of these neuron classes must properly process their synaptic input to generate an appropriate spike train to convey to the next processing center. However, how these neurons integrate these inputs is still largely unknown.

1.5 Purkinje cells

Due to their central role in cerebellar processing, Purkinje cells have been extensively studied and a great deal is now known about their physiology. Of particular interest have been the wide array of ion channels that are present and differentially distributed across their somatodendritic axis. Purkinje cells express nearly every type of VGCC, including Cav1 (Hell et al., 1993; Gruol et al., 2006), Cav2.1 (Usowicz et al., 1992; Womack et al., 2004), Cav2.2 (Westenbroek et al., 1992), Cav2.3 (Yokoyama et al., 1995), and Cav3 channels (Raman and Bean, 1999; McKay et al., 2006; Hildebrand et al., 2009) channels. Furthermore, they also express many subtypes of both K_{Ca} and voltage-dependent K^+ channels which control spike shape and firing frequency, among other functions (Edgerton and Reinhart, 2003; McKay and Turner, 2004; McKay et al., 2005). Importantly, $K_{Ca}1.1$ and $K_{Ca}2$ channels are both present in abundance (Cingolani et al., 2002; Womack et al., 2004), as are HCN channels (Angelo et al., 2007).

As previously mentioned, cerebellar Purkinje cells receive excitatory input from two sources: PFs originating from cerebellar granule cells and a CF originating from the inferior olive. While the CF input is an integral part of the cerebellar circuit, they are not the current focus of this thesis and will not be discussed in detail. The PF-Purkinje cell synapse has long been thought to be central to cerebellar function and has been proposed to be the site of cerebellar memory formation (Marr, 1969; Albus, 1971; Ito and Kano, 1982; Ito et al., 1982; De Schutter, 1995; Barlow, 2002; Steuber et al., 2007). Specifically, long-term depression of the PF input due to coincident activation with CF input has been postulated to underlie motor learning (Ito, 1989, 1990, 1993; De Schutter, 1995, 1997; Steuber et al., 2007), although this is theory is not unopposed (Bloedel and Kelly, 1992; Bloedel et al., 1993; Lisberger, 1995; Schonewille et al., 2011). While plasticity at the PF-Purkinje cell synapse as a model of cerebellar learning has been a long-standing hypothesis, the effect such plasticity would have on PC output and the computations of the cerebellar circuit have not yet been determined. In fact, recent studies investigating the effect of learning on Purkinje cell output have produced contending results (Jirenhed et al., 2007; Steuber et al., 2007). However, regardless of the role of long-term plasticity, the PF synapse itself is a source of nonlinearity in the cerebellar circuit, showing signifi-

cant frequency-dependent presynaptic facilitation. Therefore, understanding how PF inputs are integrated under normal conditions is critical to determining cortical processing. It is currently known that PF EPSPs activate a variety of postsynaptic ion channels, including VGCCs and HCN channels (Eilers et al., 1996; Williams et al., 2002; Hildebrand et al., 2009); however, relatively little is known regarding activation of Cav3 channels during PF bursts or how Purkinje cells respond to facilitating inputs. Determining how postsynaptic ion channels contribute to the processing of PF input is crucial to understanding how the cerebeller cortex translates sensory and motor information into a meaningful signal for downstream neurons.

1.5.1 Cav3 Ca^{2+} channels in Purkinje cells

Immunolabel or mRNA for all three Cav3 isoforms have been found in Purkinje cells throughout the soma and dendrites (Craig et al., 1999; Talley et al., 1999; McKay et al., 2006; Hildebrand et al., 2009), yet the role of these channels in Purkinje cell function is not well understood. It is known that I_T can generate low threshold Ca^{2+} spikes in Purkinje cell dendrites (Cavelier and Bossu, 2003). A significant proportion of Ca^{2+} current during burst firing is also carried by Cav3 channels (Swensen and Bean, 2003). However, these firing patterns are not seen under normal physiological conditions. Furthermore, application of mibefradil, a specific blocker of Cav3 channels, has no effect on tonic firing frequency in Purkinje cells (Womack et al., 2004), precluding their role in sustaining pacemaker activity, as has been seen in other cell types (Wolfart and Roeper, 2002). Cav3 channels must, therefore, have some other physiological function in Purkinje cells.

Cav3 channels may play a role in the integration of the many excitatory synaptic inputs that impinge on Purkinje cells. It has been previously demonstrated that synaptic integration can be controlled by differential expression and distribution of voltage-gated channels in the dendrites (Westenbroek et al., 1992; Magee et al., 1998; Hofmann et al., 1999). Indeed, Cav3 channels are present in Purkinje cell dendritic spines and shafts (Eilers et al., 1995a; Mouginot et al., 1997; Isope and Murphy, 2005; Hildebrand et al., 2009) and are thus in an ideal location to affect the integration of synaptic inputs. I_T could play a role in subthreshold Ca^{2+} signalling within the dendrites, including the recruitment

of Ca^{2+}-sensitive channels, synaptic plasticity, or modulation of biochemical processes. Indeed, it has already been shown that Cav3.1 channels are associated with group I metabotropic glutamate receptors (mGluR1) in Purkinje cell dendrites (Hildebrand et al., 2009). Therefore, it is possible that Cav3 channels are also associated with other postsynaptic ion channels.

1.5.2 K_{Ca} channels in Purkinje cells

Purkinje cells express both $K_{Ca}1.1$ and $K_{Ca}2$ channels, which regulate spike firing through the generation of spike-associated AHPs (Edgerton and Reinhart, 2003; McKay and Turner, 2004; Womack et al., 2004; Walter et al., 2006; Hosy et al., 2011; Ohtsuki et al., 2012). Properties of $K_{Ca}1.1$ channels in Purkinje cells have been thoroughly characterized (Womack and Khodakhah, 2002) and are selectively activated by Ca^{2+} influx through Cav2.1 Ca^{2+} channels (Womack et al., 2004). $K_{Ca}1.1$-mediated current contributes to the spike-associated fast AHP and regulates spike firing, as blocking Cav2.1 channels or $K_{Ca}1.1$ channels with specific blockers reduces fast AHP amplitude and increases spike frequency (Womack et al., 2004). Similarly, $K_{Ca}2$-mediated current generates a slow AHP and occlusion of $K_{Ca}2$ current by apamin increases spike firing and results in an inability to produce sustained tonic activity (Edgerton and Reinhart, 2003; McKay et al., 2007). $K_{Ca}2$ channels are also involved in synaptic integration. $K_{Ca}2$ current decrease PF EPSP amplitude and downregulation of $K_{Ca}2$ channels within specific dendritic compartments results in long-term potentiation of PF and CF inputs (Hosy et al., 2011; Ohtsuki et al., 2012). Therefore, K_{Ca} channels perform diverse functions in Purkinje cells. Because of their common dendritic distribution and the tendency for K_{Ca} channels to associate with VGCCs, it is possible that Cav3 channels activate K_{Ca} channels to control synaptic integration.

1.5.3 Hypothesis

Based on the reasoning above, I hypothesized that: ***Cav3 channels are recruited during subthreshold synaptic events and activate K_{Ca} channels to control PF EPSP summation***. Based on this hypothesis, I sought to answer the following research questions in Purkinje cells:

1. *Do Cav3 channels interact with K_{Ca} channels in the subthreshold range?*
2. *Are the properties of Cav3 channels conferred onto K_{Ca} channels?*
3. *How do Cav3 channels affect synaptic integration in Purkinje cells?*

1.6 DCN neurons

All output from cerebellar cortex must pass through the DCN before continuing to extracerebellar targets. Therefore, neurons of the DCN must encode and communicate all information processed in the cortical layer. Since input from Purkinje cells is inhibitory, information processing in the DCN poses a unique problem, as inhibitory innervation would presumably result in a decrease in spike output and information transfer. However, extensive *in vitro* work has revealed that DCN neurons respond to inhibitory input with a subsequent rebound burst (Tadayonnejad et al., 2010). Neuronal bursting is important in that it will invert the inhibitory signal provided by Purkinje cells and can increase the fidelity of information transferred within a narrow time window (Lisman, 1997). Therefore, an understanding of the bursting properties of DCN neurons, particularly in response to *in vivo*-like synaptic input, is necessary to determine how cerebellar output is generated.

Bursting in DCN neurons is not without controversy. Several *in vitro* studies have provided evidence that inhibitory synaptic inputs are sufficient to reach threshold for rebound burst generation (Gardette et al., 1985b; Llinas and Muhlethaler, 1988; Aizenman et al., 1998; Aizenman and Linden, 1999; Zhang et al., 2004; Tadayonnejad et al., 2009; Zheng and Raman, 2009). There is also evidence that sensory input and direct stimulation of MF or CF inputs *in vivo* invoke a series of synaptic excitation-inhibition that is reflected in a decrease and then rebound increase in firing of DCN cells (Ito et al., 1970; Armstrong et al., 1973; Armstrong et al., 1975; Kitai et al., 1977; McCrea et al., 1977; Schwartz et al., 1987; MacKay, 1988; Ohtsuka and Noda, 1991; Gruart et al., 1997; Ruigrok, 1997; Delgado-Garcia and Gruart, 2005; Rowland and Jaeger, 2005; Chen and Evinger, 2006; Rowland and Jaeger, 2008). However, the probability of evoking rebound bursts with synaptic inhibitory inputs either *in vitro* or *in vivo* was recently questioned (Alvina et al., 2008), although our own reassessment of this issue indicates a high proba-

bility of evoking rebound responses *in vitro* when stimulus intensities are appropriately considered (Tadayonnejad et al., 2009).

Our own *in vitro* studies have also established that DCN cells exhibit two phenotypes of rebound bursting that are identified as Weak Burst or Transient Burst neurons (Molineux et al., 2006; Molineux et al., 2008). Following a hyperpolarization, Transient Burst cells generate a high frequency (> 100 Hz) burst of 2-5 spikes followed by a large AHP and long interspike interval (Tadayonnejad et al., 2010). Weak Burst neurons generate bursts of less than 100 Hz with a continuous decline in frequency over several seconds. Furthermore, Weak Burst neurons are negative for glutamate decarboxylase (GAD-67), indicating this phenotype corresponds to non-GABAergic (putative excitatory) neurons (Molineux et al., 2006). On the other hand, both GAD-positive and GAD-negative Transient Burst cells have been found, meaning that the Transient Burst phenotype can be associated with both GABAergic and non-GABAergic neurons (Molineux et al., 2006). Since only GABAergic neurons project to the inferior olive, Transient Burst neurons may be responsible for creating the cortico-nucleo-olivary feedback loop. Given the importance of bursting in information transmission and the potentially separate roles that these two phenotypes may perform, it is important to understand the mechanisms controlling burst generation during the integration of IPSPs in DCN neurons.

Cells of the deep cerebellar nuclei (DCN) were among the first cells identified to generate rebound bursts following membrane hyperpolarizations *in vitro* (Gardette et al., 1985b; Jahnsen, 1986b; Llinas and Muhlethaler, 1988). The ionic contributions to a rebound response have been examined in numerous studies *in vitro* (Gardette et al., 1985a, b; Jahnsen, 1986b; Muri and Knopfel, 1994; Aizenman and Linden, 1999; Czubayko et al., 2001; Gauck et al., 2001; Molineux et al., 2006; Molineux et al., 2008; Pugh and Raman, 2008; Alvina et al., 2009; Zheng and Raman, 2009; Sangrey and Jaeger, 2010). From this work, two ion channels commonly believed to underlie rebound depolarizations are Cav3 and HCN channels (Jahnsen and Llinas, 1984; McCormick and Pape, 1990; Muri and Knopfel, 1994; Huguenard, 1996; Molineux et al., 2008; Biel et al., 2009). Both channels are characterized by unique kinetic and voltage-dependent properties that allow their availability to increase in response to a membrane hyperpolarization.

Cav3 are nearly fully inactivated at resting membrane potential, but recover during hyperpolarization (Perez-Reyes, 2003; Iftinca et al., 2006). HCN channels activate with increasing levels of hyperpolarization, such as can occur during a train of inhibitory inputs (Biel et al., 2009). When these currents are present, direct activation of I_T and an inward tail current resulting from the slow deactivation of I_H can result in a rebound depolarization following a release of inhibition.

1.6.1 Cav3 Ca^{2+} channels in DCN neurons

We have previously examined the ionic mechanisms underlying burst generation in DCN neurons, finding that each rebound burst phenotype correlates with the expression of a specific Cav3 isoform (Molineux et al., 2006). Transient Burst neurons consistently express immunolabel for Cav3.1 protein, but not Cav3.3, whereas the Weak Burst phenotype was correlated with Cav3.3 expression. As mentioned above, both cell types generate a burst of action potentials when released from hyperpolarization induced either by current injection or activation of a train of IPSPs. Burst frequency and duration are correlated with the depth and duration of the hyperpolarization, which suggests that bursting behaviour is generated by a voltage-gated current. Indeed, it was shown that Transient Burst neurons generate seven times more I_T following a hyperpolarization than Weak Burst neurons, indicating that Cav3 channels provide a significant amount of the current underlying at least the immediate spike burst (Molineux et al., 2008).

While there is solid evidence that I_T underlies bursts following strong hyperpolarizations, the role of Cav3 channels in processing physiological trains of inhibitory inputs had not been carefully examined. Because of their low voltage for activation and inactivation, Cav3 channels are more inactivated at resting potentials. Theoretically, hyperpolarizations must be of a certain depth and duration for inactivation to be removed from Cav3 channels. It is seems likely, therefore, that bursts would only be generated in response to particularly strong or long inhibitory inputs (as proposed by Zheng and Raman (2009)). In this case, burst generation would act as a feature detector of particular patterns of inputs.

1.6.2 HCN channels in DCN neurons

DCN neurons express HCN channels, indicated by the characteristic "sag" that is seen during hyperpolarization (Aizenman and Linden, 1999; Raman et al., 2000). Initial studies of the role of I_H in DCN neurons suggested that it was involved in the rebound burst following a hyperpolarization (Aizenman and Linden, 1999). However, more recent studies reported that the rebound burst is dependent on I_T, rather than I_H (Molineux et al., 2006; Molineux et al., 2008; Steuber et al., 2011). I_H does appear to have a role in at least the timing of the rebound burst and may coordinate with I_T to control rebound frequency (Sangrey and Jaeger, 2010; Steuber et al., 2011). Nevertheless, none of these questions have been addressed in the context of minimal, physiological levels of membrane hyperpolarizations to determine the exact role(s) that I_H may have in governing DCN cell output.

1.6.3 Hypothesis

The current knowledge on the roles of I_T and I_H in DCN neurons led me to the following hypothesis: ***Physiological depths and durations of hyperpolarization recruit I_T and I_H to control the frequency and temporal fidelity of rebound bursts in DCN neurons***. Therefore, I examined the following research questions in DCN neurons:

1. *How do I_T and I_H contribute to rebound frequency and latency?*
2. *How does the size and duration of hyperpolarization affect activation of I_T and I_H?*
3. *What is the role of I_H on the precision of the rebound burst?*

1.7 Acknowledging Collaborators

Since the publications resulting from my work involved extensive collaborative interactions, I wish to provide full acknowledgement for the primary roles of M. Kruskic and Drs. R. Rehak, H. Asmara, S. Hameed, and G.W. Zamponi in providing the immunohistochemical, protein biochemical, and molecular analyses presented here. Contributions to electrophysiological recordings or analyses were further provided by Drs. D. Anderson, B.E. McKay, R. Tadayonnejad, and W.H. Mehaffey, with any additional support as indicated in the authorship of publications. The work conducted by these collabo-

rators is presented here as necessary to provide the information needed to fully understand the data arising from my recordings and modelling.

Chapter Two: General Methods

2.1 General solutions

Chemicals were obtained from Sigma (St. Louis, MO) unless otherwise indicated. Artificial cerebrospinal fluid (aCSF) was composed of 125 mM NaCl, 3.25 mM KCl, 1.5 mM $CaCl_2$, 1.5 mM $MgCl_2$, 25 mM $NaHCO_3$ and 25 mM D-glucose continuously bubbled with carbogen gas. Picrotoxin (50 μM), 10 μM 6,7-dinitroquinoxolinedione (DNQX; Tocris, Ellisville MO), 25 μM DL-2-Amino-5-phosphonopentanoic acid (DL-AP5) (Ascent Scientific, Princeton NJ), and 1 μM CGP55485 (Tocris) were added to the aCSF for all recordings that did not require stimulation.

For current clamp recordings the pipette electrolyte consisted of 130 mM K-gluconate, 0.1 mM EGTA, 10 mM HEPES, 7 mM NaCl, 0.3 mM $MgCl_2$ (pH adjusted to 7.3 with KOH), providing an E_{Cl} of -76 mV and E_K of -97 mV. Di-tris-creatine phosphate (5 mM), 2 mM Tris-ATP and 0.5 mM Na-GTP were added daily from frozen stock solutions to all pipette solutions. A junction potential of -10.7 mV was subtracted from current clamp recordings. For whole-cell voltage clamp recordings, the pipette solution consisted of 140 mM KCl, 0.1 mM EGTA, 10 mM 4-(2-hydroxyethyl)-1-piperazineethanesulfonic acid (HEPES), and 2.5 mM $MgCl_2$ (pH adjusted to 7.3 with KOH). High concentrations of BAPTA (10 mM) or EGTA (10 mM) were included in the electrode where specified. Outside-out voltage clamp recordings of K^+ currents were obtained using an electrolyte of 140 mM KCl, 1 mM $MgCl_2$, 5 mM EGTA, and 10 mM HEPES (pH adjusted to 7.3 with KOH). Whole-cell voltage clamp recordings of Purkinje cell I_T were taken from P10-P12 animals to avoid space-clamp errors due to a developed dendritic tree (McKay and Turner, 2005) using an electrolyte consisting of 140 mM CsCl, 1 mM $MgCl_2$, 5 mM EGTA, and 10 mM HEPES (pH adjusted to 7.3 with CsOH). Outside-out voltage clamp recordings of HVA Ca^{2+} currents were obtained from somata of P18-25 Purkinje cells using an electrolyte consisting of 140 mM CsCl, 1 mM $MgCl_2$, 5 mM EGTA, and 10 mM HEPES, (pH adjusted to 7.3 with KOH). On-cell recordings of single channels were carried out with an internal electrolyte of HEPES-buffered aCSF

containing 150 mM NaCl, 3.25 mM KCl, 1.5 mM $CaCl_2$, 1.5 mM $MgCl_2$, 10 mM HEPES, and 20 mM D-glucose (pH adjusted to 7.3 with NaOH).

2.2 Pharmacology

Bath perfused channel blockers and ionophores were applied at concentrations of 100 nM TTX, 100 - 300 μM $NiCl_2$, 1 μM mibefradil, 30 μM $CdCl_2$, 2 μM A23187, 100 nM apamin, 5 mM TEA, 5 mM 4-aminopyradine (4-AP), 2 mM $CsCl_2$, 100 nM (1-[(2-chlorophenyl) diphenylmethyl]-1H-pyrazole (TRAM-34; Tocris)(Wulff et al., 2000), 100 nM paxilline, 6 μM cyclopiazonic acid (Ascent Scientific), 2.5 μM AM-251, 10 μM ryanodine and 1.5 μM JNJ16259685. Heparin (4mg/ml) or camstatin (5 μM) was included in the pipette electrolyte where indicated. Toxins applied locally were ejected from a pressure electrode containing HEPES (10 mM)-buffered aCSF as carrier medium at concentrations of 100 nM charybdotoxin (ChTx), 200 nM iberiotoxin (IbTx), 200 nM ω-agatoxin IVA (AgTx), 1 μM ω-conotoxin GVIA, 1 μM nifedipine and 200 nM SNX-482. All synaptic blockers were included in the HEPES-buffered aCSF at the concentrations described above. Food coloring (1:100) was also included to allow visualization of the area of drug ejection. BSA (0.1%) was included to prevent non-specific adhesion of the drugs. Apamin was first dissolved in 50 mM acetic acid before preparing stock solution and all toxins were prepared daily from frozen stock solutions.

When isolating $K_{Ca}3.1$ or Cav3 currents during on-cell single-channel recordings or voltage-clamp recordings (whole-cell and outside-out configurations), TTX, apamin, TEA, 4-AP, $CdCl_2$, and CsCl were bath applied. When isolating HVA Ca^{2+} current in outside-out patches from Purkinje cells, $NiCl_2$ and TRAM-34 were also included added.

2.3 Tissue preparation

Timed-pregnant Sprague-Dawley rats (obtained from Charles River, Saint-Constant, PQ) were maintained according to conditions of the Canadian Council on Animal Care. For Purkinje cell recordings, P18-P30 male pups were used unless otherwise indicated. Younger animals (P12-P18) were used for DCN recording in order to allow for visualization of cell bodies. Rats were anaesthetized by inhalation of isoflurane until unresponsive to tail pinch. The cerebellum was removed and constantly perfused with oxy-

genated, ice-cold aCSF during slice preparation. Parasagittal slices (240 – 300 μm) were cut by Vibratome and incubated at 35°C for 60 min, after which slices were kept at room temperature for up to 6 hours. Slices were subsequently transferred to a recording chamber on a Zeiss Axioskop FS-2 or Axioexaminer Z1 microscope (Thornwood, NY) and maintained at 33-35°C as a submerged preparation. Purkinje and DCN cells were directly visualized using differential interference contrast optics with infrared light (DIC-IR).

2.4 Electrophysiology

2.4.1 Conventional patch-clamp recording

Whole-cell current and voltage clamp somatic recordings were made using either an Axoclamp 2A amplifier/Digidata 1322 or a Multiclamp 700B amplifier/Digidata1440A (Molecular Devices). Data was collected with pClamp 8.1 or 10 software with a DC-10 kHz bandpass filter. Single channel recordings in on-cell mode were collected at 40 kHz sample frequency using a 4 kHz Bessel filter and analyzed using Clampfit (1 kHz Bessel filter) to identify channel openings and to calculate amplitude distribution histograms (5 min, 0.25 pA bin width). Command potentials were delivered from +30 mV to 0 mV in -10 mV steps to calculate single channel conductance according to the slope of unit current amplitudes against step potential. Pipettes were constructed from 1.5 mm O.D. fibre-filled glass (A-M Systems) with resistances of 4-8 MΩ. Series resistance was compensated with the bridge balance circuitry for current clamp recordings and with up to 80% compensation during voltage clamp recordings.

Purkinje cells were identified based on cell size and position in the cerebellar cortex between the molecular and granule cell layers. In general, recordings were restricted to the vermis, as the dendritic trees were more likely to be preserved in parasagittal slices; however, no systematic effort was made to track the location of Purkinje cell recordings. Purkinje cells were deemed to be healthy if: bridge balance did not change significantly during the recording; a stable baseline could be maintained; and less than 1.0 nA of negative bias current was necessary to maintain Purkinje cell resting potential at ~-75 mV and below the level of tonic firing.

DCN recordings were made from the interpositus nucleus and restricted to large diameter cells (> 15 μm) that displayed a fast AHP, DAP and slow AHP (Uusisaari et al., 2007; Uusisaari and Knopfel, 2010). Cells were considered healthy if: bridge balance did not change significantly during recorings; the neuron was capable of maintaining tonic firing; and a stable baseline voltage could be maintained during the recording. Baseline voltage during tonic firing was measured as the base of the AHP trough. DCN cells maintained at a resting potential of -60 mV tonically fired at a rate of 13.6 ± 6.1 Hz (n = 30) (Tadayonnejad et al., 2010).

2.4.2 Dynamic clamp recordings

Dynamic clamp recordings were made using a Multiclamp 700B amplifier and National Instuments BNC-2090. Real-time Experimental Interface (RTXI, National Institutes of Health)(Dorval et al., 2001) was used to control dynamic clamp calculations and current injection as well as record data. RTXI was installed on a custom computer running OpenSUSE 11.1 compiled with a real-time kernel. To compensate for bridge imbalance during current injection, Purkinje cell somata were patched with two recording electrodes, one to measure membrane voltage and another to inject current.

2.4.3 Stimulation

Stimulation of PF inputs was performed using a monopolar recording electrode placed in the molecular layer above the target PC soma in parasagittal slices. When coronal slices were used to preserve feedforward inhibition, the stimulating electrode was placed 100 – 200 μm lateral to the recording site to activate PF beams. Successful PF stimulation was defined by a clear separation of the PF EPSP rise time from the stimulation artefact and potentiation with repetitive stimulation

Purkinje cell inputs to DCN cells were triggered using a stimulus isolation unit (0.1 - 0.2 ms) with a concentric bipolar electrode (Frederic Haer, Bowdoin, Maine) placed dorsal to the recording site and outside of the DCN nuclei. Where indicated, the baseline amplitude of evoked inhibitory synaptic responses was first assessed under whole-cell voltage clamp and the IPSC adjusted to ~60% (214 ± 27 pA; n = 13) of the maximal

stimulus intensity. For other current clamp measurements, stimulus intensity was set to 60% of that which evoked a maximal rebound frequency increase.

2.4.4 Simulated EPSPs

Alternatively, PF-evoked EPSPs were simulated by injecting simulated EPSCs (simEPSC) at the soma. In brief, simEPSCs were calculated by digitally removing stimulus artefacts associated with PF stimulation under voltage clamp conditions. The sum of two exponentials was then used to simultaneously fit both rise and decay time constants of the synaptic response and the mean kinetics used to construct simEPSCs in Matlab. Rise and decay time constants of EPSCs were 1.0 ms and 8.9 ms respectively. Equations were of the form:

$$f(t) = A_1 e^{-t/\tau_{rise}} + A_2 e^{-t/\tau_{decay}}$$

where A_1 and A_2 were arbitrarily assigned such that functions began at 0 and rose to a peak at 1. simEPSCs were delivered to the command input of the amplifier as a scaled signal current command to evoke PF simEPSPs over a range of amplitudes (1 – 10 mV). Unless otherwise indicated, measurements cited for EPSP amplitude or rate of decay refer to EPSPs initially evoked with a 5 mV amplitude.

2.5 Modelling

Simulations were created using custom Matlab scripts and were performed in Matlab R2007b (Mathworks, MA) using the fourth-order Runge-Kutta method of solving ordinary differential equations. Since different models were used in Chapters 4 and 5, each model is explained in the Specific Methods section of the relevant chapter.

2.6 Data analysis

While the exponential time constant is often used to quantify rate of decay of synaptic inputs, the presence of the AHP introduced several overlapping exponential phenomena, making reduction to a single time constant difficult. I observed that the rate of decay approached a linear function in many cells between 90% and 10% of the EPSP height. Therefore, when quantifying PF EPSP decay, rate of decay was defined as the ve-

locity of voltage decay as measured by the slope between 90% and 10% of the EPSP height.

In all cases with stimulation, stimulus artefacts were removed prior to analysis. Analysis was performed either in Clampfit 10 or using custom Matlab R2007B scripts. OriginPro 8 (OriginLab Corp, MA) was used for statistical analysis. Figures were created in Adobe Illustrator (Adobe Systems Inc, San Jose, CA). Unless otherwise indicated, paired-sample Student's t-tests were used to determine significance. The Tukey HSD *post-hoc* comparison was used to determine significant difference between means following one-way or repeated measures ANOVA. Average values are expressed as mean ± s.e.m. * $p < 0.05$, ** $p < 0.01$, *** $p < 0.001$.

Chapter Three: The effect of the Ca_v3-$K_{Ca}3.1$ complex on parallel fibre summation

3.1 Introduction

As the site of convergence for both motor and sensory information in the cerebellar cortex, Purkinje cells receive a large number of excitatory and inhibitory synaptic inputs. This degree of convergence poses a problem for Purkinje cells, as they must be able to process this barrage of information into an appropriate series of spikes to be conveyed to the DCN. When only excitatory inputs are considered, Purkinje cells receive up to 150,000 PF inputs, each of which derive from granule cells tonically discharging at rates of ~1-4 Hz (Chadderton et al., 2004; Ekerot and Jorntell, 2008). From this enormous level of background activity Purkinje cells must be able to respond to short duration, high-frequency bursts of granule cell discharge characteristic of sensory input (Chadderton et al., 2004; Rancz et al., 2007; Ekerot and Jorntell, 2008; D'Angelo and De Zeeuw, 2009).

While the passive dendritic and somatic properties of a neuron form the backbone for electrical signalling and computation (London and Hausser, 2005), the active properties conferred by ion channels provide important nonlinear functions to the neuron. For example, dendritic currents can perform synaptic scaling and subthreshold boosting of synaptic inputs to improve synaptic processing in neurons with large dendritic trees. Purkinje cells express a wide array of ion channels, many of which have defined roles in synaptic processing. Previous work has shown that PF EPSP summation can be shaped by feedforward synaptic inhibition and the hyperpolarization-activated current I_H (Mittmann et al., 2005; Angelo et al., 2007). While we know that Purkinje cells also express all three Cav3 isoforms (McKay et al., 2006; Molineux et al., 2006), the role of these channels in signal processing is unclear. Previous studies have shown that blocking Cav3 channels with mibefradil has no effect on Purkinje cell tonic firing, which is highly sensitive to blockade of Cav2.1 channels (Womack et al., 2004). Conversely, up to 80% of the Ca^{2+} influx during spontaneous bursts is mediated by Cav3 channels (Swensen and Bean, 2003), suggesting some functional role. Due to the low-voltage range for activation of Cav3 channels, they would seem ideally suited to affect subthreshold synaptic inputs. Indeed, Cav3 channels associate with mGluR1 in the dendritic spines of Purkinje cells (Hildebrand et al., 2009). Synaptic activation of mGluR1 shifts the Cav3 activation curve

to more hyperpolarized potentials, resulting in increased I_T during PF EPSPs (Hildebrand et al., 2009). However, this association has only been demonstrated for Cav3.1 channels, while the role of the other isoforms is not known.

Ca^{2+} influx activates K_{Ca} channels in neurons to provide a negative feedback mechanism which controls excitability. $K_{Ca}1.1$ and $K_{Ca}2$ are both expressed in Purkinje cells and are activated by voltage-dependent Ca^{2+} influx associated with action potentials to control spike output (Edgerton and Reinhart, 2003; Swensen and Bean, 2003; Womack et al., 2004; Hosy et al., 2011). As previously mentioned, $K_{Ca}1.1$ channels are both voltage- and Ca^{2+}-dependent and are sensitive to micromolar concentrations of $[Ca^{2+}]_i$. Due to their low Ca^{2+} sensitivity, $K_{Ca}1.1$ channels form molecular complexes with HVA Ca^{2+} channels to gain access to the high $[Ca^{2+}]_i$ within the Ca^{2+} channel nanodomain (Grunnet and Kaufmann, 2004; Berkefeld et al., 2010). In Purkinje cells, $K_{Ca}1.1$ channels associate with Cav2.1 channels which are activated during action potentials to modulate the repolarization of action potentials (Edgerton and Reinhart, 2003; Womack et al., 2004). Of the three subtypes of $K_{Ca}2$ channels ($K_{Ca}2.1$, $K_{Ca}2.2$, $K_{Ca}2.3$), only $K_{Ca}2.2$ is expressed in mature Purkinje cells (Cingolani et al., 2002; Hosy et al., 2011; Ohtsuki et al., 2012). $K_{Ca}2$ channels have several roles in Purkinje cells, the most evident of which is sustaining tonic firing (Edgerton and Reinhart, 2003). $K_{Ca}2.2$ channels are also downregulated during long-term potentiation of PF EPSPs (Ohtsuki et al., 2012). While a specific Ca^{2+} source for $K_{Ca}2$ activation in Purkinje cells has not been identified, the lack of effect of mibefradil on tonic firing frequency suggests that Cav3 channels do not activate $K_{Ca}2$ channels. This is further supported by the fact that no molecular association has been found between Cav3 channels and $K_{Ca}2$ channels, with only a functional coupling between these ion channels reported in a limited number of neuronal cell types (Smith et al., 2002; Wolfart and Roeper, 2002; Cueni et al., 2008).

$K_{Ca}3.1$ channels exist in several cell types throughout the body, including microglia, lymphocytes, endothelial cells, and enteric neurons. Nevertheless, no studies have demonstrated $K_{Ca}3.1$ expression in central neurons. Like $K_{Ca}2$ channels, $K_{Ca}3.1$ has a high Ca^{2+} sensitivity with an IC_{50} ranging from 100 - 300 nM (Ishii et al., 1997b; Joiner et al., 1997) that might respond to the small Ca^{2+} influx through Cav3 channels. Further-

more, the large single-channel conductance of $K_{Ca}3.1$ would allow it to be highly effective in controlling subthreshold events.

We now report that Purkinje cells express $K_{Ca}3.1$ channels, the first evidence for this channel in a CNS neuron. Moreover, $K_{Ca}3.1$ channels are linked at the molecular level to Cav3 channels that allows even subthreshold PF EPSPs to invoke Ca^{2+} influx to activate a long duration AHP. The Cav3-$K_{Ca}3.1$ complex proves to exert a frequency-dependent suppression of temporal summation of EPSPs, such that low frequency PF inputs are suppressed. The Cav3-$K_{Ca}3.1$ complex thus creates a high-pass filter that reduces the effectiveness of background PF input and allows Purkinje cells to respond to higher frequencies of PF input indicative of sensory input.

3.2 Specific Methods

General methods pertaining to animal care, slice preparation and obtaining electrophysiological recordings are provided in **Chapter 2**. The following provides details specific to experiments testing the molecular and physiological ionic interactions underlying PF-evoked synaptic responses in Purkinje cells.

3.2.1 tSA-201 Cells.

Cav3.2 cDNA was kindly provided by T. Snutch (Vancouver, University of British Columbia). tsA-201 cells were transfected with cDNA for Cav3.1, 3.2 and 3.3 calcium channels (5 µg/µl), or cDNA for the Cav2.3 calcium channel (5 µg/µl) coexpressed with alpha2-delta (5 µg/µl) and beta-1b (5 µg/µl) subunits. All transfections included cDNA for GFP to identify cells successfully transfected. Currents were recorded at room temperature in aCSF consisting of 120 mM NaCl, 3 mM $NaHCO_3$, 4.2 mM KCl, 1.2 mM KH_2PO_4, 1.5 mM $MgCl_2$, 10 mM D-Glucose, 10 mM HEPES and 1.5 mM $CaCl_2$ (pH adjusted to 7.3 with NaOH). Electrodes were filled with 110 mM potassium gluconate, 30 mM KCl, 1 mM EGTA, 5 mM HEPES and 0.5 mM $MgCl_2$ (pH adjusted to 7.3 with KOH).

3.2.2 Immunohistochemistry

Adult males (~250 g) were deeply anesthetized with an overdose of sodium pentobarbital and perfused intracardially with 250 ml or 0.1 M phosphate buffer (PB, pH 7.4) followed by 100 ml of 4% paraformaldehyde (PARA, pH 7.4) at room temperature for 1 hr and overnight at 4°C. Free-floating 40-50 μm sections were cut by vibratome and transferred to a working solution of 3% normal donkey or horse serum (Jackson Immuno-Research), 0.2% TWEEN and 2% dimethylsulphoxide in PB. Primary antibodies were reacted for 48 hrs at 4°C and washed in working solution 3 X 15 min and secondary antibodies for 4 hrs at room temperature. After washing in PB, sections were mounted on gel-coated slides and coverslipped with anti-fade medium and stored at -20°C. Primary antibodies were mouse monoclonal anti IK-1(D-5) (1:100 Santa Cruz), rabbit polyclonal anti-Cav3.2 (H-300) (1:200 Santa Cruz), and mouse monoclonal anti-calbindin (1:1000; Swant). Secondary antibodies (1:1000) were the appropriate AlexaFluor-488 or -594 conjugated donkey IgGs (Molecular Probes). Controls consisted of omitting the primary antibodies. Images were obtained using a Zeiss AxioImager, Apotome Grid and Colibri LED illumination and processed in Abobe Photoshop and Illustrator.

3.2.3 Co-immunoprecipitation Assay

Fresh rat cerebellum was homogenized in lysis buffer (10% w/v, 150 mM NaCl, 50 mM Tris pH 7.5 and 1% NP-40 including protease inhibitors). The homogenate was centrifuged at ~16,000 x *g* for 10 min at 4 °C in a micro-centrifuge and supernatant collected. Protein concentration was estimated using the Bradford assay (BioRad). The supernatants (containing 200 μg total proteins) were incubated with mouse monoclonal anti-K_{Ca}3.1 antibody (sc-365265, Santa Cruz) at a 5 μg/ml final concentration overnight at 4 °C. The mixtures were then incubated with protein G-beads (Amersham) for 2 hrs to bring down the antibody-antigen complexes. The beads were washed three times with lysis buffer by centrifugation (700 X g)/re-suspension. The immune complexes were eluted using 40 μl of 2x SDS-PAGE sample buffer and heating for 5 min at 95 °C. Twenty μl eluents along with 40 μg of total protein from lysate were separated on SDS-PAGE gels. The primary antibodies used for Western blotting were rabbit polyclonal anti-

Cav3.2 (1:2500) (McKay et al., 2006) and rabbit polyclonal anti-Cav2.1 (4.75 µg/ml). The bands were detected by HRP linked secondary antibody (1:5000) and ECL+ (GE Healthcare, Quebec).

3.2.4 RT-PCR

3.2.4.1 Single cell samples

The cytoplasmic contents of Purkinje cells were extracted through whole-cell recordings in the slice preparation for RT-PCR analysis following procedures of Toledo-Rodriguez and Markram (Toledo-Rodriguez and Markram, 2007). Before recording, both the recording bath and lines were cleaned with HCl, and recording and bath electrodes were cleaned and rechlorided. The internal electrolyte for current-clamp recordings used to identify Purkinje cell firing patterns was the standard K-gluconate based solution (detailed in **Chapter 2**). To prevent RNA degradation by RNA nucleases, RNase inhibitor (200 U/ml) was included in the internal solution. Purkinje cells were patched under visual inspection by DIC-IR and the identity further confirmed by injecting depolarizing current steps to identify the pattern of action potential discharge (McKay and Turner, 2005). Negative pressure was then applied for 5 – 10 min and holding current was monitored in voltage clamp to ensure the integrity of the seal. After the internal contents of the cell were extracted, an outside-out patch configuration was attained upon withdrawing the electrode to prevent contamination of the single cell sample. Samples were transferred to a sterile centrifuge tube and immediately frozen on dry ice and stored at -80^{o}C.

3.2.4.2 Whole cerebellar samples

Whole cerebella were taken from rats at P18 and put in trizol solution (Invitrogen). The cerebellar RNA lysate was prepared by the acid-guanidinium thiocyanate-phenol chloroform extraction method (Chomczynski and Sacchi, 1987) with commercially available tri-reagent/trizol (Invitrogen). This method consists of several steps: cell lysis, phase separation, RNA precipitation, RNA wash, and redissolving RNA. The extract RNA was dissolved and stored as precipitate in RNase free water at -80^{o}C.

3.2.4.3 RT-PCR reaction

The mRNA from single cell samples and cerebellar RNA lysate were reverse transcribed using an Omniscript reverse transcriptase (Qiagen) and oligo d(T) primers in final volume of 20 μl. After 60 min incubation at 37°C, the cDNA was frozen and stored at -20°C before further processing. The cDNA samples were then amplified by PCR using *Taq* DNA polymerase (Invitrogen) and primers specific to the desired product.

Primers for K_{Ca}3.1 channels were:

IK1F: 5'- ATG GGC GGG GAG CTG GTG ACT GGC CTG GGG -3'

IK2F: 5'- GGC CAT GCT GCT ACG TCT CTA CCT GGT GCC TCG -3'

IK3R: 5'- GCT GAT GCC TGC GAG CCG CTC GGG AGT CC -3'

IK4R: 5'- CTA TGT GGC CTC CTG GAT GGG TTC TGG CGG CTG C -3'

Primers for Microglial Response Factor-1/ MRF-1 (Tanaka et al., 2000) were:

MRF-1 F: 5'-TCTGAGGAGCTATGAGCCAG-3'

MRF-1 R: 5'-TCCACCTCCAATTAGGGCAAC-3'

Primers for KCa1.1 channels (kindly provided by Dr. A. Braun) were:

hBKCa F: 5'- GGAATTCCAGTATCACAACAAGGCCCATCTG -3'

hBKCa R: 5'- GGAATTCAAGGACAGACCCACGAAGGCA -3'

Primers for KCa2.2 channels (kindly provided by Dr. A. Braun) were:

hSKCa2 F: 5'- GGTGGACTTGDCAAAGACCCAG -3'

hSKCa2 R: 5'- CTAGCTACTCTCTGATGAAGTTGG -3'.

Primers of K_{Ca}3.1 and MRF-1 were based on rat nucleotide sequences, and primers for K_{Ca}1.1 and K_{Ca}2.2 channel were based on human nucleotide sequences (accession numbers: NM_023021.1 for K_{Ca}3.1 channel, AB000818 for MRF-1, NM_181361.1 for K_{Ca}1.1 channels, and NM_021614.2 for K_{Ca}2.2 channels).

A two-round PCR was performed on cDNA of K_{Ca}3.1 channels, using the product obtained after the first round as template for the second round, while for others single-round PCR was performed. The first PCR of K_{Ca}3.1 was performed after adding PCR buffer, $MgCl_2$ (2.5 mM), 2.5 U Taq Polymerase and corresponding primers (IK1F and

IK4R) to the RT product (final volume 25 μl). Forty-five cycles were performed (denaturation at 95°C, 1 min; annealing at 65°C, 2 min for the first 5 cycles, and at 52°C, 1 min, for the remaining cycles; extension at 72°C, 2 min; final elongation at 72°C, 10 min), and an aliquot (5 μl) of the first round PCR product was used as template for the second PCR using the nested primers (IK2F and IK3R) with the same cycles and condition as described as above.

The single-round PCR tests were performed using 35 cycles (denaturation at 94°C, 1 min; annealing at 60°C, 1 min; extension at 72°C, 1 min; and final elongation at 72°C, 15 min). Negative controls for contaminations from genomic DNA were run as described above, but without adding reverse transcriptase to the RT reaction to ensure that genomic DNA did not contribute to the PCR products. A contamination from extraneous sources was ruled out by replacing the mRNA cellular template with water.

All products were identified by agarose gel electrophoresis (1%, stained with ethidium bromide) and documented with Alpha Innotech Gel Doc System. All $K_{Ca}3.1$ PCR products were confirmed by sequencing analyses**.**

3.2.4.4 Endothelial cell cultures

Endothelial cells were derived from a cultured human umbilical cell line, EA.hy926, stored as a pellet at -80°C (kindly provided by Dr. A. Braun, University of Calgary). The pellet was lysed in internal solution (the same solution for the Purkinje cell sample solution) and prepared for PCR using primers for $K_{Ca}3.1$ channels and a two-round PCR performed as for $K_{Ca}3.1$ channels. The negative controls were run as for Purkinje cells and whole cerebellar RT-PCR, and all products were identified the same as described above.

3.3 Results

3.3.1 PF EPSPs activate a Ca^{2+}-dependent AHP

To examine the potential for PF EPSPs to activate postsynaptic currents, we required a method to apply pharmacological agents while avoiding confounding presynaptic effects. We first stimulated PF inputs to examine the postsynaptic waveform. Stimulations were performed in the presence of GABA receptor antagonists picrotoxin and CGP55845 to block GABAergic transmission. The subthreshold evoked PF EPSP was followed by a graded AHP of up to ~250 ms duration which increased with the amplitude of the EPSP (**Fig. 3.1*A***). We then simulated EPSPs by injecting simulated EPSC (simEPSC) waveforms at the soma in the presence of inhibitory and excitatory synaptic blockers. Importantly, simEPSCs injected at the soma were capable of reproducing physiological voltage responses triggered by direct stimulation of PF inputs, including a graded EPSP and AHP (**Fig. 3.1*A***). This was important in providing a means of examining postsynaptic contributions to the PF EPSP while avoiding presynaptic effects.

It has been shown previously that some portion of the AHP following a PF EPSP can be attributed to deactivation of I_H (Angelo et al., 2007). I considered blocking I_H to study the sEPSP-AHP in isolation, but given that blocking I_H substantially changes the membrane time constant, all experiments were conducted with I_H intact. Furthermore, recordings were made from a membrane potential of -75 mV to restrict analysis to the subthreshold range and avoid generating action potentials. It has been previously shown that subthreshold EPSPs are capable of recruiting Ca^{2+} current in hippocampal CA1 pyramidal cell dendrites (Magee et al., 1995). Cav3 Ca^{2+} channels have been localized to both the soma and dendrites of Purkinje cells (Cavelier and Bossu, 2003; Isope and Murphy, 2005; McKay et al., 2006), with increases in internal [Ca^{2+}] detected during subthreshold synaptic inputs (Eilers et al., 1995a; Eilers et al., 1996; Watanabe et al., 1998). I thus hypothesized that PF EPSPs would be capable of recruiting Ca^{2+} currents in Purkinje cell dendrites.

To test this hypothesis, I applied blockers against HVA or LVA Ca^{2+} channels to measure the effect on the simEPSP-AHP. I found no significant effect on the simEPSP-AHP by the Cav2.1 channel blocker AgTx (200nM, $n = 4$, $p > 0.05$) (**Fig. 3.1*B***).

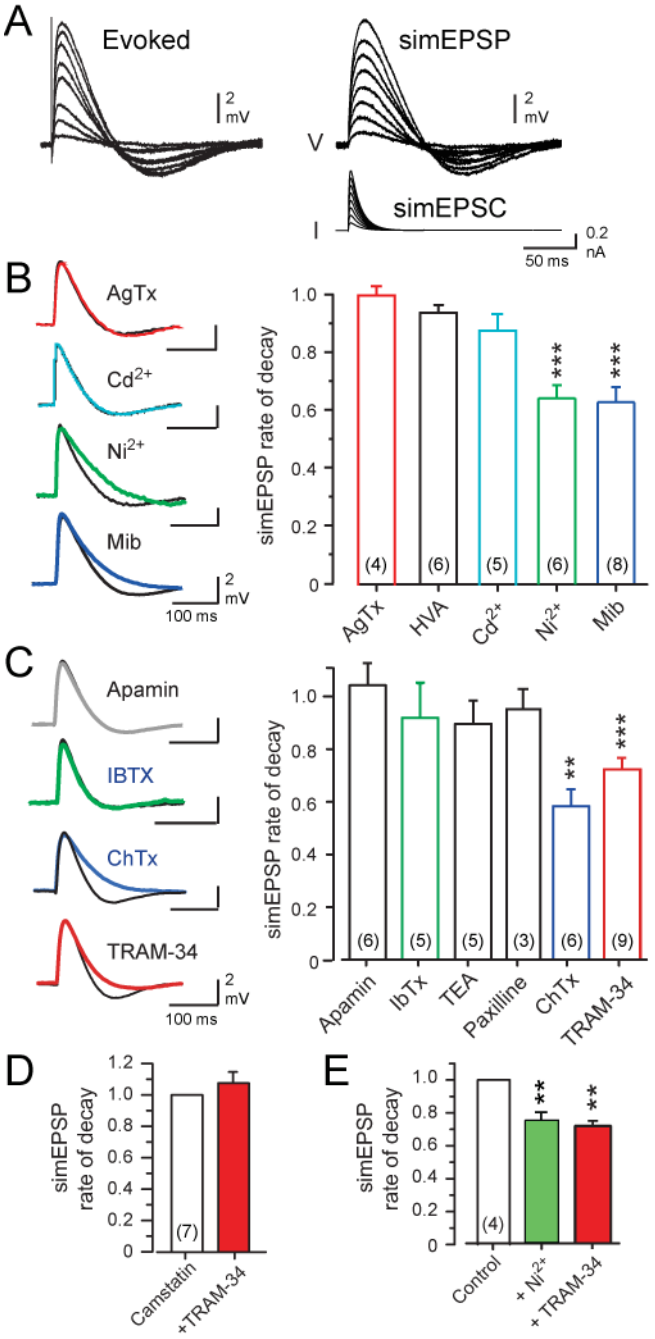
A
Evoked
2 mV
simEPSP
2 mV
V
simEPSC
I
0.2 nA
50 ms
B
AgTx
Cd2+
Ni2+
Mib
2 mV
100 ms
simEPSP rate of decay
1.0
0.8
0.6
0.4
0.2
0
***
***
(4)
(6)
(5)
(6)
(8)
AgTx
HVA
Cd2+
Ni2+
Mib
C
Apamin
IBTX
ChTx
TRAM-34
2 mV
100 ms
simEPSP rate of decay
1.0
0.8
0.6
0.4
0.2
0
**
***
(6)
(5)
(5)
(3)
(6)
(9)
Apamin
IbTx
TEA
Paxilline
ChTx
TRAM-34
D
simEPSP rate of decay
1.2
1.0
0.8
0.6
0.4
0.2
0
(7)
Camstatin
+TRAM-34
E
simEPSP rate of decay
1.0
0.8
0.6
0.4
0.2
0
**
**
(4)
Control
+ Ni2+
+ TRAM-34

Figure 3.1: Subthreshold PF EPSPs generate an AHP consistent with an activation of $K_{ca}3.1$.

All recordings were evoked using simEPSCs to test postsynaptic channel contributions, with drug effects on the rate of EPSP decay normalized to the control 5 mV simEPSP. **(A)** Representative recordings of evoked and simEPSPs from the same Purkinje cell show that simEPSC injection can replicate many of the evoked EPSP features. **(B, C)** Representative recordings (*left*) and bar plots (*right*) showing the effects of Ca^{2+} and K^{+} channel blockers. **(B)** The simEPSP rate of decay is not significantly affected by AgTx (200 nM) or other HVA Ca^{2+} channel blockers (ω-conotoxin GVIA, 1 μM; nifedipine, 1 μM; SNX-482, 200 nM) or Cd^{2+} (30 μM), but is reduced by putative Cav3 channel blockers Ni^{2+} (100 μM) and mibefradil (Mib,1 μM). **(C)** The simEPSP rate of decay is unaffected by the KCa2.x blocker apamin (100 nM), or KCa1.1 blockers IbTx (200 nM), TEA (5 mM), or paxilline (100 nM), but is significantly reduced by ChTx (100 nM) and TRAM-34 (100 nM). **(D)** Internal dialysis of Camstatin (5 μM) occludes the effect of TRAM-34 on the simEPSP rate of decay. **(E)** Pre-treatment with Ni^{2+} occludes the action of TRAM-34 on the simEPSP rate of decay. Sample numbers are shown in brackets at the base of bar graphs. Experiments performed by J Engbers.

Similarly, no effects were obtained upon pressure ejection of a cocktail of other HVA Ca^{2+} channel blockers, including ω-conotoxin GVIA (1 μM), nifedipine (1 μM), and SNX-482 (200 nM) ($n = 6$, $p > 0.05$), or bath application of the general HVA blocker Cd^{2+} (30 μM, $n = 5$, $p > 0.05$) (**Fig. 3.1*B***), despite verification that 30 μM Cd^{2+} abolished 90% of HVA Ca^{2+} current in outside-out patches from Purkinje cell somata (**Fig. 3.2*A***). However, both the simEPSP rate of decay and AHP were significantly reduced by low concentrations of the putative Cav3 channel blockers Ni^{2+} (100 μM, $n = 6$, $p < 0.001$) and mibefradil (1 μM, $n = 8$, $p < 0.001$) (**Fig. 3.1*B***) (McDonough and Bean, 1998; Lee et al., 1999). Indeed, Ni^{2+} could affect several aspects of the simEPSP-AHP, including the time to peak and rate of rise of the simEPSP (**Fig. 3.3*A***), but the most reliable effect was a reduction in the simEPSP rate of decay, suggesting that Ca^{2+} influx through Cav3 channels activates an outward current (**Fig. 3.1*B***).

The relative lack of specificity of Cav3 channel blockers leaves open the possibility that these effects were not entirely mediated through T-type channels. First, Ni^{2+} and mibefradil also block Cav2.3 Ca^{2+} channels (Zamponi et al., 1996; Randall and Tsien, 1997). However, a lack of effect by SNX-482 on the simEPSP ruled out Cav2.3 channel involvement (**Fig. 3.1*B***). Furthermore, a low concentration of Cd^{2+} was effective at blocking Cav2.3 channels in tSA-201 cells (**Fig. 3.2*B***), but had no effect on the simEPSP-AHP, precluding Cav2.3 channel involvement in this mechanism. The effects of Ni^{2+} on the simEPSP-AHP were also separate from those of blocking I_H, providing an additional decrease rate of decay after application of Cs^+ (2 mM) (**Fig. 3.3*B***). ZD-7228 was not used to test I_H given non-specific actions on Cav3 channels (Sanchez-Alonso et al., 2008). It is possible that internal calcium stores may be released during the depolarization and may activate an outward current. However, the effects of Ni^{2+} were further maintained in the presence of internal heparin (4 mg/ml) and bath applied cyclopiazonic acid (6 μM) ($n = 4$, $p < 0.01$), indicating no involvement of IP_3-mediated Ca^{2+} release or Ca^{2+}-ATPases (**Fig. 3.3*C***). K_{Ca} channels can also be activated by ryanodine receptor-mediated Ca^{2+} induced Ca^{2+} release (Vogalis et al., 2001; van de Vrede et al., 2007); however, ryanodine (10 μM) had no significant effect on the simEPSP rate of decay ($n = 4$, $p > 0.05$)(**Fig. 3.3*D***). Together these data suggest that the simEPSP activates Ca^{2+}

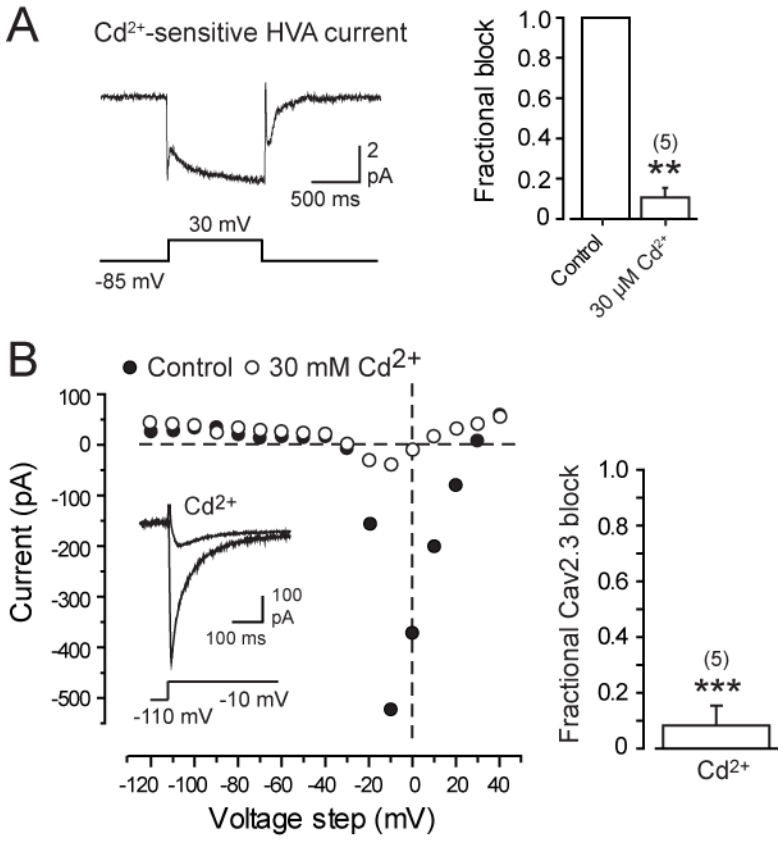
A
Cd2+-sensitive HVA current
2
pA
500 ms
30 mV
-85 mV
Fractional block
1.0
0.8
0.6
0.4
0.2
0
(5)
**
Control
30 μM Cd2+
B
Control
30 mM Cd2+
Current (pA)
100
0
-100
-200
-300
-400
-500
Cd2+
100
pA
100 ms
-110 mV
-10 mV
-120 -100 -80 -60 -40 -20 0 20 40
Voltage step (mV)
Fractional Cav2.3 block
1.0
0.8
0.6
0.4
0.2
0
(5)
***
Cd2+

Figure 3.2 The efficacy of Cd^{2+} as a HVA calcium channel blocker.

(A) Example of Cd^{2+} (30 μM) -sensitive HVA calcium current (presumed P/Q-type) recorded in outside-out patches from the soma of a P18-25 Purkinje cell. Patches were stepped from -85 mV to 30 mV to evoke HVA calcium current. Record represents the difference current between control and Cd^{2+}-treated tissue in the presence of 100 μM Ni^{2+} to block Cav3 T-type calcium currents. Mean bar plots indicate a near complete block of HVA calcium current by 30 μM Cd^{2+}. **(B)** Representative current-voltage plot and recording (*inset*) of R-type current recorded at room temperature in tSA-201 cells following co-transfection of Cav2.3 cDNA with α2-δ and β1-b subunits. Substantial block is obtained upon perfusion of 30 μM Cd^{2+}. Bar plot at right illustrates the average block of R-type calcium current by 30 μM Cd^{2+} in tSA-201 cells. Experiments performed by D Anderson and WH Mehaffey.

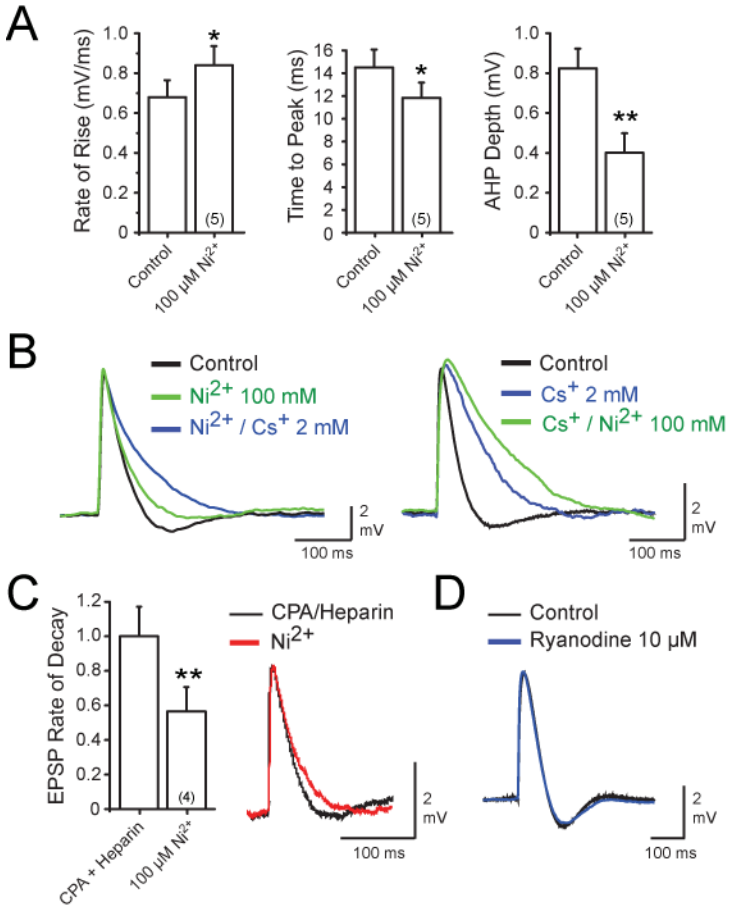
A
Rate of Rise (mV/ms)
Time to Peak (ms)
AHP Depth (mV)
Control
100 μM Ni2+
(5)
B
Control
Ni2+ 100 mM
Ni2+ / Cs+ 2 mM
Cs+ 2 mM
Cs+ / Ni2+ 100 mM
2 mV
100 ms
C
EPSP Rate of Decay
CPA + Heparin
(4)
CPA/Heparin
Ni2+
D
Ryanodine 10 μM

Figure 3.3: The effects of Ni^{2+} on the simEPSP.

(A) Ni^{2+} (100 μM) causes a significant increase in the simEPSP rate of rise and decreases both the simEPSP time to peak and AHP depth. **(B)** The effect of Ni^{2+} on the simEPSP rate of decay and AHP are distinct from Cs^{+}-sensitive I_H. Ni^{2+} application slows the rate of decay of a simEPSP and decreases AHP amplitude whether applied before or after Cs^{+} to block I_H. Shown are superimposed recordings of simEPSPs in control medium (*black*) and after perfusion of Ni^{2+} (thick *green*) or Cs^{+} (*blue*). **(C)** Bar plots and representative recordings indicating that the effect of Ni^{2+} on the simEPSP rate of decay is maintained in the presence of cyclopiazonic acid (CPA, 6 μM) and internal heparin (4 mg/ml). **(D)** Recordings showing the lack of effect by ryanodine (10 μM) on simEPSP rate of decay. Drug effects were normalized to the control 5 mV simEPSP. Experiments performed by J Engbers.

influx through Cav3 Ca^{2+} channels to control an outward current with an onset early enough to affect both the EPSP rate of decay and AHP.

3.3.2 EPSP rate of decay is shaped by a K^+ current consistent with $K_{Ca}3.1$ K^+ channels

Since Ca^{2+} influx was activating an outward current, I hypothesized that a K_{Ca} channel was being activated during the EPSP. Therefore, I next examined the identity of K^+ channels activated by the simEPSP. The most likely candidates were $K_{Ca}1.1$ and $K_{Ca}2$ channels that underlie the generation of AHPs in virtually all central neurons, both of which are expressed in cerebellar Purkinje cells. Surprisingly, the simEPSP rate of decay was entirely unaffected by bath application of the $K_{Ca}2$ channel blocker apamin (100 nM, $n = 6$, $p > 0.05$) or by the $K_{Ca}1.1$ channel blockers IbTx (200 nM, $n = 5$, $p > 0.05$), TEA (5 mM, $n = 5$, $p > 0.05$), or paxilline (100 nM, $n = 3$, $p > 0.05$) (**Fig. 3.1*C***), despite confirmed effects of each drug on spontaneous firing. In contrast, the simEPSP rate of decay was reduced by 41.7 ± 6.4% by ChTx (100 nM, $n = 6$, $p < 0.01$) (**Fig. 3.1*C***). ChTx is known to block $K_{Ca}1.1$ and $K_{Ca}3.1$ channels and specific isoforms of voltage-gated K^+ channels of the Kv1 family (Coetzee et al., 1999; Wei et al., 2005). However, the lack of effect of three other blockers for $K_{Ca}1.1$ essentially ruled out this channel as the target for ChTx. Kv1 channels are also not dependent on Ca^{2+} influx, as found in terms of a reduction in the simEPSP rate of decay by Ni^{2+} or mibefradil. This led to the surprising alternative hypothesis that the $K_{Ca}3.1$ may be responsible for the outward current underlying the AHP, despite the lack of evidence for $K_{Ca}3.1$ expression in central neurons. $K_{Ca}3.1$ channels are apamin-insensitive but have specific binding sites for ChTx and the clotrimazole-related compound TRAM-34 (Rauer et al., 2000; Wulff et al., 2001). TRAM-34 has been established as a selective $K_{Ca}3.1$ blocker with no effects on $K_{Ca}1.1$, $K_{Ca}2.2$, or a wide array of Kv channels (Wulff et al., 2000; Wulff et al., 2001). I thus applied TRAM-34 (100 nM) and found that the simEPSP rate of decay was reduced by 24.7 ± 3.9% ($n = 9$, $p < 0.001$) (**Fig. 3.1*C***).

As the sensitivity of Cav3 channels to TRAM-34 had not been previously tested, we examined the effect of TRAM-34 on all three Cav3 isoforms to test for any nonspecific effects that could account for a secondary reduction of the K^+ current following the simEPSP. tSA-201 cells were transfected with one of three Cav3 isoforms and the effect

of TRAM-34 (100 nM) was examined. However, we found no decrease in Ca^{2+} current by TRAM-34 with any of the Cav3 isoforms (**Fig. 3.4**). These findings suggested that TRAM-34 was indeed blocking $K_{Ca}3.1$ channels expressed in Purkinje cells. In support of this, the simEPSP also proved to be insensitive to TEA at concentrations < 25 mM (n = 13), a finding consistent with $K_{Ca}3.1$ channels but eliminating several other potassium channel subtypes ($K_{Ca}1.1$, Kv1.1, Kv1.6, Kv2.x, Kv3.x channels) (Coetzee et al., 1999). Finally, since $K_{Ca}3.1$ channels are gated by CaM which provides Ca^{2+}-sensitivity to the channel, I attempted to prevent activation of $K_{Ca}3.1$ by including the CaM blocker camstatin in the internal solution (Slemmon et al., 1996). Inclusion of camstatin in the electrode (5 μM) occluded the effects of TRAM-34 (**Fig. 3.1*D***, n = 7, $p > 0.05$), confirming that the Ca^{2+}-dependence of the K^+ channel underlying the AHP depends on CaM.

These results strongly implicate $K_{Ca}3.1$ channels given that $K_{Ca}1.1$ channels are highly sensitive to TEA (Coetzee et al., 1999) and neither $K_{Ca}1.1$ nor Kv1.x channels are CaM dependent (Pedarzani and Stocker, 2008). Furthermore, while $K_{Ca}2$ is gated by CaM, it is highly sensitive to apamin, which had no effect on the simEPSP-AHP. There was also no significant difference between the effects of Ni^{2+}, mibefradil, ChTx, or TRAM-34 on the simEPSP rate of decay (F = 2.37, one-way ANOVA), suggesting the antagonists acted on a common pathway. In support of this, the effects of TRAM-34 on the simEPSP-AHP were occluded by prior Ni^{2+} treatment (**Fig. 3.1*E***, n = 4, $p > 0.05$). Altogether, these data reveal a postsynaptic current with a pharmacological profile that is unique to $K_{Ca}3.1$ channels (Coetzee et al., 1999; Wulff et al., 2000) and activated by Cav3-mediated Ca^{2+} influx.

3.3.3 Purkinje cells express $K_{Ca}3.1$ channels

Identifying an outward current with $K_{Ca}3.1$-like properties was unexpected. Although KCCN4 mRNA, which encodes the $K_{Ca}3.1$ α-subunit, had been detected in the cerebellar Purkinje cell layer (Lein et al., 2007), $K_{Ca}3.1$ expression had not been reported in CNS neurons (Pedarzani and Stocker, 2008). Of the three Cav3 channel isoforms expressed in Purkinje cells (McKay et al., 2006; Molineux et al., 2006; Hildebrand et al., 2009), Cav3.2 is preferentially blocked by 100 μM Ni^{2+} (Lee et al., 1999), as found for

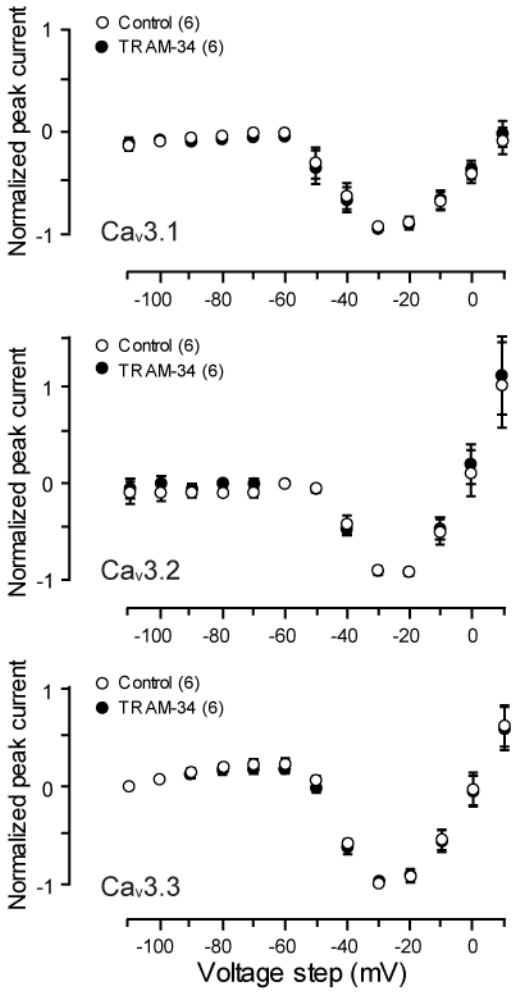
Control (6)
TRAM-34 (6)
Normalized peak current
1
0
-1
Cav3.1
-100
-80
-60
-40
-20
0
Control (6)
TRAM-34 (6)
Normalized peak current
1
0
-1
Cav3.2
-100
-80
-60
-40
-20
0
Control (6)
TRAM-34 (6)
Normalized peak current
1
0
-1
Cav3.3
-100
-80
-60
-40
-20
0
Voltage step (mV)

Figure 3.4: TRAM-34 has no effect on Cav3 calcium currents.

Current-voltage plots are shown for each of the Cav3 calcium channel isoforms expressed in tSA-201 cells. Currents were recorded at room temperature and evoked by steps from -110 mV to 10 mV before and after perfusion of TRAM-34 (100 nM). Experiments performed by D Anderson.

the evoked AHP (**Fig. 3.1*B***). We thus used dual-label immunocytochemistry to detect $K_{Ca}3.1$ protein in relation to Cav3.2 protein or calbindin, a cytosolic protein distributed throughout the Purkinje cell soma and dendrites (**Figs. 3.5, 3.6**). $K_{Ca}3.1$ immunolabel was detected at the soma and over restricted segments of primary and secondary dendritic branches of Purkinje cells, regions that were closely matched by that of Cav3.2 immunolabel, revealing colocalization (**Fig. 3.5*A-F*, 3.6**). To further test for $K_{Ca}3.1$ expression, we performed RT-PCR using primers directed against a 602 bp length of rat KCCN4 mRNA that includes the pore region of the $K_{Ca}3.1$channel (Nguyen et al., 2007). We also tested for the expression of Microglial Response Factor-1 (MRF-1) as a specific marker for microglia, which also express $K_{Ca}3.1$ channels and are a possible source of contamination (Kaushal et al., 2007). These tests revealed the presence of $K_{Ca}3.1$ cDNA at the predicted product weight in homogenates of rat cerebellum, as well as $K_{Ca}1.1$, $K_{Ca}2.2$, and $K_{Ca}3.1$ in cytosolic extracts from single Purkinje cells (**Fig. 3.5*G***). As predicted by a reported decrease in $K_{Ca}2.2$ mRNA through development (Cingolani et al., 2002), the $K_{Ca}2.2$ band was detectable but relatively faint compared to $K_{Ca}1.1$ or $K_{Ca}3.1$ (**Fig. 3.5*G***). The band for $K_{Ca}3.1$ in Purkinje cell samples also matched that of $K_{Ca}3.1$ in lysates of cultured endothelial cells known to express $K_{Ca}3.1$ (**Fig. 3.5*G***) (Hannah et al., 2011). In contrast, MRF-1 cDNA was present only in cerebellar homogenate (**Fig. 3.5*G***), indicating that $K_{Ca}3.1$ mRNA in Purkinje cell samples did not reflect microglial contamination. Furthermore, sequence analysis of the purified $K_{Ca}3.1$ band in Purkinje cells confirmed that the product represented the region spanning the $K_{Ca}3.1$ channel pore, and included the known binding sites for TRAM-34 and ChTx (Nguyen et al., 2007) but not an apamin binding site (Ishii et al., 1997a).

Direct tests for the expression of K^+ channels that were both Ca^{2+}-sensitive and of intermediate conductance were carried out using on-cell recordings from Purkinje cell somata. On-cell patch electrodes were filled with HEPES-buffered aCSF to provide a physiological level of Ca^{2+} outside, along with TTX (200 nM), Cd^{2+} (30 μM), apamin (100 nM), TEA (5 mM), 4-AP (5 mM), and Cs^+ (2 mM) in both the electrode and external medium to block sodium, HVA Ca^{2+}, $K_{Ca}2$, $K_{Ca}1.1$, Kv, and HCN channels. Cav3 channel blockers were specifically excluded and the availability of Cav3 channels

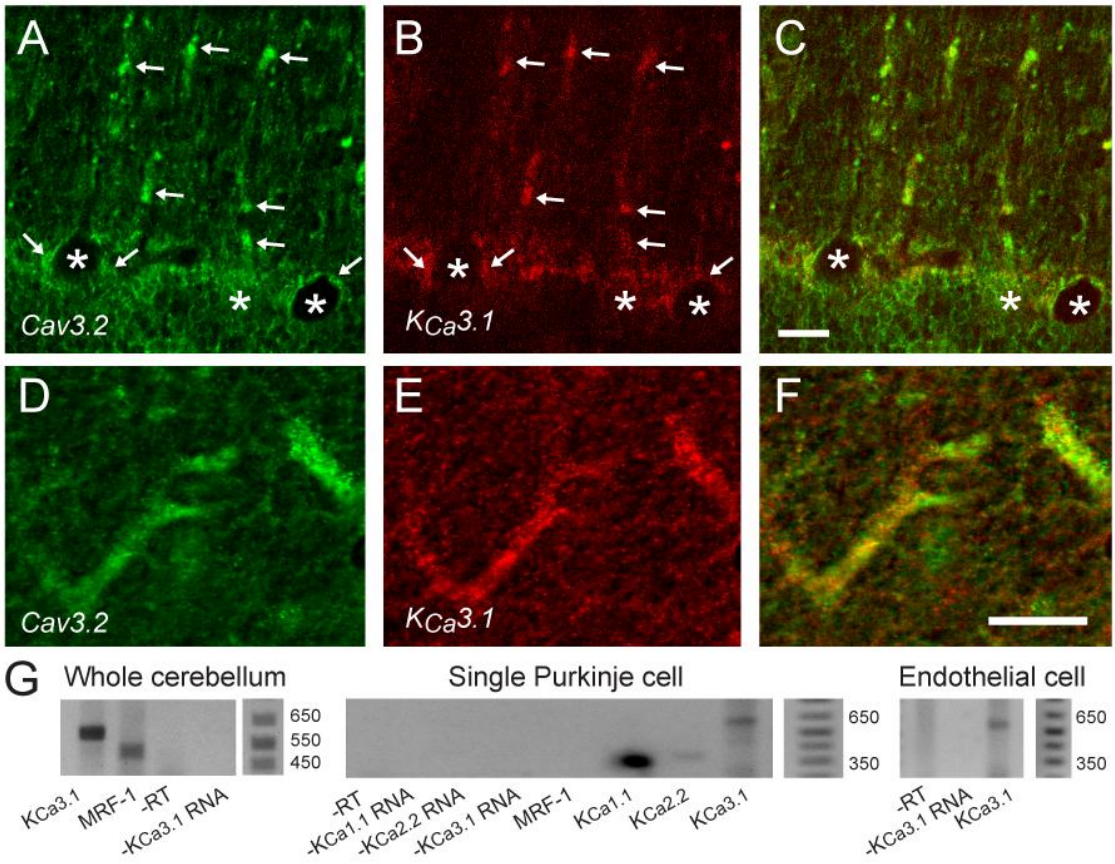
A
B
C
Cav3.2
KCa3.1
D
E
F
Cav3.2
KCa3.1
G
Whole cerebellum
650
550
450
KCa3.1
MRF-1
-RT
-KCa3.1 RNA
Single Purkinje cell
650
350
-RT
-KCa1.1 RNA
-KCa2.2 RNA
-KCa3.1 RNA
MRF-1
KCa1.1
KCa2.2
KCa3.1
Endothelial cell
650
350
-RT
-KCa3.1 RNA
KCa3.1

Figure 3.5: Purkinje cells express K_{Ca}3.1 channels that colocalize with Cav3.2 protein.

(A-C) Dual label immunocytochemistry for Cav3.2 **(A)** and K_{Ca}3.1 **(B)** in a coronal section reveals protein colocalized (*arrows*) at the soma (*asterisks*) and restricted segments of dendritic branches **(C)**. **(D-F)** High power view of Purkinje cell dendrites in a sagittal section dual labeled for Cav3.2 **(D)** and K_{Ca}3.1 protein **(E)**, with overlay in **(F)** illustrating colocalization over specific segments of dendritic branches. **(G)** RT-PCR reveals K_{Ca}3.1 and MRF-1 mRNA in whole cerebellum (*left*), and K_{Ca}1.1, K_{Ca}2.2 and K_{Ca}3.1 but not MRF-1 in single Purkinje cell cytoplasmic extracts (*middle*). The K_{Ca}3.1 product in Purkinje cells matches that found in endothelial cells (*right*). Scale bars: 20 μm. Immunohistochemistry performed by M Kruskic. Single cell RNA extraction performed by J Engbers and RT-PCR by H Asmara.

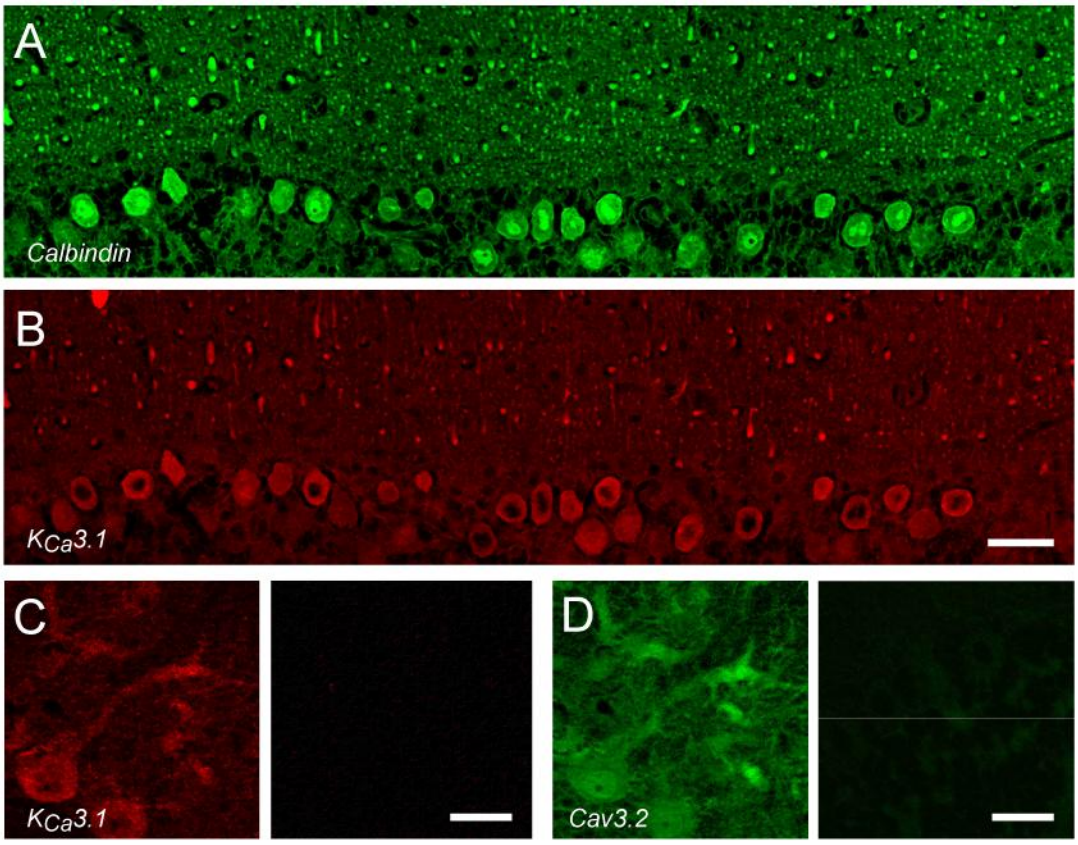
A
Calbindin
B
$K_{Ca}3.1$
C
$K_{Ca}3.1$
D
Cav3.2

Figure 3.6: K_{Ca}3.1 channels are expressed in Purkinje cells.

(**A, B**) Low power montage of the cerebellar Purkinje cell layer and proximal molecular layer in a coronal tissue section dual labeled for calbindin (**A**) and K_{Ca}3.1 (**B**) showing K_{Ca}3.1expression in Purkinje cell somata and restricted regions of dendrites. (**C, D**) Higher power image in sections cut in the sagittal plane showing K_{Ca}3.1 immunolabel (**C**) and Cav3.2 immunolabel (**D**) on Purkinje cell somata and proximal dendrites, with associated controls consisting of omission of primary antibody. Control and test images were matched for light intensity during imaging and processing. Scale bars: **A**, 50 μm; **C, D**, 20 μm. Immunohistochemistry performed by M Kruskic.

promoted by applying a +60 mV potential to the pipette at rest to hyperpolarize the patch transmembrane potential. Channel conductance was determined by applying steady-state commands (5 min) up to +30 mV from the resting condition to depolarize the patch to within the subthreshold voltage range. Spontaneous channel openings were readily detected in all patches, with either single or multiple channel openings per patch that changed linearly in amplitude with applied voltage (**Fig. 3.7*A,B***). Mean conductance, as determined from unit amplitude over a range of voltage steps, was 36.3 ± 0.1 pS (**Fig. 3.7*B***, $n = 5$), a value within the range previously reported for $K_{Ca}3.1$ channels (Ishii et al., 1997b). Importantly, bath application of the Ca^{2+} ionophore A23187 (2 μM, $n = 6$) dramatically increased single channel activity (**Fig. 3.7*C***), indicating an increase in open probability with rises in $[Ca^{2+}]_i$. Moreover, channel openings were blocked by perfusion of TRAM-34 ($n = 6$), a lipophilic drug that acts at the cytoplasmic face (**Fig. 3.7*C***) (Wulff et al., 2001). These results, combined with the mRNA, immunolabel, and pharmacological profiles established in **Figs. 3.1**, **3.5**, and **3.6** provide strong evidence that $K_{Ca}3.1$ channels are expressed in Purkinje cells.

3.3.4 Cav3 and $K_{Ca}3.1$ channels exhibit nanodomain coupling to evoke a transient voltage-dependent K^+ current

The selective reduction of the simEPSP rate of decay by Cav3 channel blockers (**Fig. 3.1*B***) raised the possibility that Cav3 and $K_{Ca}3.1$ channels are part of a physical signalling complex. We tested for an association between Cav3.2 and $K_{Ca}3.1$ channels, finding that Cav3.2 channels coimmunoprecipitated with $K_{Ca}3.1$ channels from homogenates of rat cerebellum (**Fig. 3.8*A***). While Cav2.1 channels have been found to be selectively linked to K_{Ca} channels in Purkinje cells, we found no coimmunoprecipitation between $K_{Ca}3.1$ and Cav2.1, indicating that the coimmunoprecipitation between $K_{Ca}3.1$ and Cav3.2 was specific (**Fig. 3.8*B***).

$K_{Ca}3.1$ channels are Ca^{2+}-activated but show no intrinsic voltage dependence (Wei et al., 2005). However, when complexed with Ca^{2+} channels, K_{Ca} channels can obtain some of the properties of the Ca^{2+} source (**Fig. 1.5**). Therefore, we used outside-out recordings from Purkinje cell somata to test the hypothesis that a closely associated Cav3 channel could confer a voltage dependence on $K_{Ca}3.1$ channels. Cav3 and $K_{Ca}3.1$

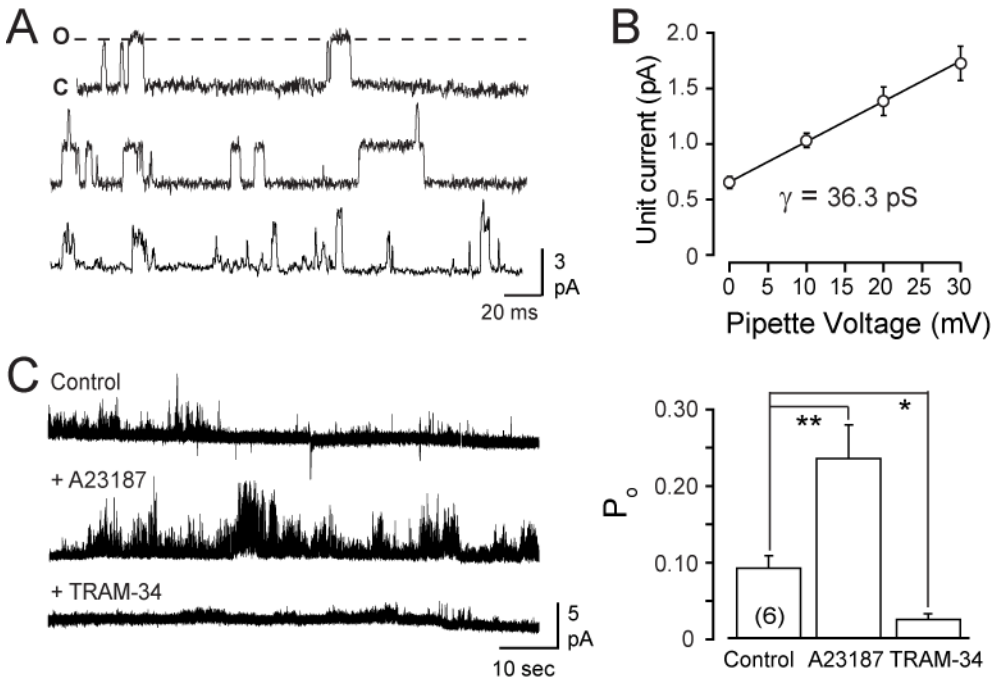
A
o
c
3
pA
20 ms
B
Unit current (pA)
2.0
1.5
1.0
0.5
0
γ = 36.3 pS
0 5 10 15 20 25 30
Pipette Voltage (mV)
C
Control
+ A23187
+ TRAM-34
5
pA
10 sec
P o
0.30
0.20
0.10
0
**
*
(6)
Control A23187 TRAM-34

Figure 3.7: Purkinje cells express $K_{Ca}3.1$ channels.

(A) Spontaneous on-cell single channel recordings from three different cells during a steady-state (5 min) pipette holding potential of 30 mV. Open (o) and closed (c) states are indicated. **(B)** Plot of mean single channel amplitudes in on-cell recordings at steady-state potentials up to +30 mV reveals a mean conductance of 36.3 pS (*n* = 5). **(C)** At *left* are long duration on-cell channel recordings (+30 mV pipette potential) before and after perfusing the Ca^{2+}ionophore A23187 (2 μM) and block by TRAM-34 (100 nM) (*n* = 6). Bar plots at *right* show channel open probability under the conditions shown in **(C)** (*n* = 6). Experiments performed by D Anderson.

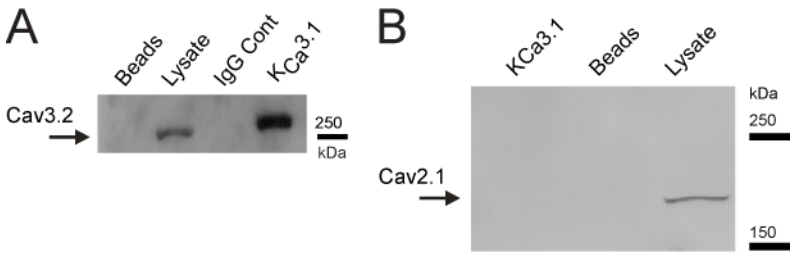
A
Beads
Lysate
IgG Cont
KCa3.1
Cav3.2
250
kDa
B
KCa3.1
Beads
Lysate
kDa
250
Cav2.1
150

Figure 3.8: Coimmunoprecipitation of Cav3.2 with $K_{Ca}3.1$ shows physical linkage between channels.

(A) Western blot showing coimmunoprecipitation of Cav3.2 and $K_{Ca}3.1$ channels from cerebellar lysate. **(B)** Western blot showing a lack of coimmunoprecipitation between Cav2.1 (P/Q-type) calcium channels and $K_{Ca}3.1$ from cerebellar homogenates. Experiments performed by S Hamid.

channels were isolated by perfusion of TTX, Cd^{2+}, apamin, TEA, 4-AP, Cs^{+}, and synaptic blockers, and the current-voltage relationship of Cav3 or $K_{Ca}3.1$ currents determined for 10 mV steps from -110 mV to 0 mV. Since Cav3 channels inactivate at depolarized potentials, we isolated the Cav3-dependent current by comparing currents evoked by steps from holding potentials of -110 mV and -40 mV, a potential that would completely inactivate Cav3 channels. These recordings revealed a voltage-dependent outward current evoked from a holding potential of -110 mV that was absent at a holding potential of -40 mV (**Fig. 3.9*A, B***). Subtraction of records obtained at -40 mV versus -110 mV isolated a transient outward current of up to 50 pA (24.8 ± 6.2 pA, $n = 6$) that was fast inactivating ($t_{1/2} = 22.6 \pm 1.4$ ms) (**Fig. 3.9*A*, Table 3.1**). Importantly, this outward current cannot reflect activation of $K_{Ca}1.1$, $K_{Ca}2.2$, Kv1, Kv3, or Kv4 channels, as these are entirely blocked by apamin or 5 mM TEA and 4-AP (Coetzee et al., 1999). HVA Ca^{2+} currents (including Cav2.3) are also effectively blocked by the 30 μM Cd^{2+} included here (**Fig. 3.2**), leaving Cav3 channels as the predicted primary source for Ca^{2+} influx in these recordings. We further isolated the Ni^{2+} and TRAM-sensitive currents evoked by steps from -110 mV using the same conditions of HVA Ca^{2+} and K^{+} channel block. These tests showed that TRAM-34 ($n = 4$) or Ni^{2+} ($n = 4$) blocked a fast inactivating current of up to 30 pA, with mean values of 11.4 ± 2.3 pA and $t_{1/2}$ inactivation of 23.6 ± 6.0 ms at -30 mV ($n = 8$) (**Fig. 3.9*A*, Table 3.1**). TRAM-34 and Ni^{2+}-sensitive currents also activated in the low voltage range in a manner similar to the inactivating current isolated by membrane voltage (**Fig. 3.9*B***).

The activation voltage for Cav3 channels is generally thought to be between -70 and -60 mV based on whole-cell current recordings. Likewise, our outside-out recordings show activation of outward current positive to -70 mV. However, current clamp recordings were performed at -75 mV, negative to the activation voltage. Furthermore, current-clamp recordings indicated a clear threshold for activation of a Ni^{2+}-sensitive AHP for membrane potentials positive to -80 mV (**Fig. 3.10*A***). While these voltages are lower than expected for I_T, such an extended voltage range is consistent with similar analyses of the activation threshold for HVA Cav2.1 calcium channels, where P-type current was detected ~20 mV below its supposed activation threshold (Awatramani et al., 2005). To test

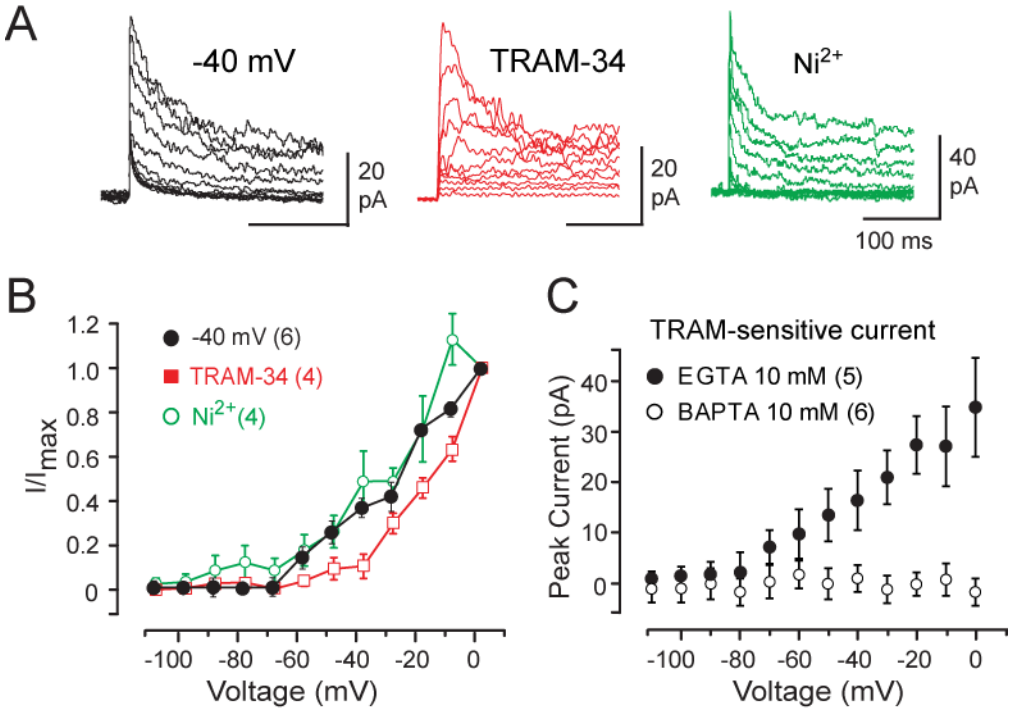
A
-40 mV
TRAM-34
Ni2+
20 pA
20 pA
40 pA
100 ms
B
-40 mV (6)
TRAM-34 (4)
Ni2+(4)
I/Imax
1.2
1.0
0.8
0.6
0.4
0.2
0
-100 -80 -60 -40 -20 0
Voltage (mV)
C
TRAM-sensitive current
EGTA 10 mM (5)
BAPTA 10 mM (6)
Peak Current (pA)
40
30
20
10
0
-100 -80 -60 -40 -20 0
Voltage (mV)

Figure 3.9: $K_{Ca}3.1$ channel activation is coupled to Cav3-mediated Ca^{2+} influx.
(A) Outside-out recordings from separate Purkinje cell somata in response to steps from -110 mV to 0 mV. Shown are currents calculated as the difference from those evoked at a -40 mV holding potential, or blocked by TRAM-34 (100 nM) or Ni^{2+} (100 μM). **(B)** Mean I-V plots for currents isolated as in **(A)** indicate a common activation in the low voltage range. **(C)** Mean I-V plots of TRAM-34-sensitive currents in outside-out recordings with either high EGTA or BAPTA in the electrode. All recordings were obtained from the somata of P18-25 Purkinje cells in 1.5 mM external Ca^{2+}. Experiments performed by D Anderson and J Engbers.

Means for isolation	**n**	**Amplitude @ -30 mV**	**$t_{1/2}$ (ms)**
Voltage (-40 mV holding potential)	(6)	24.8 ± 6.2 pA	22.6 ± 1.4 ms
TRAM-34 (100 nM)	(4)	8.1 ± 3.3 pA	26.5 ± 9.3 ms
Ni^{2+} (100 μM)	(4)	14.8 ± 2.2 pA	20.8 ± 8.7 ms

Table 3.1. Properties of outward current isolated from Purkinje cell somatic outside-out macropatch recordings.

Currents were elicited under steady state conditions from a holding potential of -110 mV. Currents were isolated by subtraction of test responses recorded in TRAM-34, Ni^{2+}, or voltage isolation by holding at -40 mV.

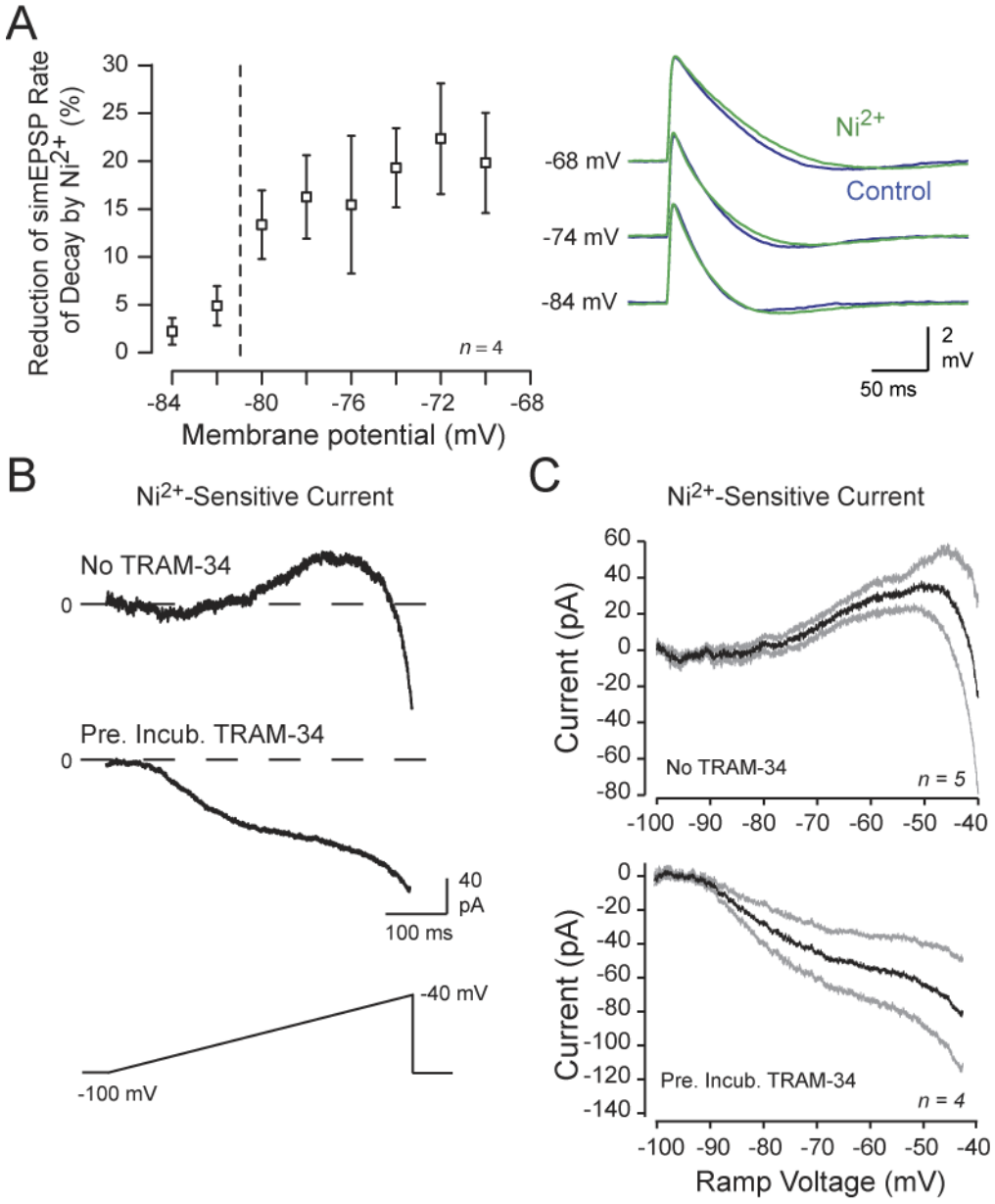
A
Reduction of simEPSP Rate of Decay by Ni2+ (%)
30
25
20
15
10
5
0
n = 4
-84
-80
-76
-72
-68
Membrane potential (mV)
Ni2+
Control
-68 mV
-74 mV
-84 mV
2 mV
50 ms
B
Ni2+-Sensitive Current
No TRAM-34
0
Pre. Incub. TRAM-34
0
40 pA
100 ms
-40 mV
-100 mV
C
Ni2+-Sensitive Current
Current (pA)
60
40
20
0
-20
-40
-60
-80
No TRAM-34
n = 5
-100 -90 -80 -70 -60 -50 -40
Current (pA)
0
-20
-40
-60
-80
-100
-120
-140
Pre. Incub. TRAM-34
n = 4
-100 -90 -80 -70 -60 -50 -40
Ramp Voltage (mV)

Figure 3.10: The Cav3-K_{Ca}3.1 complex is active over a wide range of subthreshold membrane potentials.

(A) The effect of Ni^{2+} on the rate of decay of simEPSPs was measured over a range of resting membrane potentials. A reduction in the simEPSP rate of decay is apparent for membrane potentials positive to -80 mV (right of *dashed line*). **(B)** Whole cell voltage-clamp recordings from mature (P18 – P30) Purkinje cells using K-gluconate recording solutions similar to those used in **(A)**. Ni^{2+}-sensitive subthreshold currents recorded in separate Purkinje cells evoked by a voltage ramp protocol (-100 to -40 mV over 500 ms, *bottom*) in the absence (*top*) or presence (*bottom*) of TRAM-34 (100 nM) in the aCSF. The aCSF also contained 200 nM TTX, 2 mM Cs^+, 5 mM TEA, 100 nM apamin and 30 μM Cd^{2+}, with $[K^+]_o$ lowered to 1.5 mM to set E_K at ~-120 mV and increase the ability to detect K^+ current at hyperpolarized voltages. Current traces represent the difference between recordings before and after application of 100 μM Ni^{2+}. In the absence of TRAM-34, an outward current can be seen with an onset voltage between -80 and -70 mV. When slices are pre-incubated with TRAM-34, an inward current is recorded with an onset between -90 and -80 mV. **(C)** Averages of Ni^{2+} sensitive currents in the absence of TRAM-34 (*top*) show an outward current for potentials greater than -80 mV. When K_{Ca}3.1 is blocked with perfusion of TRAM-34 (*bottom*), an inward current is revealed for potentials positive to -90 mV. Black trace indicates the mean value and gray traces indicate the SEM. A junction potential of -10.7 mV was subtracted from all recordings. Experiments performed by J Engbers.

the hypothesis that a small amount of I_T was active at potentials below the observed whole-cell activation threshold, I applied voltage ramp commands to Purkinje cell somata (-100 to -40 mV over 500 ms) to allow discrimination of small amplitude currents. A K-gluconate-based internal was used to avoid activation of a Cl^- current that was observed when using a KCl-based internal. $[K^+]_o$ was lowered to 1.5 mM to set E_K at ~-120 mV and increase the ability to detect K^+ current at hyperpolarized voltages. In the absence of TRAM-34, Ni^{2+}-sensitive outward currents were observed with an onset voltage between -80 and -70 mV, followed by an inward current at potentials greater than -50 mV (**Fig. 3.10*B,C***). When slices were pre-incubated with TRAM-34, an underlying inward current was recorded for potentials positive to -90 mV (**Fig. 3.10*B,C***). Therefore, I_T was observed at potentials up to 20 mV below the activation threshold typically reported for whole-cell currents evoked by step commands. The inward Cav3 current also activated a measurable amount of $K_{Ca}3.1$ current between -80 and -70 mV, potentials relevant to the previous current clamp recordings.

Several studies have shown nanodomain associations between Ca^{2+} sources and K_{Ca} channels. The coimmunoprecipitation results and the observation that Cav3 channels confer voltage sensitivity onto $K_{Ca}3.1$ channels led us to hypothesize that $K_{Ca}3.1$ channels are within the Cav3 nanodomain. To test the functional proximity of Cav3 to $K_{Ca}3.1$ channels, we used outside-out recordings to measure TRAM-34-sensitive current in the presence of either EGTA or BAPTA (10 mM) in the internal electrolyte, as microdomain and nanodomain interactions can be differentiated due to the different dissociation constants (K_D) of these Ca^{2+} chelators. We found that TRAM-34-sensitive current was only recorded in the presence of internal EGTA (n = 5) but not BAPTA (n = 6) (**Fig. 3.9*C***), indicating an interaction at the nanodomain level (Fakler and Adelman, 2008).

Given that $K_{Ca}3.1$ channel open probability is only a function of internal Ca^{2+} concentration (Oliver et al., 2000), the voltage dependence of $K_{Ca}3.1$ activation must indirectly reflect the voltage dependence of I_T. Taken together, these data indicate that an association between Cav3 and $K_{Ca}3.1$ channels at the nanodomain level allows Cav3-mediated Ca^{2+} influx to activate $K_{Ca}3.1$ as a Ca^{2+}-dependent and transient outward current in the low voltage range.

3.3.5 Cav3-K_{Ca}3.1 interaction controls temporal summation of PF EPSP trains

Synaptic integration time, or the maximum period during which summation can occur, is determined by a number of postsynaptic factors, including membrane time constant and postsynaptic ion channels. Persistent Ca^{2+} currents, in conjunction with persistent Na^{+} currents, have been shown to slow EPSP rate of decay and increase integration time in spinal lamina I neurons (Prescott and De Koninck, 2005). Therefore, I hypothesized that, by *increasing* EPSP rate of decay, the Cav3-K_{Ca}3.1 complex will shorten PF integration time, reducing summation of low-frequency inputs. To test the hypothesis, I stimulated PF inputs at 25 Hz for 2 sec during whole-cell current clamp recordings in Purkinje cell somata. Stimulus intensity was adjusted to evoke an initial EPSP amplitude of 2 mV, with presynaptic facilitation causing the EPSP amplitude to reach ~5 mV by the end of stimulus trains. Under control conditions, an initial summation of the EPSP was reduced within 250 ms to a lower, stable amplitude that remained below spike threshold for the duration of the stimulus train (**Fig. 3.11*A***). However, we found a rapid summation of EPSPs within the first 5 stimuli after applying either Ni^{2+} ($n = 8$, $p < 0.001$) or TRAM-34 ($n = 4$, $p < 0.05$) to block the Cav3-K_{Ca}3.1 interaction (**Fig. 3.11*A, B***). Measuring the baseline membrane voltage immediately preceding each stimulus indicated a rapid increase over the first ~20 stimuli that reached a sustained level 8-10 mV beyond initial baseline (**Fig. 3.11*A, B***). As a result, PF-evoked EPSPs surpassed spike threshold within 5-10 stimuli to reliably generate spike output.

Based on these results, it appears that the Cav3-K_{Ca}3.1 complex shortens integration time and suppresses low-frequency PF inputs. However, there are several mechanisms that exist in Purkinje cells and PFs which could increase PF summation and have a similar timecourse of activation as that seen in these experiments. These mechanisms need to be examined before we can conclusively state the role of the Cav3-K_{Ca}3.1 complex. Activation of extrasynaptic mGluR receptors has been reported to activate a long lasting depolarizing current (Tempia et al., 2001) and Cav3.1 channels associate with mGluR1 receptors in Purkinje cell dendritic spines (Hildebrand et al., 2009). Elevated Ca^{2+} in Purkinje cell dendrites also causes endocannabinoid release which depresses PF synapses (Brenowitz and Regehr, 2003; Brenowitz et al., 2006). However, we found no

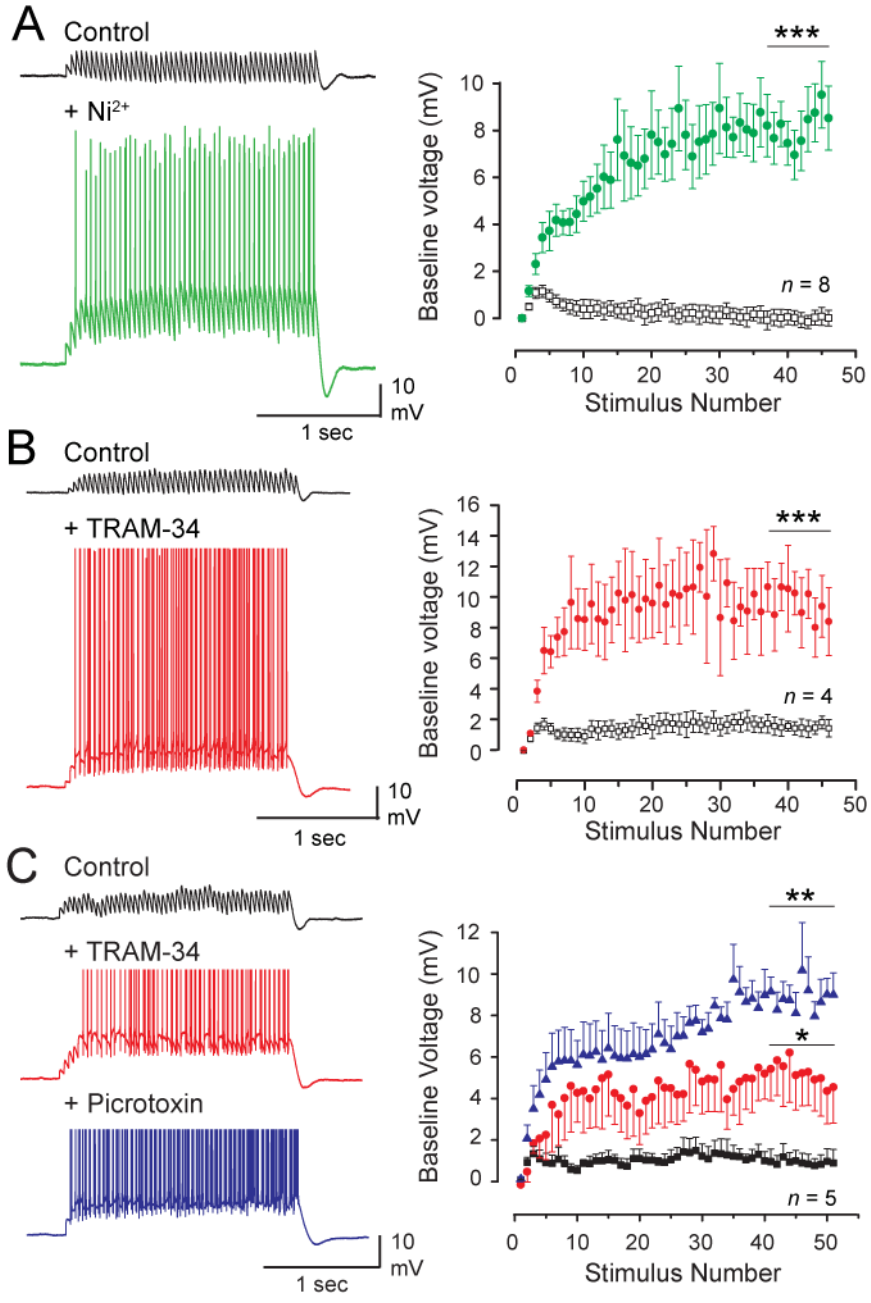
A
Control
+ Ni2+
10
mV
1 sec
***
Baseline voltage (mV)
n = 8
Stimulus Number
B
Control
+ TRAM-34
10
mV
1 sec
***
Baseline voltage (mV)
n = 4
Stimulus Number
C
Control
+ TRAM-34
+ Picrotoxin
10
mV
1 sec
**
*
Baseline Voltage (mV)
n = 5
Stimulus Number

Figure 3.11:The Cav3-K_{Ca}3.1 complex regulates temporal summation of PF EPSPs. (**A,B**) Representative recordings and plots of the baseline membrane voltage during 25 Hz trains of PF evoked EPSPs before and after applying Ni^{2+} (**A**, 100 μM, *green*) or TRAM-34 (*B*, 100 nM, *red*). Stimulus intensity was adjusted to evoke an initial EPSP of 2 mV. (**C**) Recordings and plots of baseline voltage during 25 Hz PF stimulus trains in a coronal slice in the absence of picrotoxin to preserve feedforward inhibition. TRAM-34 (*red*) substantially increases temporal summation, with an additional increase upon addition of picrotoxin (50 μM, *blue*) to block GABAergic inhibition. Statistical significance tested for last 10 pulses of stimulus trains in (**A-C**, indicated by *bars*). Spikes were truncated in (**A-C**). Experiments performed by J Engbers.

role for mGluR1 receptor activation or presynaptic endocannabinoid (CB1) receptors, as neither the group I mGluR antagonist JNJ16259685 (1.5 μM) nor the CB1 receptor blocker AM-251 (2.5 μM) occluded the effect of Ni^{2+} ($n = 4$) during these stimuli. In addition, the PF-evoked EPSP paired-pulse ratio was unaffected by either Ni^{2+} ($n = 7$, $p > 0.05$) or TRAM-34 ($n = 7$, $p > 0.05$) (**Fig. 3.12*A, B***), indicating that the increase in temporal summation did not involve presynaptic effects.

Temporal summation of PF EPSPs has also been shown to be controlled through feedforward inhibition (Mittmann et al., 2005). However, when we repeated these tests in coronal slices in the absence of picrotoxin to preserve feedforward inhibition, application of TRAM-34 still caused an increased temporal summation of PF-evoked EPSPs (**Fig. 3.11*C***, $n = 5$, $p < 0.05$, one-way ANOVA with post-hoc Tukey test). Subsequent addition of picrotoxin to block GABAergic inputs led to a further increase in summation during the stimulus train (**Fig. 3.11*C***, $n = 5$, $p = 0.08$, one-way ANOVA with post-hoc Tukey test). These results indicate that postsynaptic control of temporal summation by the Cav3-K_{Ca}3.1 complex is effective in the presence of feedforward inhibition.

3.3.6 Cav3-K_{Ca}3.1 complex is active during membrane depolarizations and tonic firing

Given that Cav3 channels inactivate upon depolarization, it is important to determine the availability of Cav3 current at physiological potentials. We thus tested if the Cav3-K_{Ca}3.1 interaction is active at more depolarized levels of membrane potential that promote spontaneous spike firing. To measure Cav3 activation and inactivation over a full voltage range we used whole-cell recordings from P10-P12 Purkinje cells when the dendritic tree has not fully developed to avoid space clamp errors (**Fig. 3.13*A,B***, $n = 7$). The Boltzmann fits for activation and inactivation data (**Fig. 3.13*B***) indicated that a Cav3 window current exists for membrane voltages up to at least ~ -20 mV, and thus well into the suprathreshold range (Raman and Bean, 1999; Swensen and Bean, 2003) (see also **Fig. 3.10*B,C***).

We further tested the degree to which PF EPSP summation could be modified by the Cav3-K_{Ca}3.1 interaction during tonic firing using current clamp recordings. Bias current was applied to sustain a tonic firing frequency of ~50 Hz (49.7 ± 1.8 Hz, $n = 9$)

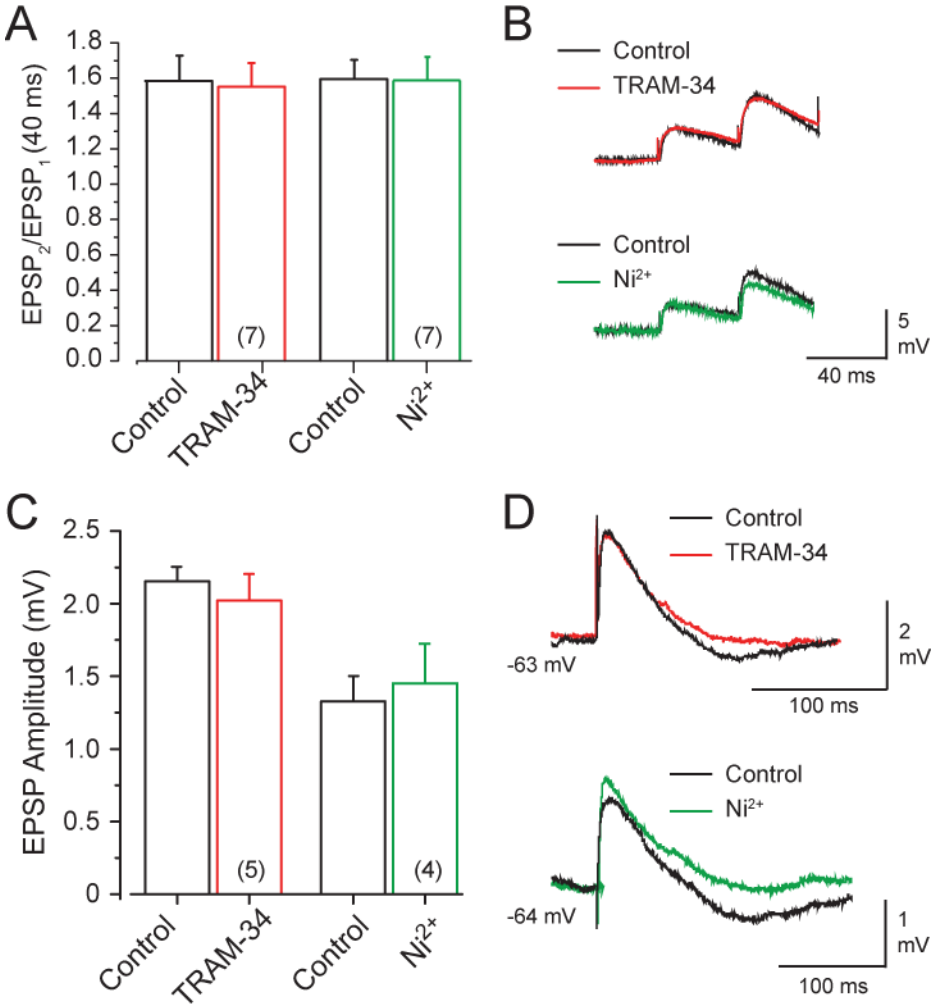
A
EPSP2/EPSP1 (40 ms)
1.8
1.6
1.4
1.2
1.0
0.8
0.6
0.4
0.2
0.0
(7)
(7)
Control
TRAM-34
Control
Ni2+
B
Control
TRAM-34
Control
Ni2+
5
mV
40 ms
C
EPSP Amplitude (mV)
2.5
2.0
1.5
1.0
0.5
0
(5)
(4)
Control
TRAM-34
Control
Ni2+
D
Control
TRAM-34
-63 mV
2
mV
100 ms
Control
Ni2+
-64 mV
1
mV
100 ms

Figure 3.12: Actions of TRAM-34 or Ni^{2+} are not the result of presynaptic effects. Purkinje cells were held at subthreshold potentials and the amplitude of PF-evoked EPSPs examined before and after application TRAM-34 or Ni^{2+}. **(A, B)** Paired pulse ratio (40 ms interstimulus interval) of the evoked EPSP is not significantly changed following application of either TRAM-34 (100 nM) or Ni^{2+} (100 μM). **(C, D)** The primary effect of both TRAM-34 and Ni^{2+} is on the EPSP rate of decay, with no significant effect on the mean value of EPSP amplitude. Experiments performed by J Engbers.

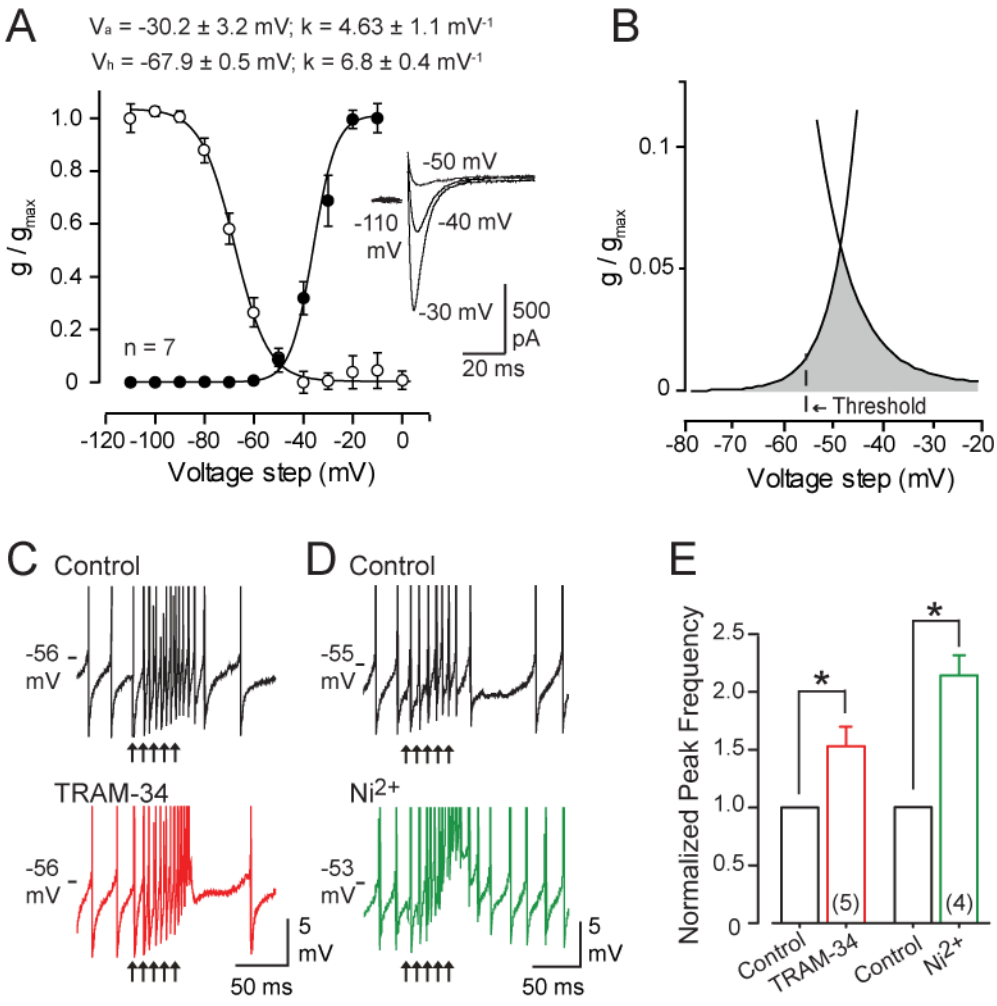
A
Va = -30.2 ± 3.2 mV; k = 4.63 ± 1.1 mV-1
Vh = -67.9 ± 0.5 mV; k = 6.8 ± 0.4 mV-1
g / gmax
1.0
0.8
0.6
0.4
0.2
0
n = 7
-50 mV
-110 mV
-40 mV
-30 mV
500 pA
20 ms
-120 -100 -80 -60 -40 -20 0
Voltage step (mV)
B
g / gmax
0.1
0.05
0
Threshold
-80 -70 -60 -50 -40 -30 -20
Voltage step (mV)
C Control
-56 mV
TRAM-34
-56 mV
5 mV
50 ms
D Control
-55 mV
Ni2+
-53 mV
5 mV
50 ms
E
Normalized Peak Frequency
2.5
2.0
1.5
1.0
0.5
0
*
*
(5)
(4)
Control
TRAM-34
Control
Ni2+

Figure 3.13: Cav3 window current straddles spike threshold in Purkinje cells and the Cav3-K_{Ca}3.1 complex affects EPSP summation under physiological conditions. **(A)** Mean conductance and inactivation plots calculated for whole-cell Cav3 current recorded from P10-12 Purkinje cells (*inset*). **(B)** Expanded view of the fits for activation and inactivation curves shown in **(A)** reveal that Cav3 window current (gray) in relation to spike threshold (dashed line). **(C-E)** The effects of blocking the Cav3-K_{Ca}3.1 complex during a 5 pulse train of PF stimulation (100 Hz, arrows). Resting potential was depolarized to a level sufficient to evoke ~50 Hz tonic firing, with spike threshold indicated at left. Blocking the Cav3-K_{Ca}3.1 complex with either TRAM-34 (C, 100 nM, red) or Ni^{2+} (**D**, 100 μM, green) reveals substantial control over EPSP summation and spike frequency **(E)**. Spikes were truncated for display in (*C*) and (*D*) and picrotoxin (50 μM) was present for all tests in **(C - E)**. Experiments performed by J Engbers and D Anderson.

before and after drug application. PF inputs were stimulated at 100 Hz (5 pulses) to mimic frequencies of input relevant to sensory stimulation (Rancz et al., 2007; Ekerot and Jorntell, 2008; Mapelli et al., 2010). The degree of PF EPSP summation under these conditions was estimated by measuring the absolute baseline voltage recorded at the time of spike discharge. After application of TRAM-34, there was an increase in both peak baseline voltage (59 ± 25.6%, $n = 5$, $p < 0.05$) and peak frequency during stimulation (53 ± 16.2 %, $n = 5$, $p < 0.05$) (**Fig. 3.13*C,E***). Similarly, Ni^{2+} increased peak baseline voltage (96 ± 36%, $n = 4$, $p < 0.05$) and spike frequency (114 ± 16.5%, $n = 4$, $p < 0.05$) during the stimulation (**Fig. 3.13*D,E***). To control for changes in EPSP amplitude before and after drug application, the size of the EPSP was measured at -75 mV before and after drug application. The observed increases in summation due to Ni^{2+} and TRAM-34 could not be attributed to a change in the amplitude of the evoked EPSP ($n = 4$ and 5, $p < 0.05$) (**Fig. 3.12*C,D***). These results are important in demonstrating that both Cav3 and $K_{Ca}3.1$ channels are available at depolarized potentials supporting tonic spike firing, and modulate temporal summation of PF inputs at physiologically relevant input frequencies.

3.4 Discussion

As shown above, we have provided the first evidence for the expression of $K_{Ca}3.1$ K^+ channels in a CNS neuron and its role in creating a postsynaptic frequency filter for synaptic input. Although $K_{Ca}3.1$ channel activation has been documented in enteric and myenteric neurons (Vogalis et al., 2002b; Neylon et al., 2004), several lines of evidence now support the expression of $K_{Ca}3.1$ channels in Purkinje cells, including single cell RT-PCR, $K_{Ca}3.1$ immunolabel, single channels with intermediate conductance, and macropatch recordings of K_{Ca} currents with a pharmacological profile that is unique to $K_{Ca}3.1$ channels. Moreover, Cav3.2 Ca^{2+} channels prove to colocalize and associate with $K_{Ca}3.1$ channels to provide Ca^{2+}-dependent regulation at the nanodomain level, identifying the first association of a Cav3 channel isoform at the molecular level with any K_{Ca} channel. Finally, recordings *in vitro* establish that this new Cav3-$K_{Ca}3.1$ complex exerts a strong influence on temporal summation of PF EPSPs over a wide range of physiologically relevant membrane potentials.

This new Cav3-K_{Ca}3.1 complex differs significantly from other T-type-mediated responses reported in previous studies. The ability to evoke the Cav3-K_{Ca}3.1 interaction using postsynaptic simEPSCs indicates that the complex does not require Ca^{2+} influx through ligand-gated channels, a known interaction for K_{Ca}2.x channels (Ngo-Anh et al., 2005). A functional coupling between Cav3 and K_{Ca}2.x channels in select neuronal subtypes (Smith et al., 2002; Wolfart and Roeper, 2002; Cueni et al., 2008) is also reported to operate at the microdomain level, compared to the nanodomain demonstrated here. A Cav3-Kv4 K^+ channel complex has been shown to employ K^+ channel interacting protein 3 to mediate Ca^{2+} sensing for voltage-gated Kv4 channels (Anderson et al., 2010b; Anderson et al., 2010a). The Cav3-K_{Ca}3.1 complex identified here instead depends on CaM that has been shown to directly gate the K_{Ca}3.1 channel (Pedarzani and Stocker, 2008). Together these findings identify the Cav3-K_{Ca}3.1 complex as an entirely novel ion channel complex in the brain.

All members of the K_{Ca}2.x and K_{Ca}3 families are known to be Ca^{2+}- but not voltage-dependent (Pedarzani and Stocker, 2008). However, the close association between Cav3 and K_{Ca}3.1 channels allows K_{Ca}3.1 to acquire the properties of a low voltage-activated current as well as the fast inactivating kinetics of Cav3 current. K_{Ca}3.1 channels can also exhibit a 2-3 times greater sensitivity to internal Ca^{2+} than K_{Ca}2.x channels (Ishii et al., 1997b; Joiner et al., 1997; Vogalis et al., 2002b). These properties are consistent with the ability for a I_T to activate K_{Ca}3.1 with little delay at the onset of an EPSP and yet generate an AHP of up to 250 ms duration. K_{Ca}3.1 channels can thus be activated by single, low-amplitude EPSPs but also exhibit a cumulative activation during repetitive activity, an advantage over other K^+ channels for modulating temporal summation of synaptic depolarizations.

I note that control over temporal summation of PF EPSPs in Purkinje cells has also been reported through other mechanisms different from the Cav3-KCa3.1 complex. One is a role for I_H to reduce EPSP width and temporal summation (Angelo et al., 2007). Since all tests conducted here were performed with I_H intact, K_{Ca}3.1 clearly has a role distinct from I_H in producing the AHP and modifying temporal summation. Molecular layer interneurons provide a feedforward inhibitory influence that reduces PF EPSP

summation (Mittmann et al., 2005). This function is different again, in that the Cav3-K_{Ca}3.1 complex exerts a significant effect on temporal summation even in the presence of feedforward inhibition. The influence of the Cav3-K_{Ca}3.1 interaction is also fully functional during tonic firing, a result attributable to the wide extent of Cav3 window current in the suprathreshold voltage range. In fact, the current work represents the most accurate calculation of Cav3 window current yet for Purkinje cells, providing evidence of a surprisingly large voltage range over which window current will enable Ca^{2+} influx. Thus, ramp commands extending from -100 mV to -40 mV revealed initial activation of Cav3 current from voltages as low as -90 mV. This is well outside the voltage range most investigators expect for I_T, and emphasizes the ability for Cav3 channel-mediated Ca^{2+} influx to modify activity in the subthreshold voltage range, and in this case, to activate K_{Ca}3.1 channels. On the other side of the scale, the overlap of Cav3 activation and inactivation curves revealed that window current extends up to ~ -20 mV, and thus well into the suprathreshold voltage range. This is, in fact, consistent with previous reports that up to 50% of the Ca^{2+} influx during an action potential in Purkinje cells is mediated by Cav3 Ca^{2+} channels (Swensen and Bean, 2003).

In summary, the current results reveal a new Cav3-K_{Ca}3.1 complex that functions synergistically with I_H and feedforward inhibition to reduce Purkinje cell responsiveness to background granule cell activity, while permitting activation by high frequency trains of PF input. Together these factors underlie a high pass filter function that allows spike bursts produced by granule cells to preferentially evoke Purkinje cell spike output (D'Angelo and De Zeeuw, 2009).

Chapter Four: High-pass filtering of PF inputs by presynaptic facilitation is augmented by Cav3-K_{Ca}3.1 complex

4.1 Introduction

An effective signal processing system must be able to discriminate a signal carrying information from background noise. While mechanisms for increasing signal-to-noise ratio (SNR) have been explored in theory and practice in a variety of fields, the methods used by neurons is still largely unknown. Central neurons receive a large number of active synaptic inputs, yet retain the capacity to detect features of sensory input from background noise. Cerebellar Purkinje cells are the sites of intense synaptic convergence, receiving ~150,000 inputs from PFs arising from granule cells. However, only a subset of these inputs will carry pertinent sensory information at any given time. Indeed, the activation of a peripheral receptive field is transmitted to the cerebellar cortex by MFs in the form of high frequency spike bursts (Chadderton et al., 2004; Rancz et al., 2007; D'Angelo and De Zeeuw, 2009). Granule cells, in turn, generate a similar high frequency burst in response to MF input (Chadderton et al., 2004; Jorntell and Ekerot, 2006; Rancz et al., 2007; Mapelli et al., 2010). Purkinje cells should then possess the means to maintain a high SNR and respond effectively to bursts of PF EPSPs that convey sensory information.

Short-term plasticity modulates synaptic strength in an activity-dependent manner in order to optimize information transmission. Short-term plasticity can operate on time scales of milliseconds to seconds and has roles in detection of transient inputs (i.e. bursts of presynaptic input)(Lisman, 1997), synaptic gain control (Abbott et al., 1997), input redundancy reduction (Goldman et al., 2002), and detection of population bursts (Richardson et al., 2005). Whether a synapse displays short-term facilitation or depression depends on the initial probability of release of presynaptic vesicles (Dittman et al., 2000; Abbott and Regehr, 2004). In short-term facilitation, initial release probability is low and each consecutive action potential causes an increase in presynaptic $[Ca^{2+}]_i$ and release probability, resulting in a larger EPSCs. Conversely, short-term depression occurs when initial release probability is high and presynaptic vesicles are rapidly depleted with

each action potential, decreasing neurotransmitter release (Dittman et al., 2000; Abbott and Regehr, 2004).

Functionally, each of these processes operate with specific temporal properties and frequency dependencies that vary from synapse to synapse, even in the same neuron (Abbott and Regehr, 2004). By increasing or decreasing the amplitude of EPSPs with repetitive presynaptic action potentials, synapses can filter presynaptic inputs. Presynaptic depression ensures that tonic input becomes less effective over time and causes the postsynaptic cell to only respond effectively to relative changes in presynaptic frequency (Abbott et al., 1997). On the other hand, short-term facilitation allows the postsynaptic cell to respond effectively to high frequency bursts of information that cause drastic increases in the amplitude of the EPSP (Lisman, 1997).

PFs exhibit significant frequency-dependent short-term facilitation. The facilitation ratio, measured as the steady-state amplitude of a train of EPSPs divided by the amplitude of the first EPSP ($EPSP_{8\text{-}10}/EPSP_1$), is approximately 4.0 at 50 Hz (Dittman et al., 2000). Facilitation at this synapse increases the responsiveness of Purkinje cells to PF bursts. However, frequency-dependent facilitation of PF inputs is maximized only at input frequencies above 50 Hz, such as that found during the spike burst that granule cells generate in response to sensory-related MF input (Chadderton et al., 2004; Jorntell and Ekerot, 2006; Rancz et al., 2007; Mapelli et al., 2010). In contrast, PF input to Purkinje cells during the low frequency spontaneous activity of granule cells (up to 4 Hz resting frequency) will not exhibit facilitation, despite providing potentially high net frequencies of input due to a high degree of PF convergence onto single Purkinje cells. Given the enormous number of PF inputs impinging on Purkinje cells, one would predict the need for postsynaptic mechanisms to help distinguish between important, facilitating inputs originating at a single PF terminal during sensory input (signal) and the background input resulting from spontaneous PF EPSPs conveying unimportant input (noise). By example, previous research in midbrain neurons of the weakly electric fish *Eigenmannia viscerens* has shown that a low-pass temporal filter established through short-term depression is enhanced by the active membrane properties of postsynaptic cells (Fortune and Rose, 1997; Rose and Fortune, 1999; Fortune and Rose, 2001). Indeed, we have already shown

that the Cav3-K_{Ca}3.1 complex exhibits some filtering capacity for PF input (**Chapter 3**). However, the full extent of frequency-dependent filtering of synaptic inputs by the Cav3-K_{Ca}3.1 complex has not been examined. The work in this chapter tested the hypothesis that the Cav3-K_{Ca}3.1 complex in Purkinje cells acts to enhance the high-pass filter implemented through short-term facilitation of PF inputs, increasing the neuron's ability to filter out background, nonfacilitating synapses from facilitating ones. These complementary mechanisms may act to increase SNR ratio and fidelity of information transmission.

4.2 Specific Methods

4.2.1 Dynamic clamp simulation of PF inputs

Custom scripts were written to simulate synaptic inputs using facilitating-depressing (FD) synapse equations (Middleton et al., 2011). If *F* and *D* are variables that increase (facilitate) and decrease (depress), respectively, with each action potential, then the following differential equations describe a general FD synapse:

$$\frac{dG}{dt} = -\frac{G}{\tau_G} + \alpha \cdot F \cdot D \sum_m \delta(t - t_m)$$

$$\frac{dF}{dt} = \frac{F_0 - F}{\tau_F}$$

$$\frac{dD}{dt} = \frac{1 - D}{\tau_D}$$

$$I = g_{syn}(V_m - E_{syn})$$

where G is the synapse conductance, α is a scaling value, τ parameters are time constants, F_0 is the initial release probability and δ is the Dirac impulse function. At the time of a spike, *F* and *D* values were updated according to the following rules: $F \rightarrow F + \Delta F \cdot (1 - F)$ and $D \rightarrow D - \Delta D \cdot D$. In my dynamic clamp experiments, $\tau_F = 100\ ms$, $\tau_D = 50\ ms$, $F_0 = 0.05$, $\alpha = 0.65$, $\tau_G = 3\ ms$, $\Delta F = 0.1$, $\Delta D = 0.2$, and $E_{syn} = 0\ mV$ for all recordings. Synaptic conductance density (g_{syn}) was adjusted for each recording. Parameters

were chosen to match PF facilitation as described by Dittman et al. (Dittman et al., 2000). A junction potential of -10.7 mV was subtracted online during all recordings to allow all calculations to be performed using the corrected membrane voltage.

4.2.2 Cav3-K_{Ca}3.1 model

4.2.2.1 Voltage-dependent currents

Subthreshold currents present in Purkinje cells (I_H, I_T, I_{leak}) were modelled with the Hodgkin-Huxley equations listed below. Parameters for Purkinje cell HCN and Cav3 channels were taken from previous studies (Fernandez et al., 2007; Hildebrand et al., 2009).

I_H activation

$$\frac{dq}{dt} = \frac{q_\infty - q}{\tau_q}, q_\infty = \frac{1}{1 + e^{\frac{V+80}{3}}}, \tau_q = 200\ ms$$

I_T activation

$$\frac{dm}{dt} = \frac{m_\infty - m}{\tau_m}, m_\infty = \frac{1}{1 + e^{\frac{V+32}{-4.5}}}, \tau_m = 7\ ms$$

I_T inactivation

$$\frac{dh}{dt} = \frac{h_\infty - h}{\tau_h}, h_\infty = \frac{1}{1 + e^{\frac{V+63.8}{-6.9}}}, \tau_h = 37\ ms$$

C = 2 μF/cm^2, g_{Ca}= 0.08 mS/cm^2, g_{IH} = 0.025 mS/cm^2 and g_{leak} = 0.025 mS/cm^2. For all simulations, reversal values were set to: E_K = -97 mV, E_{IH} = -20 mV, E_{Ca} = 30 mV and E_{leak} = -77 mV. All simulations were constructed in Matlab R2007b using a fourth-order Runge-Kutta algorithm with a time step (dt) of 0.0001 ms.

4.2.2.2 Ca^{2+} diffusion

In order to determine K_{Ca} channel activation, Ca^{2+} diffusion away from the Cav3 Ca^{2+} source was modelled using 10 hemispherical compartments with Ca^{2+} diffusion determined using the following explicit equation (Koch and Segev, 1998):

$$\frac{d[Ca^{2+}]_i}{dt} = D_{Ca}\left(\frac{a_{i,i+1}}{v_i \delta_{i,i+1}}\right)([Ca^{2+}]_i - [Ca^{2+}]_{i+1})$$

where D_{Ca} is the diffusion coefficient for calcium (0.220 $\mu m^2 ms^{-1}$), $a_{i,i+1}$is the surface area between the adjacent compartments, v_i is the volume of the first compartment, $\delta_{i,i+1}$ is the distance between compartments, and the term in the brackets represents the concentration gradient. The radius of the smallest compartment was 20 nm and the radius of each following compartment was consecutively increased by 20 nm. The activation of K_{Ca} channels was made to depend on the $[Ca^{2+}]$ of a particular compartment. Therefore, the effect of Ca^{2+} on K_{Ca} channels could be observed for distances of up to 200 nm from the Ca^{2+} source. To calculate Ca^{2+} influx through the Cav3 channel, we assumed a single channel conductance of 1.7 pS ($\hat{g}_T$ = 1.7 pS) (Weber et al., 2010). To simulate multiple Cav3 channels, $\hat{g}_{CaT}$ was multiplied by the number of desired channels. The number of incoming Ca^{2+} ions (N_{Ca}) was determined by:

$$N_{Ca} = \frac{-\hat{g}_{CaT} \cdot m \cdot h \cdot (V - E_{Ca})}{2F}$$

where F is Faraday's constant ($9.649 \cdot 10^4$ coulombs/mol)

4.2.2.3 $K_{Ca}3.1$ model

The gating model for $K_{Ca}3.1$ channels adapted a previous study of $K_{Ca}2$ channels (Hirschberg et al., 1998), as $K_{Ca}2$ channels have similar CaM-dependent activation and no model of $K_{Ca}3.1$ activation currently exists (Xia et al., 1998). The rate of Ca^{2+}-dependent state transitions was increased to set the IC_{50} between 100 and 300 nM, consistent with $K_{Ca}3.1$ Ca^{2+} sensitivity (Ishii et al., 1997b; Joiner et al., 1997; Jensen et al., 2001; Vogalis et al., 2002b).

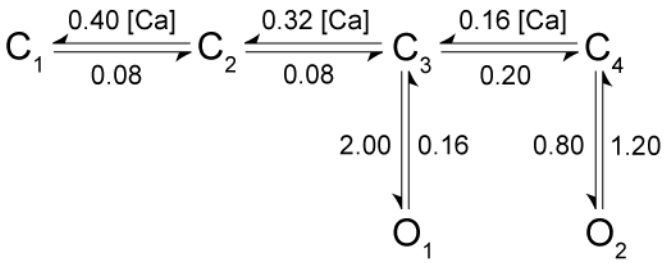

Single-channel conductance of $K_{Ca}3.1$ ($\hat{g}_{IK}$) was assumed to be 40 pS (**Fig. 3.7**)(Vogalis et al., 2002b; Engbers et al., 2012b). The conductance density of $K_{Ca}3.1$ was set the conductance density of Cav3 multiplied by the ratio of $K_{Ca}3.1$ and Cav3 single-channel conductances, such that $g_{KCa} = g_{ca} \cdot (\hat{g}_{KCa}/\hat{g}_{Ca})$

4.3 Results

We previously established the ability for single PF simEPSCs injected at the Purkinje cell soma to replicate PF-evoked EPSPs (Engbers et al., 2012b)(**Chapter 3**). However, while simEPSCs can faithfully replicate many of the features of synaptic inputs, presynaptic plasticity mechanisms are not represented during repetitive simEPSC injections. This was of direct advantage, as it allowed us to compare the response of the postsynaptic neuron to facilitating PF-evoked EPSPs and nonfacilitating simEPSPs.

PF inputs exhibit frequency-dependent facilitation, showing up to a 4x increase in EPSP amplitude for frequencies up to 100 Hz (Dittman et al., 2000). To compare the response of Purkinje cells to different frequencies of PF input with and without facilitation, we either stimulated PFs directly (**Fig. 4.1*A***, *top*) or injected trains of simEPSCs at the soma (**Fig. 4.1*A***, *bottom*) while holding the Purkinje cell initially subthreshold at -75 mV (n = 5, 5 stimuli, 15 – 75 Hz). Differences in the postsynaptic response to PF-evoked or simEPSPs were immediately apparent. With direct stimulation of PF inputs, EPSP summation exceeded spike threshold (*suprathreshold summation*), and spikes were generated at frequencies below 50 Hz in 4 out of 5 cells. Up to 13 spikes were elicited in these cells during the last 2-3 EPSPs. In contrast, when simEPSCs were injected into the same cells, only 2 of the 5 cells exhibited suprathreshold summation for frequencies up to 75 Hz. Even then, higher frequencies were required to reach suprathreshold potentials in these

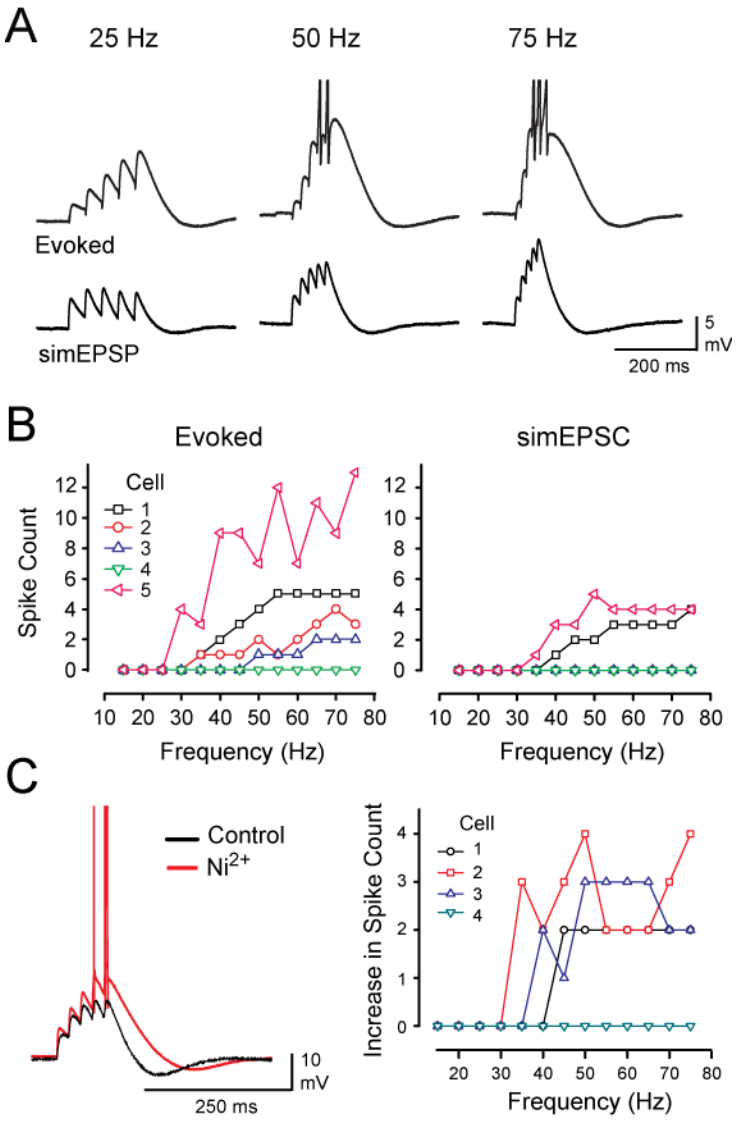
A
25 Hz
50 Hz
75 Hz
Evoked
simEPSP
5
mV
200 ms
B
Evoked
simEPSC
Cell
1
2
3
4
5
Spike Count
Frequency (Hz)
C
Control
Ni2+
10
mV
250 ms
Increase in Spike Count
Cell
1
2
3
4
Frequency (Hz)

Figure 4.1: Difference in postsynaptic summation between evoked and simulated EPSPs.

(A) Recordings from Purkinje cell somata during different frequencies of direct PF stimulation or injection of postsynaptic simEPSCs at the soma illustrate that PF-evoked EPSPs exhibit greater degrees of summation than corresponding frequencies of simEPSPs in the same cell. **(B)** Quantification of spike count versus synaptic stimulus frequency demonstrates that trains of evoked EPSPs are more capable of causing suprathreshold summation than trains of simEPSCs. **(C)** Superimposed simEPSPs at 50 Hz show that bath application of 100 μM Ni^{2+} increases summation of simEPSPs and elicits spike discharge (*left*). A scatter plot (*right*) of simEPSP frequency and relative increase in spike count after application of 100 μM Ni^{2+} reveals that spike output is increased for lower input frequencies with threshold frequency becoming comparable to those evoked under control conditions by PF-evoked EPSPs (cf. **B,C**). Experiments performed by J Engbers.

cells and 2 - 3 fewer spikes were generated during the 50 Hz simEPSP train when compared to the 50 Hz PF-evoked EPSP trains (**Fig. 4.1*B***).

The summation of PF-evoked inputs is suppressed by the Cav3-K_{Ca}3.1 complex at low frequencies (25 Hz) (**Chapter 3**) (Engbers et al., 2012b). However, the results here suggest that there is also a differential filtering of PF-evoked and simEPSC stimuli at higher frequencies, with the Cav3-K_{Ca}3.1 complex providing a greater suppression of the nonfacilitating simEPSP trains. To quantify the filter established by the Cav3-K_{Ca}3.1 complex, I defined the *threshold frequency* as the frequency at which suprathreshold summation occurs for a given set of stimuli and examined the effect of Cav3 channel blockers on the threshold frequency for simEPSP trains (**Fig. 4.1*C***). After application of 100 μM Ni^{2+}, 3 of 4 cells showed an increase in the number of spikes elicited for frequencies below 50 Hz for simEPSP trains, corresponding to a 29% decrease in the threshold frequency required to elicit spikes, from 70 ± 6.12 Hz to 50 ± 10.21 Hz ($n = 4$, $p < 0.05$, one-tailed Student's t-test).

This data is consistent with the interpretation that the Cav3-K_{Ca}3.1 complex suppresses nonfacilitating simEPSP input trains to a greater degree than PF-evoked EPSPs (**Fig. 4.1*C***). Facilitating inputs exhibit a lower threshold frequency under control conditions, suggesting that facilitating inputs overcome the Cav3-K_{Ca}3.1 filter, while nonfacilitating inputs are suppressed. However, several alternate explanations for the difference in threshold frequencies exist. It is important to recognize that these two methodologies differ in important ways that result in recruitment of different complements of ion channels. Firstly, evoked inputs are filtered by the dendritic tree, which has a different distribution and expression pattern of ion channels from the soma that can change the shape of postsynaptic responses. For instance, Cav3 channels have been reported throughout the dendritic tree of Purkinje cells at expression levels capable of conducting a full calcium-dependent spike (Isope and Murphy, 2005), with selective distribution patterns of different Cav3 channel isoforms (Craig et al., 1999; McKay et al., 2006; Hildebrand et al., 2009). The pattern of K_{Ca}3.1 immunolabel also differs over the somatodendritic axis, with a uniform label at the somatic level, but a more punctate label found over the proximal dendritic shaft and initial secondary dendritic branches (Engbers

et al., 2012b). There may thus be a differential recruitment of Cav3 and $K_{Ca}3.1$ channels with dendritic (PF-evoked) compared to somatic (simEPSC) stimuli. Secondly, the amplitude of evoked inputs may be greater than that of simEPSPs due to facilitation. I attempted to control for this difference and maintain an equivalent charge transfer by increasing the initial amplitude of simEPSPs compared to PF-evoked trains. The trains of simEPSPs thus started at a significantly larger amplitude (4.19 ± 0.17 mV) than the evoked EPSPs (1.86 ± 0.15 mV, $n = 5$, $p < 0.001$). I hypothesized that the difference in summation between PF-evoked and simEPSC stimuli was due to the pattern of amplitude increase during facilitating inputs, rather than dendritic influences or differences in total charge transfer. In order to test whether the Cav3-$K_{Ca}3.1$ complex selectively filters nonfacilitating inputs, I used a method called *dynamic clamp*.

4.3.1 Cav3-K_{Ca}3.1 complex selectively suppresses nonfacilitating inputs

Dynamic clamp allows for the artificial addition of conductances to neurons by calculating, in real time, the current that would be generated by a particular conductance (e.g. ionotropic AMPA receptors) according to Hodgkin-Huxley formalism (Sharp et al., 1993; Christini et al., 1999; Butera et al., 2001). It is more accurate than conventional current-clamp recordings in controlling the exact timing and magnitude of specific ionic currents in relation to the distance of the instantaneous membrane voltage from the ionic reversal potential. As conductances can be either added or subtracted on a microsecond interval, dynamic clamp can be used to directly assess the role that specific conductances have on neuronal function. In the cerebellum, dynamic clamp has been used to examine the origin of the complex spike in Purkinje cells (Davie et al., 2008), the contribution of $K_{Ca}2$ channels to spike output in DCN neurons (Feng and Jaeger, 2008), and the effects of synaptic inputs on Purkinje cell (Jaeger and Bower, 1999) and DCN cell output (Gauck and Jaeger, 2003). However, dynamic clamp has not been used to simulate facilitation of EPSCs in these neurons.

The frequency-dependence of PF facilitation has been well characterized in a previous study (Dittman et al., 2000). To replicate these results, I created a model of PF facilitation using an FD-synapse as described by Middleton et al. (2011) (see **Section 4.2.1**, **Fig. 4.2*A, B***). This model showed a facilitation ratio ($EPSP_{8\text{-}10}/EPSP_1$) of 4.5 at 50 Hz

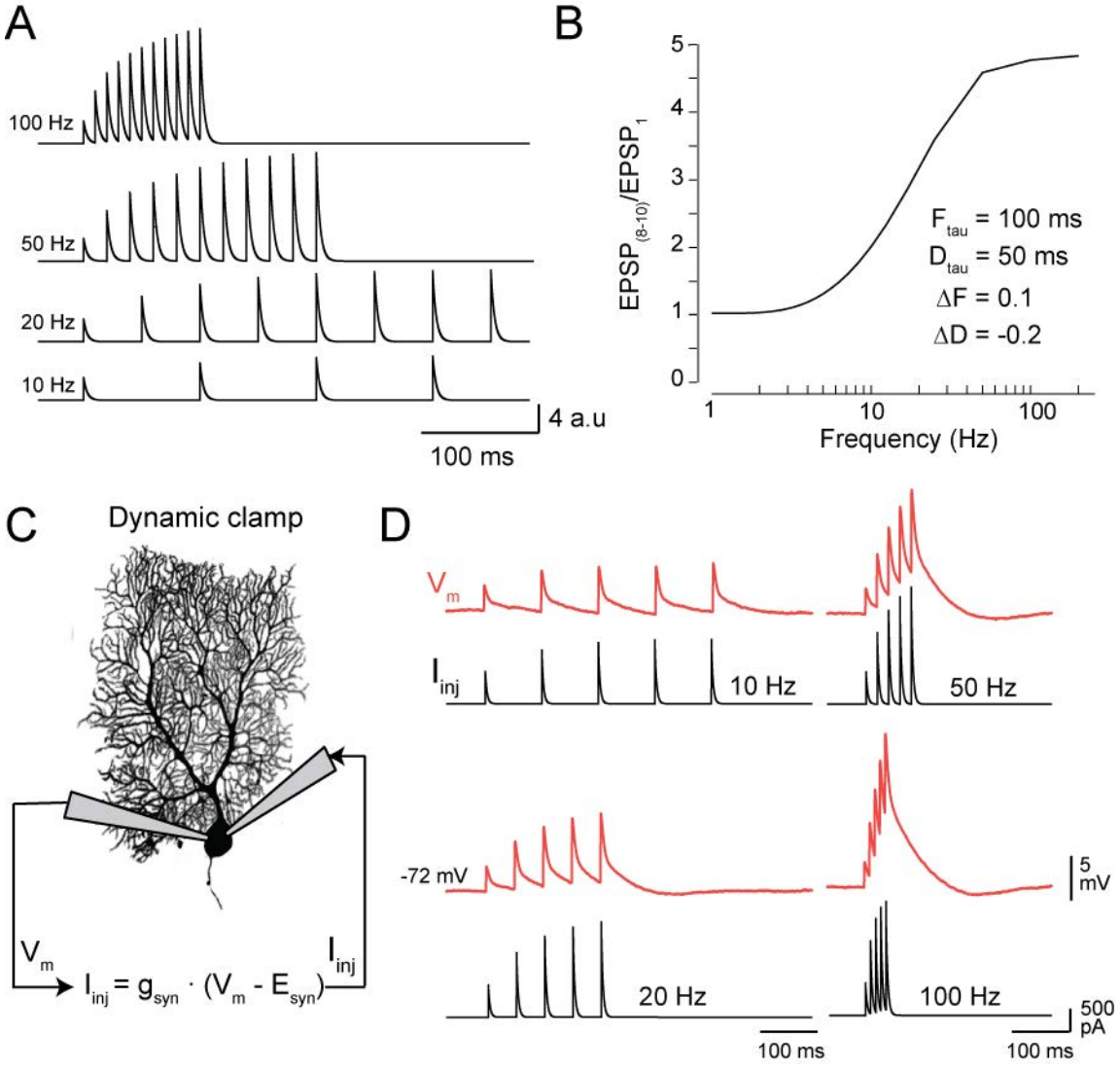
A
100 Hz
50 Hz
20 Hz
10 Hz
4 a.u
100 ms
B
EPSP(8-10)/EPSP1
5
4
3
2
1
0
1
10
100
Frequency (Hz)
Ftau = 100 ms
Dtau = 50 ms
ΔF = 0.1
ΔD = -0.2
C
Dynamic clamp
Vm
Iinj
Iinj = gsyn · (Vm - Esyn)
D
Vm
Iinj
10 Hz
50 Hz
-72 mV
5 mV
20 Hz
100 Hz
500 pA
100 ms
100 ms

Figure 4.2: Dynamic clamp model of facilitating PF synapses simulates physiological PF inputs

(A) Simulation of PF synaptic facilitation using a FD synapse model, designed to match the frequency-dependence of synaptic plasticity established in physiological recordings. Traces show the relative change in conductance during different input frequencies. **(B)** A plot of the ratio of $EPSP_{8\text{-}10}/EPSP_1$ amplitude of an input train (as in **A**) illustrates that the model synapse demonstrates frequency-dependent facilitation comparable to directly evoked PF EPSPs. **(C)** Illustration of the dynamic clamp setup where the somata of a Purkinje cell is dual patched with one electrode providing voltage measurements to the computer (RXTI software) while a second electrode provides current injection into the Purkinje cell somata. **(D)** Examples of dynEPSP voltage recordings (*top*) and current injections (*bottom*) during dynamic clamp simulation of 5 pulse PF EPSP trains at the indicated frequencies. Experiments performed by J Engbers.

and a maximal facilitation of 4.7 at 110 Hz (**Fig. 4.2*B)***. This model was then used in RTXI to dynamically inject synaptic conductances (dynEPSC) into Purkinje cell somata to generate an EPSP according to the instantaneous driving force of an underlying AMPA receptor conductance (dynEPSP) (**Fig. 4.2*C***). Furthermore, the FD-synapse parameters could be changed online to either allow or remove facilitation and to adjust conductance amplitude, enabling me to compare facilitating and nonfacilitating trains of equal charge transfer in the same cell. Because of the low input resistance of Purkinje cells, using a single electrode to both measure voltage and inject large, constantly changing currents would result in errors due to bridge imbalance (Davie et al., 2008). Therefore, I dual patched Purkinje cell somata and used one electrode to record voltage and the other to inject current through the same amplifier (**Fig. 4.2*C***). Purkinje cells were held subthreshold between -70 and -74 mV and PF dynEPSCs of increasing frequency were delivered to the soma, resulting in dynEPSPs with physiological levels of frequency-dependent facilitation (**Fig. 4.2*D***).

Injection of increasing frequencies of PF dynEPSCs resulted in increasing summation of PF dynEPSPs (**Fig. 4.2*D***). At sufficiently high frequencies, both facilitating and nonfacilitating dynEPSPs exhibited suprathreshold summation, although with different threshold frequencies. When facilitating dynEPSCs were provided to Purkinje cells (10 – 110 Hz; 10 Hz increments; 5 stimuli), threshold frequency was between 30 and 50 Hz with a mean value of 37.50 ± 2.50 Hz (n = 4, **Fig. 4.3*A, C***). In contrast, injection of nonfacilitating dynEPSPs into the same cells resulted in a right-shift in threshold frequency (**Fig. 4.3*A,*** *bottom*). Threshold frequencies ranged from 40 - 90 Hz with a mean value of 55.00 ± 11.90 Hz, significantly higher than that of facilitating inputs (n = 4, p < 0.05) (**Fig. 4.3*A, C***). While it may seem intuitive that facilitating inputs would summate more than nonfacilitating inputs due to an increasing amplitude during the train, I controlled for the difference in amplitudes by increasing conductance of nonfacilitating inputs and ensuring that overall charge transfer was not significantly different between the two conditions (facilitating: 0.170 ± 0.031 nC; nonfacilitating: 0.168 ± 0.028 nC, n = 4, p > 0.05). Therefore, the difference in summation depends on the pattern of dynEPSP amplitude change, rather than an increased charge transfer in one condition.

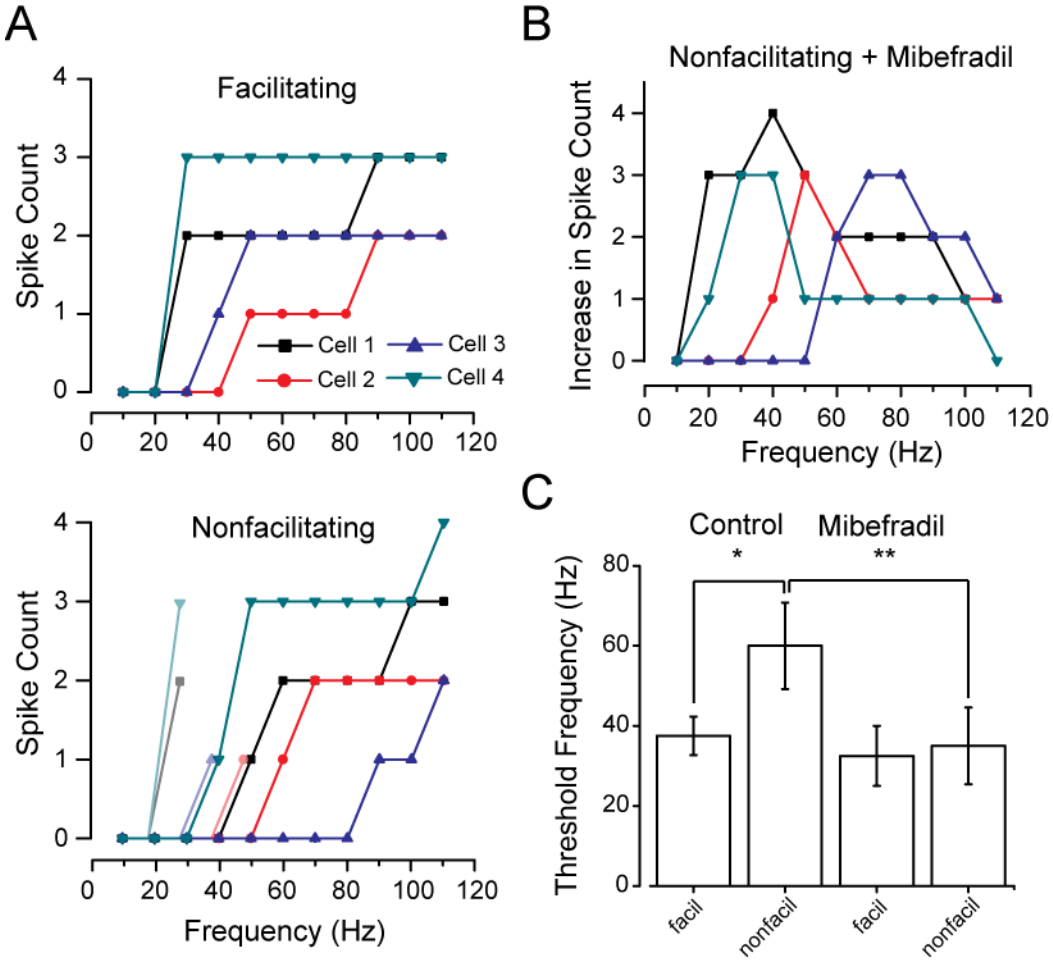
A
Facilitating
Spike Count
Cell 1
Cell 2
Cell 3
Cell 4
Nonfacilitating
Frequency (Hz)
B
Nonfacilitating + Mibefradil
Increase in Spike Count
Frequency (Hz)
C
Control
Mibefradil
*
**
Threshold Frequency (Hz)
facil
nonfacil
facil
nonfacil

Figure 4.3: Effect of Cav3-K_{Ca}3.1 complex on threshold frequency for facilitating and non-facilitating synapses

(A) Facilitating and nonfacilitating PF dynEPSCs of various frequencies (5 stimuli) were given to Purkinje cells and spike count was observed. Amplitudes of facilitating and nonfacilitating inputs were matched so that there was no significant difference in charge transfer between the two conditions. Facilitating inputs (*top*) elicited spikes at lower frequencies than nonfacilitating inputs (*bottom*). Transparent points from the facilitating inputs are shown overlapped with non-facilitating inputs for comparison. **(B)** Following application of mibefradil, increased spike output at lower frequencies is observed for nonfacilitating inputs. **(C)** Comparison of the threshold frequency for the four conditions shows that under control conditions, facilitating inputs have a significantly lower threshold frequency than nonfacilitating inputs. After application of 1 μM mibefradil, no change is observed in the threshold frequency for facilitating inputs, but nonfacilitating inputs show a significant decrease in threshold frequency, such that it equals facilitating inputs. Experiments performed by J Engbers.

Based on my initial observation that blocking the Cav3-K_{Ca}3.1 complex results in increased summation of simEPSPs (**Fig. 4.1**), I hypothesized that blocking Cav3 channels may decrease the threshold frequency for nonfacilitating dynEPSPs. Indeed, application of mibefradil (1 μM) resulted in a left-shift in the frequency dependence of nonfacilitating inputs, shown as an increase in action potentials at low frequencies (**Fig. 4.3*B, C***). Mean threshold frequency of nonfacilitating inputs after block of Cav3 channels by mibefradil (1 μM) was significantly decreased to 35.00 ± 9.57 Hz (range: 20 – 60 Hz, $n = 4$, $p < 0.05$), a value not significantly different from that of facilitating inputs in control conditions ($n = 4$, $p > 0.05$) (**Fig. 4.3*C***). In stark contrast, the threshold frequency for facilitating inputs did not show a significant change after mibefradil (27.50 ± 4.79 Hz, $n = 4$, $p > 0.05$) (**Fig. 4.3*C***). Therefore, it appears that the Cav3-K_{Ca}3.1 complex does selectively suppress nonfacilitating inputs.

In this experiment, synaptic inputs were injected into the soma, bypassing the complexities introduced by the dendritic tree when comparing evoked and simulated EPSPs (**Fig. 4.1**). Furthermore, charge transfer was equalized between the conditions to control for the advantage facilitating inputs have when examining summation. By using dynamic clamp, the effect of a decreasing driving force during summation is retained, compared to simEPSPs which inject a static amount of current regardless of membrane potential. These results clearly demonstrate a selective repression of nonfacilitating inputs and preference for inputs exhibiting physiological facilitating ratios.

4.3.2 Cav3-K_{Ca}3.1 complex filters out net high-frequency background activity

Because of the large number of synaptic inputs that the Purkinje cell receives, it is likely that a large number of spatially distributed inputs will arrive in close temporal proximity to each other. The net sum of these inputs will appear as high-frequency EPSP trains at the soma, even if the presynaptic sources are firing at low frequencies. In order to maintain a high SNR, the Purkinje cell must be able to filter out these net high-frequency background inputs, yet still maintain the ability to respond to single source high-frequency trains representing sensory input. One important difference between background inputs and singular inputs is presynaptic facilitation. Facilitation will be much higher for a single PF providing 50 Hz input to the dendritic tree than for 10 un-

synchronized PF inputs providing 5 Hz input. Therefore, I hypothesized that the suppression of nonfacilitating inputs performed by the Cav3-K_{Ca}3.1 complex (**Fig. 4.3**) would allow Purkinje cells to differentiate between single source and background inputs of similar frequency content.

To test this hypothesis, I recorded from Purkinje cells while stimulating at independent sites on opposite sides of their dendritic tree (**Fig. 4.4*A, D, G***). The amplitude of each stimulation site was tuned to elicit ~2 mV EPSPs. I first characterized the response of the Purkinje cell to 50 Hz stimulation at either site under control conditions. Each cell exhibited suprathreshold summation by the end of the stimulus train (10 stimuli), regardless of the stimulation site, with up to 31 cumulative spikes elicited by $EPSP_{10}$ (**Fig. 4.4*B, E***). There was no significant difference in the number of spikes elicited by either site (n = 4, $p > 0.05$). As expected for 50 Hz stimulation, a high degree of facilitation was observed (**Fig. 4.4*C, F***). To approximate the presence of net high-frequency background input, I interleaved 25 Hz stimulation at both sites, resulting in a net presynaptic input frequency of 50 Hz at the soma (**Fig. 4.4*G***). By stimulating at lower frequencies at both sites, a lesser degree of presynaptic facilitation should be elicited while still maintaining a high net frequency. Indeed, at 25 Hz, each site exhibited lower presynaptic facilitation (~ 3X facilitation at 25 Hz vs 4X at 50 Hz). The interleaved stimulus pattern resulted in a lower degree of summation of the soma and a significantly smaller number of action potentials than 50 Hz stimulation at either site (n = 4, $p < 0.01$) (**Fig. 4.4*H, I***). This was expected, given the lesser degree of facilitation at each stimulation site. Interestingly, summation followed a linear pattern with interleaved stimuli, rather than the more exponential summation observed at single sites.

Based on the lower facilitation ratio at 25 Hz stimulation compared to 50 Hz and the dynamic clamp experiment that demonstrated the selective suppression of nonfacilitating inputs, I hypothesized that the Cav3-K_{Ca}3.1 complex was selectively suppressing inputs exhibiting submaximal facilitation ratios. To test this hypothesis, I blocked Cav3 channels with mibefradil (1 μM) and observed the effect on PF-evoked EPSP summation. Application of mibefradil increased summation of PF-evoked EPSPs

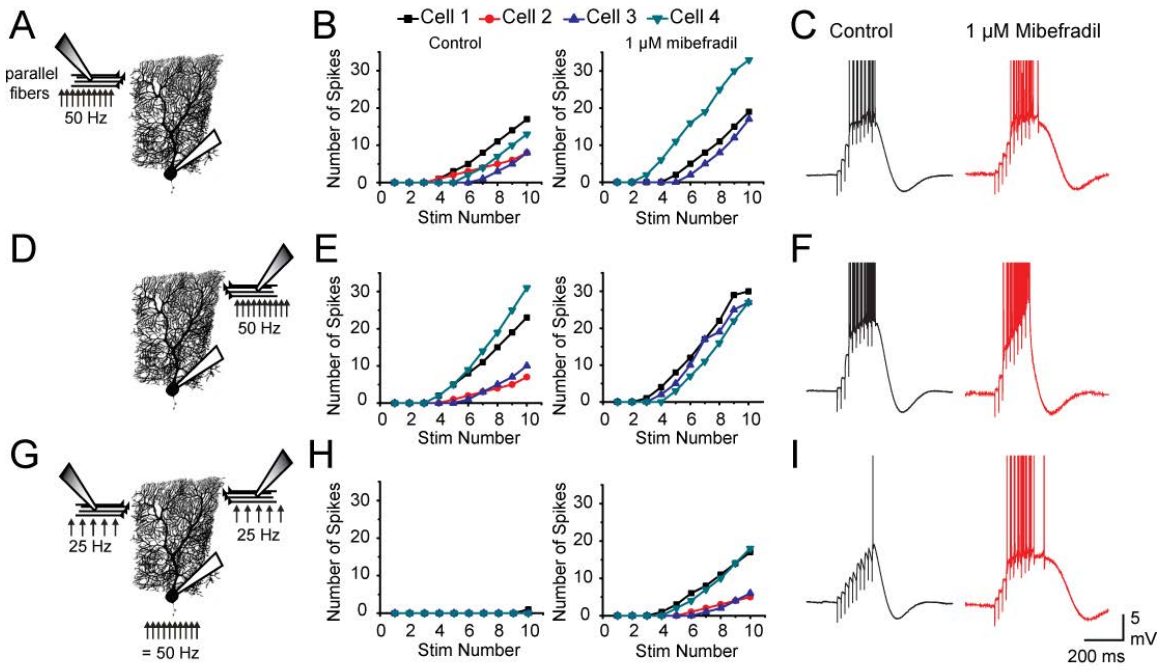
A
parallel fibers
50 Hz
B
Cell 1
Cell 2
Cell 3
Cell 4
Control
1 μM mibefradil
Number of Spikes
Stim Number
C
Control
1 μM Mibefradil
D
50 Hz
E
F
G
25 Hz
25 Hz
= 50 Hz
H
I
5 mV
200 ms

Figure 4.4: Cav3-K_{Ca}3.1 complex selectively reduces summation of distributed, high-frequency PF inputs

(A, D, G) Illustration of experimental paradigm where PFs are stimulated on either side of the dendritic tree at 50 Hz **(A, D)** or interleaved at 25 Hz for a net stimulation frequency of 50 Hz **(G)**. **(B, E)** Counts of action potentials elicited during 10 stimuli 50 Hz trains. When either side of the dendritic tree is stimulated at 50 Hz, suprathreshold summation and a large number of spikes are elicited in control conditions (*left*). A similar number of spikes are elicited from either site after application of 1 μM mibefradil **(C, F)**. **(H, I)** Spike count for simultaneous but interleaved stimulation at both sites (5 stimuli 25 Hz trains). No spikes are elicited in the majority of cases, with a single action potential being elicited in one cell at $EPSP_{10}$. Application of 1 μM mibefradil causes a significant increase the number of elicited spikes during the stimulus trains. **(I)** The output of Purkinje cells during two-site simulation after block of Cav3 channels is indistinguishable from output during simulation at either site. Experiments performed by J Engbers.

in all cases, but only caused a significant increase in the number of spikes in the interleaved configuration (control: 0.25 ± 0.25 spikes; mibefradil: 11.5 ± 3.48 spikes; $n = 4$; $p < 0.05$) (**Fig. 4.4*B, E, H***). From these results, it appears that the Cav3-K_{Ca}3.1 complex suppresses the summation of PF inputs that do not exhibit facilitation ratios indicative of single-source, high frequency input. The direct stimulation comparisons provided here reinforce results obtained by simEPSPs and dynEPSPs. By using physiological stimulation and incorporating the full dendritic tree along with all its nonlinearities and filtering abilities, this experiment demonstrates that the Cav3-K_{Ca}3.1 complex augments the high-pass filter implemented by presynaptic facilitation under physiological conditions. Specifically, the Cav3-K_{Ca}3.1 complex provides a mechanism by which Purkinje cells can filter out uninformative background information while allowing single-source facilitating inputs to summate and generate spike output necessary for cerebellar function.

4.3.3 K_{Ca}3.1 activation increases during the synaptic input train

While the previous results demonstrate the ability for the Cav3-K_{Ca}3.1 complex to generate a filter based on the extent of presynaptic facilitation, the exact mechanism behind this filtering operation has not yet been determined. To assess activation of the K_{Ca}3.1 channel during the synaptic input train, I examined the change in rate of decay of PF simEPSPs during a 25 Hz input train, a frequency which I previously showed to be sensitive to blockade of the Cav3-K_{Ca}3.1 complex (**Fig. 3.11**).

I first characterized the amplitude dependence of the PF simEPSP rate of decay by injecting simEPSCs of increasing amplitude. SimEPSP rate of decay showed a linear dependence on simEPSP amplitude (**Fig. 4.5*A***). When normalized to the rate of decay of the 5 mV simEPSP, it is apparent that the rate of decay for a single simEPSP increases or decreases by 20% for each mV (**Fig. 4.5*A***, $n = 5 – 6$). For example, a 3 mV simEPSP exhibits a rate of decay that is 60% of the value of the 5 mV simEPSP. Furthermore, application of Ni^{2+} results has a divisive effect on the linear relationship between simEPSP amplitude and rate of decay. Because of the linear relationship between EPSP height and rate of decay in both control and test conditions, it is possible to predict what the rate of

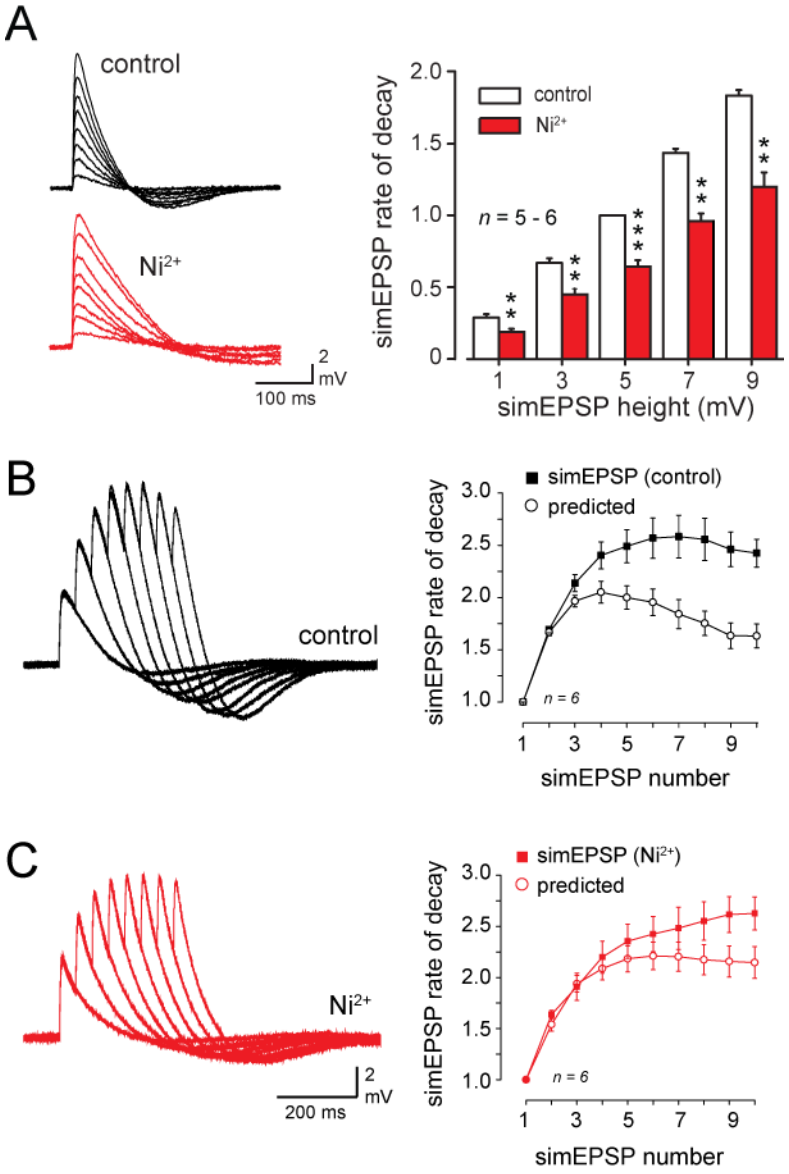
A
control
Ni2+
2
mV
100 ms
simEPSP rate of decay
control
Ni2+
n = 5 - 6
simEPSP height (mV)
B
control
simEPSP (control)
predicted
n = 6
simEPSP number
C
Ni2+
2
mV
200 ms
simEPSP (Ni2+)
predicted
n = 6
simEPSP number

Figure 4.5: Supralinear activation of $K_{Ca}3.1$ during PF EPSP trains

(A) Rate of decay for simEPSPs of different amplitudes (1 – 9 mV) measured under control conditions (*black*) and after application of 100 μM Ni^{2+} (*red*). Example traces (*left*) show that blocking Cav3 channels results in a decrease of rate of decay for all amplitudes. Population data (*right*) reveals a significant decrease in rate of decay for all simEPSP heights. Rate of decay has a linear relationship with simEPSP height both before and after Ni^{2+} application. **(B, C)** 25 Hz simEPSP trains injected in the presence of 200 nM TTX to prevent spiking. 10 trains delivered in control conditions **(B)** and after application of 100 μM Ni^{2+} **(C)**, with each consecutive train having an additional simEPSP (*left*). The rate of decay for each consecutive simEPSP is measured and compared to a linear prediction based on the amplitude of the simEPSP (*right*). Experiments performed by J Engbers.

decay should be for an EPSP of a given height if the rate of decay for the 5 mV EPSP is known and if $K_{Ca}3.1$ activation remains constant.

To examine the activation of $K_{Ca}3.1$ during a PF simEPSP train, PF simEPSC trains (25 Hz) were injected into the Purkinje cell soma, with the number of PF simEPSCs increasing by one for each consecutive train (**Fig. 4.5*B***). To avoid complication of action potentials during the summation of the PF simEPSP train, TTX (200 nM) was bath applied during all recordings. simEPSC amplitudes were adjusted to elicit a ~5 mV initial simEPSP (4.55 ± 0.12 mV, n = 6). Two values were determined for each simEPSP in the train: the experimental rate of decay and the predicted rate of decay based on the linear relationship described above. Under control conditions, simEPSPs showed nonmonotonic summation which reached a maximum of 9.90 ± 0.53 mV at $simEPSP_4$. Based on the approximate doubling of simEPSP height, the normalized rate of decay was predicted to reach a normalized maximum of 2.05 ± 0.10 before decreasing as simEPSP height decreased. However, the measured rate of decay displayed a supralinear increase after $simEPSP_3$, reaching a normalized maximum of 2.58 ± 0.20 at $simEPSP_7$. The greatest difference was seen at $simEPSP_{10}$, where measured values were 2.42 ± 0.13 and predicted were 1.63 ± 0.11 (n = 6, $p < 0.01$) (**Fig. 4.5*B***).

One possible explanation for this supralinear increase in the rate of decay is increasing activation of $K_{Ca}3.1$ via Cav3-mediated Ca^{2+} influx with each consecutive simEPSP. To test this hypothesis, Ni^{2+} (100 μM) was applied to block Cav3 channels. Following application of Ni^{2+}, simEPSP trains showed increased summation, as expected based on previous observations (**Fig. 3.11**), despite no significant difference in the initial simEPSP height (4.55 ± 0.17 mV, n = 6, $p > 0.05$). Membrane voltage at $simEPSP_{10}$ in the presence of Ni^{2+} was 10.42 ± 0.87 mV compared to the 7.77 ± 0.64 mV obtained by control (n = 6, $p < 0.01$). Interestingly, simEPSP rate of decay approached the predicted rate of decay following occlusion of Cav3 channels. By $simEPSP_{10}$, the predicted normalized rate of decay was 2.15 ± 0.16 while the measured rate of decay was 2.63 ± 0.16 (n = 6) (**Fig. 4.5*C***). Thus, after removal of the $K_{Ca}3.1$-mediated outward current, simEPSP trains exhibited a near linear increase in the rate of decay compared to the supralinear increase observed when the Cav3-$K_{Ca}3.1$ complex was intact (**Fig. 4.5*C***).

There are several possible explanations for the remaining nonlinearity in the rate of decay. HCN channels will deactivate during depolarization, resulting in less inward current. However, blocking HCN channels results in a large increase in membrane time constant and a dramatic slowing of EPSP rate of decay (**Fig. 3.3**)(Angelo et al., 2007). $K_{Ca}1.1$ and $K_{Ca}2$ currents were also intact during these experiments, but previous experiments have showed no effect of $K_{Ca}1.1$ and $K_{Ca}2$ blockers on the rate of decay of single simEPSPs (**Fig. 3.1**). The most likely explanation is incomplete block of the Cav3-$K_{Ca}3.1$ complex. Nevertheless, these results clearly demonstrate that the Cav3-$K_{Ca}3.1$ complex exerts dominant control over subthreshold EPSP rate of decay.

4.3.4 Model of Cav3-$K_{Ca}3.1$ interaction reveals increased $K_{Ca}3.1$ activation during repetitive stimulation

To further explore the mechanism by which the Cav3-$K_{Ca}3.1$ complex filters nonfacilitating inputs, I developed a model of the Purkinje cell subthreshold membrane that included a Ca^{2+} diffusion model to simulate the interaction between the Cav3 and $K_{Ca}3.1$ channels. Briefly, Ca^{2+} diffusion was simulated from the Cav3 channel through 10 hemispherical compartments. $K_{Ca}3.1$ activation could be made to depend on the $[Ca^{2+}]$ in any one of the compartments, thus allowing me to test the effect of channel distance on $K_{Ca}3.1$ activation kinetics. Since no model of $K_{Ca}3.1$ currently exists, a model of $K_{Ca}2$ channel gating was adapted to simulate the increased Ca^{2+} sensitivity of $K_{Ca}3.1$ channels (**Section 4.2.2.3**). To simulate subthreshold membrane properties, I_H and I_{leak} currents were also included.

In order for the model to have predictive value, it must first be able to replicate experimental results. I thus first examined whether the simulated Cav3-$K_{Ca}3.1$ complex was capable of replicating the effect of the Cav3-$K_{Ca}3.1$ of PF EPSP rate of decay. When only a single Cav3 channel with physiological single channel conductance (g = 1.7 pS) was used (Weber et al., 2010), activation of $K_{Ca}3.1$ channel was not possible (*data not shown*). However, increasing the single channel conductance by four times (g = 6.8 pS) allowed for sufficient activation of the $K_{Ca}3.1$ channel when placed in close proximity (20 nm) of the Cav3 channel (**Fig. 4.6*A***). This suggests that the $K_{Ca}3.1$ channel may associated with multiple Cav3 channels, similar to the $K_{Ca}1.1$ supercomplex (**Fig. 1.5**).

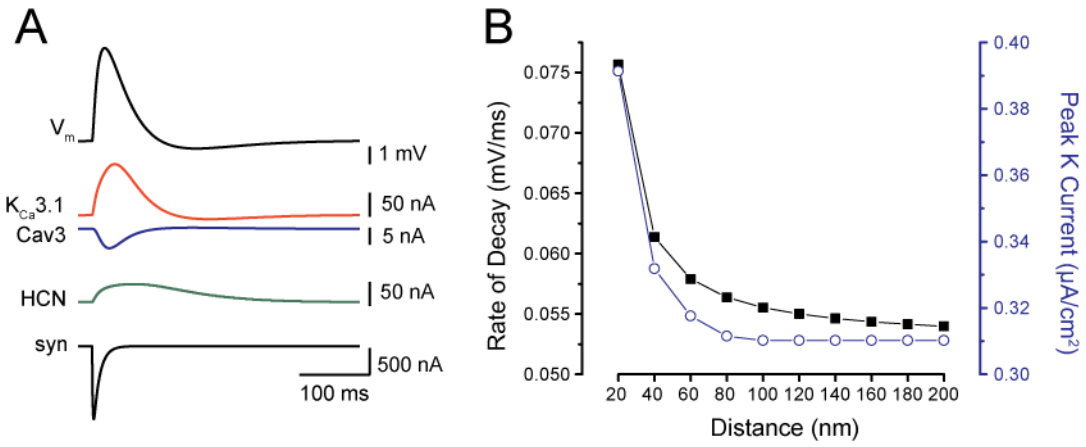
A
V_m
1 mV
K_{Ca}3.1
50 nA
Cav3
5 nA
HCN
50 nA
syn
500 nA
100 ms
B
Rate of Decay (mV/ms)
0.075
0.070
0.065
0.060
0.055
0.050
20 40 60 80 100 120 140 160 180 200
Distance (nm)
0.40
0.38
0.36
0.34
0.32
0.30
Peak K Current (μA/cm²)

Figure 4.6: Characterization of Cav3-K_{Ca}3.1 model

(A) A model containing I_H, I_{leak}, I_{syn}, I_{Cav3} and I_{KCa} replicates the activation of K_{Ca}3.1 during a 5 mV EPSP via Cav3-mediated Ca^{2+} influx. The K_{Ca}3.1 channel is located within 20 nm of the Cav3 channel. Model voltage and currents are plotted. **(B)** The EPSP rate of decay and peak K^+ current show a steep dependence on the distance between the K_{Ca}3.1 and Cav3 channels. Physiological rates of decay are only achieved when the K_{Ca}3.1 channel is within 20 nm of the Cav3 channel. Model created and simulations performed by J Engbers.

When $K_{Ca}3.1$ was activated, PF EPSP rate of decay increased from 0.049 mV/ms (without the $K_{Ca}3.1$ channel) to 0.076 mV/ms (**Fig. 4.6*A, B***). Thus, removal of the $K_{Ca}3.1$ channel resulted in a 35.5% decrease in the rate of EPSP decay in the model, an equivalent effect to that observed by Cav3 channel blockers in slice recordings (**Chapter 3**)(Engbers et al., 2012b). As the distance between the channels was increased, peak I_{Kca} decreased until no effect on rate of decay was observed (**Fig. 4.6*B***). These results confirm the close proximity of the $K_{Ca}3.1$ channel to the Cav3 channel (**Fig. 3.8, 3.9**).

The relationship between rate of decay and EPSP amplitude in the model was examined to verify its ability to replicate the results from slice recordings. The model rate of decay showed a linear dependence on EPSP height (0.0155 ms^{-1}) when the Cav3-$K_{Ca}3.1$ complex was included (**Fig. 4.7*A, B***). This linear dependence closely matched physiological values, with EPSP rate of decay changing at 21.3%/mV relative to the 5 mV EPSP. When the Cav3-$K_{Ca}3.1$ complex was removed from the model, EPSP rate of decay was significantly slowed (0.076 mV/ms compared to 0.133 mV/ms (43% decrease) for a 9 mV EPSP) and the linear slope was decreased by 45% to a value of 0.0086 ms^{-1} (**Fig. 4.7*A, B***). This decrease in the rate of decay was consistent with what was observed in slice recordings when Cav3 channels were blocked (**Fig. 4.5*A***).

I next determined whether the model could reproduce the supralinear increase in rate of decay seen during a 50 Hz simEPSP train. The model was provided with nonfacilitating EPSCs and the rate of decay for consecutive EPSPs was measured (**Fig. 4.7*C***). The EPSP train showed a nonmonotonic summation, peaking at $EPSP_4$ (10.17 mV) and then decreasing to a steady-state of 9.56 mV (**Fig. 4.7*C***). Based on these EPSP heights, the rate of decay was predicted to increase to 0.157 mV/ms and decrease to 0.148 mV/ms (**Fig. 4.7*D*,** *left*). Instead, a supralinear increase in the rate of decay was observed, reaching a steady-state value near 0.183 mV/ms by $EPSP_4$ (**Fig. 4.7*D*,** *left*). To compare the model results to physiological recordings, the rates of decay were normalized to the first EPSP. Normalized rates of decay were similar to those observed in slice recordings, with the rate of decay increasing by 255% at $EPSP_{10}$ compared to a predicted value of 195% (**Fig. 4.7*D***, *right*). When the Cav3-$K_{Ca}3.1$ complex was not included in the model, significantly greater summation was observed (**Fig. 4.7*E***). EPSP summation was

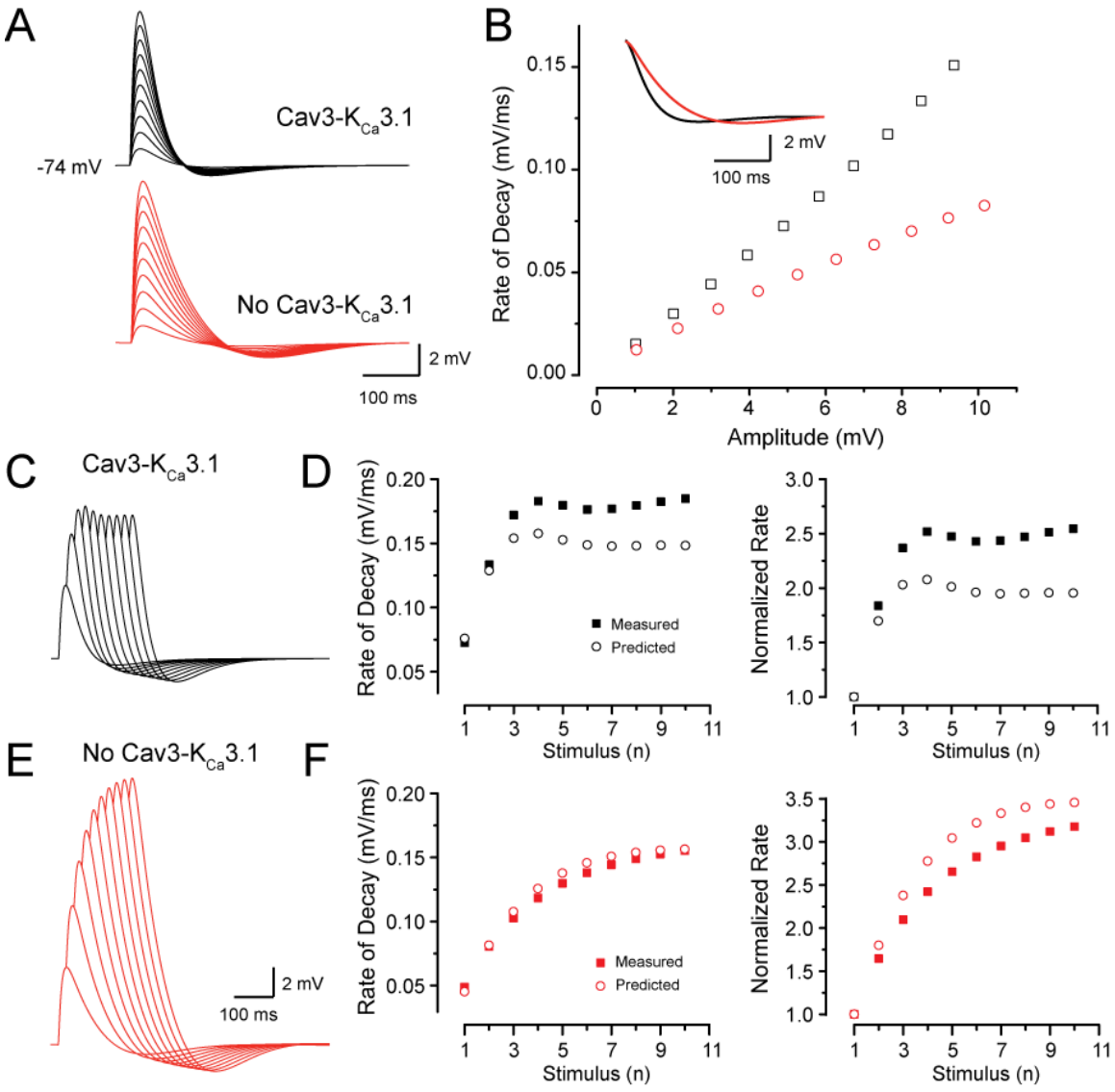
A
Cav3-K$_{Ca}$3.1
-74 mV
No Cav3-K$_{Ca}$3.1
2 mV
100 ms
B
Rate of Decay (mV/ms)
0.15
0.10
0.05
0.00
2 mV
100 ms
0
2
4
6
8
10
Amplitude (mV)
C
Cav3-K$_{Ca}$3.1
D
Rate of Decay (mV/ms)
0.20
0.15
0.10
0.05
Measured
Predicted
1
3
5
7
9
11
Stimulus (n)
Normalized Rate
3.0
2.5
2.0
1.5
1.0
Stimulus (n)
E
No Cav3-K$_{Ca}$3.1
2 mV
100 ms
F
Rate of Decay (mV/ms)
Measured
Predicted
Stimulus (n)
Normalized Rate
3.5
3.0
2.5
2.0
1.5
1.0
Stimulus (n)

Figure 4.7: Cav3-K_{Ca}3.1 model replicates supralinear increase in EPSP rate of decay

(A) Increasing amplitudes of EPSCs are given to the model with and without the Cav3-K_{Ca}3.1 complex interaction. Removal of the Cav3-K_{Ca}3.1 channel results in a decrease in rate of EPSP rate of decay. **(B)** EPSP rate of decay is linearly related to EPSP amplitude in the model. Addition of the Cav3-K_{Ca}3.1 complex results in an approximate doubling of the rate of decay for large amplitudes. *Inset* shows a comparison of the decay of 5 mV EPSPs with (*black*) and without (*red*) the Cav3-K_{Ca}3.1 model. **(C – F)** 50 Hz EPSC trains given to the model with each consecutive train containing an additional EPSC. **(C)** With the Cav3-K_{Ca}3.1 complex, the model displays a decrease in summation after $EPSP_4$. **(D)** Plots of measured rate of decay vs. predicted rate of decay shows a supralinear increase in rate of decay. **(E)** Without the Cav3-K_{Ca}3.1 complex, EPSPs show a monotonic increase in summation. **(F)** Plots of measured rate of decay vs. predicted rate of decay show that a linear prediction closely matches measured values. Simulations performed by J Engbers.

monotonic and logarithmic, reaching 18.19 mV by $EPSP_{10}$ (**Fig. 4.7*E***). The measured rate of decay closely matched the predicted linear value throughout the train, reaching values of 0.155 mV/ms and 0.156 mV/ms by the end of the train (**Fig. 4.7*F***, *left*). When normalized to the initial rate of decay ($EPSP_1$), some differences between the measured and predicted values were magnified, showing that the measured values were consistently less than predicted values (**Fig. 4.7*F,* *right***). Since I_H would be the most influential current when the Cav3-K_{Ca}3.1 model is removed (**Fig. 3.3*B***)(Angelo et al., 2007), this slowing of the measured rate of decay could reflect a decrease in I_H activation during the EPSP train and corresponding increase in time constant throughout the train.

4.3.5 Early activation of K_{Ca}3.1 channel causes suppression of nonfacilitating inputs

Having established that the model is capable of replicating many of the experimental results, I next used the model to examine the mechanism behind the selective suppression of nonfacilitating inputs. The dynamic clamp results established that a 50 Hz PF input is below the threshold frequency for nonfacilitating inputs, but capable of eliciting action potentials when given as a facilitating pattern (**Fig. 4.3*C***). Furthermore, occlusion of the Cav3 channel causes nonfacilitating inputs to achieve suprathreshold summation at this frequency. Therefore, I tested the ability for facilitating and nonfacilitating inputs to summate in the model with and without the Cav3-K_{Ca}3.1 complex (**Fig. 4.8**).

To control for the greater amplitude achieved by facilitating inputs, synaptic current amplitudes were adjusted to ensure the same charge transfer was given during the 50 Hz (5 stimulus) train in both the facilitating and nonfacilitating cases (71.8 nC vs 71.6 nC with Cav3-K_{Ca}3.1; 67.8 nC vs. 68.1 nC without Cav3-K_{Ca}3.1). When the model contained the Cav3-K_{Ca}3.1 complex, facilitating inputs reached a higher degree of summation than nonfacilitating inputs with the same charge transfer (**Fig. 4.8*A, D***). The two sets of inputs displayed different patterns of integration. Facilitating inputs showed monotonic summation, with some small reduction in the rate of summation by $EPSP_5$. In comparison, nonfacilitating inputs displayed nonmonotonic summation, showing significant reduction in EPSP height after $EPSP_3$. Facilitating inputs showed greater summation than the nonfacilitating train after $EPSP_3$, reaching 12.87 mV compared to 10.14 mV (2.73 mV difference). To compare to a membrane lacking Cav3-K_{Ca}3.1, simulations with a model

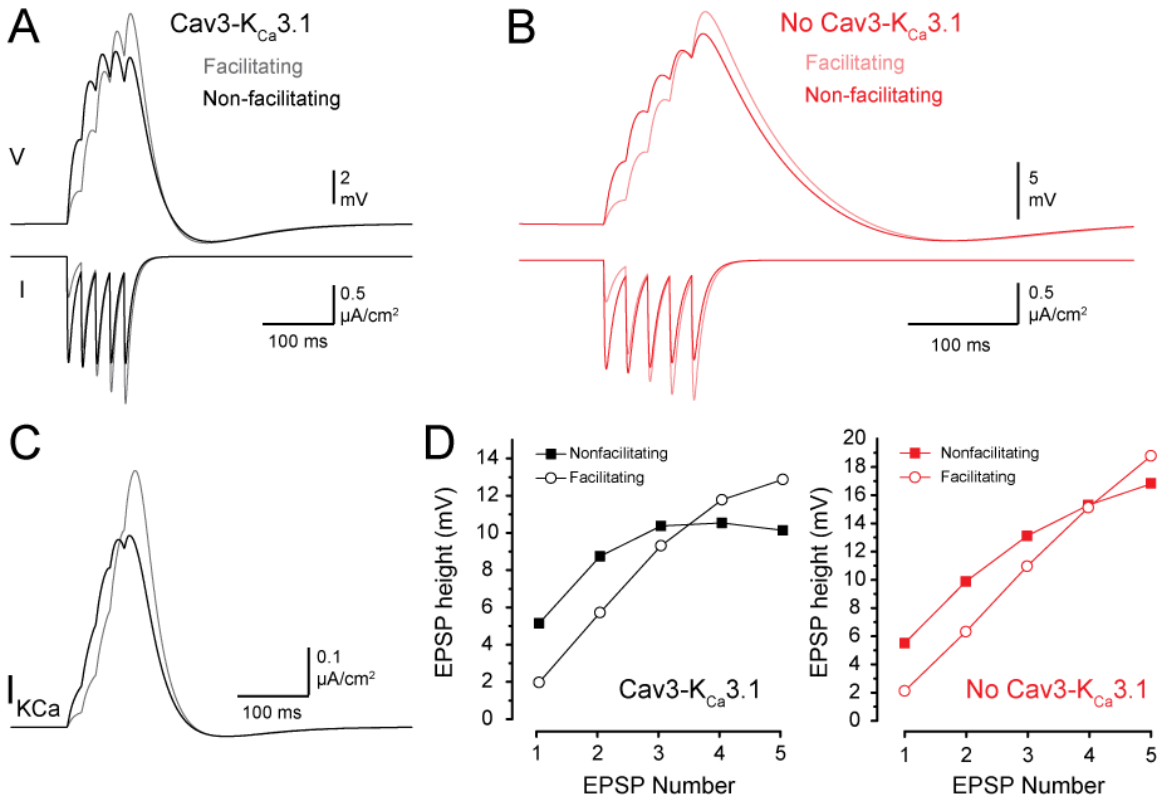
A
Cav3-K$_{Ca}$3.1
Facilitating
Non-facilitating
V
2 mV
I
0.5 µA/cm²
100 ms
B
No Cav3-K$_{Ca}$3.1
Facilitating
Non-facilitating
5 mV
0.5 µA/cm²
100 ms
C
I$_{KCa}$
0.1 µA/cm²
100 ms
D
Nonfacilitating
Facilitating
EPSP height (mV)
EPSP Number
Cav3-K$_{Ca}$3.1
No Cav3-K$_{Ca}$3.1

Figure 4.8: Differential timecourse of $K_{Ca}3.1$ activation during facilitating and nonfacilitating trains

(A) Model membrane voltage and synaptic currents for facilitating and nonfacilitating 50 Hz EPSCs with the Cav3-$K_{Ca}3.1$ model. The facilitating input trains attains a higher degree of summation. The nonfacilitating train is suppressed and shows nonmonotonic summation. **(B)** Membrane voltage and synaptic currents in a model lacking the Cav3-$K_{Ca}3.1$ complex. Both facilitating and nonfacilitating trains show monotonic summation. **(C)** Traces of I_{KCa} during facilitating (*grey*) and nonfacilitating (*black*) inputs. I_{KCa} shows earlier and greater activation during the nonfacilitating train for $EPSP_{1\text{-}4}$. **(D)** Plots of peak EPSP amplitude during facilitating and nonfacilitating trains in models with (*left*) and without (*right*) Cav3-$K_{Ca}3.1$. Simulations performed by J Engbers.

containing only I_H and I_{leak} were performed. In this case, both facilitating and nonfacilitating traces showed monotonic summation (**Fig. 4.8*B***). While the facilitating train still showed increased summation, the difference was less (1.94 mV difference) (**Fig. 4.8*B, D***). Both trains also reached greater degrees of summation than the model containing Cav3-K_{Ca}3.1, despite similar overall charge transfers.

The difference between facilitating and nonfacilitating summation was only 0.8 mV smaller when the Cav3-K_{Ca}3.1 channel was not present. However, small changes in voltage near threshold can have significant effects on Na^+ channel recruitment. Furthermore, the nonmonotonic trend for nonfacilitating inputs that is observed in the presence of the Cav3-K_{Ca}3.1 complex would be expected to continue to increase the difference in summation between the facilitating and nonfacilitating trains. Overall, these results confirm that the Cav3-K_{Ca}3.1 complex reduces the summation of PF EPSP trains and strongly suppresses nonfacilitating inputs.

To examine the mechanism underlying this selective suppression of the nonfacilitating inputs, the underlying K_{Ca}3.1 mediated current (I_{KCa}) was examined (**Fig. 4.8*C***). During the nonfacilitating train, I_{KCa} had a rapid onset, with significant activation during $EPSP_1$. I_{KCa} continued to increase throughout the train, peaking during $EPSP_5$, despite the decrease in summation after $EPSP_3$. However, during the facilitating train, I_{KCa} showed delayed activation, with minimal activation during $EPSP_1$. In fact, I_{KCa} evoked during the facilitating train remains less than that evoked during the nonfacilitating train until $EPSP_5$ (**Fig. 4.8*C***). Based on these observations, it appears that the pattern of EPSP amplitudes causes differential activation of the Cav3-K_{Ca}3.1 complex. If an input remains at a constant amplitude, increasing activation of I_{KCa} rapidly suppresses the input train. On the other hand, during facilitating trains, the rapid increase in EPSP amplitude offsets the increase of I_{KCa} and inputs continue to summate.

4.4 Discussion

Central neurons are the sites of synaptic convergence, with many receiving between 10^4 to 10^5 synaptic inputs. Neurons must be able to filter their inputs and respond only to inputs that carry important information. Purkinje cells represent an extreme example, re-

ceiving up to 150,000 excitatory PF inputs that carry sensory information, of which only a subset carry important information at any given time. Therefore, they must have some mechanisms to increase the SNR for relevant information. Here, I used a combination of experimental and computational technique to demonstrate that the Cav3-K_{Ca}3.1 complex enhances the ability for presynaptic facilitation to increase the SNR for presynaptic bursts.

4.4.1 Cav3-K_{Ca}3.1 complex augments the filtering role of presynaptic facilitation

Short-term plasticity is an important nonlinear mechanism used by synapses to increase information transfer (Abbott and Regehr, 2004). Short-term facilitation can act as a high-pass filter, emphasizing high frequency patterns of input, such as bursts (Lisman, 1997). The frequency-dependence of facilitation determines which inputs receive greater emphasis in the postsynaptic neuron. In the cerebellar cortex, granule cells fire at low frequencies in the absence of sensory stimulus (0.5 to 4 Hz) (Chadderton et al., 2004), which is below the threshold for facilitation at the PF-Purkinje cell synapse. However, at any given time, there will be a large number of low-frequency inputs arriving at the Purkinje cell, resulting in net high-frequency inputs to the soma. The distinguishing feature between these inputs and inputs indicative of sensory information will be the ~4X facilitation that is seen for inputs above 50 Hz (Dittman et al., 2000). In order to increase the SNR for these inputs, the Cav3-K_{Ca}3.1 complex selectively suppresses nonfacilitating inputs while allowing facilitating inputs to overcome increasing K_{Ca}3.1 activation.

Many studies have examined either the mechanisms behind short-term facilitation of synapses or the effect of facilitation on information transfer (Lisman, 1997; Dittman et al., 2000; Abbott and Regehr, 2004). However, relatively few studies have examined the interaction between presynaptic and postsynaptic dynamics. Studies in locust demonstrated that activation of postsynaptic K_{Ca} channels during synaptic input creates a "forward masking" effect, where the presence of an intense stimulus suppresses subsequent inputs (Sobel and Tank, 1994). In others, postsynaptic mechanisms have been shown to augment the low-pass filter implemented by synaptic depression (Fortune and Rose, 1997). Depolarization of the postsynaptic membrane is necessary to relieve Mg^{2+} block of NMDA receptors, thus creating a state-dependent change in the action of glutamate that

depends on the postsynaptic membrane. However, the present study provides the novel finding that a VGCC-K_{Ca} complex tunes the postsynaptic membrane to respond not only to particular frequencies, but also to inputs which exhibit facilitation.

4.4.2 Modelling Ca^{2+} and K_{Ca} channel interactions

Here, I modelled the interaction between the Cav3 and $K_{Ca}3.1$ channel. Previous models have been made of the interaction between Ca^{2+} and K_{Ca} channels within nano- and microdomains (Fakler and Adelman, 2008; Feng and Jaeger, 2008). However, the majority of the models have been used solely to examine the distance between the two channels based on the efficacy of various Ca^{2+} chelators. Using the Ca^{2+} diffusion model combined with the membrane model described here, I demonstrated that $K_{Ca}3.1$ channels can be sufficiently activated even during subthreshold EPSPs to affect membrane voltage. This model has been used recently to examine the interaction between Cav3 and $K_{Ca}1.1$ channels in the medial vestibular nucleus (Rehak et al., 2013), demonstrating that cooperation between many Cav3 Ca^{2+} domains is necessary for low voltage activation of $K_{Ca}1.1$ channels.

Just like all models which are abstractions of complicated biological systems, this model has limitations. The current model lacks explicit descriptions of the intracellular Ca^{2+} binding proteins parvalbumin and calbindin, both of which are present in high concentrations in Purkinje cells (Hartmann and Konnerth, 2005). Calbindin has been shown to significantly lower the Ca^{2+} response elicited by PF and CF inputs (Barski et al., 2003; Hartmann and Konnerth, 2005). The presence of these buffers would then further restrict the spatial and temporal extent of increases in $[Ca^{2+}]_i$. Therefore, the distance between the Cav3 and $K_{Ca}3.1$ channel demonstrated in the current model represents a maximum effective distance between the channels and greater restriction likely exists. Likewise, the number of Cav3 channels required for $K_{Ca}3.1$ activation represents a minimal, rather than exact estimate. However, it should be noted that other studies have compared models with explicit simulation of diffusible Ca^{2+} buffers to simplified models of Ca^{2+} pools (Anwar et al., 2012). Ca^{2+} dynamics were approximately equal for the low $[Ca^{2+}]_i$ described here. Furthermore, the extremely close interaction of 20 nm shown here between Cav3 and $K_{Ca}3.1$ channels may not be susceptible to the action of slow Ca^{2+} binding pro-

teins, as the interaction can only be disrupted by the rapid Ca^{2+} chelator BAPTA (**Fig. 3.9*C***).

4.4.3 Future studies

While the current study examined the interaction between short-term plasticity and the Cav3-K_{Ca}3.1 complex, long-term plasticity could also involve the K_{Ca}3.1 channel. It has been shown in Purkinje cells that downregulation of K_{Ca}2.2 channels underlies long-term potentiation of the PF synapse (Ohtsuki et al., 2012). Long-term depression is also a well-studied phenomenon in the cerebellar cortex whose role in learning is widely debated (Ito, 1989, 1990; Bloedel and Kelly, 1992; Bloedel et al., 1993; Ito, 1993; De Schutter, 1995; Lisberger, 1995; De Schutter, 1997; Steuber et al., 2007). Increased or decreased expression of the Cav3-K_{Ca}3.1 complex could conceivably affect the amplitude of individual PF EPSPs, leading to potentiation or depression of the input. Furthermore, long-term modulation of the Cav3-K_{Ca}3.1 complex could affect the sensitivity of the frequency filter, allowing for a wide range of Purkinje cell responses.

I demonstrated here that K_{Ca}3.1 becomes increasingly active throughout a synaptic input train. Therefore, this increased hyperpolarizing influence should affect the sensitivity of Purkinje cells to subsequent inputs, potentially providing a tuneable filter based upon the history of inputs arriving at the Purkinje cells (Sobel and Tank, 1994). This shifting filter could act to dynamically adjust the sensitivity of the Purkinje cell to presynaptic inputs, thus maintaining the SNR for important sensory inputs.

Short-term plasticity is not only present at the PF-Purkinje cell synapse, but also at the PF-stellate cell and stellate cell-Purkinje cell synapses (Bao et al., 2010). Feed-forward inhibition plays an important role in the cerebellar cortex (Mittmann et al., 2005). I previously showed that the Cav3-K_{Ca}3.1 complex functions in the presence of feed-forward inhibition (**Fig. 3.11*C***). Yet, the interplay between depression of feed-forward inhibition and facilitation of excitation provides yet another layer of complexity for processing synaptic inputs. Inhibition may allow for increased deinactivation of Cav3 channel during tonic firing, thus increasing the activation of K_{Ca}3.1 channels, dynamically adjusting postsynaptic filtering properties.

Chapter Five: Distinct roles for I_T and I_H in the integration of inhibitory inputs

5.1 Introduction

As the principal output neuron of cerebellar cortex, Purkinje cells need to integrate primarily excitatory synaptic input. In stark contrast, the DCN neurons that represent the primary output cell of the entire cerebellum receive primarily inhibitory input from Purkinje cells of the overlying cerebellar cortex. Integrating a set of inhibitory inputs to generate appropriate spike output poses an interesting set of problems. While an excitatory input can directly increase the response of a postsynaptic cell, achieving an increase in postsynaptic output in response to inhibitory input requires specific ion channel mechanisms. A *rebound burst*, an increase in postsynaptic firing following a period of inhibition, is the most common mechanism of transforming inhibitory inputs to a series of action potentials, but is found in relatively few cell types in the brain (Jahnsen and Llinas, 1984; Jahnsen, 1986a; Huguenard and Prince, 1992; Ulrich and Huguenard, 1997; Destexhe et al., 1998). Spike bursts are driven by a rebound depolarization that depends on the magnitude of the preceding period of inhibition (Jahnsen and Llinas, 1984; Steriade et al., 1993; Ulrich and Huguenard, 1997; Aizenman and Linden, 1999; Tadayonnejad et al., 2009; Pedroarena, 2010; Sangrey and Jaeger, 2010). The underlying rebound repolarization can provide a computational advantage by producing not only a spike burst whose frequency and duration relates to the preceding hyperpolarization, but also by regulating first spike latency (FSL) (Kepecs and Lisman, 2003; Heil, 2004; Person and Perkel, 2005; Sangrey and Jaeger, 2010) and spike precision (Person and Perkel, 2005). Yet the ion channel mechanisms that underlie the integration of inhibitory inputs and conversion to rebound responses have not been fully identified. As DCN neurons are the sole output of the cerebellum to motor and thalamic centers, understanding the mechanisms that control rebound bursts is critical to determining how the cerebellum controls motor output.

I_T and I_H have emerged as key potential contributors to the rebound response in DCN cells. Thus, direct activation of I_T at the end of a hyperpolarization has been proposed to mediate the spike frequency increase, with different rebound phenotypes

correlated to the expression of specific Cav3 channel isoforms (Molineux et al., 2006; Molineux et al., 2008). A recent study indicated that blockers of HCN channels increase the FSL of DCN cells and revealed an inverse relationship between membrane voltage and FSL that will act to control a temporal aspect of rebound firing (Sangrey and Jaeger, 2010). A rebound response or spike burst can, therefore, serve multiple roles in signal processing and circuit function, some of which may be implemented by DCN cells when integrating cerebellar cortical input. High frequency burst discharges have been shown capable of detecting the onset or features of a given stimulus (i.e. intensity), emphasizing the important potential role for I_T in DCN cell function (Cattaneo et al., 1981; Eggermont, 1998; Sherman, 2001; Kepecs et al., 2002; Oswald et al., 2004; Oswald et al., 2007). On the other hand, spike timing plays a crucial role in neural coding (Kepecs and Lisman, 2003; Heil, 2004). Since both I_T and I_H activate in the low voltage regime, the final output of a cell may reflect a complex interplay between the effects of their biophysical properties on membrane potential. Thus, the generation of a rebound depolarization and its effects on spike output may be differentially shaped by the actions of I_T vs I_H on spike latency (timing) or frequency. A key question that has not yet been examined in DCN cells is the ability to generate rebound spike output with temporal precision, a feature that would be consistent with the known temporal processing requirements of cerebellar function (Timmann et al., 1999; Zackowski et al., 2002; Jacobson et al., 2009; De Zeeuw et al., 2011).

When attempting to understand how a neuron processes synaptic inputs and the role of postsynaptic conductances in integrating inputs, it is important to examine responses using physiologically relevant stimuli. While much progress has been made in understanding DCN conductances, much of the work conducted *in vitro* has routinely incorporated steps to levels of hyperpolarization well below that expected to occur naturally. Even though DCN cells receive a massive inhibitory projection from cerebellar cortical Purkinje cells, $GABA_A$ receptor-mediated IPSPs do not extend below a value for E_{Cl} of ~-72 mV (Aizenman and Linden, 1999; Alvina et al., 2008; Zheng and Raman, 2009). In fact, the level of hyperpolarization evoked by synaptic

inputs was recently suggested to be less than that required to promote sufficient recovery of Cav3 channels from inactivation to contribute to rebound depolarizations (Alvina et al., 2008; Zheng and Raman, 2009). The reported voltage for activation of I_H in DCN cells (-90 mV) is also more negative than that expected to be reached during periods of synaptically evoked inhibition (Raman et al., 2000). These issues are magnified by the fact that Purkinje cell-evoked IPSPs in DCN cells exhibit frequency-dependent depression during repetitive stimulation (Telgkamp and Raman, 2002; Pedroarena and Schwarz, 2003), further decreasing the extent of hyperpolarization available to remove I_T inactivation and to activate I_H. The specific roles for I_T and I_H in contributing to rebound responses thus remain to be defined in the context of physiologically relevant membrane hyperpolarizations.

Due to the close interaction and overlapping voltage dependence of these channels, it is difficult to differentiate the effects of I_T and I_H on rebound bursts experimentally. As such, a computational model of DCN cells incorporating I_T and I_H would be instrumental in elucidating the mechanisms by which these currents regulate rebound bursts. A multi-compartmental model of the DCN neuron has recently been developed that is capable of reproducing DCN rebound bursts and many firing characteristics (Steuber et al., 2011). However the alternate use of a reduced model of DCN firing dynamics would allow for more accessible analysis of the role of postsynaptic conductances in controlling rebound responses.

In the work described in this chapter, we sought to fully delineate the roles for I_T and I_H in controlling rebound responses in DCN cells in relation to physiologically relevant stimuli. We first characterize the amount of I_T and I_H recruited during physiological levels of membrane hyperpolarization. We find that I_T and I_H are in fact sufficiently activated by these minimal levels of membrane hyperpolarization to contribute to rebound responses, and even exhibit distinct roles in controlling the frequency, FSL, and precision of a rebound response. Using these results, I develop a two-compartment model of the Transient Burst DCN cell that can replicate many features of DCN firing, rebound bursts and FSL. This model is used to further explore

the respective roles of I_T and I_H and reveals a novel, synergistic relationship between these currents in controlling spike output of DCN cells.

5.2 Specific Methods

5.2.1 Modelling

A two-compartment model of the DCN neuron was constructed and simulations were performed in Matlab R2007b using a fourth-order Runge-Kutta algorithm with a 0.01 ms time step (*dt*). Ion channel models followed the Hodgkin-Huxley formulism. The somatic compartment of the model included: voltage-gated Na^+ current, I_H (HCN channels), delayed rectifier K^+ current, non-specific cation current (to sustain tonic firing), and leak current. The dendritic compartment included: I_T, slow K^+ current, leak current, and synaptic conductances where applicable. I_T was placed in the dendritic compartment given work indicating that LVA Ca^{2+} fluorescence can be recorded in DCN cell dendrites (Muri and Knopfel, 1994; Gauck et al., 2001; Zhang et al., 2004; Pugh and Raman, 2008; Schneider et al., 2013), with IPSP bursts or rebound responses producing the largest Ca^{2+} transients in distal dendritic regions (Zhang et al., 2004; Pugh and Raman, 2008).

Na^+ activation

$$\frac{dm}{dt} = \frac{m_\infty - m}{\tau_m}, m_\infty = \frac{1}{1 + e^{\frac{(V+33)}{-2.8}}}, \tau_m = 0.09\ ms$$

Na^+ inactivation

$$\frac{dh}{dt} = \frac{h_\infty - h}{\tau_h}, m_\infty = \frac{1}{1 + e^{\frac{(V+40)}{2.9}}}, \tau_h = \left(\frac{464}{\pi}\left(\frac{20}{2(V+39)^2 + 20^2}\right)\right) 0.2\ ms$$

K^+ activation

$$\frac{dn}{dt} = \frac{n_\infty - n}{\tau_n}, n_\infty = \frac{1}{1 + e^{\frac{(V-20)}{-2.7}}}, \tau_n = 0.6\ ms$$

Slow K^+ activation

$$\frac{dn_d}{dt} = \frac{n_{d\infty} - n_d}{\tau_{n_d}}, n_{d\infty} = \frac{1}{1 + e^{\frac{(V+30)}{-3.5}}}, \tau_{n_d} = 25\ ms$$

I_H activation

$$\frac{dq_f}{dt} = \frac{q_{f\infty} - q_f}{\tau_{q_f}}, \frac{dq_s}{dt} = \frac{q_{s\infty} - q_s}{\tau_{q_s}}, q_\infty = \frac{1}{1 + e^{\frac{(V+92.1)}{11.4}}}, \tau_{q_f} = 20\ ms, \tau_{q_s} = 75\ ms$$

I_T activation

$$\frac{dm_t}{dt} = \frac{m_{t\infty} - m_t}{\tau_{m_t}}, m_{t\infty} = \frac{1}{1 + e^{\frac{(V+31.3)}{-4.5}}}, \tau_{m_t} = 7\ ms$$

I_T inactivation

$$\frac{dh_t}{dt} = \frac{h_{t\infty} - h_t}{\tau_{h_t}}, h_{t\infty} = \frac{1}{1 + e^{\frac{(V+63.8)}{6.9}}}, \tau_{h_t} = 37\ ms$$

Somatic voltage

$$C_s \frac{dV_s}{dt} = \frac{(V_d - V_s)}{R} + I - g_{Na} m h (V_s - E_{Na}) - g_K n (V_s - E_K) - g_{IH} q_f q_s (V_s - E_{IH}) - g_{leak_s} (V_s - E_{leak}) - g_{NaCa} (V_s - E_{NaCa})$$

Dendritic voltage

$$C_d \frac{dV_d}{dt} = \frac{(V_s - V_d)}{R} + I - g_{K_d} n_d (V_d - E_K) - g_{Ca} m_t h_t (V_d - E_{Ca}) - g_{leak_d} (V_d - E_{leak}) - g_{exc} (V_d - E_{exc}) - g_{inh} (V_d - E_{inh})$$

For all simulations, the following constants were used:

C_s= 1.5 or 3 μF/cm^2, C_d = 3 μF/cm^2, R = 1/3, g_{Na} = 58 mS/cm^2, g_K = 17.5 mS/cm^2, g_{Kd} = 25 mS/cm^2, g_{leaks} = 0.1 mS/cm^2, g_{leakd} = 0.1 mS/cm^2, g_{NaCa} = 0.05 mS/cm^2.

For simulations with I_H and/or I_T: g_{IH} = 0.8 mS/cm^2, g_{Ca} = 4.25 mS/cm^2.

Background synaptic inputs were added to the dendritic compartment and modelled as stochastic conductances using an Ornstein-Uhlenbeck process (Uhlenbeck and Ornstein, 1930):

$$\frac{dg_{syn}}{dt} = -\frac{g_{syn}}{\tau} + \sqrt{\frac{D}{\tau}}\xi(t)$$

where τ is the correlation time constant, D is the "diffusion" coefficient and ξ is a noise term (generated by Matlab's *randn()* function). To ensure no negative conductance values were used, g_{syn} was set to 0 if a negative value was detected. For inhibitory synaptic input, τ = 40 ms, D = 0.7 mS/cm^2 and E_{inh} = -77 mV. For excitatory synaptic input, τ = 20 ms, D = 0.2 mS/cm^2 and E_{exc} = 0 mV.

5.2.2 Rebound response measurements

The absolute membrane voltage attained during a hyperpolarization was measured 20 ms before the end of a current pulse or 20 ms after the last stimulus of a presynaptic stimulus train. Rebound bursts were statistically defined according to an elevation in firing frequency following a hyperpolarization that exceeded two standard deviations beyond the mean of tonic frequency determined over 1 sec immediately preceding the stimulus. This definition has been applied to both an early peak of firing frequency (< 100 ms) and a later phase of firing frequency increase (Sangrey and Jaeger, 2010; Tadayonnejad et al., 2010), but all work in the present study focused on the early phase of the rebound response. Mean burst frequencies were plotted as the maximum difference in firing frequency above initial tonic firing levels. FSL was defined as the time from the offset of a current-evoked hyperpolarizing stimulus or the final stimulus of a presynaptic train to the first spike of the rebound response, and expressed as a ratio of FSL to the mean interspike interval (ISI) of tonic firing determined over 1 sec preceding the stimulus.

5.2.3 Specifics regarding DCN recordings

To calculate gain (Hz/100 pA), the frequency response to different levels of depolarizing current injection was measured and the slope of a linear fit was determined. Ramp

depolarizations under voltage clamp designed to mimic IPSP depression during repetitive stimulation were delivered at a rate of 0.026 mV/ms.

5.3 Results

5.3.1 Inhibitory input to DCN cells

DCN cells receive massive GABAergic inhibitory input from Purkinje cells of the overlying cerebellar cortex. The output of Purkinje cells is governed by either PF or CF input that can induce brief structured patterns of firing as well as subsequent pauses in the rate of firing (McKay et al., 2007; Shin et al., 2007; Steuber et al., 2007). Purkinje cell output can thus act to inhibit DCN cells and then relieve inhibition for a sufficient period of time to allow for rebound changes in DCN cell output.

The effects of repetitive trains of Purkinje cell inhibitory input on DCN cells have been well characterized (Aizenman et al., 1998; Aizenman and Linden, 1999; Tadayonnejad et al., 2009; Hoebeek et al., 2010; Pedroarena, 2010; Sangrey and Jaeger, 2010). Depending on the synchronicity of Purkinje cell inputs (IPSP amplitude), frequency, or number of presynaptic stimuli, trains of IPSPs can be followed by a rebound increase in firing frequency (De Schutter and Steuber, 2009; Hurlock et al., 2009; Hoebeek et al., 2010; Pedroarena, 2010; Sangrey and Jaeger, 2010; Tadayonnejad et al., 2010; Bengtsson et al., 2011). Shin et al. (Shin et al., 2007) also reported that simple spike trains of Purkinje cells recorded *in vivo* can display patterns of firing, as determined by CV_2 analysis. This study revealed a relationship between the number and frequency of simple spikes that comprise a pattern, with one of the most common patterns represented by 100 Hz output for durations of up to 30 spikes (Shin et al., 2007) (their Fig. 4). Delivering 100 Hz trains of stimuli to Purkinje cell afferents *in vitro* evokes a period of GABAergic mediated inhibition that rapidly shifts membrane potential to near E_{Cl} (~-72 mV) (**Fig. 5.1*A***) (Jahnsen, 1986b; Aizenman and Linden, 1999; Zheng and Raman, 2009). IPSP amplitude then exhibits a frequency-dependent depression within the first 10 stimuli, resulting in a slow depolarizing shift in membrane potential during a stimulus train (**Fig. 5.1*A, B***) (Telgkamp and Raman, 2002; Pedroarena and Schwarz, 2003; Telgkamp et al., 2004; Pedroarena, 2010). This is important, in that full recovery of I_T

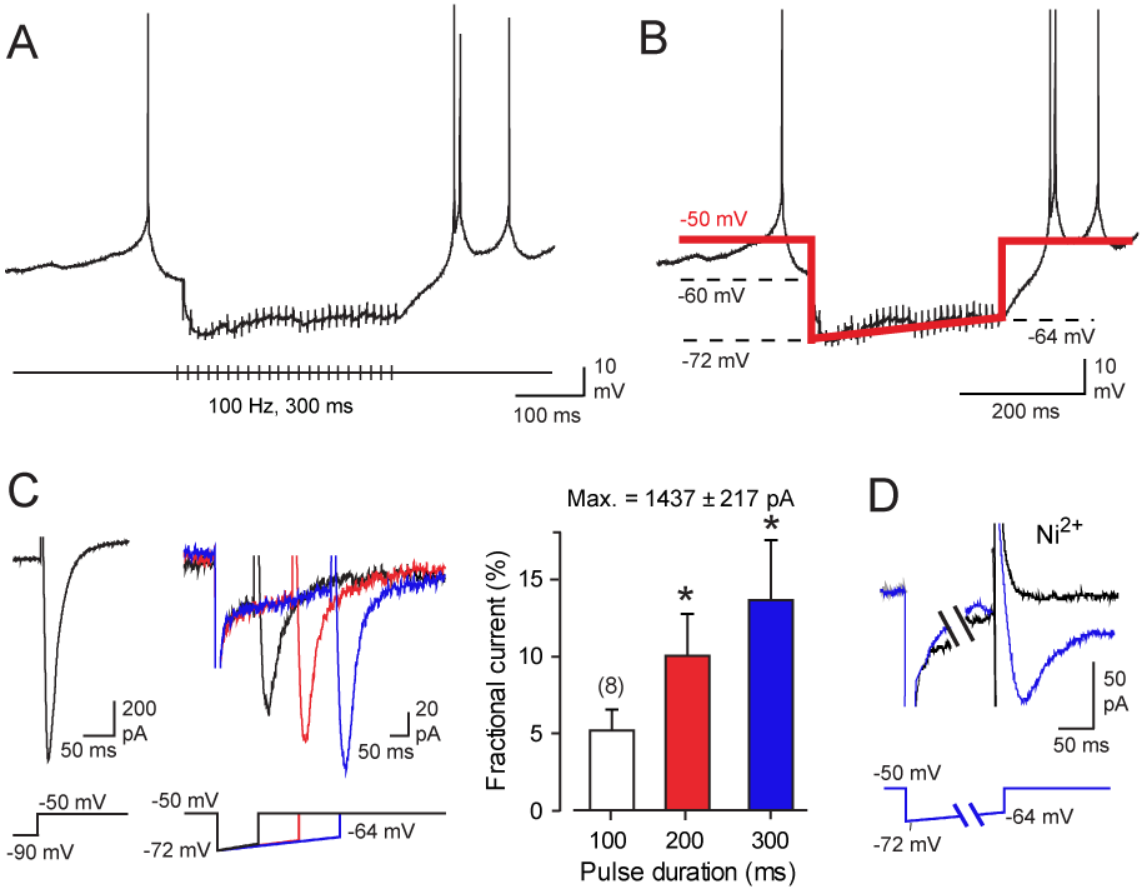
A
100 Hz, 300 ms
10 mV
100 ms
B
-50 mV
-60 mV
-72 mV
-64 mV
10 mV
200 ms
C
200 pA
50 ms
-50 mV
-90 mV
20 pA
50 ms
-50 mV
-72 mV
-64 mV
Max. = 1437 ± 217 pA
Fractional current (%)
0
5
10
15
(8)
*
*
100
200
300
Pulse duration (ms)
D
Ni2+
50 pA
50 ms
-50 mV
-64 mV
-72 mV

Figure 5.1: Physiological hyperpolarizations are capable of eliciting I_T in DCN neurons

(A, B) An representative trace from a Transient Burst DCN neuron during 100 Hz stimulation (300 ms) shows that physiological stimulation causes a maximal hyperpolarization to -72 mV that gradually depolarizes to -64 mV during the stimulus train. A voltage command consisting of a ramp from -72 mV to -64 mV and repolarization to -50 mV reproduces the important voltage features of this stimulus. **(C)** When the voltage command is provided to a DCN neuron where I_T has been isolated pharmacologically, a transient inward current is measured following repolarization. The amplitude of the inward current is directly related to the duration of the ramp. **(D)** Application of Ni^{2+} (300 μM) completely abolishes the inward current. Experiments and analysis performed by D Anderson and R Tadayonnejad.

from inactivation and the reactivation of I_H are both voltage- and time-dependent (Raman et al., 2000; Perez-Reyes, 2003; Iftinca et al., 2006; Biel et al., 2009; Zheng and Raman, 2009) and thus require a minimal level and duration of membrane hyperpolarization. The role for I_T or I_H in generating a rebound response is thus questionable given that the relatively small shift in membrane potential induced by IPSPs (from ~-60 mV to -72 mV) may not substantially increase current availability (Iftinca et al., 2006; Zheng and Raman, 2009). Depression of the IPSP during repetitive stimulation also introduces a gradual depolarizing shift in membrane potential that will further inactivate any I_T that does become available, and will deactivate I_H. Thus, consideration of the hyperpolarization present during an input train needs to include the extent of IPSP depression. The duration of a hyperpolarizing stimulus is also important, in that the magnitude of a rebound response increases in relation to the duration of a hyperpolarizing current pulse or the number of presynaptic stimuli, even in the presence of a progressive decrease in IPSP amplitude during a stimulus train (Aizenman and Linden, 1999; De Schutter and Steuber, 2009; Pedroarena, 2010; Sangrey and Jaeger, 2010). Therefore, we chose 100-300 ms as representative durations for hyperpolarizing stimuli that we could relate to the patterns of Purkinje cell firing described by Shin et al. (Shin et al., 2007), invoked either as a 100 Hz train of 10-30 synaptic stimuli or as varying durations of voltage or current commands.

We have previously identified two rebound burst phenotypes in DCN cells, termed Transient and Weak Burst cells. These different phenotypes have been shown to reflect differences in the magnitude of at least I_T (Molineux et al., 2006; Molineux et al., 2008; Hurlock et al., 2009; Tadayonnejad et al., 2009; Tadayonnejad et al., 2010). While we have examined the differences in synaptic input and currents between these cell types, in this chapter, we will limit our discussion to Transient Burst cells unless otherwise indicated. However, the values of Weak and Transient Burst cells were combined in some experiments and we have indicated values that reflect these combined populations.

Under our stimulus conditions, IPSP amplitude cells began to depress within 20 - 30 ms of the beginning of the stimulus train and decreased to a similar and relatively stable value of ~-64 ± 0.42 mV mV by 30 stimuli (n = 18). These values are consistent with previous studies of the depression of Purkinje cell synapses (Telgkamp and Raman, 2002;

Pedroarena and Schwarz, 2003). With these parameters, we could then move to presenting a voltage clamp protocol that reproduced these voltage changes postsynaptically to test for the ability to evoke I_T or I_H.

5.3.2 I_T and I_H are activated by physiologically relevant membrane hyperpolarizations

To best control the postsynaptic voltage that determines ion channel availability, we used whole-cell voltage clamp to simulate membrane hyperpolarizations at physiological temperatures (32-34 ºC). In each case we first established the total I_T available by stepping from -90 mV to -50 mV (**Fig. 5.1*C***). The magnitude of I_T available for activation had a mean value of 1437 ± 217 pA (n = 8) in Transient Burst cells, corresponding with previous studies showing a large amount of I_T in these cells (Molineux et al., 2006; Molineux et al., 2008; Tadayonnejad et al., 2010). Step-ramp commands were then used under voltage clamp to simulate the onset and subsequent depression of IPSPs that occurs during a 30 pulse 100 Hz train of Purkinje cell input. To increase the degree of inactivation of I_T expected during resting conditions, we set the holding potential at -50 mV, a value just below spike threshold in DCN cells (threshold of -47.4 ± 0.65 mV, n = 14). The step-ramp command consisted of a step from -50 mV to -72 mV followed by a slow ramp depolarization that rose to a total value of -64 mV over 300 ms (**Fig. 5.1*B***).

We found that in the presence of 2 mM Cs^+ to block I_H and 30 µM Cd^{2+} to block HVA Ca^{2+} channels, a fast activating and fast inactivating inward current consistently followed step-ramp commands (n = 8) (**Fig. 5.1*C***), evoking 10 - 140 pA of inward current even following a 100 ms stimulus. The magnitude of inward current evoked then increased with the duration of the ramp command despite the steady depolarization mimicking IPSP depression, reaching values of 50 - 500 pA at 300 ms (n = 8, one-way repeated measures ANOVA) (**Fig. 5.1*C***). Finally, perfusion of 300 µM Ni^{2+} as a Cav3 Ca^{2+} channel blocker in DCN cells (Molineux et al., 2008) eliminated the fast inactivating current (n = 3, **Fig. 5.1*D***).

We note that the step-ramp protocol used here is not a perfect mimic of the hyperpolarization associated with a train of IPSPs. Apart from being applied only at the soma, it does not include the last depolarizing shift that characterizes the return of mem-

brane potential at the end of an IPSP train to the resting state (**Fig. 5.1*A,B***). However, under voltage clamp we are constrained by the need to eliminate capacitance transients with an immediate step back to the resting level in order to isolate the ionic currents. The currents obtained with this approach can thus be expected to represent the maximum current available at the end of the hyperpolarizing stimulus, with potential for some loss of I_T through inactivation during the return to rest. With these limitations in mind, the currents evoked by step-ramp commands represented only a small fraction of the total current available in each cell (**Fig. 5.1*C***). Thus, for a 100 ms step-ramp command, the evoked current reflected a small fraction of the total current available, representing only ~5% for 100 ms and ~14% for 300 ms. Notably, this range of I_T availability is within that previously reported for DCN cells following steady-state voltage commands to near E_{Cl} for 500 ms (Zheng and Raman, 2009). We also found that the availability of I_T was highly sensitive to preconditioning and test potentials in the physiological range. For instance, little current was recorded if membrane potential was not first stepped close to E_{Cl} or was returned at the end of a step-ramp command to only -60 mV (data not shown); both results are consistent with the known steep relationship for inactivation and activation curves for Cav3 channels (Perez-Reyes, 2003; Molineux et al., 2005; Iftinca et al., 2006). Finally, given that Ca^{2+} channels underlying the rebound response are thought to be preferentially distributed to dendritic membranes of DCN cells (Muri and Knopfel, 1994; Gauck et al., 2001; Zhang et al., 2004; Pugh and Raman, 2008), we expect that the magnitude of I_T recorded here may underestimate the true effectiveness of a train of IPSPs that synapse in dendritic regions (Aizenman and Linden, 1999).

To determine the extent to which I_H can be activated by physiologically relevant hyperpolarizations, we repeated the above tests to examine the properties of Cs^+-sensitive current at 32-34 ºC. The conditions required to isolate I_H prevented us from first identifying Transient and Weak Burst cell phenotypes, but we did not detect any differences in the amount of Cs^+-sensitive current between cells. The V_a for specific isoforms of HCN channels can also be altered by cyclic nucleotide binding (Biel et al., 2009), but we found no difference in voltage-dependence for recordings made with or without ATP added to the pipette (n = 6 with ATP, n = 8 without ATP, $P > 0.05$). For these reasons all data on

I_H were combined, and expected to reflect the activity of both Transient and Weak Burst cells. To first examine steady-state properties and the maximum I_H available, voltage commands of 1.5 sec were delivered from a holding potential of -50 mV in -10 mV steps to -140 mV and 2 mM Cs^+ perfused to calculate Cs^+-sensitive currents by subtracting test from control responses (**Fig. 5.2*A*, *B***). These recordings revealed a Cs^+-sensitive inward current that was slow activating and non-inactivating, reaching a steady-state peak within ~1 sec of stimulus onset (**Fig. 5.2*A***). Initial activation of whole-cell current was detected at ~-60 mV, with activation increasing with membrane hyperpolarization to a stable peak by ~-140 mV (V_a = -92.1 ± 2.4, n = 14) (**Fig. 5.2*A*, *B***). Of specific potential relevance to rebound responses was an inward tail current of up to 1 nA (upon return from -140 mV) at the end of command steps that deactivated over 500 ms (**Fig. 5.2*A***).

To more directly test the ability for physiological stimuli to activate I_H, we delivered the step-ramp commands that simulate hyperpolarizations induced by 100 Hz trains of IPSPs (100 - 300 ms). These tests also revealed the slow activation of an inward current of 4 -15 pA that was detectable even during 100 ms stimuli as a slowly activating inward current (n = 8, **Fig. 5.2*C***). The end of a 100 ms pulse was followed by an inward tail current of up to 12 pA, that for a 300 ms stimulus could be detected for up to 300 ms. Furthermore, the amplitude of tail currents significantly increased for step-ramp commands between 100 and 300 ms despite the slow ramp depolarization that would be predicted to deactivate I_H (**Fig. 5.2*C*,** one-way repeated measures ANOVA). Comparison of these values to those evoked at steady state (**Fig. 5.2*A***) indicated that the I_H evoked by step-ramp commands was at a level corresponding to ≤ 20% of the maximum I_H available for activation (**Fig. 5.2*C***).

5.3.3 I_T and I_H have distinct roles in controlling rebound responses

It is known that increasing the magnitude or duration of hyperpolarizations will increase the rebound response of DCN cells (Aizenman and Linden, 1999; Tadayonnejad et al., 2009; Hoebeek et al., 2010; Pedroarena, 2010; Sangrey and Jaeger, 2010; Bengtsson et al., 2011). Yet given that the magnitudes of I_T and I_H activated by physiological stimuli represent only a small fraction of the maximum current available, it raises questions as to

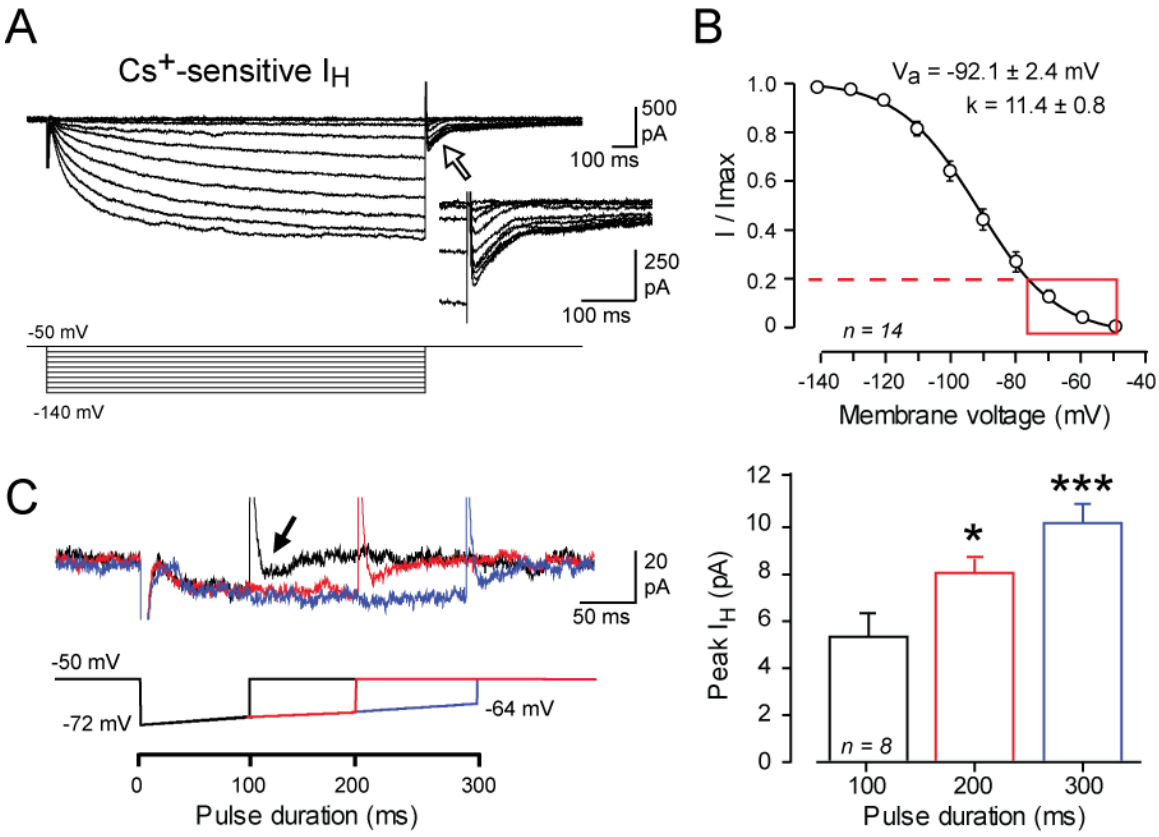
A
Cs+-sensitive IH
500 pA
100 ms
250 pA
100 ms
-50 mV
-140 mV
B
Va = -92.1 ± 2.4 mV
k = 11.4 ± 0.8
I / Imax
n = 14
Membrane voltage (mV)
C
20 pA
50 ms
-50 mV
-72 mV
-64 mV
Pulse duration (ms)
Peak IH (pA)
n = 8
Pulse duration (ms)

Figure 5.2: Physiological levels of hyperpolarization are capable of activating I_H. **(A)** HCN channels were isolated in DCN neurons and a set of hyperpolarizing steps were applied to activate I_H. Cs^+ was bath applied to block I_H and the Cs^+-sensitive currents were examined to determine the voltage dependence of HCN channels in DCN neurons. A slow activating inward current was observed and a significant, long-lasting tail current (*inset*) could be seen. **(B)** The activation curve for I_H shows that HCN channels show up to 20% activation for physiological hyperpolarizations. **(C)** Application of the ramp command shows a small inward tail current upon repolarization (*arrow*) that increases with increasing duration. Experiments and analysis performed by D Anderson.

their potential role in modifying rebound spike output (Zheng and Raman, 2009). We thus tested the role of I_T and I_H in modifying the rebound response following modest current pulse injections of up to 300 ms. In this regard, previous studies emphasize that the voltage- and time-dependence of I_T and I_H dictate that even small differences in the absolute voltage during a preconditioning pulse can substantially change current availability (Aizenman and Linden, 1999; Tadayonnejad et al., 2009; Zheng and Raman, 2009; Sangrey and Jaeger, 2010; Steuber et al., 2011). The profile of I_H activation presents a further issue when comparing a hyperpolarizing response at different time points, since I_H introduces a depolarizing sag that will continually change the membrane voltage over time (Aizenman and Linden, 1999; Raman et al., 2000). Since the depolarizing sag stabilized by 150 - 200 ms after the onset of a current pulse, we adjusted the level of hyperpolarizing current injection to generate a constant membrane voltage shift to -72 mV by 300 ms, providing an equivalent response from which to compare rebounds between cells.

A resting level of tonic spike discharge was first established by adjusting bias current injection to set the peak trough of spike AHPs to ~-60 mV, and a hyperpolarizing current pulse was delivered. We found that hyperpolarization to -72 mV was sufficient to induce a statistically defined increase in rebound firing frequency in all cells examined (**Fig. 5.3**). Burst frequency attained a maximum of 397 Hz following a 300 ms prepulse (**Fig. 5.3*A*, *B***) (expressed as increases in frequency above the initial tonic firing level). To test the roles for I_T and I_H in the rebound response, we perfused Ni^{2+} (300 μM) or Cs^+ (2 mM) (**Fig. 5.3*A*, *B***). We found that Ni^{2+} significantly reduced, but did not completely block, rebound increases in firing frequency, with an average reduction after a 300 ms pulse of 47.6 ± 10.5% (n = 8, $p < 0.05$) (**Fig. 5.3*A*, *C***). It is important to consider that Ni^{2+} will also block Cav2.3 channels (Randall and Tsien, 1997), which are also fast inactivating. However, we found that pressure ejections of the Cav2.3 channel blocker SNX-482 (200 nM) had no effect on the early phase of rebound frequency (data not shown; n = 7). Bath application of Cs^+ (2 mM) also significantly reduced rebound frequency by 45.9 ± 16.3 % (n = 8, $p < 0.05$) (**Fig. 5.3*B*, *C***). These data revealed that rebound frequency increases in Transient Burst cells result from a combination of I_T and I_H.

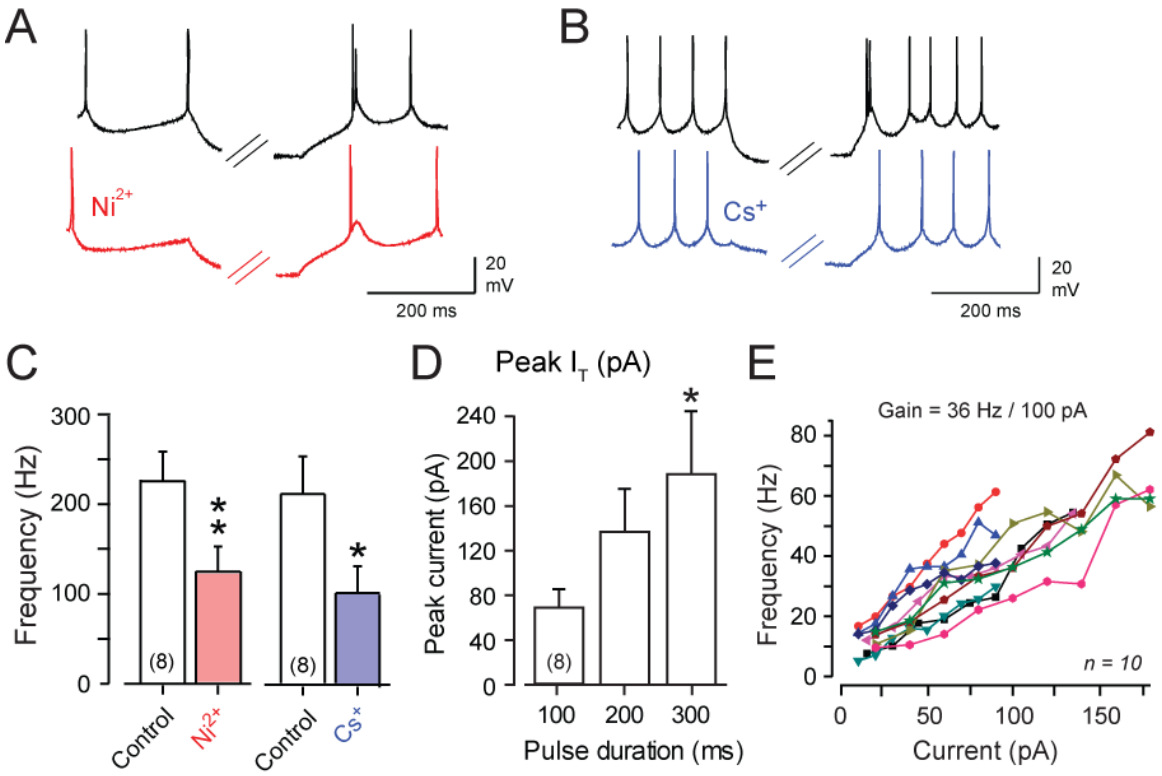
A
Ni2+
20 mV
200 ms
B
Cs+
20 mV
200 ms
C
Frequency (Hz)
300
200
100
0
(8)
(8)
Control
Ni2+
Control
Cs+
D
Peak IT (pA)
Peak current (pA)
240
200
160
120
80
40
0
(8)
100
200
300
Pulse duration (ms)
E
Gain = 36 Hz / 100 pA
Frequency (Hz)
80
60
40
20
0
n = 10
0
50
100
150
Current (pA)

Figure 5.3: Rebound burst is controlled by both I_T and I_H

(A) Representative Transient Burst cell rebound responses immediately following 300 ms hyperpolarizing steps to ~-72 mV, and the effects of perfusing Ni^{2+} (**A**, 300 μM; red traces) or Cs^{+} (**B**, 2 mM, blue traces). **(C)** Bar plots of the average effects of Ni^{2+} or Cs^{+} on rebound frequency in Transient cells indicate a substantial, but incomplete, reduction of rebound frequency increases by either blocker. **(D)** A comparison between the absolute values of peak IT recorded in the step-ramp commands of **Figure 5.1C** to the gain of firing as measured in frequency-current (F-I) plots. The F-I plots of **(D)** were calculated from a separate population of cells in response to depolarizing current pulses from a resting level of -60 mV and data from 10 cells are plotted superimposed for comparison. Rebound frequencies in **(D)** are plotted as frequency increases above the level of tonic firing frequency preceding the stimulus for the immediate phase of the rebound response. Sample numbers for mean values in bar plots are shown in brackets. Experiments performed by R Tadayonnejad and data analysis performed by J Engbers and R Tadayonnejad.

We next considered the ability for I_T to contribute to rebound bursts evoked by direct stimulation of Purkinje cell inhibitory inputs. At most central synapses, transmitter release from presynaptic terminals is mediated by one or more HVA Ca^{2+} channels (particularly Cav2.x channels) (Evans and Zamponi, 2006; Kisilevsky and Zamponi, 2008). However, earlier work suggested that transmitter release at inhibitory synapses in cerebellum incorporates Ca^{2+} channels that do not fit the pharmacological profile for HVA Ca^{2+} channels (Doroshenko et al., 1997). Previous work has also reported modulation of synaptic function at the Purkinje to DCN cell synapse by I_H (Saitow et al., 2009). It was therefore important to determine if presynaptic function at the Purkinje cell synapse would be affected by blockers of Cav3 or HCN channels. **Figure 5.4** shows the results of blocking Cav3 Ca^{2+} or HCN channels on IPSCs evoked at 60% of the maximal intensity in DCN cells in the presence of glutamate receptor blockers. Surprisingly, the Cav3 channel blockers Ni^{2+} (300 μM, $n = 6$) and mibefradil (1 μM, $n = 6$) both substantially reduced the amplitude of evoked IPSCs (**Fig. 5.4*A***). In contrast, the Cav2.3 channel blocker SNX-482 had no effect (200 nM, $n = 3$) (**Fig. 5.4*B***), indicating that the effects of Ni^{2+} and mibefradil on the IPSC were not mediated through R-type Ca^{2+} channels. Interestingly, a reduction of the IPSC was also obtained with the putatively selective HCN channel blocker ZD-7228 (40 μM, $n = 6$) but not Cs^+ (2 mM, $n = 6$) (**Fig. 5.4*C***). Since ZD-7228 has also been reported to block Cav3 Ca^{2+} channels (Sanchez-Alonso et al., 2008), these results are consistent with a role for Cav3 but not HCN channels in contributing to GABA release at the Purkinje-to-DCN cell synapse.

Given these results, it was not possible to directly assess the contribution of I_T to rebound frequencies generated following trains of synaptic input. We previously found a high correlation between the maximal amount of I_T recorded in DCN cells and the rebound frequencies generated from preconditioning pulses to -90 mV (Molineux et al., 2008). We thus examined whether the amount of I_T recorded in response to step-ramp commands under voltage clamp (see **Fig. 5.1*C***) could be predicted to increase the firing frequency following a train of inhibitory input. The mean values of I_T recorded following 100 - 300 ms commands under voltage clamp revealed currents less than ~250 pA for Transient Burst cells (**Fig. 5.3*D***). Although these are relatively small currents in absolute

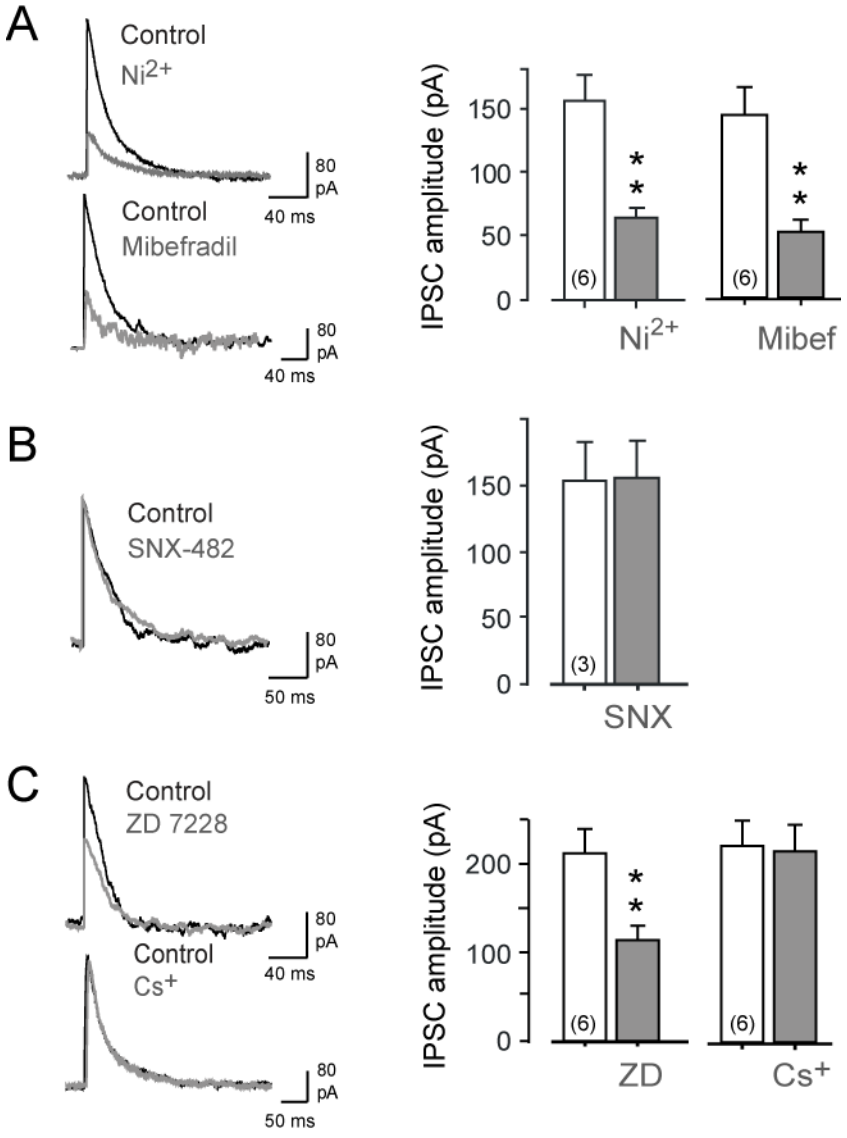
A
Control
Ni2+
80 pA
40 ms
Control
Mibefradil
80 pA
40 ms
IPSC amplitude (pA)
150
100
50
0
**
(6)
(6)
Ni2+
Mibef
B
Control
SNX-482
80 pA
50 ms
IPSC amplitude (pA)
150
100
50
0
(3)
SNX
C
Control
ZD 7228
80 pA
40 ms
Control
Cs+
80 pA
50 ms
IPSC amplitude (pA)
200
100
0
**
(6)
(6)
ZD
Cs+

Figure 5.4: Purkinje cell IPSCs are sensitive to Cav3 channel blockers

Shown on the *left* are representative and superimposed recordings of the effects of Ca^{2+} or HCN channel blockers on evoked IPSCs. Bar plots of drug effects on mean IPSC amplitudes are shown on the *right*. Stimulus intensities were set to ~60% of that required to evoke a maximal IPSC. **(A)** Perfusion of Ni^{2+} (300 μM) or mibefradil (1 μM) significantly reduces the amplitude of the evoked IPSC. **(B)**, Focal ejection of SNX-482 (200 nM) has no effect on IPSCs. **(C)** Perfusion of ZD-7228 (40 μM) significantly reduces IPSC amplitude while Cs^{+} (2 mM) has no effect. Sample numbers for mean values in bar plots are shown in brackets. Experiments performed by R Tadayonnejad.

magnitude, they may well be relevant in the context of the gain of firing frequency in DCN cells (Raman et al., 2000). We examined frequency-current (F-I) plots and found a high gain of firing in response to depolarizing current injections (**Fig. 5.3*E***). Specifically, Transient Burst cells exhibited a gain of 36 ± 2.8 Hz / 100 pA (n = 10). A comparison of the peak values of I_T generated by step-ramp commands to these steep F-I relations predict that even a small amount of I_T could have a measureable effect on rebound firing frequency (**Fig. 5.3*D, E***). Thus, despite substantial inactivation of I_T near resting potential (Zheng and Raman, 2009), a physiologically relevant membrane hyperpolarization can promote sufficient recovery from inactivation as to generate I_T capable of contributing to increases in rebound frequency in DCN cells. The effects of ~12 pA of I_H recorded following a 100 ms step-ramp hyperpolarization (**Fig. 5.2**) is also predicted to increase rebound frequency, although the influence of this current proves to be more complex (considered in further detail below).

5.3.4 I_H mediated reductions in FSL

It has been shown that synaptically evoked periods of inhibition produce a graded change in the latency to rebound firing in DCN cells (Tadayonnejad et al., 2009; Pedroarena, 2010; Sangrey and Jaeger, 2010), and that applying Cs^+ to block I_H increases FSL, revealing a new role for I_H (Sangrey and Jaeger, 2010). Since the resident level of tonic firing in a DCN cell will establish a given ISI at rest, distinguishing an actual change from this value following a hyperpolarizing stimulus requires that one normalize the measure of FSL to preceding tonic activity. Thus to identify a change in FSL, we expressed the latency to rebound as a ratio of FSL to the ISI of preceding tonic spike discharge. In this way a genuine reduction in FSL is indicated by a decrease in the FSL/ISI ratio, while an increase in FSL compared to the tonic firing ISI is indicated by an increase in the FSL/ISI ratio. We found that following a hyperpolarizing stimulus of -72 mV for 300 ms, the FSL/ISI ratio was 0.39 ± 0.05 (n = 8).

To determine if the FSL/ISI ratio depends on the duration of presynaptic spike trains (as has been reported for thalamic neurons (Person and Perkel, 2005)), we delivered 5 - 30 pulse 100 Hz repetitive stimulus trains to Purkinje cell afferents. Stimulus intensity was adjusted to evoke ~60% of the maximal IPSC in each cell (**Fig. 5.5*A***). As

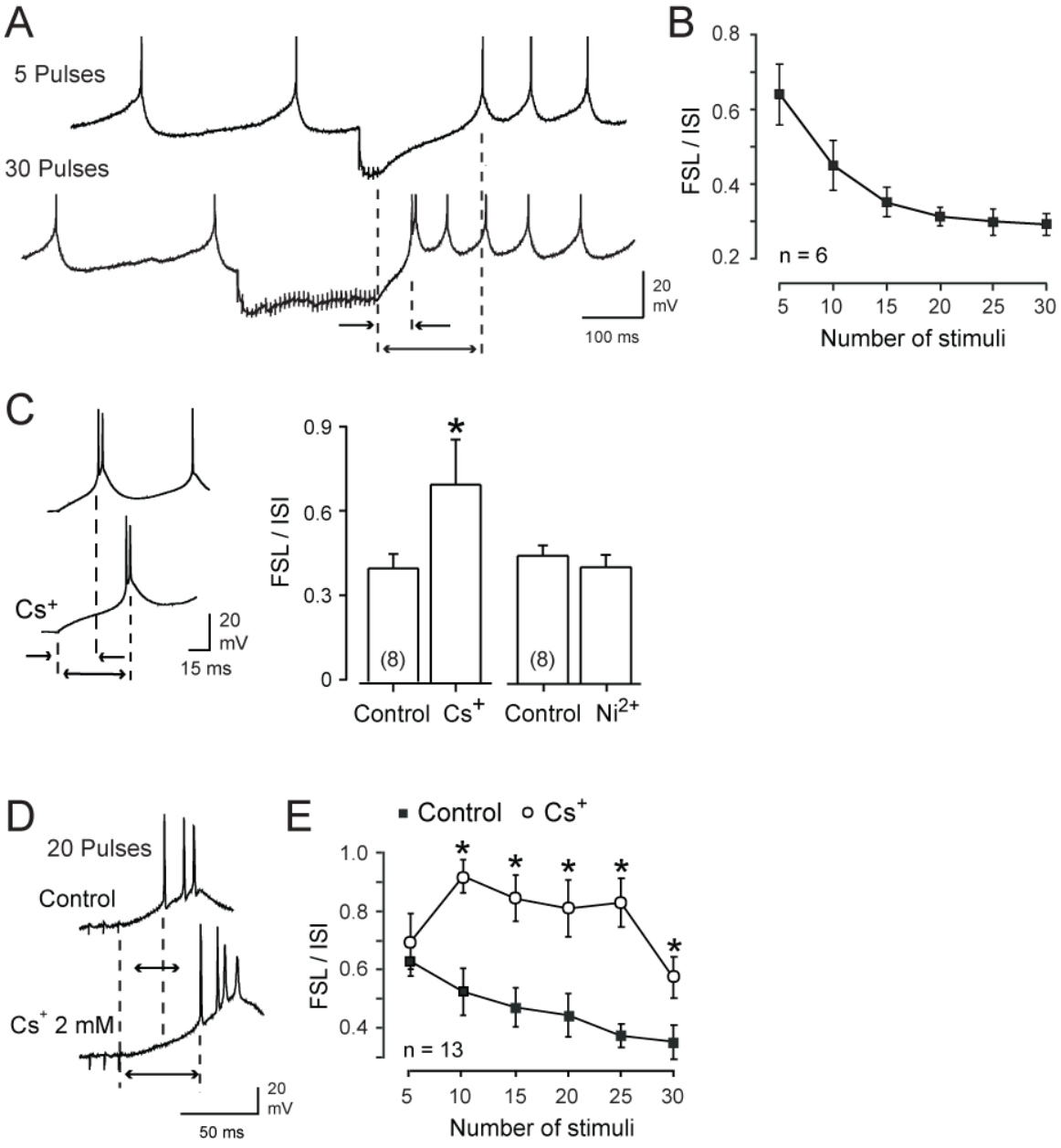
A
5 Pulses
30 Pulses
20 mV
100 ms
B
FSL / ISI
0.8
0.6
0.4
0.2
n = 6
5 10 15 20 25 30
Number of stimuli
C
Cs+
20 mV
15 ms
FSL / ISI
0.9
0.6
0.3
0
*
(8)
(8)
Control Cs+ Control Ni2+
D
20 Pulses
Control
Cs+ 2 mM
20 mV
50 ms
E
Control Cs+
FSL / ISI
1.0
0.8
0.6
0.4
*
n = 13
5 10 15 20 25 30
Number of stimuli

Figure 5.5: I_H but not I_T underlies a graded shift in FSL following physiologically relevant hyperpolarizations

(A) Representative recordings of the change in FSL following 100 Hz trains of either 5 or 30 IPSPs evoked by stimulating Purkinje cell afferents (60% of maximal intensity). Dashed lines indicate the FSL as measured from the end of a stimulus train to the first spike of the rebound response, indicating a substantial reduction in FSL with more repetitive stimuli. **(B)** Mean values of the FSL/ISI ratio in response to varying numbers of stimuli delivered to Purkinje cell afferents at 100 Hz reveal a decrease in FSL/ISI with increasing numbers of stimuli. **(C)** Representative recordings of rebound responses (*left*) following a current-evoked membrane hyperpolarization to -72 mV (300 ms) reveal an increase in FSL with external Cs^+ (2 mM). Bar plots of the FSL/ISI ratio following 300 ms hyperpolarizations to -72 mV are shown at *right* before and after perfusion of Cs^+ (2 mM) or Ni^{2+} (300 μM). **(D)** Recordings of the rebound response following a 100 Hz 20 pulse train of IPSPs showing an increase in FSL upon perfusion of Cs^+ (2 mM). **(E)** A plot of the mean FSL/ISI for evoked trains of IPSPs and its block by perfusion of Cs^+ (2 mM). Transient and Weak Burst cell data are combined in **(E)**. Sample numbers for mean values in bar plots of **(C)** are shown in brackets. Experiments performed by R Tadayonnejad. Data analysis performed by J Engbers and R Tadayonnejad.

found for current-evoked hyperpolarizations, the FSL/ISI ratio following a 5 pulse inhibitory stimulus train was 0.63 ± 0.06 (n = 6) (**Fig. 5.5*B***). Increasing the number of stimuli produced a graded reduction in the FSL/ISI ratio with the number of stimuli (**Fig. 5.5*B***). Thus, 30 stimuli reduced the FSL/ISI ratio from that following 5 stimuli by 43.3 ± 11.45 % to a value of 0.35 ± 0.05 (n = 13, Transient and Weak Burst cells combined) (**Fig. 5.5*B***). We further verified that these values did not reflect any dialysis under whole-cell conditions, as the range of FSL/ISI for this intensity and stimulus numbers were equivalent under on-cell recording conditions (*data not shown*).

Since both I_H and I_T generate inward currents it is possible that both could reduce FSL following periods of inhibition. When we applied Cs^+ (2 mM) to cells preconditioned with a hyperpolarizing current pulse to -72 mV for 300 ms, the FSL/ISI ratio increased by 67.9 ± 13.23 % (n = 8) (**Fig. 5.5*C***). However, perfusion of Ni^{2+} (300 μM) to cells undergoing the same level of preconditioning had no significant effect on the FSL/ISI ratio (**Fig. 5.5*C***). These tests are important in establishing that I_H and I_T, two currents that increase in availability with hyperpolarization, contribute to distinct aspects of rebound firing in DCN cells.

We next examined the effects of blocking I_H on the FSL/ISI ratio invoked by repetitive presynaptic stimuli. Perfusing Cs^+ (2 mM) confirmed a role for I_H in regulating the FSL following 100 Hz trains of synaptically evoked inhibition, as indicated by a significant increase in the FSL/ISI ratio of the rebound response (**Fig. 5.5*D*, *E***). Interestingly, the effects of Cs^+ were prominent for 10 stimuli or greater, as would be predicted for a gradual activation of I_H during an inhibitory stimulus (**Fig. 5.5*E***).

5.3.5 Modelling delineates roles for I_H and I_T during rebound responses

The results to this point indicate distinct roles for I_H and I_T in controlling some aspects of rebound responses (i.e. FSL) but synergistic roles for others (i.e. frequency). I_T recordings presented here in response to physiological levels of hyperpolarization demonstrate the availability of significant amounts of I_T during the rebound depolarization (**Fig. 5.1*C, D***). By comparison, voltage clamp recordings of I_H and measurements of I_H-dependent shifts in FSL indicated that a much smaller amount of I_H is available upon repolarization (**Fig. 5.2**). Yet, Cs^+ proved to block almost 50% of the rebound frequency

increase (**Fig. 5.3*C***). The ability for I_H to increase rebound frequency may then indicate an interplay with the properties of I_T and its influence on spike frequency.

A more complete understanding of the factors underlying these results is difficult to obtain through recordings and pharmacological block, since any effects on membrane resistance and time constant can make it difficult to definitively identify the role of each current. To gain a better understanding of the effects of each current on rebound responses, I developed a reduced model of the DCN neuron to test hypotheses arising from slice experiments. A two-compartment model was sufficient to reproduce many important spike features of DCN neurons, including the DAP, AHPs, rebound bursting and a graded FSL **(Fig. 5.6**). The dendritic compartment contained conductances for leak, a slow K^+ current, and I_T where applicable. As a full voltage clamp analysis of I_T has not yet been reported for DCN cells, I used parameters for activation and inactivation kinetics of I_T from a previous study in Purkinje cells (Hildebrand et al., 2009). The somatic compartment had fast Na^+, fast K^+, leak, and HCN conductances (see **Section 5.2**). The activation curve for I_H determined in the voltage clamp experiments in **Figure 5.2** was used and time constants for current activation were chosen to generate currents with similar kinetics. Holding current was adjusted to sustain a tonic spike firing rate of 10 Hz. To determine the effect of HCN and Cav3 conductances on rebound bursts, I_H and I_T were either included or omitted from the model and FSL/ISI and burst frequency was measured in response to a wide range of hyperpolarization depths (8 increments to a final voltage of -77 mV at 300 ms) and durations (50 – 300 ms; 50 ms increments) (**Fig. 5.6**). Burst frequency was measured as the peak frequency within the initial 100 ms of the spike response following release from hyperpolarization.

5.3.5.1 I_T and I_H in FSL and rebound frequency:

Analysis of the rebound bursts produced by different combinations of conductance again revealed distinct roles for I_H and I_T in controlling FSL and rebound frequency increases. When I_H was present in the model, longer and deeper hyperpolarizations generated shorter FSL/ISI ratios (**Fig. 5.6*A*, *B***). However, when only I_T was present (**Fig. 5.6*C***), or when both I_T and I_H were removed (**Fig. 5.6*D***), stronger hyperpolarizations generated a progressively longer FSL, as predicted for a shift in FSL determined

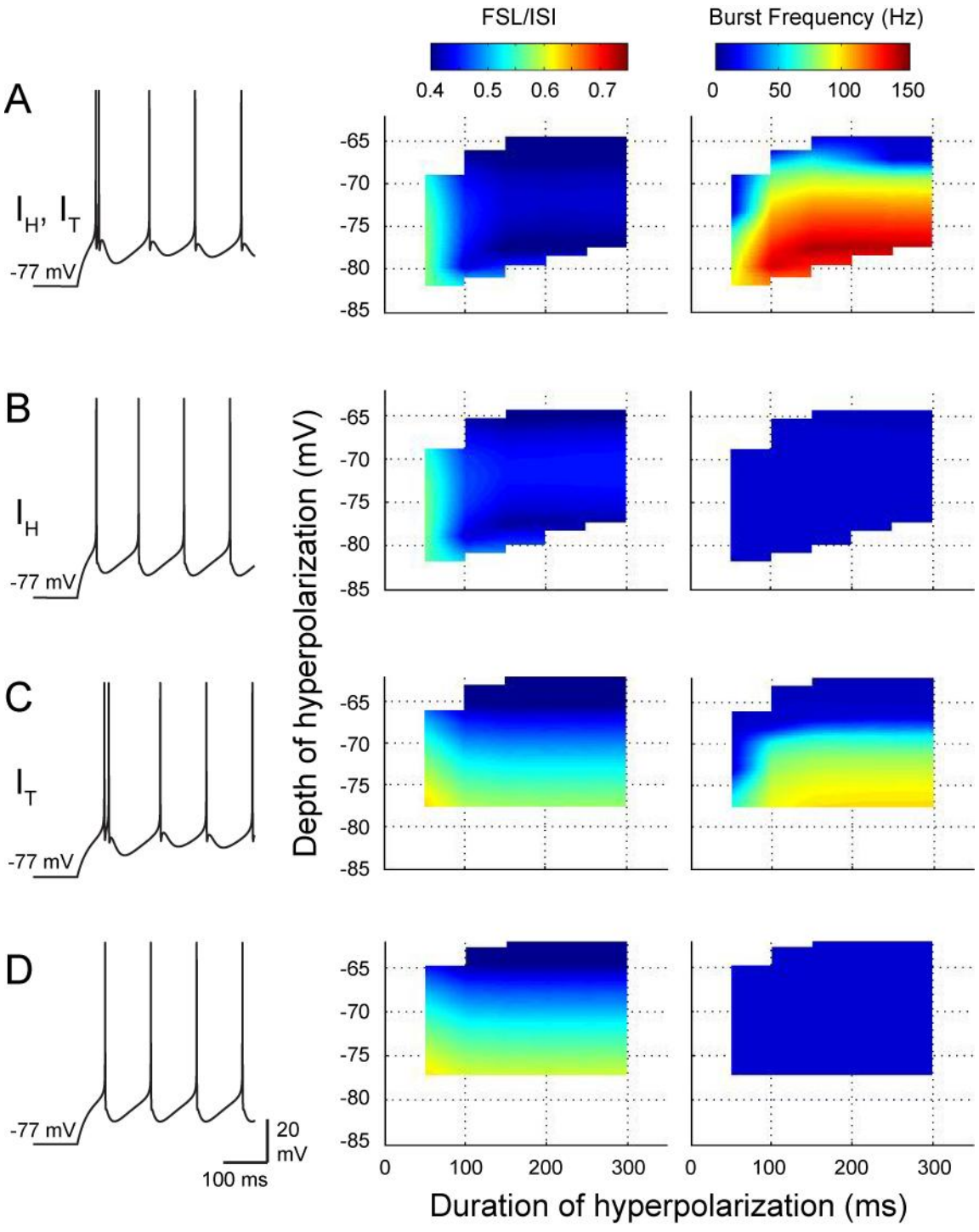
FSL/ISI
0.4 0.5 0.6 0.7
Burst Frequency (Hz)
0 50 100 150
A
I_H, I_T
-77 mV
B
I_H
-77 mV
C
I_T
-77 mV
D
-77 mV
20 mV
100 ms
Depth of hyperpolarization (mV)
-65 -70 -75 -80 -85
0 100 200 300
Duration of hyperpolarization (ms)

Figure 5.6: A reduced model reveals distinct functions for I_T and I_H in the rebound response

(A-D), Simulations were performed using two-compartment models containing different combinations of I_T and I_H, with representative spike output indicated by records at *left*. Three dimensional plots on the *right* compare FSL/ISI and burst frequency between models for various depths and durations of a preceding hyperpolarization. Note that as the magnitude or duration of a preceding hyperpolarization increases, the FSL/ISI progressively shortens and burst frequency increases in a model that contains both I_T and I_H **(A)**. Removing I_T **(B)** blocks rebound burst frequency increases without affecting FSL. Removing I_H **(C)** substantially alters the FSL profile but also reduces burst frequency. Removing both I_T and I_H **(D)** retains the same FSL profile as I_T alone in **(C)** but entirely removes any increase in rebound frequency. Model created and simulations performed by J Engbers.

primarily by the time constant and return of membrane potential to spike threshold from a hyperpolarized state. These results then confirmed the lack of influence of I_T on FSL and the unique role I_H has in controlling FSL following a hyperpolarization.

In contrast, a rebound increase in spike frequency could only be generated in the model in the presence of I_T (**Fig. 5.6*A, C***). Interestingly, when both I_H and I_T were present, burst frequencies of up to 146 Hz were produced (**Fig. 5.6*A***). But when only I_T was included in the model, the peak rebound frequency dropped by 30.83% to 101 Hz (**Fig. 5.6*C***). This result was consistent with those shown in **Figure 5.3*C***, where application of Cs^+ reduced rebound frequency. However, no burst was seen when only I_H was present (**Fig. 5.6*B***), suggesting that the decrease in rebound frequency observed upon removing I_H does not reflect a direct contribution by I_H to burst generation, but rather a secondary effect that increases the efficacy of I_T.

5.3.5.2 Synergy in actions of I_H and I_T in rebound spike responses

Blocking I_H had significant effects on membrane resistance and time constant in *in vitro* current clamp recordings. Likewise, the omission of I_H from the model increased the membrane time constant. I hypothesized that by decreasing the membrane time constant, I_H decreases the inactivation of I_T during the rebound burst, allowing for greater burst frequency. To test this, a new model ($DCN_{lowC,IT}$) was generated without I_H but with a lower somatic capacitance (from 3 $\mu F/cm^2$ to 1.5 $\mu F/cm^2$) to retain a similar time constant to the model containing both I_T and I_H ($DCN_{IH,IT}$) (**Fig. 5.7*A***), allowing me to distinguish the effects of time constant from the voltage dependence and activation kinetics of I_H.

My simulations showed that reducing membrane capacitance ($DCN_{lowC,IT}$ model) enabled high frequency bursts similar to a model with I_H and I_T intact ($DCN_{IH,IT}$ model) (**Fig. 5.7*B, C***), but was unable to reproduce the membrane voltage-FSL relationship normally generated by I_H (**Figs. 5.6*A, B* and 5.7*D***). These results indicate that I_H enhances the ability of I_T to generate rebound bursts, but does not directly contribute to the rebound burst. To further determine why a change in time constant affects burst frequency, I examined the inactivation variable for I_T at the voltage threshold of the second spike in the burst (**Fig. 5.7*E***). At the time of the second spike, the model with I_T alone (DCN_{IT}) showed more inactivation than models that included either I_H ($DCN_{IH,IT}$) or lower somatic

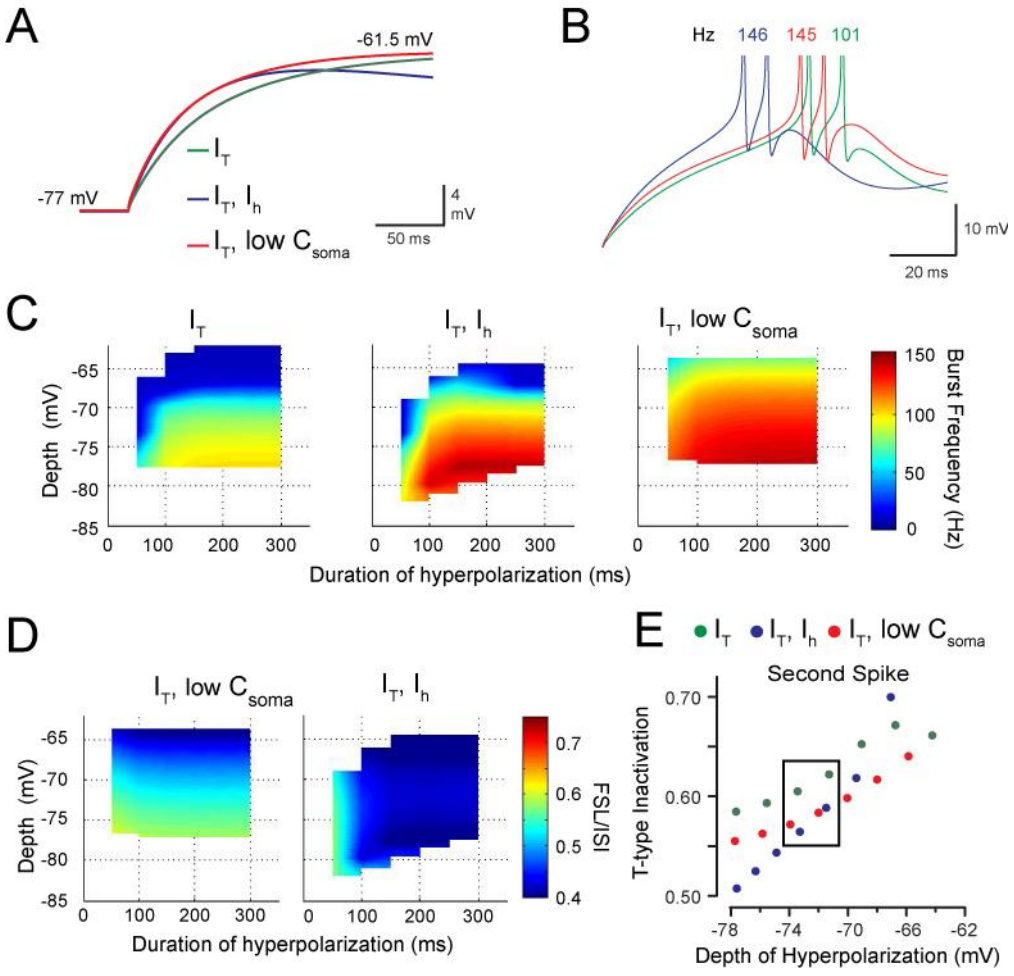
A
-61.5 mV
-77 mV
I_T
I_T, I_h
I_T, low C_{soma}
4 mV
50 ms
B
Hz 146 145 101
10 mV
20 ms
C
I_T
I_T, I_h
I_T, low C_{soma}
Depth (mV)
-65
-70
-75
-80
-85
0 100 200 300
Duration of hyperpolarization (ms)
150
100
50
0
Burst Frequency (Hz)
D
I_T, low C_{soma}
I_T, I_h
Depth (mV)
Duration of hyperpolarization (ms)
0.7
0.6
0.5
0.4
FSL/ISI
E
I_T I_T, I_h I_T, low C_{soma}
Second Spike
T-type Inactivation
0.70
0.60
0.50
-78 -74 -70 -66 -62
Depth of Hyperpolarization (mV)

Figure 5.7: The effect of I_H on time constant acts synergistically with I_T to increase rebound burst frequency

(A) An expanded view of the charging profiles of the model during repolarization from -77 mV shown superimposed for the indicated model parameters. I_T was held constant while somatic membrane capacitance was lowered in a model lacking I_H (low C_{soma}, *red trace*) until the membrane time constant was similar to a model that contains I_H (*blue trace*). **(B)** Overlays of rebound bursts from each of the models in (**A)** to compare the effects of substituting I_H with a reduction in membrane capacitance. In the absence of I_H, a decrease in capacitance ($DCN_{lowC,IT}$ model, *red trace*) increases burst frequency and decreases FSL compared to models containing I_T alone (DCN_{IT} model, *green trace*). The model containing I_H and I_T ($DCN_{IH,IT}$ model, *blue trace*) still exhibits a shorter FSL than $DCN_{lowC,IT}$, but similar burst frequency, indicating that the effect of I_H on burst frequency is due to a reduction in time constant. (**C)** Three dimensional plots compare the relationship between burst frequency and hyperpolarization depth and duration for DCN_{IT} (*left*) and $DCN_{IH,IT}$ (*center*) models to the $DCN_{lowC,IT}$ model (*right*). Data for DCN_{IT} and $DCN_{IH,IT}$ are reproduced from **Fig. 6** for comparison. Note that $DCN_{IH,IT}$ and $DCN_{lowC,IT}$ reach the same peak frequency of 150 Hz, which is significantly higher than the rebound frequency of DCN_{IT}. These results demonstrate that a reduction in time constant increases burst frequency in the absence of I_H. **(D)** The voltage-FSL relationship for $DCN_{lowC,IT}$ does not exhibit the same inverse relationship with hyperpolarization depth and duration as $DCN_{IH,IT}$ ($DCN_{IH,IT}$ data reproduced from **Fig. 6** for comparison), indicating that the voltage dependence and kinetics of I_H are required to decrease FSL in response to strong hyperpolarization. **(E)** A comparison of the amount of I_T inactivation during the rebound (at the onset of the second spike of the rebound response) between the three models shows that $DCN_{lowC,IT}$ and $DCN_{IH,IT}$ exhibit less T-type current inactivation than DCN_{IT}. For hyperpolarization near E_{Cl} (-72 mV *in vitro*, *black box*), $DCN_{lowC,IT}$ and $DCN_{IH,IT}$ exhibit similar levels of T-type channel inactivation, emphasizing the importance of membrane time constant on the degree of I_T inactivation during the rebound burst. Model created and simulations performed by J Engbers.

capacitance ($DCN_{lowC,IT}$) for all voltages less than -70 mV (**Fig. 5.7*E***). Furthermore, for hyperpolarizations near E_{Cl} (~-72 mV), $DCN_{IH,IT}$ and $DCN_{lowC,IT}$ displayed similar levels of T-type inactivation (**Fig. 5.7*E***, *black box*). However, for voltages positive to -70 mV, $DCN_{LowC,IT}$ had less T-type inactivation than $DCN_{IH,IT}$, consistent with a voltage-dependent activation of I_H. For depolarized voltages, I_H is deactivated and T-type inactivation approaches DCN_{IT}. However, in $DCN_{LowC,IT}$ where somatic capacitance is lowered globally, there is a global frequency increase and lower I_T inactivation over all voltages. Shortening the membrane time constant thus decreases the extent of T-type inactivation during the first ISI of the rebound response, allowing I_T to generate higher rebound frequencies. Furthermore, a general decrease in time constant will increase the effectiveness of transient currents by increasing the rate of voltage change while the current is reaching its peak. Therefore, the activation of I_H during hyperpolarization results in a decrease in time constant during repolarization, decreasing inactivation of I_T during repolarization and allowing I_T to be more effective at driving depolarization and action potentials.

5.3.5.3 I_H increases precision of FSL

The ability for central neurons to integrate inhibitory and excitatory synaptic input and produce consistent spike output (spike precision) is critical for the proper operation of neuronal networks. DCN neurons are innervated by a multitude of inhibitory as well as excitatory synapses, each of which are capable of providing independent inputs to the cell (Gauck and Jaeger, 2000, 2003; Uusisaari and De Schutter, 2011). Furthermore, DCN neurons have been shown to respond with a high degree of precision to synaptic input (Gauck and Jaeger, 2000, 2003). I wished to examine the role of I_H in controlling the precision of spike output in the presence of noisy synaptic input. Excitatory and inhibitory synaptic conductances were added to the model and conductance values were varied using an Ornstein-Uhlenbeck noise process (see Methods). For each model (DCN_{IT}, $DCN_{IH,IT}$, and $DCN_{lowC,IT}$), 100 simulations with noisy synaptic conductances were performed. Holding current was adjusted to provide a mean tonic firing frequency of 10 Hz prior to presenting a hyperpolarization to -75 mV for 300 msec. The population of first spike latencies was then measured to assess the precision of rebound spike output (**Fig. 5.8*A***).

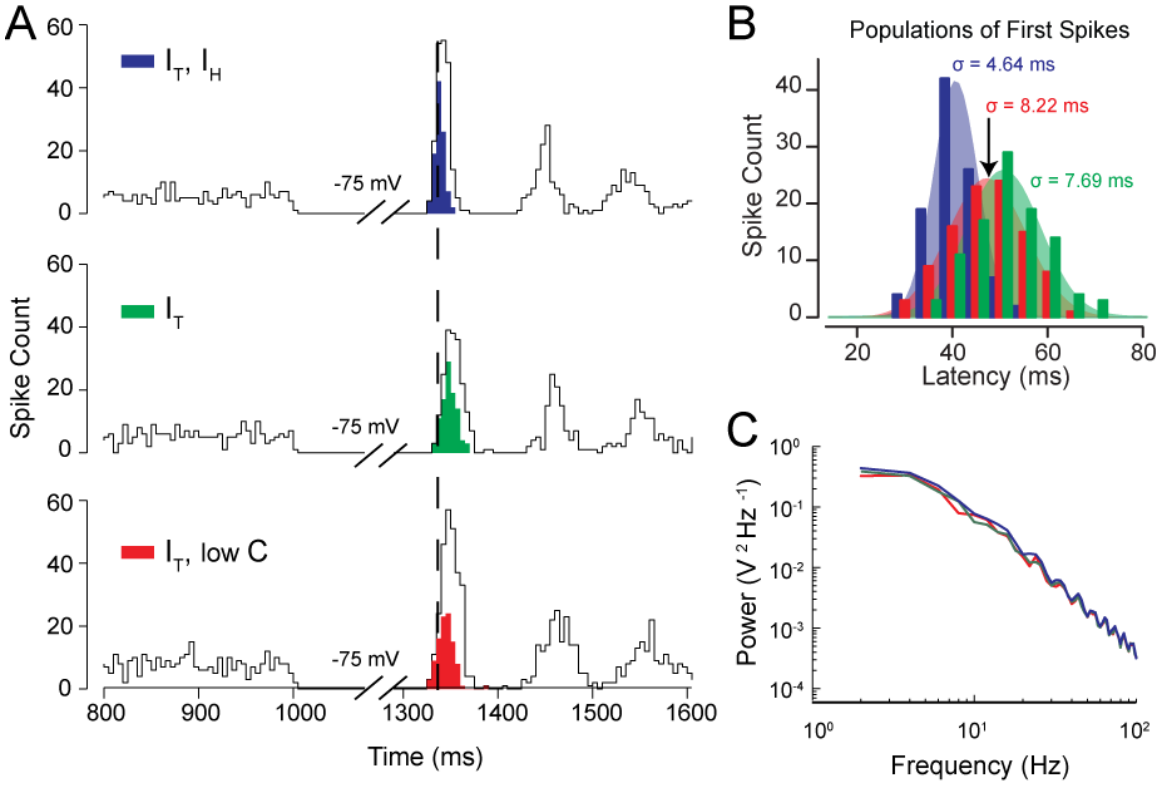
A
B
C
Spike Count
Time (ms)
I_T, I_H
I_T
I_T, low C
-75 mV
Populations of First Spikes
σ = 4.64 ms
σ = 8.22 ms
σ = 7.69 ms
Latency (ms)
Power (V^2 Hz^{-1})
Frequency (Hz)

Figure 5.8: I_H controls the precision of the first spike following a hyperpolarization **(A)** Histograms of spike count in three different models for 100 simulations with stochastic excitatory and inhibitory synaptic conductances to measure the relative timing (latency) and precision (standard deviation) of the population of first spikes generated following a hyperpolarizing stimulus. Open bins denote the total spike count, while the first spike (following release from inhibition) of each of the 100 simulations in the population of rebound responses are denoted by filled bins. Simulations had a baseline firing rate of 10 Hz for 1000 ms preceding a hyperpolarization to -75 mV for 300 ms (the full extent of the preceding 1000 ms stimulus was truncated for display purposes). The mean latency and standard deviation of FSL between three models incorporating the indicated combinations of I_T, I_H or low capacitance (low C) indicate that I_H has an effect on both the timing and precision of the population of first spikes. **(B)** Gaussian fits of the population of first spikes for each model shown in **(A)** demonstrates that when I_H is present (*blue*), FSL falls over a narrow distribution and with small standard deviation (depicted by the breadth of overlying coloured Gaussian fits) compared to either the model lacking I_H (*green*) or the low capacitance model (*red*). **(C)** A comparison of the power spectral density for a 10 sec simulation at -75 mV for each of the three models shows that there is no significant difference in the frequency content of membrane fluctuations between the models that could account for the difference in spike precision in **(A)** and **(B)**. Model created and simulations performed by J Engbers.

$DCN_{IH,IT}$ had the shortest mean FSL (40.67 ± 0.08 ms) whereas DCN_{IT} produced the longest mean FSL of 50.72 ± 0.37 ms (**Fig. 5.8*A*, *B***). Finally, $DCN_{lowC,IT}$ produced a mean latency of 47.22 ± 0.18 ms. When each of the first spike populations were fit with a Gaussian distribution, the spike population recorded from simulations in the $DCN_{IH,IT}$ model showed the most precision, as measured by the standard deviation of FSL (σ = 4.64 ms), whereas FSL was more variable for both $DCN_{lowC,IT}$ (σ = 8.22 ms) and DCN_{IT} (σ = 7.69 ms) models (**Fig. 5.8*B***). I confirmed that these differences in spike precision were not due to differences in the frequency content of membrane fluctuations by examining the power spectral density of simulations performed using the same noise parameters while the model was held at -75 mV. No differences in the power spectral density were observed between the three models (**Fig. 5.8*C***). Furthermore, the amplitudes of membrane fluctuations in each model were similar (SD: $DCN_{IH,IT}$ = 1.30 mV; DCN_{IT} = 1.38 mV; $DCN_{lowC,IT}$ = 1.56 mV), indicating that the observed increase in precision was due to the presence of I_H. These results thus demonstrate that I_H increases the precision of the first rebound spike through a decrease in membrane time constant rather than a direct depolarizing effect of I_H.

5.4 Discussion

The ability for membrane hyperpolarizations to trigger a rebound increase in spike frequency in DCN cells has been of long standing interest in the field of cerebellar physiology. Extensive work *in vitro* has implicated I_T and I_H as primary contributing factors in controlling the frequency and latency of rebound responses. However, experimental protocols used to test these currents in the past have raised questions as to whether Purkinje cell-evoked GABAergic IPSPs are sufficient to allow I_T and I_H to provide meaningful contributions to rebound responses. The experiment results shown in this chapter indicate that hyperpolarizations relevant to inhibitory synaptic input (-72 mV) indeed evoke sufficient recovery of I_T from inactivation and activation of I_H to allow these currents to contribute to the immediate phase of rebound responses. Moreover, I developed a model using physiological I_T and I_H kinetics that is capable of reproducing the roles of I_T and I_H in rebound frequency and latency. Using the model, I found that I_T and I_H have distinct roles in controlling rebound fre-

quency, FSL and spike precision, and yet are complementary, as I_H acts to increase the effectiveness of I_T.

5.4.1 Role of I_T in rebound responses

The primary issue regarding a role for I_T in rebound responses is that DCN cells intrinsically generate a tonic spike output that is expected to inactivate a substantial portion of Cav3 channels. As inhibitory synaptic inputs provide only a small hyperpolarizing shift (from ~-60 to -72 mV) it may not be sufficient to recover enough Cav3 channels from inactivation to contribute to rebounds (Iftinca et al., 2006; Zheng and Raman, 2009). Here, we reassessed the contribution of I_T to rebound responses using hyperpolarizations no greater than the established reversal of evoked IPSPs (-72 mV). These tests confirmed that I_T exhibits detectable recovery from inactivation even during 100 ms hyperpolarizations, and somewhat surprisingly, continue to increase in magnitude over a 300 ms test pulse despite a simulated depression of IPSP amplitude. Nevertheless, the final level of I_T recovery from inactivation represented less than ~18% of the maximal current available to a given cell (**Figs. 5.1*C***). This value is slightly higher than that reported by Zheng and Raman (Zheng and Raman, 2009) who came to an estimate of 9.3% availability of I_T in mouse DCN cells for similar voltage shifts. However, it is possible that both values underestimate the total current available in the region of dendritic inhibitory synapses where Cav3 channels have been proposed to be localized (Aizenman and Linden, 1999; Gauck et al., 2001; Pugh and Raman, 2006; Schneider et al., 2013). Given the high gain of firing in DCN cells, we predict that even a small change in I_T availability will be physiologically relevant to rebound responses. Indeed, a contribution by I_T to rebound frequency was supported by application of a Cav3 channel blocker during current-evoked hyperpolarizations to -72 mV, or removal of I_T from a model of DCN cells (**Figs. 5.3*A, C*** and **5.6*B, D***). It is important to note that we never obtained a complete block of the rebound spike frequency increase, with only ~50% reduction in rebound frequency upon block of I_T. This could reflect the incomplete block of I_T *in situ*, as 300 μM Ni^{2+} is just above the reported IC_{50} for expressed Cav3.1 and Cav3.3 Ca^{2+} channels (Lee et al., 1999). On the other hand, it may indicate that the immediate phase of

a rebound response must incorporate additional factors beyond I_T as an excitatory influence. Our own assessment revealed an additional influence of I_H on rebound frequency (considered further below), while the work by the groups of Raman and Jaeger (Zheng and Raman, 2009; Sangrey and Jaeger, 2010; Zheng and Raman, 2011) has implicated a rapid recruitment of HVA Ca^{2+} channels. Thus at this time we can state that I_T represents a primary, but not exclusive, ionic factor responsible for generating the increase in spike frequency during the immediate phase of a rebound response in DCN cells.

5.4.2 Role of I_H in rebound responses

The potential expression of I_H in DCN cells was recognized in some of the first intracellular recordings *in vitro* (Jahnsen, 1986b; Aizenman and Linden, 1999). Initial voltage clamp work in dissociated DCN cells indicated partial activation of I_H at ~-90 mV and only ~3 pA at -58 mV, a value that would seem to be outside a required degree of activation (Raman et al., 2000). However, recent work using blockers of I_H in the slice preparation reported a novel role for this current in driving a graded reduction in FSL as hyperpolarizations were increased (Sangrey and Jaeger, 2010). Consistent with this, the whole-cell voltage clamp analysis presented here conducted on intact DCN cells at physiological temperatures revealed a voltage dependence that encompassed the range of membrane potentials relevant to inhibitory inputs. Thus, under these conditions, I_H was detectable at ~ -60 mV, with the end of a step command followed by an inward tail current with a duration relevant to the time frame of rebound responses. I_H was also detected during the initial 100 ms of the more subtle step-ramp command, along with a tail current at the end of the pulse. Moreover, the magnitude of I_H continued to increase over 300 ms despite an expected deactivation of I_H during the depolarization of the ramp command, a similar result to I_T. The absolute values of I_H evoked by these stimuli were again small, ranging from ~5-10 pA over 100-300 ms (only ~20% of the total current available in a given cell). However, a series of tests incorporating current clamp recordings and modelling confirmed that I_H is activated in response to physiological stimuli and contributes to three different aspects of rebound responses: spike frequency increases, FSL, and spike precision.

5.4.2.1 I_H and rebound spike frequency increases

While some studies of DCN cells show variable expression of I_H and even recordings that putatively lack I_H, I_H was expressed in all cells examined here. While our results confirmed the role of I_H in controlling spike latency, I_H also had a significant effect on the frequency of rebound discharge in Transient Burst cells. Selective modulation of membrane parameters in DCN cell models illustrated that the effect of I_H on spike frequency can be accounted for by its influence on the membrane time constant (**Figs. 5.6, 5.7**). Specifically, a reduction of the time constant by I_H decreases the extent of I_T inactivation that can occur during the first ISI of the burst, maintaining I_T during the burst (**Fig. 5.7*E***). Although we can not entirely rule out a contribution by the I_H tail current to the rebound depolarization, at this time the effect on time constant is sufficient to account for our results. I_H thus acts synergistically with I_T to increase rebound frequency by at least 60% of the total response, experimentally. As short-term facilitation and depression are known to be highly frequency dependent (Dittman et al., 2000), the ability for I_H to increase the range of frequencies generated during rebound responses (compare **Fig. 5.6*A*** and **5.6*C***) could have important physiological consequences at downstream postsynaptic targets of DCN cells (Babalyan and Fanardzhyan, 1991).

A potential interaction between I_H and I_T has been considered in other cell types, but with different end results. In cortical layer III pyramidal cells, HCN1 channels colocalize with Cav3.2 channels in the presynaptic terminals of glutamatergic inputs, but act to increase Cav3 inactivation by depolarizing the terminal (Huang et al., 2011). Similar effects of I_H increasing I_T inactivation have been reported for dendrites of hippocampal CA1 pyramidal neurons (Tsay et al., 2007). However, here we show that the effect of I_H on membrane time constant instead enhances rebound frequency in DCN cells by decreasing the extent I_T inactivation (**Fig. 5.7*E***).

5.4.2.2 I_H role in FSL

Consideration of FSL in DCN cells is important in that these cells receive primarily inhibitory input and thus must respond to a period of disinhibition (i.e. a pause in the firing rate of Purkinje cells) with spike output within a minimal period of time.

The timing of the first spike in a burst can also carry the most information about stimulus features and thus convey key information to downstream neurons (Kepecs and Lisman, 2003; Oswald et al., 2004; Oswald et al., 2007). Here, we demonstrated that I_H controls FSL of the rebound in DCN neurons, a finding that was confirmed recently by similar study (Sangrey and Jaeger, 2010), and in response to physiologically relevant levels of stimuli.

It is important to note that an increase in I_H acts to *decrease* FSL, creating an inverse relationship between voltage and FSL. We have encountered a similar influence of I_H on FSL in cerebellar Purkinje cells (ML Molineux, unpublished observations), and an inverse voltage-FSL relationship has been reported in thalamic and some auditory neurons (Heil, 2004; Person and Perkel, 2005), indicating that I_H may subserve this function in many different cell types. Interestingly, the nature of I_H control over FSL is opposite to that encountered in cells that express transient A-type potassium currents, in which FSL *increases* directly with the extent of hyperpolarization (Shibata et al., 2000; Heil, 2004; Molineux et al., 2005). The computational necessities that require opposite forms of control over FSL through expression of either I_H or I_A are uncertain at this time. However, given that DCN cells must transpose the magnitude of an inhibitory input to an excitatory output, an inverse voltage-FSL relationship produced by I_H may serve to translate a larger inhibitory stimulus to spike output with a shorter delay. In the cerebellum, the control that I_H exerts over FSL could also have implications for stimulus training. For example, conditioned and unconditioned stimuli during eyeblink conditioning must be separated by at least 100 ms for training to occur (Schneiderman and Gormezano, 1964; Smith, 1968; Ohyama et al., 2003). By shortening the time needed for a DCN neuron to generate a rebound burst, I_H may decrease the minimum stimulus interval required for conditioning. It would be interesting to determine whether animal models lacking I_H exhibit a longer minimum stimulus interval during training.

5.4.2.3 I_H role in spike precision

In previous studies, DCN neurons have been shown to respond to a given pattern of synaptic input with high temporal precision from one presentation to the next,

particularly during periods of disinhibition (Gauck and Jaeger, 2000). My work with the DCN model now indicates that I_H acts to increase the temporal precision of the first spike of the rebound, resulting in a highly reproducible response to membrane hyperpolarizations. Furthermore, this increase in precision is due to the direct depolarizing effects of I_H, rather than the indirect effects observed on rebound frequency brought about through a change in time constant. By increasing the ability for DCN neurons to respond in a stereotyped manner to the same input, I_H may then act to ensure the fidelity of cerebellar computations that require high temporal precision (D'Angelo and De Zeeuw, 2009; De Zeeuw et al., 2011). Interestingly, I_H has also been shown to increase temporal precision of rebound bursts in hippocampal CA1 pyramidal neurons (Orban et al., 2006; Gastrein et al., 2011) and cortical layer V pyramidal neurons (Kole et al., 2006), indicating a physiological action relevant to many other cell types.

5.4.2.4 Remaining factors

The current study reveals that I_T and I_H make distinct contributions to a rebound response, but also that neither can fully account for the immediate increase in rebound frequency. It is thus important to recognize that these are only two of the potential factors that contribute to the early phase of rebound responses examined here (Molineux et al., 2008; Pedroarena, 2010; Sangrey and Jaeger, 2010; Tadayonnejad et al., 2010). For instance, we previously described differences in the ionic basis and extent of K^+-mediated AHPs between Transient and Weak Burst phenotypes (Molineux et al., 2008; Tadayonnejad et al., 2010). Zheng and Raman (Zheng and Raman, 2009) described a decrease in the level of $[Ca^{2+}]_i$ during membrane hyperpolarizations that may temporarily reduce the availability of Ca^{2+} to drive spike-associated AHPs during the rebound, and thus increase rebound spike frequency. Recent work proposed an additional contribution by persistent Na^+ current to the rebound depolarization (Sangrey and Jaeger, 2010). Although no evidence has yet been reported in DCN cells, an interesting possibility is a potential depolarizing shift in E_{Cl} during repetitive inputs (Staley et al., 1995), providing an additional depolarizing influence. Related to this could be the potential influence of a GABA-mediated con-

ductance change and the time required for transmitter reuptake and related recovery from a train of IPSPs. At this time it is difficult to predict how this might contribute and over what time frame, but the potential exists for a synaptically evoked conductance change to modify the membrane time constant and thus rebound frequency.

Of particular importance when considering the response of DCN cells to inhibition is the synchrony of Purkinje cell inputs that would be required to generate sustained inhibition. As shown in Shin et al (Shin et al., 2007), high frequency simple spike firing in Purkinje cells is most often grouped into long and regular firing patterns. I have already demonstrated that the Cav3-K_{Ca}3.1 complex in Purkinje cells acts to emphasize high frequency PF input indicative of sensory signals (**Chapter 4**). It is then feasible that populations of Purkinje cells would respond in similar manners to sensory signals and generate these regular patterns simultaneously. Indeed, paired recordings of Purkinje cells show that 35% of simple spikes are synchronized between cells located < 100 μm apart, and this percentage of synchronization is expected to be present in the converging population of Purkinje cells onto a DCN neuron (Shin and De Schutter, 2006). A greater degree of synchronization is also observed for short ISIs, likely due to firing rate co-modulation (Shin and De Schutter, 2006). As the longest regular patterns generated by Purkinje cells are comprised of short ISIs, a sufficient proportion of Purkinje cell inputs may synchronize for 100 – 300 ms to produce a level of inhibition capable of invoking the contributions of I_T and I_H shown here.

It is expected that at least HVA Ca^{2+} channels will contribute to the late phase of the rebound (Zheng and Raman, 2009), a component of the DCN cell response to hyperpolarization that has received little attention to date. It is even possible that the early phase of rebound could be influenced by HVA Ca^{2+} channels, activated either directly or subsequent to a low threshold Ca^{2+} spike (Zheng and Raman, 2009). A new study reported the existence of a nifedipine-sensitive, non-inactivating (L-type) Ca^{2+} current in DCN cells which contributes to the late phase of a rebound frequency increase and is potentiated by mGluR receptor activation (Zheng and Raman, 2011). It should be noted that this L-type current is distinct from the currents studied here in

that 5 μM nifedipine does not block the T-type mediated LVA Ca^{2+} spike underlying the initial component of a rebound response (Molineux et al., 2006). Nevertheless, the finding of a novel contribution by a HVA Ca^{2+} current to the generation of rebound responses emphasizes the complexity of ionic factors that may contribute to DCN cell output.

Finally, the current study was restricted to examining the patterns inherent to simple spike firing recorded in Purkinje cells of anesthetized rats (Shin et al., 2007). Work *in vivo* suggests that detectable rebound responses in DCN cells are even more effectively evoked using the intraburst frequencies typical of Purkinje cell complex spike responses (Hoebeek et al., 2010; Bengtsson et al., 2011). By using 100 Hz stimulation and considering the effects of IPSP depression during more prolonged input durations, the current study essentially tested the minimal stimulus that might influence I_T and I_H activation. Inhibitory input from Purkinje cells evoked by complex spike discharge may then be even more effective in recruiting I_T and I_H contributions to rebound responses, particularly given a greater predicted degree of synchronization (Shin and De Schutter, 2006). The difficulty of predicting how different spike trains will contribute to rebound responses *in vivo* emphasizes the need for future work to consider the output of DCN cells in response to Purkinje cell spike trains inherent to awake and unanesthetized animals.

Chapter Six: Discussion

This thesis explored several mechanisms by which postsynaptic ion channels control synaptic integration. Neurons contain several layers of interacting nonlinearities which allow them to perform complex computations such as discrimination and decision making. One of those layers is the complement of ion channels expressed in the membrane. Complex voltage-dependent relationships and temporal dynamics allow voltage-gated ion channels to contribute significantly to information processing, with each channel subtype performing distinct roles. While HVA Ca^{2+} channels are activated during action potentials, LVA Cav3 channels provide Ca^{2+} signals in the subthreshold voltage range. While K_{Ca} channels act to decrease summation of EPSPs, HCN channels increase the neuronal output following trains of IPSPs. The body of work I presented here demonstrates several new roles and interactions for these ion channels, particularly centered around Cav3 channels. I showed that Cav3 channels perform a different role in synaptic integration than HVA Ca^{2+} channels by controlling the summation of subthreshold inputs through a novel interaction with $K_{Ca}3.1$ channels. Furthermore, a synergistic relationship between Cav3 and HCN channels allows for the generation of high-frequency rebound bursts with high temporal precision following inhibition. These results reveal a general role of Cav3 channels in synaptic processing that is likely to be present throughout the nervous system.

In **Chapter 3**, I demonstrated that cerebellar Purkinje cells express $K_{Ca}3.1$ channels, the first evidence for $K_{Ca}3.1$ expression in central neurons. $K_{Ca}3.1$ channels are selectively coupled to Cav3 channels and are activated during even small subthreshold PF EPSPs. While previous work has demonstrated linkages between K_{Ca} and HVA Ca^{2+} channels (Turner et al., 2011), this is the first demonstration of a Cav3-K_{Ca} complex. The Cav3-$K_{Ca}3.1$ complex increases the rate of decay of PF EPSPs, shaping their waveform and controlling summation of evoked PF trains, thus implementing a high-pass filter. This high-pass filter works in conjunction with I_H and feedforward-inhibition to allow Purkinje cells to respond selectively to high-frequency input, both in the subthreshold and tonic firing regime. I extended this work in **Chapter 4**, where I examined the interplay between short-term facilitation at the PF synapse and the Cav3-$K_{Ca}3.1$ complex. Using

standard patch clamp techniques, as well as dynamic clamp, I explored the effect of the Cav3-K_{Ca}3.1 complex on facilitating and nonfacilitating inputs, finding that the Cav3-K_{Ca}3.1 complex acts to specifically suppress nonfacilitating inputs indicative of a convergence of low-frequency background activity. This selective filtering increases the SNR for facilitating PF inputs that carry sensory information. Using a computational model of the subthreshold Purkinje cell membrane, I explored the activation of the Cav3-K_{Ca}3.1 complex during PF inputs, showing that K_{Ca}3.1 activation is delayed during facilitating input trains. This allows the facilitating PF inputs to overcome the influence of the Cav3-K_{Ca}3.1 complex. These studies establish the Cav3-K_{Ca}3.1 complex as an important player in controlling synaptic integration in cerebellar Purkinje cells.

While the previous chapters examined integration of excitatory inputs, in **Chapter 5**, I examined the roles of Cav3 and HCN channels in the processing of inhibitory inputs in DCN neurons. Using experimental approaches, we established that physiological levels of hyperpolarization are capable of activating I_T and I_H. We also demonstrated that I_T and I_H control the frequency of the rebound burst response, while I_H alone controls FSL. I developed a reduced model of the DCN neuron that was capable of reproducing the frequency and FSL relationships seen in *in vitro* recordings. The model showed that I_T is solely responsible for generating rebound bursts, while I_H augments burst frequency by decreasing membrane time constant and I_T inactivation. Finally, I demonstrated that I_H not only decreases FSL, but also increases the precision of the first spike, controlling the temporal fidelity of information transmission from the cerebellar cortex to efferent cerebellar targets. These results emphasize the interaction between Cav3 channels and subthreshold currents, demonstrating that Cav3 and HCN channels work synergistically to generate subthreshold dynamics that control synaptic integration in DCN neurons.

The work presented here explored several novel mechanisms by which Cav3 channels interact with pre- and postsynaptic determinants to control the neuronal response to synaptic inputs. The complex interactions that were observed between coexpressed ion channels emphasize that computation is not performed by any single group of ion channels, but by the interplay of a grand variety of ion channel families. Here, I will explore

this concept in more detail, relating my findings to our understanding of ion channel function and synaptic integration in the brain.

6.1 $K_{Ca}3.1$ expression in central neurons

K_{Ca} channels are important for controlling neuronal excitability and have a variety of roles ranging from spike repolarization to spike frequency adaptation to synaptic plasticity (Sah and Davies, 2000; Ohtsuki et al., 2012). There has previously been a dogmatic understanding that only two families of K_{Ca} channels are expressed in central neurons, namely the $K_{Ca}1$ (BK) and $K_{Ca}2$ (SK) families. These channels underlie spike-associated AHPs in virtually all neurons, with $K_{Ca}1.1$ channels generating the fast AHP and $K_{Ca}2$ channels the medium and slow AHPs (Stocker, 2004; Fakler and Adelman, 2008). However, I showed here that a third type of K_{Ca} channel, $K_{Ca}3.1$, is expressed in at least cerebellar Purkinje cells.

$K_{Ca}3.1$ channels have a wide range of functions in other cell types. For example, they are responsible for migration of lung mast cells, activation of microglia and T cells, and cell volume regulation (for a review, see: Wulff et al. (2007)). They are also highly expressed in enteric neurons and generate the slow AHP following action potentials in these neurons. However, no previous studies have reported expression of $K_{Ca}3.1$ in central neurons, making my discovery of their expression in Purkinje cells highly novel.

Whether $K_{Ca}3.1$ has a wider range of expression in the brain is an important question that remains to be answered and could have wide-reaching implications. Indeed, many cells in the brain have an I_{sAHP}, the molecular basis of which has yet to be identified. It is possible that $K_{Ca}3.1$ could serve a similar function to its role in enteric neurons and generate the slow AHP in central neurons. While no conclusive evidence for $K_{Ca}3.1$ expression in neurons expressing an I_{sAHP} has been found, my findings here set a precedent to explore the possibility for $K_{Ca}3.1$ expression in these neurons. Identifying $K_{Ca}3.1$ as the definitive molecular substrate for the slow AHP would allow for studies into methods for regulating spike firing in many central neurons.

6.2 Cav3-associated K_{Ca} complexes

It is well known that HVA Ca^{2+} channels associate with K_{Ca} channels, forming important signalling complexes. Activation of K^+ channels closely following Ca^{2+} influx allows for rapid negative feedback, maintaining membrane potential and ensuring the temporal and spatial precision of Ca^{2+} influx. Early studies showed near immediate activation of $K_{Ca}1.1$ channels following Cav2.2 channel activation (Marrion and Tavalin, 1998), suggesting a nanodomain interaction between $K_{Ca}1.1$ and Cav2.2 channels, a fact that was confirmed in later studies (Berkefeld et al., 2006; Berkefeld and Fakler, 2008). Activation of $K_{Ca}2$ channels, on the other hand, was found to be due to microdomain interactions with a variety of Ca^{2+} sources, including Cav1, Cav2 and Cav3 channels. These macromolecular signalling complexes play important roles in neuronal function. However, until the work shown here, nanodomain association with Cav3 channels had not previously been shown.

The unique properties of Cav3 channels, including its low open probability and low single-channel conductance (Chen and Hess, 1990; Weber et al., 2010), make it an ideal candidate for subthreshold regulation of synaptic inputs. However, these same properties mean the associated change in $[Ca^{2+}]_i$ during subthreshold voltage deflections is small. Therefore, any K_{Ca} channel depending on Cav3-mediated Ca^{2+} influx would have to be exquisitely sensitive to $[Ca^{2+}]$. Interestingly, $K_{Ca}3.1$ is the most sensitive of the K_{Ca} channels (Ishii et al., 1997b; Joiner et al., 1997). Furthermore, a large conductance compared to $K_{Ca}2$ channels allows small changes in open probability to have a greater effect on membrane voltage. The molecular association between Cav3 and $K_{Ca}3.1$ channels is thus an ideal pairing of signal and transducer, with the K_{Ca} channel being tuned to sense the range of $[Ca^{2+}]_i$ changes associated with Cav3 influx.

6.3 Cav3 window current

When examining the functional properties of the Cav3-$K_{Ca}3.1$ complex, one of the surprising findings was the extent of $K_{Ca}3.1$ channel activation at hyperpolarized potentials (**Fig. 3.10*A***). Likewise, physiological hyperpolarizations to E_{Cl} in DCN neurons were able to activate a substantial amount of I_T, enough to generate high-frequency rebound bursts (**Fig. 5.1*C***). These results suggested that the Cav3 window current extends

to a more hyperpolarized range than previously thought. Indeed, careful measurement of I_T during depolarizing ramps in Purkinje cells revealed that Cav3 channels are active at potentials as low as -90 mV, 20 - 30 mV below the activation voltage suggested by steady-state activation plots (cf. **Fig. 3.10*B, C*; Fig. 3.13*A, B***). With this extended voltage range for window current, Cav3 channels are ideally suited to be the primary source for Ca^{2+} signals in the subthreshold regime. By interacting with K_{Ca} channels ($K_{Ca}3.1$) or other ion channels that are active at these subthreshold potentials (e.g. HCN channels), Cav3 channels can provide Ca^{2+}-dependent regulation of cell excitability and synaptic integration which cannot be supplied by HVA Ca^{2+} channels.

6.4 Cav3-$K_{Ca}3.1$ complex and synaptic plasticity

Previous studies have examined the activation of postsynaptic Ca^{2+} channels in Purkinje cells during EPSPs. Since Purkinje cells lack NMDA receptors (but cf. Piochon et al. (2007)) and Ca^{2+}-permeable AMPA receptors, Ca^{2+} signals required for induction of synaptic plasticity must come from VGCCs. Cav2.1 channels are activated during both CF and PF inputs (Eilers et al., 1995a; Eilers et al., 1995b; Eilers et al., 1996) and are required for induction of PF long-term depression (Ito, 2001). Since Cav3 channels are the other principle subtype of VGCCs expressed in PCs, it is interesting to speculate on their role in synaptic plasticity. Indeed, Cav3 channels associate with mGluR1 receptors in Purkinje cells. Activation of mGluR1 causes a left-shift in the Cav3.1 activation curve, increasing synaptically evoked current (Hildebrand et al., 2009). Thus, Cav3 channels can be modulated by synaptic input. At CF and PF synapses, downregulation of $K_{Ca}2.2$ channels within specific compartments causes localized potentiation of EPSPs (Ohtsuki et al., 2012). It, therefore, seems conceivable that the Cav3-$K_{Ca}3.1$ complex could be modulated to change the properties of the postsynaptic membrane and thus responses to synaptic inputs. Positive modulation of this complex could induce long-term depression-like effects, while negative modulation, either by down-regulation or dissociation of this complex, could cause potentiation. This would represent a novel form of plasticity in the cerebellum.

There are several possible sites for regulation of the Cav3-$K_{Ca}3.1$ complex. The Cav3 channel conductance can be modulated by phosphorylation and a variety of neuro-

transmitters (Talavera and Nilius, 2006). Likewise, $K_{Ca}3.1$ channels are modulated by, at least, phosphorylation and arachidonic acid (Wulff et al., 2007). Therefore, the association between the Cav3 and $K_{Ca}3.1$ channels could be disrupted by phosphorylation or extracellular ligands. It would be interesting to see the effects of disrupting this protein-protein interaction on cellular function. Preliminary data shows that the $K_{Ca}3.1$ C-terminus links with the Cav3 C-terminus and II-III linker (*data not shown*). Using a Tat-peptide targeted to the C-terminus of either protein could prevent complex formation, allowing us to assess the role of the individual channels separate from the complex itself. Alternatively, several $K_{Ca}3.1$ knock-out mice exist and, while we have yet to determine whether this complex is present in the mouse, comparison of the information processing abilities of Purkinje cells in wild-type and knock-out mice could elucidate the complete function of this unique channel complex.

6.5 Interactions between HCN and Cav3 channels – roles in coding

The requirement for a neuron to process primarily inhibitory input poses an interesting neural coding problem: how can information about a presynaptic spike train be encoded in a series of action potentials if that same input reduces spike output? The inhibitory inputs from Purkinje cells, which carry information about the precise timing and amplitude of sensory and motor events, must be transformed by DCN neurons and transmitted with high temporal fidelity. Several current theories have been proposed regarding the transformation of Purkinje cell input to DCN cells. One theory postulates that the pauses in Purkinje cell output are the most important signal, since a pause will cause disinhibition of nuclear neurons and result in output to downstream targets (Gauck and Jaeger, 2000, 2003; Kleine et al., 2003; Wetmore et al., 2008). This idea is the basis for more detailed theories, such as the "lock-and-key" hypothesis where formation of cerebellar memory traces result in pauses of sufficient duration to cause rebound burst output (Wetmore et al., 2008). Rebound currents, such as I_T and I_H, have important roles when considering a disinhibition mechanism. I_T will determine the strength of DCN output as greater inhibition will cause more deinactivation of Cav3 channels, increasing the frequency of the rebound burst (**Fig. 5.6**). Thus, information about the strength of inhibition is encoded in the frequency of the rebound burst and is relayed to downstream targets. By

decreasing FSL for stronger stimuli (**Fig. 5.6**), I_H determines whether the response will be generated quickly enough during the pause. The stronger the inhibition, the shorter the pause that is required. Therefore, I_T and I_H can have important roles in encoding the strength of inhibition and duration of Purkinje cell pauses. Interestingly, recordings of memory trace acquisition in Purkinje cells show a decrease in spike output during the unconditioned stimulus following learning, suggesting that the cortex will disinhibit the DCN during the conditioned response (Jirenhed et al., 2007). However, another study showed that induction of long-term depression actually decreases pauses in Purkinje cells, indicating that there will be more inhibition following learning (Steuber et al., 2007).

Recently, a study in DCN neurons has suggested a different mechanism for integrating Purkinje cell inputs that does not rely on rebound burst output (Person and Raman, 2012). The authors observed that DCN neurons become entrained to synchronous IPSPs from Purkinje cells. When converging Purkinje cell inputs are desynchronized, DCN output is suppressed as inhibition remains relatively constant. However, increasing degrees of synchronization result in more membrane deflections and DCN cells become phase-locked to cortical inputs (Person and Raman, 2012). This model, therefore, suggests that rebound responses are not responsible for encoding Purkinje cell spike trains. Rather, DCN output reflects the degree of synchronization of the overlying cortical layer, and the firing frequency of DCN neurons directly correlates with the synchronized frequency of Purkinje cells. Indeed, there is evidence of synchronization between Purkinje cells (Shin and De Schutter, 2006) and, with the at least 40:1 convergence between Purkinje and DCN cells (Person and Raman, 2012), some degree of synchronization will be required for DCN cells to escape inhibition. However, this study assumed that Purkinje cell output is highly regular when, in reality, it has a coefficient of variation greater than 1.0 *in vivo* and regular patterns in Purkinje cell output only appear for brief periods of time (Shin et al., 2007). Finally, by acting merely as a relay for the consensus firing rate of Purkinje cells, DCN neurons would destroy much of the timing and amplitude information about the sensory or motor stimuli. Thus, while the degree of synchrony

among cortical inputs is important information and is transmitted in this model, too much information is potentially lost.

I think that some combination of these models is most likely. Let us suppose that output from DCN neurons should reflect the occurrence of particular events or stimuli. Furthermore, the cerebellum must be temporally precise, responding quickly when an important signal is detected, whatever that may be. Based on these assumptions, it is advantageous that the main source of input to DCN neurons be inhibitory, as their output can be suppressed when Purkinje cells are firing tonically and are desynchronized (Gauck and Jaeger, 2000, 2003). This could be considered the basal state of the cerebellum when no output is required. Now, suppose a conditioned stimulus is detected. To generate the appropriate response, Purkinje cells become synchronized, either by correlated PF or CF input, as is likely to occur within a cerebellar module. Synchronization of action potentials causes *increased* inhibition of DCN neurons, resulting in deinactivation of I_T and activation of I_H (Wetmore et al., 2008; Tadayonnejad et al., 2009; Sangrey and Jaeger, 2010; Tadayonnejad et al., 2010; Steuber et al., 2011). Analogous to the loading a spring, increased inhibition creates a greater potential for a high-frequency rebound response. Conversely, synchronized *pauses* in Purkinje cell output, caused by CF input (Barmack and Yakhnitsa, 2003; Yartsev et al., 2009), movement to a quiescent state (Fernandez et al., 2007; Engbers et al., 2012a), or molecular layer inhibition (Mittmann et al., 2005), provide an opportunity for DCN output. If the pause is of sufficient duration, where sufficiency is determined by the degree of I_H activation, a rebound response occurs and timing and amplitude information is sent to downstream targets.

Since we now have models of both Purkinje and DCN neurons (Fernandez et al., 2007; Engbers et al., 2011) (**Chapter 5**), it is possible to test this prediction in a small-scale network. Using a method for examining neuronal responses to correlations within a population of stochastic inputs (Hong et al., 2012), I have performed preliminary simulations on a small network consisting of 10 Purkinje cells and 1 DCN neuron (**Fig. 6.1**). Initial results support my theory and show that increased synchronization between Purkinje cells results in an increased frequency of DCN output, despite no change in presynaptic frequency. Furthermore, rebound bursts can be observed for high degrees of

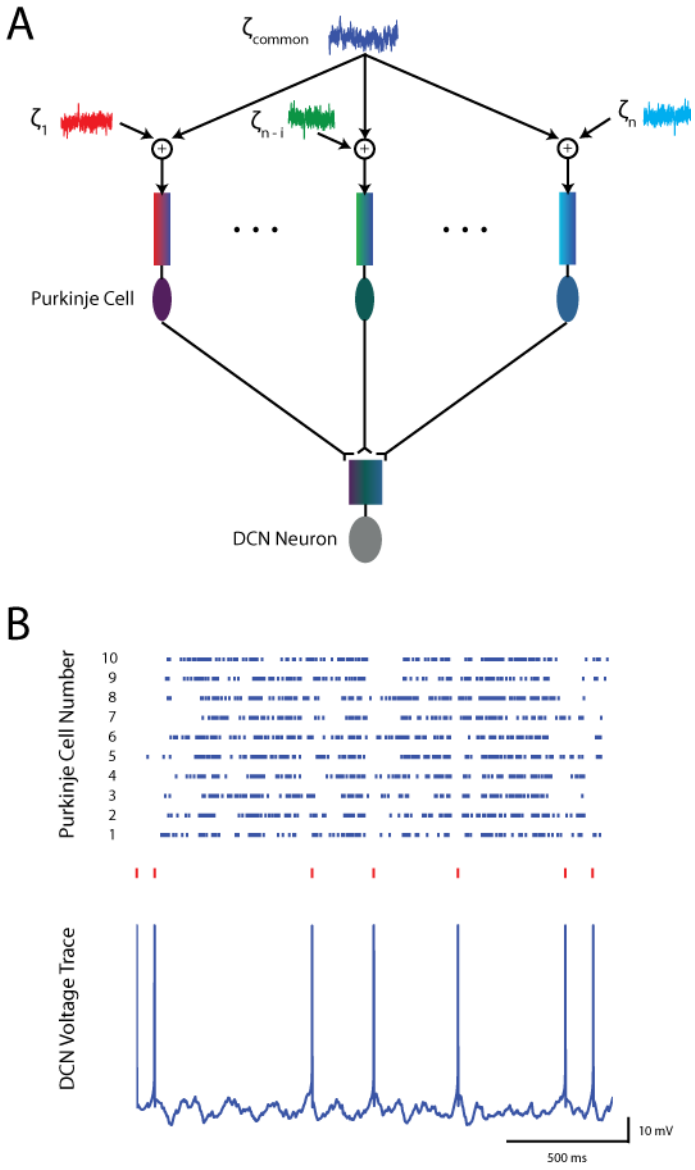
A
ζcommon
ζ1
ζn - i
ζn
Purkinje Cell
DCN Neuron
B
Purkinje Cell Number
10
9
8
7
6
5
4
3
2
1
DCN Voltage Trace
10 mV
500 ms

Figure 6.1: Network model of Purkinje cell synchronization and convergence onto DCN neuron

(A) Stochastic inputs are given to a reduced Purkinje cell model. Each Purkinje cell receives an independent noise input (ζ_i) as well as a common noise input (ζ_{common}). By adjusting the ratio of the two noise inputs, the synchronization of the Purkinje cells can be controlled. All the Purkinje cells converge onto a DCN neuron, providing IPSC trains that depress with physiological characteristics. **(B)** Raster plots of Purkinje cell models (*top*) with a correlation ratio of 0.5. The DCN model voltage is show *below*, with spikes corresponding to pauses in Purkinje cell output.

synchronization, as would be present during sensory or motor tasks, and are correlated with pauses in Purkinje cell population output. We have also seen similar results in slice recordings where Purkinje cell axons are stimulated with physiological patterns obtained from *in vivo* recordings. Thus, the roles of I_T and I_H in generating rebound bursts and controlling the timing of spike output are likely critical for cerebellar function.

6.6 Concluding Remarks

The brain is an amazing and complex machine, capable of performing vastly parallel computations in real-time and allowing us to react and adapt to our environments. The nonlinear nature of neuronal excitability and communication underpins the computational capacity of the nervous system. Here, I have explored several new interactions between ion channels in cerebellar neurons and their role in integrating synaptic inputs. These findings improve our understanding of how the cerebellum functions and how its principal cells integrate vastly different forms of input. These interactions have wide-ranging implications for our understanding of synaptic integration in the nervous system.

APPENDIX A: INCLUSION OF WORK PUBLISHED OR SUBMITTED BY CANDIDATE

Chapter 3:

Engbers JDT, Anderson D, Asmara H, Rehak R, Mehaffey WH, Hameed S, McKay BE, Kruskic M, Zamponi GW, Turner RW (2012) Intermediate conductance calcium-activated potassium channels modulate summation of parallel fiber input in cerebellar Purkinje cells. Proc Natl Acad Sci U S A 109:2601-2606. [JDTE designed, performed and analyzed experiments]

Chapter 4:

Engbers JDT, Turner RW. Cav3-K_{Ca}3.1 complex augments high-pass filtering of parallel fibre inputs due to presynaptic facilitation. *In preparation*. [JDTE designed, performed and analyzed all experiments and modelling]

Chapter 5:

Engbers JDT, Anderson D, Tadayonnejad R, Mehaffey WH, Molineux ML, Turner RW (2011) Distinct roles for I(T) and I(H) in controlling the frequency and timing of rebound spike responses. J Physiol 589:5391-5413. [JDTE designed the DCN model, performed and analyzed all simulations. JDTE designed and analyzed experimental data]

APPENDIX B: COPYRIGHT LICENSE AGREEMENTS

License agreement for **Figure 1.4C**

This is a License Agreement between Jordan DT Engbers ("You") and Nature Publishing Group ("Nature Publishing Group") provided by Copyright Clearance Center ("CCC"). The license consists of your order details, the terms and conditions provided by Nature Publishing Group, and the payment terms and conditions.

All payments must be made in full to CCC. For payment instructions, please see information listed at the bottom of this form.

License Number	3119580517070
License date	Mar 31, 2013
Licensed content publisher	Nature Publishing Group
Licensed content publication	Nature Reviews Neuroscience
Licensed content title	Ca2 -activated K channels: molecular determinants and function of the SK family
Licensed content author	Martin Stocker
Licensed content date	Oct 1, 2004
Volume number	5
Issue number	10
Type of Use	reuse in a thesis/dissertation
Requestor type	academic/educational
Format	print and electronic
Portion	figures/tables/illustrations
Number of figures/tables/illustrations	1
High-res required	no
Figures	Figure 2 - panel C
Author of this NPG article	no
Your reference number	
Title of your thesis / dissertation	Determinants of Synaptic Integration in Cerebellar Neurons
Expected completion date	Apr 2013
Estimated size (number of pages)	225
Total	0.00 USD
Terms and Conditions	

License agreement for **Figure 1.5C**

This is a License Agreement between Jordan DT Engbers ("You") and Nature Publishing Group ("Nature Publishing Group") provided by Copyright Clearance Center ("CCC"). The license consists of your order details, the terms and conditions provided by Nature Publishing Group, and the payment terms and conditions.

All payments must be made in full to CCC. For payment instructions, please see information listed at the bottom of this form.

License Number	3119580517070
License date	Mar 31, 2013
Licensed content publisher	Nature Publishing Group
Licensed content publication	Nature Reviews Neuroscience
Licensed content title	Ca2 -activated K channels: molecular determinants and function of the SK family
Licensed content author	Martin Stocker
Licensed content date	Oct 1, 2004
Volume number	5
Issue number	10
Type of Use	reuse in a thesis/dissertation
Requestor type	academic/educational
Format	print and electronic
Portion	figures/tables/illustrations
Number of figures/tables/illustrations	1
High-res required	no
Figures	Figure 2 - panel C
Author of this NPG article	no
Your reference number	
Title of your thesis / dissertation	Determinants of Synaptic Integration in Cerebellar Neurons
Expected completion date	Apr 2013
Estimated size (number of pages)	225
Total	0.00 USD
Terms and Conditions	

License agreement for **Figure 1.8**

This is a License Agreement between Jordan DT Engbers ("You") and Nature Publishing Group ("Nature Publishing Group") provided by Copyright Clearance Center ("CCC"). The license consists of your order details, the terms and conditions provided by Nature Publishing Group, and the payment terms and conditions.

All payments must be made in full to CCC. For payment instructions, please see information listed at the bottom of this form.

License Number	3119540158192
License date	Mar 31, 2013
Licensed content publisher	Nature Publishing Group
Licensed content publication	Nature Reviews Neuroscience
Licensed content title	Anatomical and physiological foundations of cerebellar information processing
Licensed content author	Richard AppsandMartin Garwicz
Licensed content date	Apr 1, 2005
Volume number	6
Issue number	4
Type of Use	reuse in a thesis/dissertation
Requestor type	academic/educational
Format	print and electronic
Portion	figures/tables/illustrations
Number of figures/tables/illustrations	1
High-res required	no
Figures	Figure 1 - Basic Structure of the cerebellar cortex
Author of this NPG article	no
Your reference number	
Title of your thesis / dissertation	Determinants of Synaptic Integration in Cerebellar Neurons
Expected completion date	Apr 2013
Estimated size (number of pages)	225
Total	0.00 USD
Terms and Conditions	

License agreement for **Chapter 5**

This is a License Agreement between Jordan DT Engbers ("You") and John Wiley and Sons ("John Wiley and Sons") provided by Copyright Clearance Center ("CCC"). The license consists of your order details, the terms and conditions provided by John Wiley and Sons, and the payment terms and conditions.

All payments must be made in full to CCC. For payment instructions, please see information listed at the bottom of this form.

License Number	3138360335785
License date	Apr 29, 2013
Licensed content publisher	John Wiley and Sons
Licensed content publication	Journal of Physiology
Licensed content title	Distinct roles for IT and IH in controlling the frequency and timing of rebound spike responses
Licensed copyright line	© 2011 The Authors. Journal compilation © 2011 The Physiological Society
Licensed content author	Jordan D. T. Engbers,Dustin Anderson,Reza Tadayonnejad,W. Hamish Mehaffey,Michael L. Molineux,Ray W. Turner
Licensed content date	Nov 14, 2011
Start page	5391
End page	5413
Type of use	Dissertation/Thesis
Requestor type	Author of this Wiley article
Format	Print and electronic
Portion	Full article
Will you be translating?	No
Total	0.00 USD
Terms and Conditions	

References

Abbott LF, Regehr WG (2004) Synaptic computation. Nature 431:796-803.

Abbott LF, Varela JA, Sen K, Nelson SB (1997) Synaptic depression and cortical gain control. Science 275:220-224.

Aizenman CD, Linden DJ (1999) Regulation of the rebound depolarization and spontaneous firing patterns of deep nuclear neurons in slices of rat cerebellum. J Neurophysiol 82:1697-1709.

Aizenman CD, Manis PB, Linden DJ (1998) Polarity of long-term synaptic gain change is related to postsynaptic spike firing at a cerebellar inhibitory synapse. Neuron 21:827-835.

Albus J (1971) A theory of cerebellar function. Mathematical Biosciences 10:25-61.

Alvina K, Ellis-Davies G, Khodakhah K (2009) T-type calcium channels mediate rebound firing in intact deep cerebellar neurons. Neuroscience 158:635-641.

Alvina K, Walter JT, Kohn A, Ellis-Davies G, Khodakhah K (2008) Questioning the role of rebound firing in the cerebellum. Nat Neurosci 11:1256-1258.

Anderson D, Rehak R, Hameed S, Mehaffey WH, Zamponi GW, Turner RW (2010a) Regulation of the K(V)4.2 complex by Ca(V)3.1 calcium channels. Channels (Austin) 4.

Anderson D, Mehaffey WH, Iftinca M, Rehak R, Engbers JD, Hameed S, Zamponi GW, Turner RW (2010b) Regulation of neuronal activity by Cav3-Kv4 channel signaling complexes. Nat Neurosci 13:333-337.

Angelo K, London M, Christensen SR, Hausser M (2007) Local and global effects of I(h) distribution in dendrites of mammalian neurons. J Neurosci 27:8643-8653.

Anwar H, Hong S, De Schutter E (2012) Controlling Ca2+-activated K+ channels with models of Ca2+ buffering in Purkinje cells. Cerebellum 11:681-693.

Apps R, Garwicz M (2005) Anatomical and physiological foundations of cerebellar information processing. Nat Rev Neurosci 6:297-311.

Apps R, Hawkes R (2009) Cerebellar cortical organization: a one-map hypothesis. Nat Rev Neurosci 10:670-681.

Arbib MA, Amari S (1985) Sensori-motor transformations in the brain (with a critique of the tensor theory of cerebellum). J Theor Biol 112:123-155.

Armstrong DM, Cogdell B, Harvey RJ (1973) Response of interpositus neurones to nerve stimulation in chloralose anesthetized cats. Brain Res 55:461-466.

Armstrong DM, Cogdell B, Harvey R (1975) Effects of afferent volleys from the limbs on the discharge patterns of interpositus neurones in cats anaesthetized with alpha-chloralose. J Physiol 248:489-517.

Atherton JF, Kitano K, Baufreton J, Fan K, Wokosin D, Tkatch T, Shigemoto R, Surmeier DJ, Bevan MD (2010) Selective participation of somatodendritic HCN channels in inhibitory but not excitatory synaptic integration in neurons of the subthalamic nucleus. J Neurosci 30:16025-16040.

Awatramani GB, Price GD, Trussell LO (2005) Modulation of transmitter release by presynaptic resting potential and background calcium levels. Neuron 48:109-121.

Babalyan AL, Fanardzhyan VV (1991) Electrophysiologic properties of red nucleus neurons in the rat brain slices. Neurophysiology 23:454-461.

Bao J, Reim K, Sakaba T (2010) Target-dependent feedforward inhibition mediated by short-term synaptic plasticity in the cerebellum. J Neurosci 30:8171-8179.

Barlow J (2002) The cerebellum and adaptive control: Cambridge Univ Pr.

Barmack NH, Yakhnitsa V (2003) Cerebellar climbing fibers modulate simple spikes in Purkinje cells. J Neurosci 23:7904-7916.

Barski JJ, Hartmann J, Rose CR, Hoebeek F, Morl K, Noll-Hussong M, De Zeeuw CI, Konnerth A, Meyer M (2003) Calbindin in cerebellar Purkinje cells is a critical determinant of the precision of motor coordination. J Neurosci 23:3469-3477.

Bastian AJ (2006) Learning to predict the future: the cerebellum adapts feedforward movement control. Curr Opin Neurobiol 16:645-649.

Bengtsson F, Ekerot CF, Jorntell H (2011) In vivo analysis of inhibitory synaptic inputs and rebounds in deep cerebellar nuclear neurons. PLoS One 6:e18822.

Benton DC, Monaghan AS, Hosseini R, Bahia PK, Haylett DG, Moss GW (2003) Small conductance Ca2+-activated K+ channels formed by the expression of rat SK1 and SK2 genes in HEK 293 cells. J Physiol 553:13-19.

Berkefeld H, Fakler B (2008) Repolarizing responses of BKCa-Cav complexes are distinctly shaped by their Cav subunits. J Neurosci 28:8238-8245.

Berkefeld H, Fakler B, Schulte U (2010) Ca2+-activated K+ channels: from protein complexes to function. Physiol Rev 90:1437-1459.

Berkefeld H, Sailer CA, Bildl W, Rohde V, Thumfart JO, Eble S, Klugbauer N, Reisinger E, Bischofberger J, Oliver D, Knaus HG, Schulte U, Fakler B (2006) BKCa-Cav channel complexes mediate rapid and localized Ca2+-activated K+ signaling. Science 314:615-620.

Biel M, Wahl-Schott C, Michalakis S, Zong X (2009) Hyperpolarization-activated cation channels: from genes to function. Physiol Rev 89:847-885.

Bloedel J, Kelly T (1992) The dynamic selection hypothesis: a proposed function for cerebellar sagittal zones. The Cerebellum Revisited New York: Springer-Verlag:267–282.

Bloedel JR, Bracha V, Larson PS (1993) Real time operations of the cerebellar cortex. Can J Neurol Sci 20 Suppl 3:S7-18.

Bloodgood BL, Sabatini BL (2007) Nonlinear regulation of unitary synaptic signals by CaV(2.3) voltage-sensitive calcium channels located in dendritic spines. Neuron 53:249-260.

Braitenberg V (1967) Is the cerebellar cortex a biological clock in the millisecond range? Prog Brain Res 25:334-346.

Brauer AU, Savaskan NE, Kole MH, Plaschke M, Monteggia LM, Nestler EJ, Simburger E, Deisz RA, Ninnemann O, Nitsch R (2001) Molecular and functional analysis of hyperpolarization-activated pacemaker channels in the hippocampus after entorhinal cortex lesion. FASEB journal : official publication of the Federation of American Societies for Experimental Biology 15:2689-2701.

Brenowitz SD, Regehr WG (2003) Calcium dependence of retrograde inhibition by endocannabinoids at synapses onto Purkinje cells. J Neurosci 23:6373-6384.

Brenowitz SD, Best AR, Regehr WG (2006) Sustained elevation of dendritic calcium evokes widespread endocannabinoid release and suppression of synapses onto cerebellar Purkinje cells. J Neurosci 26:6841-6850.

Butera RJ, Jr., Wilson CG, Delnegro CA, Smith JC (2001) A methodology for achieving high-speed rates for artificial conductance injection in electrically excitable biological cells. IEEE Trans Biomed Eng 48:1460-1470.

Cattaneo A, Maffei L, Morrone C (1981) Two firing patterns in the discharge of complex cells encoding different attributes of the visual stimulus. Exp Brain Res 43:115-118.

Cavelier P, Bossu JL (2003) Dendritic low-threshold Ca2+ channels in rat cerebellar Purkinje cells: possible physiological implications. Cerebellum 2:196-205.

Chadderton P, Margrie TW, Hausser M (2004) Integration of quanta in cerebellar granule cells during sensory processing. Nature 428:856-860.

Chan-Paly V (1978) Cerebellar Dentate Nucleus: Organization, Cytology and Transmitters. Ann Neurology 4:588.

Chen CF, Hess P (1990) Mechanism of gating of T-type calcium channels. J Gen Physiol 96:603-630.

Chen FP, Evinger C (2006) Cerebellar modulation of trigeminal reflex blinks: interpositus neurons. J Neurosci 26:10569-10576.

Chomczynski P, Sacchi N (1987) Single-step method of RNA isolation by acid guanidinium thiocyanate-phenol-chloroform extraction. Analytical biochemistry 162:156-159.

Christini DJ, Stein KM, Markowitz SM, Lerman BB (1999) Practical real-time computing system for biomedical experiment interface. Ann Biomed Eng 27:180-186.

Cingolani LA, Gymnopoulos M, Boccaccio A, Stocker M, Pedarzani P (2002) Developmental regulation of small-conductance Ca2+-activated K+ channel expression and function in rat Purkinje neurons. J Neurosci 22:4456-4467.

Coetzee WA, Amarillo Y, Chiu J, Chow A, Lau D, McCormack T, Moreno H, Nadal MS, Ozaita A, Pountney D, Saganich M, Vega-Saenz de Miera E, Rudy B (1999) Molecular diversity of K+ channels. Ann N Y Acad Sci 868:233-285.

Craig PJ, Beattie RE, Folly EA, Banerjee MD, Reeves MB, Priestley JV, Carney SL, Sher E, Perez-Reyes E, Volsen SG (1999) Distribution of the voltage-dependent calcium channel alpha1G subunit mRNA and protein throughout the mature rat brain. Eur J Neurosci 11:2949-2964.

Cueni L, Canepari M, Lujan R, Emmenegger Y, Watanabe M, Bond CT, Franken P, Adelman JP, Luthi A (2008) T-type Ca2+ channels, SK2 channels and SERCAs gate sleep-related oscillations in thalamic dendrites. Nat Neurosci 11:683-692.

Czubayko U, Sultan F, Thier P, Schwarz C (2001) Two types of neurons in the rat cerebellar nuclei as distinguished by membrane potentials and intracellular fillings. J Neurophysiol 85:2017-2029.

D'Angelo E, De Zeeuw CI (2009) Timing and plasticity in the cerebellum: focus on the granular layer. Trends Neurosci 32:30-40.

Davie JT, Clark BA, Hausser M (2008) The origin of the complex spike in cerebellar Purkinje cells. J Neurosci 28:7599-7609.

De Schutter E (1995) Cerebellar long-term depression might normalize excitation of Purkinje cells: a hypothesis. Trends Neurosci 18:291-295.

De Schutter E (1997) A new functional role for cerebellar long-term depression. Prog Brain Res 114:529-542.

De Schutter E, Steuber V (2009) Patterns and Pauses in Purkinje Cell Simple Spike Trains: Experiments, Modeling and Theory. Neuroscience 162:816-826.

De Zeeuw CI, Hoebeek FE, Bosman LW, Schonewille M, Witter L, Koekkoek SK (2011) Spatiotemporal firing patterns in the cerebellum. Nat Rev Neurosci 12:327-344.

Dean P, Porrill J (2008) Adaptive-filter models of the cerebellum: computational analysis. Cerebellum 7:567-571.

Dean P, Porrill J, Ekerot CF, Jorntell H (2010) The cerebellar microcircuit as an adaptive filter: experimental and computational evidence. Nat Rev Neurosci 11:30-43.

Delgado-Garcia JM, Gruart A (2005) Firing activities of identified posterior interpositus nucleus neurons during associative learning in behaving cats. Brain Res Brain Res Rev 49:367-376.

Destexhe A, Neubig M, Ulrich D, Huguenard J (1998) Dendritic low-threshold calcium currents in thalamic relay cells. J Neurosci 18:3574-3588.

Dittman JS, Kreitzer AC, Regehr WG (2000) Interplay between facilitation, depression, and residual calcium at three presynaptic terminals. J Neurosci 20:1374-1385.

Doroshenko PA, Woppmann A, Miljanich G, Augustine GJ (1997) Pharmacologically distinct presynaptic calcium channels in cerebellar excitatory and inhibitory synapses. Neuropharmacology 36:865-872.

Dorval AD, Christini DJ, White JA (2001) Real-Time linux dynamic clamp: a fast and flexible way to construct virtual ion channels in living cells. Ann Biomed Eng 29:897-907.

Dreyfus FM, Tscherter A, Errington AC, Renger JJ, Shin HS, Uebele VN, Crunelli V, Lambert RC, Leresche N (2010) Selective T-type calcium channel block in thalamic neurons reveals channel redundancy and physiological impact of I(T)window. J Neurosci 30:99-109.

Edgerton JR, Reinhart PH (2003) Distinct contributions of small and large conductance Ca2+-activated K+ channels to rat Purkinje neuron function. J Physiol 548:53-69.

Eggermont JJ (1998) Is there a neural code? Neurosci Biobehav Rev 22:355-370.

Eilers J, Augustine GJ, Konnerth A (1995a) Subthreshold synaptic Ca2+ signalling in fine dendrites and spines of cerebellar Purkinje neurons. Nature 373:155-158.

Eilers J, Plant T, Konnerth A (1996) Localized calcium signalling and neuronal integration in cerebellar Purkinje neurones. Cell Calcium 20:215-226.

Eilers J, Callewaert G, Armstrong C, Konnerth A (1995b) Calcium signaling in a narrow somatic submembrane shell during synaptic activity in cerebellar Purkinje neurons. Proc Natl Acad Sci U S A 92:10272-10276.

Ekerot CF, Jorntell H (2008) Synaptic integration in cerebellar granule cells. Cerebellum 7:539-541.

Engbers JD, Fernandez FR, Turner RW (2012a) Bistability in Purkinje neurons: Ups and downs in cerebellar research. Neural networks : the official journal of the International Neural Network Society.

Engbers JD, Anderson D, Tadayonnejad R, Mehaffey WH, Molineux ML, Turner RW (2011) Distinct roles for I(T) and I(H) in controlling the frequency and timing of rebound spike responses. J Physiol 589:5391-5413.

Engbers JD, Anderson D, Asmara H, Rehak R, Mehaffey WH, Hameed S, McKay BE, Kruskic M, Zamponi GW, Turner RW (2012b) Intermediate conductance calcium-activated potassium channels modulate summation of parallel fiber input in cerebellar Purkinje cells. Proc Natl Acad Sci U S A 109:2601-2606.

Evans RM, Zamponi GW (2006) Presynaptic Ca2+ channels--integration centers for neuronal signaling pathways. Trends Neurosci 29:617-624.

Faber ES (2010) Functional interplay between NMDA receptors, SK channels and voltage-gated Ca2+ channels regulates synaptic excitability in the medial prefrontal cortex. J Physiol 588:1281-1292.

Faber ES, Delaney AJ, Sah P (2005) SK channels regulate excitatory synaptic transmission and plasticity in the lateral amygdala. Nat Neurosci 8:635-641.

Fakler B, Adelman JP (2008) Control of K(Ca) channels by calcium nano/microdomains. Neuron 59:873-881.

Feng SS, Jaeger D (2008) The role of SK calcium-dependent potassium currents in regulating the activity of deep cerebellar nucleus neurons: a dynamic clamp study. Cerebellum 7:542-546.

Fernandez FR, Engbers JD, Turner RW (2007) Firing dynamics of cerebellar purkinje cells. J Neurophysiol 98:278-294.

Fortune ES, Rose GJ (1997) Passive and active membrane properties contribute to the temporal filtering properties of midbrain neurons in vivo. J Neurosci 17:3815-3825.

Fortune ES, Rose GJ (2001) Short-term synaptic plasticity as a temporal filter. Trends Neurosci 24:381-385.

Gardette R, Debono M, Dupont JL, Crepel F (1985a) Electrophysiological studies on the postnatal development of intracerebellar nuclei neurons in rat cerebellar slices maintained in vitro. II. Membrane conductances. Brain Res 352:97-106.

Gardette R, Debono M, Dupont JL, Crepel F (1985b) Electrophysiological studies on the postnatal development of intracerebellar nuclei neurons in rat cerebellar slices maintained in vitro. I. Postsynaptic potentials. Brain Res 351:47-55.

Garwicz M, Ekerot CF, Jorntell H (1998) Organizational Principles of Cerebellar Neuronal Circuitry. News Physiol Sci 13:26-32.

Gastrein P, Campanac E, Gasselin C, Cudmore R, Bialowas A, Carlier E, Fronzaroli-Molinieres L, Ankri N, Debanne D (2011) The role of hyperpolarization-activated cationic current (Ih) in spike-time precision and intrinsic resonance in cortical neurons in vitro. J Physiol.

Gauck V, Jaeger D (2000) The control of rate and timing of spikes in the deep cerebellar nuclei by inhibition. J Neurosci 20:3006-3016.

Gauck V, Jaeger D (2003) The contribution of NMDA and AMPA conductances to the control of spiking in neurons of the deep cerebellar nuclei. J Neurosci 23:8109-8118.

Gauck V, Thomann M, Jaeger D, Borst A (2001) Spatial distribution of low- and high-voltage-activated calcium currents in neurons of the deep cerebellar nuclei. J Neurosci 21:RC158.

Gebhart AL, Petersen SE, Thach WT (2002) Role of the posterolateral cerebellum in language. Ann N Y Acad Sci 978:318-333.

Gillessen T, Alzheimer C (1997) Amplification of EPSPs by low Ni(2+)- and amiloride-sensitive Ca2+ channels in apical dendrites of rat CA1 pyramidal neurons. J Neurophysiol 77:1639-1643.

Goldman MS, Maldonado P, Abbott LF (2002) Redundancy reduction and sustained firing with stochastic depressing synapses. J Neurosci 22:584-591.

Gruart A, Pastor AM, Armengol JA, Delgado-Garcia JM (1997) Involvement of cerebellar cortex and nuclei in the genesis and control of unconditioned and conditioned eyelid motor responses. Prog Brain Res 114:511-528.

Grunnet M, Kaufmann WA (2004) Coassembly of big conductance Ca2+-activated K+ channels and L-type voltage-gated Ca2+ channels in rat brain. J Biol Chem 279:36445-36453.

Gruol DL, Netzeband JG, Schneeloch J, Gullette CE (2006) L-type Ca2+ channels contribute to current-evoked spike firing and associated Ca2+ signals in cerebellar Purkinje neurons. Cerebellum 5:146-154.

Hannah RM, Dunn KM, Bonev AD, Nelson MT (2011) Endothelial SK(Ca) and IK(Ca) channels regulate brain parenchymal arteriolar diameter and cortical cerebral blood flow. J Cereb Blood Flow Metab 31:1175-1186.

Hartmann J, Konnerth A (2005) Determinants of postsynaptic Ca2+ signaling in Purkinje neurons. Cell Calcium 37:459-466.

Heil P (2004) First-spike latency of auditory neurons revisited. Curr Opin Neurobiol 14:461-467.

Hell JW, Westenbroek RE, Warner C, Ahlijanian MK, Prystay W, Gilbert MM, Snutch TP, Catterall WA (1993) Identification and differential subcellular localization of the neuronal class C and class D L-type calcium channel alpha 1 subunits. The Journal of cell biology 123:949-962.

Hildebrand ME, Isope P, Miyazaki T, Nakaya T, Garcia E, Feltz A, Schneider T, Hescheler J, Kano M, Sakimura K, Watanabe M, Dieudonne S, Snutch TP (2009) Functional coupling between mGluR1 and Cav3.1 T-type calcium channels contributes to parallel fiber-induced fast calcium signaling within Purkinje cell dendritic spines. J Neurosci 29:9668-9682.

Hirschberg B, Maylie J, Adelman JP, Marrion NV (1998) Gating of recombinant small-conductance Ca-activated K+ channels by calcium. J Gen Physiol 111:565-581.

Hodgkin AL, Huxley AF (1952) A quantitative description of membrane current and its application to conduction and excitation in nerve. J Physiol 117:500-544.

Hoebeek FE, Witter L, Ruigrok TJ, De Zeeuw CI (2010) Differential olivo-cerebellar cortical control of rebound activity in the cerebellar nuclei. Proc Natl Acad Sci U S A 107:8410-8415.

Hofmann F, Lacinova L, Klugbauer N (1999) Voltage-dependent calcium channels: from structure to function. Rev Physiol Biochem Pharmacol 139:33-87.

Hong S, Ratte S, Prescott SA, De Schutter E (2012) Single neuron firing properties impact correlation-based population coding. J Neurosci 32:1413-1428.

Hosy E, Piochon C, Teuling E, Rinaldo L, Hansel C (2011) SK2 channel expression and function in cerebellar Purkinje cells. J Physiol 589:3433-3440.

Huang Z, Lujan R, Kadurin I, Uebele VN, Renger JJ, Dolphin AC, Shah MM (2011) Presynaptic HCN1 channels regulate Cav3.2 activity and neurotransmission at select cortical synapses. Nat Neurosci 14:478-486.

Huguenard JR (1996) Low-threshold calcium currents in central nervous system neurons. Annual review of physiology 58:329-348.

Huguenard JR, Prince DA (1992) A novel T-type current underlies prolonged Ca(2+)-dependent burst firing in GABAergic neurons of rat thalamic reticular nucleus. J Neurosci 12:3804-3817.

Huguenard JR, McCormick DA (1992) Simulation of the currents involved in rhythmic oscillations in thalamic relay neurons. J Neurophysiol 68:1373-1383.

Hurlock EC, Bose M, Pierce G, Joho RH (2009) Rescue of motor coordination by Purkinje cell-targeted restoration of Kv3.3 channels in Kcnc3-null mice requires Kcnc1. J Neurosci 29:15735-15744.

Iftinca M, McKay BE, Snutch TP, McRory JE, Turner RW, Zamponi GW (2006) Temperature dependence of T-type calcium channel gating. Neuroscience 142:1031-1042.

Iftinca M, Hamid J, Chen L, Varela D, Tadayonnejad R, Altier C, Turner RW, Zamponi GW (2007) Regulation of T-type calcium channels by Rho-associated kinase. Nat Neurosci 10:854-860.

Iftinca MC, Zamponi GW (2009) Regulation of neuronal T-type calcium channels. Trends Pharmacol Sci 30:32-40.

Ishii TM, Maylie J, Adelman JP (1997a) Determinants of apamin and d-tubocurarine block in SK potassium channels. J Biol Chem 272:23195-23200.

Ishii TM, Silvia C, Hirschberg B, Bond CT, Adelman JP, Maylie J (1997b) A human intermediate conductance calcium-activated potassium channel. Proc Natl Acad Sci U S A 94:11651-11656.

Isope P, Murphy TH (2005) Low threshold calcium currents in rat cerebellar Purkinje cell dendritic spines are mediated by T-type calcium channels. J Physiol 562:257-269.

Ito M (1989) Long-term depression. Annu Rev Neurosci 12:85-102.

Ito M (1990) A new physiological concept on cerebellum. Rev Neurol (Paris) 146:564-569.

Ito M (1993) Synaptic plasticity in the cerebellar cortex and its role in motor learning. Can J Neurol Sci 20 Suppl 3:S70-74.

Ito M (2001) Cerebellar long-term depression: characterization, signal transduction, and functional roles. Physiol Rev 81:1143-1195.

Ito M (2002) Historical review of the significance of the cerebellum and the role of Purkinje cells in motor learning. Ann N Y Acad Sci 978:273-288.

Ito M (2006) Cerebellar circuitry as a neuronal machine. Prog Neurobiol 78:272-303.

Ito M, Kano M (1982) Long-lasting depression of parallel fiber-Purkinje cell transmission induced by conjunctive stimulation of parallel fibers and climbing fibers in the cerebellar cortex. Neurosci Lett 33:253-258.

Ito M, Sakurai M, Tongroach P (1982) Climbing fibre induced depression of both mossy fibre responsiveness and glutamate sensitivity of cerebellar Purkinje cells. J Physiol 324:113-134.

Ito M, Yoshida M, Obata K, Kawai N, Udo M (1970) Inhibitory control of intracerebellar nuclei by the purkinje cell axons. Exp Brain Res 10:64-80.

Jacobson GA, Rokni D, Yarom Y (2008) A model of the olivo-cerebellar system as a temporal pattern generator. Trends Neurosci 31:617-625.

Jacobson GA, Lev I, Yarom Y, Cohen D (2009) Invariant phase structure of olivo-cerebellar oscillations and its putative role in temporal pattern generation. Proc Natl Acad Sci U S A 106:3579-3584.

Jaeger D, Bower JM (1999) Synaptic control of spiking in cerebellar Purkinje cells: dynamic current clamp based on model conductances. J Neurosci 19:6090-6101.

Jahnsen H (1986a) Electrophysiological characteristics of neurones in the guinea-pig deep cerebellar nuclei in vitro. J Physiol 372:129-147.

Jahnsen H (1986b) Extracellular activation and membrane conductances of neurones in the guinea-pig deep cerebellar nuclei in vitro. J Physiol 372:149-168.

Jahnsen H, Llinas R (1984) Ionic basis for the electro-responsiveness and oscillatory properties of guinea-pig thalamic neurones in vitro. J Physiol 349:227-247.

Jensen BS, Strobaek D, Olesen SP, Christophersen P (2001) The Ca2+-activated K+ channel of intermediate conductance: a molecular target for novel treatments? Curr Drug Targets 2:401-422.

Jirenhed DA, Bengtsson F, Hesslow G (2007) Acquisition, extinction, and reacquisition of a cerebellar cortical memory trace. J Neurosci 27:2493-2502.

Joiner WJ, Wang LY, Tang MD, Kaczmarek LK (1997) hSK4, a member of a novel subfamily of calcium-activated potassium channels. Proc Natl Acad Sci U S A 94:11013-11018.

Jorntell H, Ekerot CF (2006) Properties of somatosensory synaptic integration in cerebellar granule cells in vivo. J Neurosci 26:11786-11797.

Kaushal V, Koeberle PD, Wang Y, Schlichter LC (2007) The Ca2+-activated K+ channel KCNN4/KCa3.1 contributes to microglia activation and nitric oxide-dependent neurodegeneration. J Neurosci 27:234-244.

Kepecs A, Lisman J (2003) Information encoding and computation with spikes and bursts. Network 14:103-118.

Kepecs A, Wang XJ, Lisman J (2002) Bursting neurons signal input slope. J Neurosci 22:9053-9062.

Khanna R, Chang MC, Joiner WJ, Kaczmarek LK, Schlichter LC (1999) hSK4/hIK1, a calmodulin-binding KCa channel in human T lymphocytes. Roles in proliferation and volume regulation. J Biol Chem 274:14838-14849.

Kisilevsky AE, Zamponi GW (2008) Presynaptic calcium channels: structure, regulators, and blockers. Handb Exp Pharmacol:45-75.

Kitai ST, McCrea RA, Preston RJ, Bishop GA (1977) Electrophysiological and horseradish peroxidase studies of precerebellar afferents to the nucleus interpositus anterior. I. Climbing fiber system. Brain Res 122:197-214.

Kleine JF, Guan Y, Buttner U (2003) Saccade-related neurons in the primate fastigial nucleus: what do they encode? J Neurophysiol 90:3137-3154.

Koch C, Segev I, eds (1998) Methods in Neuronal Modeling: From Ions to Networks, 2nd Edition. Cambridge: The MIT Press.

Kole MH, Hallermann S, Stuart GJ (2006) Single Ih channels in pyramidal neuron dendrites: properties, distribution, and impact on action potential output. J Neurosci 26:1677-1687.

Lancaster B, Nicoll RA (1987) Properties of two calcium-activated hyperpolarizations in rat hippocampal neurones. J Physiol 389:187-203.

Lee JH, Gomora JC, Cribbs LL, Perez-Reyes E (1999) Nickel block of three cloned T-type calcium channels: low concentrations selectively block alpha1H. Biophys J 77:3034-3042.

Lein ES et al. (2007) Genome-wide atlas of gene expression in the adult mouse brain. Nature 445:168-176.

Lisberger SG (1995) Learning. A mechanism of learning found? Curr Biol 5:221-224.

Lisman JE (1997) Bursts as a unit of neural information: making unreliable synapses reliable. Trends Neurosci 20:38-43.

Liu S, Rasmusson RL (1997) Hodgkin-Huxley and partially coupled inactivation models yield different voltage dependence of block. The American journal of physiology 272:H2013-2022.

Llinas R, Muhlethaler M (1988) Electrophysiology of guinea-pig cerebellar nuclear cells in the in vitro brain stem-cerebellar preparation. J Physiol 404:241-258.

London M, Hausser M (2005) Dendritic computation. Annu Rev Neurosci 28:503-532.

Luthi A, McCormick DA (1998) H-current: properties of a neuronal and network pacemaker. Neuron 21:9-12.

MacKay WA (1988) Unit activity in the cerebellar nuclei related to arm reaching movements. Brain Res 442:240-254.

Magee J, Hoffman D, Colbert C, Johnston D (1998) Electrical and calcium signaling in dendrites of hippocampal pyramidal neurons. Annual review of physiology 60:327-346.

Magee JC (1999) Dendritic Ih normalizes temporal summation in hippocampal CA1 neurons. Nat Neurosci 2:848.

Magee JC, Johnston D (1995) Synaptic activation of voltage-gated channels in the dendrites of hippocampal pyramidal neurons. Science 268:301-304.

Magee JC, Christofi G, Miyakawa H, Christie B, Lasser-Ross N, Johnston D (1995) Subthreshold synaptic activation of voltage-gated Ca2+ channels mediates a localized Ca2+ influx into the dendrites of hippocampal pyramidal neurons. J Neurophysiol 74:1335-1342.

Mapelli J, Gandolfi D, D'Angelo E (2010) High-pass filtering and dynamic gain regulation enhance vertical bursts transmission along the mossy fiber pathway of cerebellum. Front Cell Neurosci 4:1-13.

Markram H, Sakmann B (1994) Calcium transients in dendrites of neocortical neurons evoked by single subthreshold excitatory postsynaptic potentials via low-voltage-activated calcium channels. Proc Natl Acad Sci U S A 91:5207-5211.

Marr D (1969) A theory of cerebellar cortex. J Physiol 202:437.

Marrion NV, Tavalin SJ (1998) Selective activation of Ca2+-activated K+ channels by co-localized Ca2+ channels in hippocampal neurons. Nature 395:900-905.

McCormick DA, Pape HC (1990) Properties of a hyperpolarization-activated cation current and its role in rhythmic oscillation in thalamic relay neurones. J Physiol 431:291-318.

McCrea RA, Bishop GA, Kitai ST (1977) Electrophysiological and horseradish peroxidase studies of precerebellar afferents to the nucleus interpositus anterior. II. Mossy fiber system. Brain Res 122:215-228.

Mcculloch WS, Pitts W (1990) A Logical Calculus of the Ideas Immanent in Nervous Activity (Reprinted from Bulletin of Mathematical Biophysics, Vol 5, Pg 115-133, 1943). Bulletin of mathematical biology 52:99-115.

McDonough SI, Bean BP (1998) Mibefradil inhibition of T-type calcium channels in cerebellar purkinje neurons. Mol Pharmacol 54:1080-1087.

McKay BE, Turner RW (2004) Kv3 K+ channels enable burst output in rat cerebellar Purkinje cells. Eur J Neurosci 20:729-739.

McKay BE, Turner RW (2005) Physiological and morphological development of the rat cerebellar Purkinje cell. J Physiol 567:829-850.

McKay BE, Molineux ML, Mehaffey WH, Turner RW (2005) Kv1 K+ channels control Purkinje cell output to facilitate postsynaptic rebound discharge in deep cerebellar neurons. J Neurosci 25:1481-1492.

McKay BE, McRory JE, Molineux ML, Hamid J, Snutch TP, Zamponi GW, Turner RW (2006) Cav3 T-type calcium channel isoforms differentially distribute to somatic and dendritic compartments in rat central neurons. Eur J Neurosci 24:2581-2594.

McKay BE, Engbers JD, Mehaffey WH, Gordon GR, Molineux ML, Bains JS, Turner RW (2007) Climbing fiber discharge regulates cerebellar functions by controlling the intrinsic characteristics of purkinje cell output. J Neurophysiol 97:2590-2604.

Middleton JW, Yu N, Longtin A, Maler L (2011) Routing the flow of sensory signals using plastic responses to bursts and isolated spikes: experiment and theory. J Neurosci 31:2461-2473.

Mittmann W, Koch U, Hausser M (2005) Feed-forward inhibition shapes the spike output of cerebellar Purkinje cells. J Physiol 563:369-378.

Molineux ML, Fernandez FR, Mehaffey WH, Turner RW (2005) A-type and T-type currents interact to produce a novel spike latency-voltage relationship in cerebellar stellate cells. J Neurosci 25:10863-10873.

Molineux ML, Mehaffey WH, Tadayonnejad R, Anderson D, Tennent AF, Turner RW (2008) Ionic factors governing rebound burst phenotype in rat deep cerebellar neurons. J Neurophysiol 100:2684-2701.

Molineux ML, McRory JE, McKay BE, Hamid J, Mehaffey WH, Rehak R, Snutch TP, Zamponi GW, Turner RW (2006) Specific T-type calcium channel isoforms are associated with distinct burst phenotypes in deep cerebellar nuclear neurons. Proc Natl Acad Sci U S A 103:5555-5560.

Mouginot D, Bossu JL, Gahwiler BH (1997) Low-threshold Ca2+ currents in dendritic recordings from Purkinje cells in rat cerebellar slice cultures. J Neurosci 17:160-170.

Muri R, Knopfel T (1994) Activity induced elevations of intracellular calcium concentration in neurons of the deep cerebellar nuclei. J Neurophysiol 71:420-428.

Neylon CB, Nurgali K, Hunne B, Robbins HL, Moore S, Chen MX, Furness JB (2004) Intermediate conductance calcium-activated potassium channels in enteric neurons of the mouse: Pharmacological, molecular and immunochemical evidence for their role in mediating the slow afterhyperpolarization. J Neurochem 90:1414-1422.

Ngo-Anh TJ, Bloodgood BL, Lin M, Sabatini BL, Maylie J, Adelman JP (2005) SK channels and NMDA receptors form a Ca2+-mediated feedback loop in dendritic spines. Nat Neurosci 8:642-649.

Nguyen TV, Matsuyama H, Baell J, Hunne B, Fowler CJ, Smith JE, Nurgali K, Furness JB (2007) Effects of compounds that influence IK (KCNN4) channels on afterhyperpolarizing potentials, and determination of IK channel sequence, in guinea pig enteric neurons. J Neurophysiol 97:2024-2031.

Ohtsuka K, Noda H (1991) Saccadic burst neurons in the oculomotor region of the fastigial nucleus of macaque monkeys. J Neurophysiol 65:1422-1434.

Ohtsuki G, Piochon C, Adelman JP, Hansel C (2012) SK2 channel modulation contributes to compartment-specific dendritic plasticity in cerebellar Purkinje cells. Neuron 75:108-120.

Ohyama T, Nores WL, Murphy M, Mauk MD (2003) What the cerebellum computes. Trends Neurosci 26:222-227.

Oliver D, Klocker N, Schuck J, Baukrowitz T, Ruppersberg JP, Fakler B (2000) Gating of Ca2+-activated K+ channels controls fast inhibitory synaptic transmission at auditory outer hair cells. Neuron 26:595-601.

Orban G, Kiss T, Erdi P (2006) Intrinsic and synaptic mechanisms determining the timing of neuron population activity during hippocampal theta oscillation. J Neurophysiol 96:2889-2904.

Oswald AM, Doiron B, Maler L (2007) Interval coding. I. Burst interspike intervals as indicators of stimulus intensity. J Neurophysiol 97:2731-2743.

Oswald AM, Chacron MJ, Doiron B, Bastian J, Maler L (2004) Parallel processing of sensory input by bursts and isolated spikes. J Neurosci 24:4351-4362.

Pedarzani P, Stocker M (2008) Molecular and cellular basis of small--and intermediate-conductance, calcium-activated potassium channel function in the brain. Cell Mol Life Sci 65:3196-3217.

Pedroarena CM (2010) Mechanisms supporting transfer of inhibitory signals into the spike output of spontaneously firing cerebellar nuclear neurons in vitro. Cerebellum 9:67-76.

Pedroarena CM, Schwarz C (2003) Efficacy and short-term plasticity at GABAergic synapses between Purkinje and cerebellar nuclei neurons. J Neurophysiol 89:704-715.

Perez-Reyes E (2003) Molecular physiology of low-voltage-activated t-type calcium channels. Physiol Rev 83:117-161.

Perez-Reyes E (2006) Molecular characterization of T-type calcium channels. Cell Calcium 40:89-96.

Person AL, Perkel DJ (2005) Unitary IPSPs drive precise thalamic spiking in a circuit required for learning. Neuron 46:129-140.

Person AL, Raman IM (2012) Purkinje neuron synchrony elicits time-locked spiking in the cerebellar nuclei. Nature 481:502-505.

Piochon C, Irinopoulou T, Brusciano D, Bailly Y, Mariani J, Levenes C (2007) NMDA receptor contribution to the climbing fiber response in the adult mouse Purkinje cell. J Neurosci 27:10797-10809.

Prescott SA, De Koninck Y (2005) Integration time in a subset of spinal lamina I neurons is lengthened by sodium and calcium currents acting synergistically to prolong subthreshold depolarization. J Neurosci 25:4743-4754.

Pugh JR, Raman IM (2006) Potentiation of mossy fiber EPSCs in the cerebellar nuclei by NMDA receptor activation followed by postinhibitory rebound current. Neuron 51:113-123.

Pugh JR, Raman IM (2008) Mechanisms of potentiation of mossy fiber EPSCs in the cerebellar nuclei by coincident synaptic excitation and inhibition. J Neurosci 28:10549-10560.

Raman IM, Bean BP (1999) Ionic currents underlying spontaneous action potentials in isolated cerebellar Purkinje neurons. J Neurosci 19:1663-1674.

Raman IM, Gustafson AE, Padgett D (2000) Ionic currents and spontaneous firing in neurons isolated from the cerebellar nuclei. J Neurosci 20:9004-9016.

Rancz EA, Ishikawa T, Duguid I, Chadderton P, Mahon S, Hausser M (2007) High-fidelity transmission of sensory information by single cerebellar mossy fibre boutons. Nature 450:1245-1248.

Randall AD, Tsien RW (1997) Contrasting biophysical and pharmacological properties of T-type and R-type calcium channels. Neuropharmacology 36:879-893.

Rauer H, Lanigan MD, Pennington MW, Aiyar J, Ghanshani S, Cahalan MD, Norton RS, Chandy KG (2000) Structure-guided transformation of charybdotoxin yields an analog that selectively targets Ca(2+)-activated over voltage-gated K(+) channels. J Biol Chem 275:1201-1208.

Rehak R, Bartoletti TM, Engbers JDT, Berecki G, Turner RW, Zamponi GW (2013) Low voltage activation of KCa1.1 current by Cav3-KCa1.1 complexes. PLoS ONE In Press.

Richardson MJ, Melamed O, Silberberg G, Gerstner W, Markram H (2005) Short-term synaptic plasticity orchestrates the response of pyramidal cells and interneurons to population bursts. J Comput Neurosci 18:323-331.

Riegel AC, Lupica CR (2004) Independent presynaptic and postsynaptic mechanisms regulate endocannabinoid signaling at multiple synapses in the ventral tegmental area. J Neurosci 24:11070-11078.

Robinson FR, Fuchs AF (2001) The role of the cerebellum in voluntary eye movements. Annu Rev Neurosci 24:981-1004.

Robinson RB, Siegelbaum SA (2003) Hyperpolarization-activated cation currents: from molecules to physiological function. Annual review of physiology 65:453-480.

Rose GJ, Fortune ES (1999) Frequency-dependent PSP depression contributes to low-pass temporal filtering in Eigenmannia. J Neurosci 19:7629-7639.

Rowland NC, Jaeger D (2005) Coding of tactile response properties in the rat deep cerebellar nuclei. J Neurophysiol 94:1236-1251.

Rowland NC, Jaeger D (2008) Responses to tactile stimulation in deep cerebellar nucleus neurons result from recurrent activation in multiple pathways. J Neurophysiol 99:704-717.

Ruigrok TJ (1997) Cerebellar nuclei: the olivary connection. Prog Brain Res 114:167-192.

Sah P, Davies P (2000) Calcium-activated potassium currents in mammalian neurons. Clin Exp Pharmacol Physiol 27:657-663.

Saitow F, Murano M, Suzuki H (2009) Modulatory effects of serotonin on GABAergic synaptic transmission and membrane properties in the deep cerebellar nuclei. J Neurophysiol 101:1361-1374.

Sanchez-Alonso JL, Halliwell JV, Colino A (2008) ZD 7288 inhibits T-type calcium current in rat hippocampal pyramidal cells. Neurosci Lett 439:275-280.

Sangrey T, Jaeger D (2010) Analysis of distinct short and prolonged components in rebound spiking of deep cerebellar nucleus neurons. Eur J Neurosci 32:1646-1657.

Santoro B, Baram TZ (2003) The multiple personalities of h-channels. Trends Neurosci 26:550-554.

Schneider ER, Civillico EF, Wang SS (2013) Calcium-based dendritic excitability and Its regulation in the deep cerebellar nuclei. J Neurophysiol.

Schneiderman N, Gormezano I (1964) Conditioning of the Nictitating Membrane of the Rabbit as a Function of Cs-Us Interval. J Comp Physiol Psychol 57:188-195.

Schonewille M, Gao Z, Boele HJ, Veloz MF, Amerika WE, Simek AA, De Jeu MT, Steinberg JP, Takamiya K, Hoebeek FE, Linden DJ, Huganir RL, De Zeeuw CI (2011) Reevaluating the role of LTD in cerebellar motor learning. Neuron 70:43-50.

Schwartz AB, Ebner TJ, Bloedel JR (1987) Responses of interposed and dentate neurons to perturbations of the locomotor cycle. Exp Brain Res 67:323-338.

Shah M, Haylett DG (2000) The pharmacology of hSK1 Ca2+-activated K+ channels expressed in mammalian cell lines. Br J Pharmacol 129:627-630.

Sharp AA, O'Neil MB, Abbott LF, Marder E (1993) Dynamic clamp: computer-generated conductances in real neurons. J Neurophysiol 69:992-995.

Sherman SM (2001) Tonic and burst firing: dual modes of thalamocortical relay. Trends Neurosci 24:122-126.

Shibata R, Nakahira K, Shibasaki K, Wakazono Y, Imoto K, Ikenaka K (2000) A-type K+ current mediated by the Kv4 channel regulates the generation of action potential in developing cerebellar granule cells. J Neurosci 20:4145-4155.

Shin SL, De Schutter E (2006) Dynamic synchronization of Purkinje cell simple spikes. J Neurophysiol 96:3485-3491.

Shin SL, Hoebeek FE, Schonewille M, De Zeeuw CI, Aertsen A, De Schutter E (2007) Regular patterns in cerebellar purkinje cell simple spike trains. PLoS ONE 2:e485.

Sidach SS, Mintz IM (2002) Kurtoxin, a gating modifier of neuronal high- and low-threshold ca channels. J Neurosci 22:2023-2034.

Slemmon JR, Morgan JI, Fullerton SM, Danho W, Hilbush BS, Wengenack TM (1996) Camstatins are peptide antagonists of calmodulin based upon a conserved structural motif in PEP-19, neurogranin, and neuromodulin. J Biol Chem 271:15911-15917.

Smith MC (1968) CS-US interval and US intensity in classical conditioning of the rabbit's nictitating membrane response. J Comp Physiol Psychol 66:679-687.

Smith MR, Nelson AB, Du Lac S (2002) Regulation of firing response gain by calcium-dependent mechanisms in vestibular nucleus neurons. J Neurophysiol 87:2031-2042.

Sobel EC, Tank DW (1994) In vivo Ca2+ dynamics in a cricket auditory neuron: an example of chemical computation. Science 263:823-826.

Staley KJ, Soldo BL, Proctor WR (1995) Ionic mechanisms of neuronal excitation by inhibitory GABAA receptors. Science 269:977-981.

Stanton GB (1980) Topographical organization of ascending cerebellar projections from the dentate and interposed nuclei in Macaca mulatta: an anterograde degeneration study. J Comp Neurol 190:699-731.

Steriade M, McCormick DA, Sejnowski TJ (1993) Thalamocortical oscillations in the sleeping and aroused brain. Science 262:679-685.

Steuber V, Schultheiss NW, Silver RA, De Schutter E, Jaeger D (2011) Determinants of synaptic integration and heterogeneity in rebound firing explored with data-driven models of deep cerebellar nucleus cells. J Comput Neurosci 30:633-658.

Steuber V, Mittmann W, Hoebeek FE, Silver RA, De Zeeuw CI, Hausser M, De Schutter E (2007) Cerebellar LTD and pattern recognition by Purkinje cells. Neuron 54:121-136.

Stocker M (2004) Ca(2+)-activated K+ channels: molecular determinants and function of the SK family. Nat Rev Neurosci 5:758-770.

Stoodley CJ (2011) The Cerebellum and Cognition: Evidence from Functional Imaging Studies. Cerebellum.

Storm JF (1987) Action potential repolarization and a fast after-hyperpolarization in rat hippocampal pyramidal cells. J Physiol 385:733-759.

Strobaek D, Jorgensen TD, Christophersen P, Ahring PK, Olesen SP (2000) Pharmacological characterization of small-conductance Ca(2+)-activated K(+) channels stably expressed in HEK 293 cells. Br J Pharmacol 129:991-999.

Swensen AM, Bean BP (2003) Ionic mechanisms of burst firing in dissociated Purkinje neurons. J Neurosci 23:9650-9663.

Tadayonnejad R, Mehaffey WH, Anderson D, Turner RW (2009) Reliability of triggering postinhibitory rebound bursts in deep cerebellar neurons. Channels (Austin) 3:149-155.

Tadayonnejad R, Anderson D, Molineux ML, Mehaffey WH, Jayasuriya K, Turner RW (2010) Rebound Discharge in Deep Cerebellar Nuclear Neurons In Vitro. Cerebellum.

Talavera K, Nilius B (2006) Biophysics and structure-function relationship of T-type Ca2+ channels. Cell Calcium 40:97-114.

Talley EM, Cribbs LL, Lee JH, Daud A, Perez-Reyes E, Bayliss DA (1999) Differential distribution of three members of a gene family encoding low voltage-activated (T-type) calcium channels. J Neurosci 19:1895-1911.

Tanaka S, Kato H, Koike T (2000) Microglial Response Factor (MRF)-1: Constitutive Expression in Ramified Microglia and Upregulation upon Neuronal Death Induced by Ischemia or Glutamate Exposure. Zoological science 17:571-578.

Telgkamp P, Raman IM (2002) Depression of inhibitory synaptic transmission between Purkinje cells and neurons of the cerebellar nuclei. J Neurosci 22:8447-8457.

Telgkamp P, Padgett DE, Ledoux VA, Woolley CS, Raman IM (2004) Maintenance of high-frequency transmission at purkinje to cerebellar nuclear synapses by spillover from boutons with multiple release sites. Neuron 41:113-126.

Tempia F, Alojado ME, Strata P, Knopfel T (2001) Characterization of the mGluR(1)-mediated electrical and calcium signaling in Purkinje cells of mouse cerebellar slices. J Neurophysiol 86:1389-1397.

Teune TM, van der Burg J, van der Moer J, Voogd J, Ruigrok TJ (2000) Topography of cerebellar nuclear projections to the brain stem in the rat. Prog Brain Res 124:141-172.

Thach WT, Bastian AJ (2004) Role of the cerebellum in the control and adaptation of gait in health and disease. Prog Brain Res 143:353-366.

Timmann D, Watts S, Hore J (1999) Failure of cerebellar patients to time finger opening precisely causes ball high-low inaccuracy in overarm throws. J Neurophysiol 82:103-114.

Toledo-Rodriguez M, Markram H (2007) Single-cell RT-PCR, a technique to decipher the electrical, anatomical, and genetic determinants of neuronal diversity. Methods Mol Biol 403:123-139.

Tsay D, Dudman JT, Siegelbaum SA (2007) HCN1 channels constrain synaptically evoked Ca2+ spikes in distal dendrites of CA1 pyramidal neurons. Neuron 56:1076-1089.

Turner RW, Anderson D, Zamponi GW (2011) Signaling complexes of voltage-gated calcium channels. Channels (Austin) 5:440-448.

Uhlenbeck GE, Ornstein LS (1930) On the theory of the Brownian motion. Phys Rev 36:0823-0841.

Ulrich D, Huguenard JR (1997) GABA(A)-receptor-mediated rebound burst firing and burst shunting in thalamus. J Neurophysiol 78:1748-1751.

Urban NN, Henze DA, Barrionuevo G (1998) Amplification of perforant-path EPSPs in CA3 pyramidal cells by LVA calcium and sodium channels. J Neurophysiol 80:1558-1561.

Usowicz MM, Sugimori M, Cherksey B, Llinas R (1992) P-type calcium channels in the somata and dendrites of adult cerebellar Purkinje cells. Neuron 9:1185-1199.

Uusisaari M, Knopfel T (2010) Functional Classification of Neurons in the Mouse Lateral Cerebellar Nuclei. Cerebellum.

Uusisaari M, De Schutter E (2011) The mysterious microcircuitry of the cerebellar nuclei. J Physiol.

Uusisaari M, Obata K, Knopfel T (2007) Morphological and electrophysiological properties of GABAergic and non-GABAergic cells in the deep cerebellar nuclei. J Neurophysiol 97:901-911.

van de Vrede Y, Fossier P, Baux G, Joels M, Chameau P (2007) Control of IsAHP in mouse hippocampus CA1 pyramidal neurons by RyR3-mediated calcium-induced calcium release. Pflugers Arch 455:297-308.

van Welie I, du Lac S (2011) Bidirectional control of BK channel open probability by CAMKII and PKC in medial vestibular nucleus neurons. J Neurophysiol 105:1651-1659.

Vogalis F, Furness JB, Kunze WA (2001) Afterhyperpolarization current in myenteric neurons of the guinea pig duodenum. J Neurophysiol 85:1941-1951.

Vogalis F, Harvey JR, Furness JB (2002a) TEA- and apamin-resistant K(Ca) channels in guinea-pig myenteric neurons: slow AHP channels. J Physiol 538:421-433.

Vogalis F, Harvey JR, Furness JB (2003) PKA-mediated inhibition of a novel K+ channel underlies the slow after-hyperpolarization in enteric AH neurons. J Physiol 548:801-814.

Vogalis F, Harvey JR, Neylon CB, Furness JB (2002b) Regulation of K+ channels underlying the slow afterhyperpolarization in enteric afterhyperpolarization-generating myenteric neurons: role of calcium and phosphorylation. Clin Exp Pharmacol Physiol 29:935-943.

Wahl-Schott C, Biel M (2009) HCN channels: structure, cellular regulation and physiological function. Cell Mol Life Sci 66:470-494.

Walter JT, Alvina K, Womack MD, Chevez C, Khodakhah K (2006) Decreases in the precision of Purkinje cell pacemaking cause cerebellar dysfunction and ataxia. Nat Neurosci 9:389-397.

Watanabe S, Takagi H, Miyasho T, Inoue M, Kirino Y, Kudo Y, Miyakawa H (1998) Differential roles of two types of voltage-gated Ca2+ channels in the dendrites of rat cerebellar Purkinje neurons. Brain Res 791:43-55.

Weber AM, Wong FK, Tufford AR, Schlichter LC, Matveev V, Stanley EF (2010) N-type Ca2+ channels carry the largest current: implications for nanodomains and transmitter release. Nat Neurosci 13:1348-1350.

Wei AD, Gutman GA, Aldrich R, Chandy KG, Grissmer S, Wulff H (2005) International Union of Pharmacology. LII. Nomenclature and molecular relationships of calcium-activated potassium channels. Pharmacol Rev 57:463-472.

Westenbroek RE, Hell JW, Warner C, Dubel SJ, Snutch TP, Catterall WA (1992) Biochemical properties and subcellular distribution of an N-type calcium channel alpha 1 subunit. Neuron 9:1099-1115.

Wetmore DZ, Mukamel EA, Schnitzer MJ (2008) Lock-and-key mechanisms of cerebellar memory recall based on rebound currents. J Neurophysiol 100:2328-2347.

Williams S, Serafin M, Muhlethaler M, Bernheim L (1997) Distinct contributions of high- and low-voltage-activated calcium currents to afterhyperpolarizations in cholinergic nucleus basalis neurons of the guinea pig. J Neurosci 17:7307-7315.

Williams SR, Christensen SR, Stuart GJ, Hausser M (2002) Membrane potential bistability is controlled by the hyperpolarization-activated current I(H) in rat cerebellar Purkinje neurons in vitro. J Physiol 539:469-483.

Wolfart J, Roeper J (2002) Selective coupling of T-type calcium channels to SK potassium channels prevents intrinsic bursting in dopaminergic midbrain neurons. J Neurosci 22:3404-3413.

Womack MD, Khodakhah K (2002) Characterization of large conductance Ca2+-activated K+ channels in cerebellar Purkinje neurons. Eur J Neurosci 16:1214-1222.

Womack MD, Chevez C, Khodakhah K (2004) Calcium-activated potassium channels are selectively coupled to P/Q-type calcium channels in cerebellar Purkinje neurons. J Neurosci 24:8818-8822.

Wulff H, Gutman GA, Cahalan MD, Chandy KG (2001) Delineation of the clotrimazole/TRAM-34 binding site on the intermediate conductance calcium-activated potassium channel, IKCa1. J Biol Chem 276:32040-32045.

Wulff H, Kolski-Andreaco A, Sankaranarayanan A, Sabatier JM, Shakkottai V (2007) Modulators of small- and intermediate-conductance calcium-activated potassium channels and their therapeutic indications. Curr Med Chem 14:1437-1457.

Wulff H, Miller MJ, Hansel W, Grissmer S, Cahalan MD, Chandy KG (2000) Design of a potent and selective inhibitor of the intermediate-conductance Ca2+-activated K+ channel, IKCa1: a potential immunosuppressant. Proc Natl Acad Sci U S A 97:8151-8156.

Xia XM, Fakler B, Rivard A, Wayman G, Johnson-Pais T, Keen JE, Ishii T, Hirschberg B, Bond CT, Lutsenko S, Maylie J, Adelman JP (1998) Mechanism of calcium gating in small-conductance calcium-activated potassium channels. Nature 395:503-507.

Yartsev MM, Givon-Mayo R, Maller M, Donchin O (2009) Pausing purkinje cells in the cerebellum of the awake cat. Front Syst Neurosci 3:2.

Yokoyama CT, Westenbroek RE, Hell JW, Soong TW, Snutch TP, Catterall WA (1995) Biochemical properties and subcellular distribution of the neuronal class E calcium channel alpha 1 subunit. J Neurosci 15:6419-6432.

Yunker AM, McEnery MW (2003) Low-voltage-activated ("T-Type") calcium channels in review. J Bioenerg Biomembr 35:533-575.

Zackowski KM, Thach WT, Jr., Bastian AJ (2002) Cerebellar subjects show impaired coupling of reach and grasp movements. Exp Brain Res 146:511-522.

Zador AM (2000) The basic unit of computation. Nat Neurosci 3 Suppl:1167.

Zamponi GW, Bourinet E, Snutch TP (1996) Nickel block of a family of neuronal calcium channels: subtype- and subunit-dependent action at multiple sites. J Membr Biol 151:77-90.

Zhang W, Shin JH, Linden DJ (2004) Persistent changes in the intrinsic excitability of rat deep cerebellar nuclear neurons induced by EPSPs or IPSP bursts. J Physiol (Lond) 561.3:703-719.

Zhang Y, Niu X, Brelidze TI, Magleby KL (2006) Ring of negative charge in BK channels facilitates block by intracellular Mg2+ and polyamines through electrostatics. J Gen Physiol 128:185-202.

Zheng N, Raman IM (2009) Ca currents activated by spontaneous firing and synaptic disinhibition in neurons of the cerebellar nuclei. J Neurosci 29:9826-9838.

Zheng N, Raman IM (2011) Prolonged postinhibitory rebound firing in the cerebellar nuclei mediated by group I metabotropic glutamate receptor potentiation of L-type calcium currents. J Neurosci 31:10283-10292.